

# The University of Sheffield



## Investigation of Torque Characteristics of Permanent Magnet and Electrically Excited Machines

**Wenqiang Chu**

A thesis submitted for the degree of Doctor of Philosophy

Department of Electronic and Electrical Engineering

The University of Sheffield

Mappin Street, Sheffield, S1 3JD, UK

**21 May 2013**

## ABSTRACT

This thesis is focused on the comparative investigation on the torque characteristics, both average torque and torque ripple, of permanent magnet (PM) and electrically excited (EE) machines for direct drive applications, which require both high torque density and low torque ripple.

The effectiveness of two of the most widely used methods, i.e., rotor shaping and skewing, for torque ripple reduction in EE and PM machines is investigated. It is found that the effectiveness of skewing largely depends on the axial variation of torque ripple phase but less on its magnitude under skewing. It is further found that, in both linear and nonlinear cases, the on-load torque ripple cannot be fully eliminated by skewing one on-load torque ripple period or any other angles, except  $360^\circ$  electrical, which is impractical. The torque ripple may be even increased by skewing, especially when the cogging torque is low and electric loading is high. An improved skewing is developed by optimising both the skewing and current phase advance angles when the conventional skewing method fails. Compared with PM machines, rotor shaping is less effective on torque ripple reduction in EE machines due to the asymmetric magnetic saturation of the stator and rotor cores. However, if rotor skewing is used then EE machines can still achieve the same low level of torque ripple as PM machines.

In order to better understand characteristics of on-load torque and hence improve it, the on-load torque separation of PM machines is investigated as well. It is found that the average torque components can be appropriately separated using the virtual work principle but not by the Maxwell stress tensor. For the on-load cogging torque calculation, which is the most difficult challenge for on-load torque ripple separation, a new method is proposed by combining the virtual work principle with an improved frozen permeability method.

For torque density optimisation, analytical methods are often desirable. This thesis develops an analytical model for PM machines having external rotor. It is shown that the torque density is maximum when the average airgap flux density is slightly lower than half of the maximum flux density in the stator. In order to compare the torque densities between EE and PM machines, a simplified analytical model of EE machines is developed as well. It is shown that, for EE machines, there is an optimal pole number to maximize the torque densities and it is more advantageous for large volume applications. PM machines can exhibit higher than  $\sqrt{2}$  times torque densities of EE machines. The designs of maximum torque per weight are more cost-effective and result in a significantly larger airgap diameter than the designs of maximum torque per volume.

## **ACKNOWLEDGEMENTS**

I give my grateful thanks to Prof. Z. Q. Zhu for his professional and successful supervision during my PhD study. His inspirations and encouragement on my research will also be preciously important to me for the rest of my life.

I would like to thank current and former members of the Electrical Machines and Drives Group at the University of Sheffield, particularly Dr. Jintao Chen, Dr Lijian Wu, Dr Zhenping Xia, and Mr. David Evans for their many helpful discussions. Further thanks to the technical staff for their helps.

I also would like to acknowledge Sheffield Siemens Wind Power Research Centre for the PhD studentship.

Finally, I have appreciation to Dr. Yumiao Tian, my girlfriend, for her support and thanks to my family for their endless care.

# Contents

<b>ABSTRACT</b>	<b>2</b>
<b>ACKNOWLEDGEMENTS</b>	<b>3</b>
<b>NOMECLATURE</b>	<b>8</b>
<b>CHAPTER 1 GENERAL INTRODUCTION</b>	<b>12</b>
1.1 Introduction	12
1.2 Electric machines	13
1.2.1 Induction Machines	15
1.2.2 Electrically Excited Machines	15
1.2.3 Permanent Magnet Machines	16
1.2.4 Comparison and Summary	20
1.3 Torque Density Maximization	21
1.4 Torque Ripple Minimization	24
1.4.1 Rotor Shaping	26
1.4.2 Skewing	33
1.4.3 Other Methods	35
1.5 On-load Torque Separation	37
1.6 Outline of Thesis	40
1.7 Major Contributions of Thesis	41
<b>CHAPTER 2 ANALYTICAL OPTIMISATION OF EXTERNAL ROTOR PERMANENT MAGNET MACHINES</b>	<b>42</b>
2.1 Introduction	42
2.2 General Analytical Torque Equation	45
2.3 Optimal Stator Split Ratio, Flux Density Ratio, and Split Ratio	47
2.3.1 Optimal Stator Split Ratio for Specific Flux Density Ratio	48
2.3.2 Optimal Split Ratio and Flux Density Ratio	49
2.4 Practical Design Considerations	52
2.4.1 Influence of Airgap Flux Density Distribution	52
2.4.2 Influence of Slot and Pole Numbers	54
2.4.3 Influence of Slot Shape	55
2.4.4 Influence of Tooth-tips and Slot Wedges	56
2.4.5 Influence of End-windings	57

<b>2.5</b>	<b>Optimisation with Fixed Rotor Yoke Thickness</b> .....	<b>58</b>
<b>2.6</b>	<b>Optimisation with Fixed Inner Diameter</b> .....	<b>58</b>
<b>2.7</b>	<b>Verification by FEA and Measurements</b> .....	<b>61</b>
<b>2.8</b>	<b>Summary</b> .....	<b>63</b>

**CHAPTER 3 INVESTIGATION OF TORQUE RIPPLE IN PERMANENT MAGNET SYNCHRONOUS MACHINE WITH SKEWING .....64**

<b>3.1</b>	<b>Introduction</b> .....	<b>64</b>
<b>3.2</b>	<b>Prototype Machines</b> .....	<b>66</b>
<b>3.3</b>	<b>Torque Waveforms and Ripples with/without Skewing by One On-load Torque Ripple Period</b> ..	<b>68</b>
<b>3.4</b>	<b>Mechanism and Effectiveness of Skewing</b> .....	<b>71</b>
3.4.1	Open-circuit .....	72
3.4.2	Half-load .....	72
3.4.3	Full-load .....	74
3.4.4	Comparison between M1 and M2 .....	76
3.4.5	Summary .....	78
<b>3.5</b>	<b>Influence of Step Skewing Number on Torque Ripple</b> .....	<b>78</b>
<b>3.6</b>	<b>Effectiveness of Skewing with Different Skewing Angles</b> .....	<b>80</b>
<b>3.7</b>	<b>Effectiveness of Skewing Under Linear Case</b> .....	<b>82</b>
3.7.1	Analytical Analysis .....	82
3.7.2	FE results .....	85
<b>3.8</b>	<b>Improved Method</b> .....	<b>86</b>
<b>3.9</b>	<b>3-D FE Verification</b> .....	<b>89</b>
<b>3.10</b>	<b>Summary</b> .....	<b>90</b>

**CHAPTER 4 AVERAGE TORQUE SEPARATION IN PERMANENT MAGNET SYNCHRONOUS MACHINES USING FROZEN PERMEABILITY .....91**

<b>4.1</b>	<b>Introduction</b> .....	<b>91</b>
<b>4.2</b>	<b>Prototype Machine</b> .....	<b>93</b>
<b>4.3</b>	<b>Frozen Permeability Method</b> .....	<b>94</b>
4.3.1	Principle and Procedure .....	94
4.3.2	Field Distributions .....	95
4.3.3	Flux Linkage Results .....	97
<b>4.4</b>	<b>Torque Calculation Methods</b> .....	<b>100</b>

<b>4.5</b>	<b>Average Torque Separation Based on Frozen Permeability Method</b>	<b>102</b>
<b>4.6</b>	<b>Variation of Average Torque Components</b>	<b>108</b>
<b>4.7</b>	<b>Summary</b>	<b>110</b>
<b>4.8</b>	<b>Appendix</b>	<b>110</b>

**CHAPTER 5 ON-LOAD COGGING TORQUE CALCULATION IN PERMENENT MAGNET MACHINES ..... 111**

<b>5.1</b>	<b>Introduction</b>	<b>111</b>
<b>5.2</b>	<b>Prototype Machine</b>	<b>113</b>
<b>5.3</b>	<b>Open-circuit Cogging Torque Calculation Methods</b>	<b>113</b>
<b>5.4</b>	<b>Existing On-load Cogging Torque Calculation Methods</b>	<b>113</b>
5.4.1	Virtual Work Methods Without Using FP Technique	114
5.4.2	Maxwell Stress Tensor Methods with FP Technique	114
<b>5.5</b>	<b>Proposed On-load Cogging Torque Calculation Method</b>	<b>115</b>
5.5.1	Proposed Method	115
5.5.2	Improved FP Method	115
<b>5.6</b>	<b>Linear Cases</b>	<b>120</b>
<b>5.7</b>	<b>Nonlinear Cases</b>	<b>122</b>
<b>5.8</b>	<b>Summary</b>	<b>125</b>

**CHAPTER 6 ANALYTICAL OPTIMISATION AND COMPARISON OF TORQUE DENSITIES BETWEEN ELECTRICALLY EXCITED AND PERMANENT MAGNET MACHINES ..... 126**

<b>6.1</b>	<b>Introduction</b>	<b>126</b>
<b>6.2</b>	<b>General Torque Equation</b>	<b>128</b>
<b>6.3</b>	<b>Maximum Torque Per Volume of PM Machines</b>	<b>130</b>
<b>6.4</b>	<b>Maximum Torque per Volume of EE Machines</b>	<b>133</b>
6.4.1	Torque Equation	133
6.4.2	Optimisation	134
<b>6.5</b>	<b>Comparison on Maximum Torque per Volume</b>	<b>138</b>
<b>6.6</b>	<b>Optimisation of Maximum Torque per Weight</b>	<b>141</b>
6.6.1	Analytical Model	141
6.6.2	Optimisation	142
6.6.3	Results and Comparison	142

6.7	Max. $T/V$ versus Max. $T/G$ .....	145
6.8	FE and Experimental Verifications .....	147
6.9	Summary .....	151
<b>CHAPTER 7 COMPARATIVE INVESTIGATION ON INFLUENCE OF ROTOR SHAPING AND SKEWING BETWEEN ELECTRICALLY EXCITED AND PERMANENT MAGNET MACHINES .....</b>		<b>152</b>
7.1	Introduction .....	152
7.2	EE and PM Prototype Machines .....	153
7.3	Influence of Rotor Shaping.....	155
7.3.1	EE Machines with Different Rotor Shapes .....	155
7.3.2	Comparison between EE and PM Machines .....	161
7.4	Influence of Skewing.....	163
7.5	Summary .....	173
<b>CHAPTER 8 GENERAL CONCLUSION AND FUTURE WORK .....</b>		<b>174</b>
8.1	Conclusions .....	174
8.1.1	Average Torque Optimisation and Comparison.....	174
8.1.2	Torque Ripple Minimization.....	175
8.1.3	On-load Torque Separation .....	175
8.2	Future Work.....	176
8.2.1	Ways of Reducing $Q$ -axis Magnetic Field in EE Machines .....	176
8.2.2	Torque Ripple Reduction in EE Machines Using Combined Rotor Shapes.....	177
<b>References .....</b>		<b>178</b>
<b>APPENDIX A ANALYTICAL MODELING AND INVESTIGATION OF TRANSIENT RESPONSE OF PM MACHINES WITH THREE-PHASE SHORT-CIRCUIT FAULT.....</b>		<b>192</b>
<b>APPENDIX B DESIGNS OF 3kW PM PROTOTYPE MACHINES.....</b>		<b>207</b>
<b>APPENDIX C DESIGN OF EE AND PM PROTOTYPE MACHINES FOR COMPARISON ON ROTOR SHAPING AND SKEWING .....</b>		<b>235</b>
<b>APPENDIX D PUBLICATIONS .....</b>		<b>240</b>

## NOMECLATURE

$a_3$	Normalised amplitude of third order harmonic
$A_a, A_f$	Total stator slot and field winding areas per machine
$b_t$	Minimum stator tooth width
$B$	Flux density
$B_{all}$	Resultant flux density with both permanent magnet (PM) and armature excitations
$B_i, B_{PM}$	Resultant flux density with armature or PM excitation only
$B_n, B_t$	Normal and tangential flux density components
$B_n(\text{open})$	Normal flux density component on open circuit
$B_t(\text{open})$	Tangential flux density component on open circuit
$B_p$	Parallel flux density component in permanent magnets
$B_m$	Maximum flux density in the lamination
$B_r$	Magnet remanence
$B_{\delta av}$	Average airgap flux density over pole arc
$B_{\delta m}$	Maximum airgap flux density over pole arc
$B(\text{FP}, i)$	Resultant flux density with armature only using frozen permeability (FP) method
$B(\text{FP}, \text{PM})$	Resultant flux density with PM excitation only using frozen permeability (FP) method
$D_o$	Outer diameters
$D_i$	Inner diameter
$D_{ro}$	Rotor outer diameter
$D_{ry}$	Diameter at outer surface of rotor yoke
$D_{sb}$	Diameter at slot bottom
$D_{so}$	Stator outer diameter
$D_\delta$	Airgap diameter
$E_a$	Phase back electromagnetic force in root mean square (RMS)
$G$	Total active material weight
$G_a, G_{sc}, G_r$	Active material weights of armature winding, stator core, and rotor
$h_t$	Equivalent tooth tip height including slot wedge
$h_{ps}$	Pole shoe height of electrically excited machines
$h_{sc}$	Stator yoke thickness
$H$	Magnetic field strength
$H_{all}$	Magnetic field strength due to permanent magnet and armature excitations
$H_i$	Magnetic field strength due to armature excitation only
$H_{pm}$	Magnetic field strength due to permanent magnet excitation only
$I_a$	Phase current in RMS
$I_{ap}$	Peak value of phase current
$I_f$	Field current of electrically excited machines in DC
$k$	Harmonic orders, $k=1, 2, 3, \dots$
$k_{5sk}, k_{7sk}$	Skewing factor of sixth-order torque ripples due to fifth and seventh flux linkages
$k_{avsk}$	Skewing factor of average torque
$k_{cksk}$	Skewing factor of $k$ th-order cogging torque component
$k_{dp}$	Winding factor
$k_m$	Magnitude ratio of airgap flux density distribution
$k_{pa}, k_{pf}$	Armature and field winding packing factors
$k_{sb}$	Stator yoke coefficient

$k_\phi$	Flux ratio of airgap flux density distribution
$L_{aend}$	Armature end winding length (single side)
$L_{dd}, L_{qq}$	$D$ - and $q$ -axis self-inductances
$L_{dq}$	Mutual inductance between $d$ - and $q$ -axes
$L_{ef}$	Effective axial length
$L_{fend}$	Field end winding length (single side)
$N$	Number of skewing steps
$N_a$	Number of turns per phase
$N_a I_a, N_f I_f$	Armature and field magnetomotive forces
$N_s$	Slot number
$p$	Number of pole pairs
$p_{cu}, p_{cua}, p_{cuf}$	Total, armature and excitation copper losses
$r$	Radius of integration path
$R_{arc}$	Radius of offset centre arc
$T$	Output torque
$T_1, T_2$	Torque components of the first and second slice of 2-step skewed machines
$T_6(em)$ ,	Sixth harmonic of electromagnetic torque
$T_6(5), T_6(7)$	Sixth torque components contributed by the fifth and seventh flux linkages
$T_{av}$	Average torque
$T_c$	Cogging torque without skewing
$T_c(k)$	Magnitude of $k$ th-order cogging torque components
$T_c(open)$	Open-circuit cogging torque
$T_c(load)$	On-load cogging torque
$T_{dq0}$	Calculated torque using classical $dq0$ model
$T_{in}$	Corresponding torque of input power
$T_{mw}$	Calculated torque using Maxwell stress tensor method
$T_{mw}(FP,i)$	Calculated torque with on-load armature field only using Maxwell stress tensor method
$T_{mw}(FP,PM)$	Calculated torque with on-load PM field only using Maxwell stress tensor method
$T_{mw}(rel)$	Calculated reluctance torque using Maxwell stress tensor method
$T_{mw}(PM)$	Calculated PM torque using Maxwell stress tensor method
$T_{PM}$	PM torque
$T_{PM}(d)$	PM torque due to $d$ -axis PM flux linkage
$T_{PM}(q)$	PM torque due to $q$ -axis PM flux linkage
$T_r$	Reluctance torque
$T_r(d-q)$	Reluctance torque due to $d$ - and $q$ -axis self-inductances
$T_r(dq)$	Reluctance torque due to mutual inductance between $d$ - and $q$ -axes
$T_{sk}$	Output torque with skewing
$T_{vir}$	Calculated torque using virtual work principle
$T_{vir}(FP,i)$	Calculated torque with on-load armature field only using virtual work principle
$T_{vir}(FP,PM)$	Calculated torque with on-load PM field only using virtual work principle
$T_{vir}(rel)$	Calculated reluctance torque using virtual work principle
$T_{vir}(PM)$	Calculated PM torque using virtual work principle
$W_m$	Magnetic energy
$W_{mlc}$	Magnetic energy stored in the system less the magnetic energy stored in the coils
$W_m'$	Magnetic co-energy
$W_m(FP,i)$	Magnetic energy with on-load armature field only

$W_m(\text{FP,PM})$	Magnetic energy with on-load PM field only
$w_m$	Magnetic energy density
$w_{\text{air}}$	Magnetic energy density in air
$w_{\text{iron}}$	Magnetic energy density in soft-magnet materials
$w_{\text{PM}}$	Magnetic energy density in hard-magnet materials
$\alpha_p$	Pole arc to pole pitch ratio
$\beta$	Current phase advance angle
$\gamma$	Flux density ratio
$\delta, \delta'$	Mechanical and equivalent airgap lengths
$\delta_{ad}$	Equivalent airgap length representing magnetic reluctance in laminations
$\theta$	Rotor position in electrical angle
$\theta_5, \theta_7$	Phase of fifth and seventh flux linkage components
$\theta_{ck}$	Phase of $k$ th-order cogging torque components
$\theta_m$	Rotor position in mechanical angle
$\theta_{sk}$	Skewing angle (electrical)
$\lambda_r$	Split ratio of inner diameter to the outer diameter
$\lambda_r$	Rotor split ratio of rotor inner diameter to the rotor outer diameter
$\lambda_s$	Stator split ratio of stator inner diameter to the stator outer diameter
$\lambda_\delta$	Split ratio of airgap diameter to the outer diameter
$\rho$	Conductor resistivity
$\sigma_s, \sigma_r$	Stator and rotor flux leakage coefficients
$\mu$	Average relative permeability of cores
$\mu_0$	Permeability of the air
$\mu_{\text{all}}$	On-load permeability
$\mu_r$	Recoil permeability
$\mu_{rp}, \mu_{rt}$	Recoil permeabilities along parallel and tangential directions
$\tau$	Pole pitch
$\Phi_m, \Phi_1$	Fundamental and maximum fluxes per pole
$\psi_m$	Maximum flux linkage per pole
$\psi_1, \psi_5, \psi_7$	Magnitude of fundamental, fifth, and seventh flux linkage components
$\psi_a$	Phase flux linkage
$\psi_d, \psi_q$	Total $d$ - and $q$ -axis flux linkages
$\psi_d(i), \psi_q(i)$	$D$ - and $q$ -axis flux linkages due to on-load armature field
$\psi_d(\text{PM})$	$D$ - axis flux linkage due to on-load PM field
$\psi_q(\text{PM})$	$Q$ -axis flux linkage due to on-load PM field
$\omega$	Electrical angular speed
$\omega_m$	Mechanical angular speed



# CHAPTER 1 GENERAL INTRODUCTION

## 1.1 Introduction

As human society has developed the energy required to fuel the progress has increased dramatically. Currently the majority of this energy is derived from fossil fuels which, although have a very high energy density, are finite sources of energy. In recent years, global stocks of fossil fuels are falling at an accelerated rate due to high demand and the side effects of burning the fossil fuel are damaging the environment on a global scale. These have created a large interest in renewable and sustainable sources of energy, such as wind power [1]-[4], solar power [5], and tidal power [6]-[8], etc. which have all been developing rapidly over the past few years [9]. Electric drives represent one of the key technologies for exploiting these renewable energy sources and exhibit the advantages of high efficiency, fast response, and accuracy. These advantages coupled with recent advances in computational capabilities and power electronics have meant that conventional mechanical, hydraulic, or pneumatic propulsion and transmission systems for various applications, such as transportation [9]-[15] and aerospace [16], have been or are in the process of being replaced by electric systems.

Electric drive systems can be divided into two groups: geared and direct-drive (DD) systems, as shown in Fig. 1.1. In a geared system, the electric machine can run at higher speed allowing a reduced machine volume. The system output torque is boosted by the gearbox. Although the employment of a mechanical gearbox has many benefits, it also has many drawbacks. For wind power generation applications, it is often stated that the mechanical gearbox increases the mass, the volume, and the cost of whole drive system and reduces the system efficiency. The system also becomes more complicated and hence less reliable [17]-[21]. Furthermore, the gearbox needs regular maintenance and can cause significant vibration and acoustic noise. By removing the gearbox, as in DD systems, the drive train is greatly simplified. Consequently, the system efficiency, reliability, and lifetime are improved significantly. Other benefits, such as low system inertia, faster and more accurate response, and higher drive stiffness, can be obtained as well. Therefore, the DD system is preferred in modern applications and has been employed in various applications, such as high performance servo system, electric vehicles, and renewable energy generation.

A key concern with DD systems is that without the gearbox, the machine speed is lower. Consequently, the electric machine is larger and heavier. The system performance largely depends on the electric machine. Therefore, torque density optimisation of electric machines

is increasingly important in the DD systems. Furthermore, since the machine shaft is connected to the load directly, the requirement to reduce the torque ripple over the operational range is also much higher for DD systems than with equivalent geared systems.

Therefore, in this thesis, the torque characteristics, both average torque and torque ripple, of the electric machines for the DD applications are comprehensively investigated.

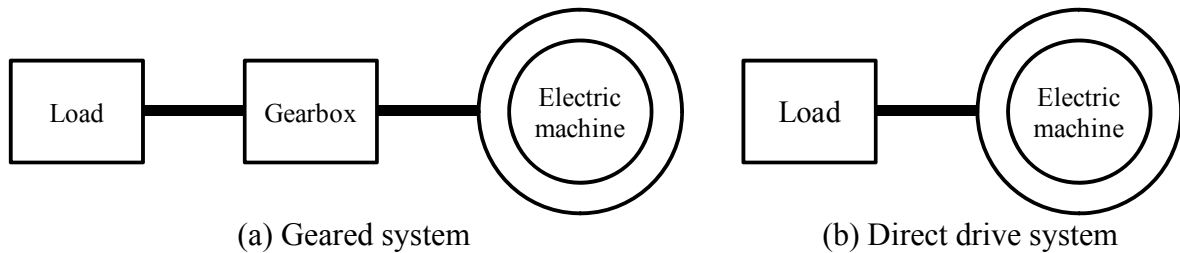


Fig. 1.1. Illustration of geared and direct drive systems.

## 1.2 Electric machines

In electric drive systems, the system performance largely depends on the electric machine employed. Progress in the development of materials, power electronics, and control technologies over the past few decades has enabled the development of various electric machines [9]-[83]. The major electric machine technologies are summarized in Figs. 1.2 and 1.3.

Historically, electric drives were dominated by induction machines (IM) and electrically excited (EE) machines. However, in more recent times, new machine technologies such as permanent magnet (PM) machines have become more popular due to high torque density and efficiency, especially when high energy permanent magnet materials are employed.

Switched reluctance (SR) and synchronous reluctance machines were developed by utilizing reluctance torque [74]-[82]. However, in order to start and smoothly run the reluctance machines, electronic controllers were inevitable. Furthermore, unlike EE and PM machines, there was no independent excitation, such as permanent magnets or field windings. Hence, the torque densities of reluctance machines were similar to IM's. Therefore, they were usually considered as alternative options to IMs.

Hybrid electric machines were developed by uniquely integrating different machine technologies. Due to the variety of ways of integration, a large number of hybrid electric machine topologies have been developed. They were very attractive to electric vehicles and became one of most popular topics under investigation [12] [83].

Amongst all these electric machines, IMs, EE machines, and PM machines remain the main

stream for electric drives.

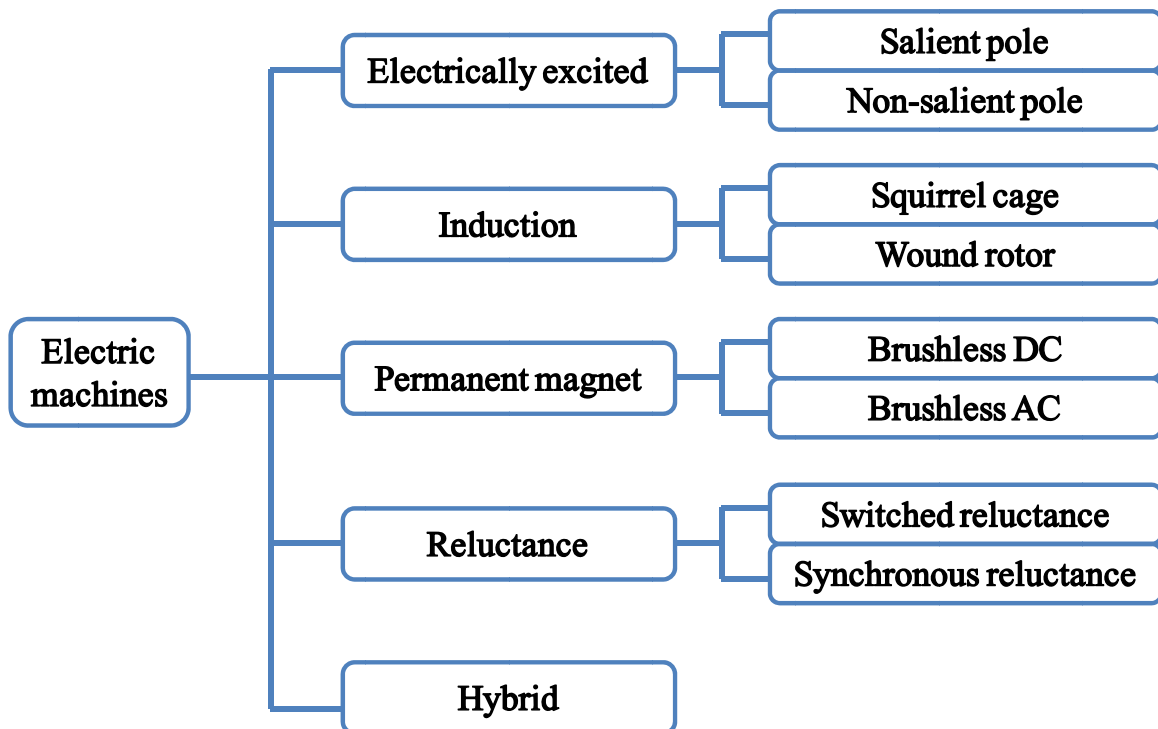


Fig. 1.2. Electric machine technologies.

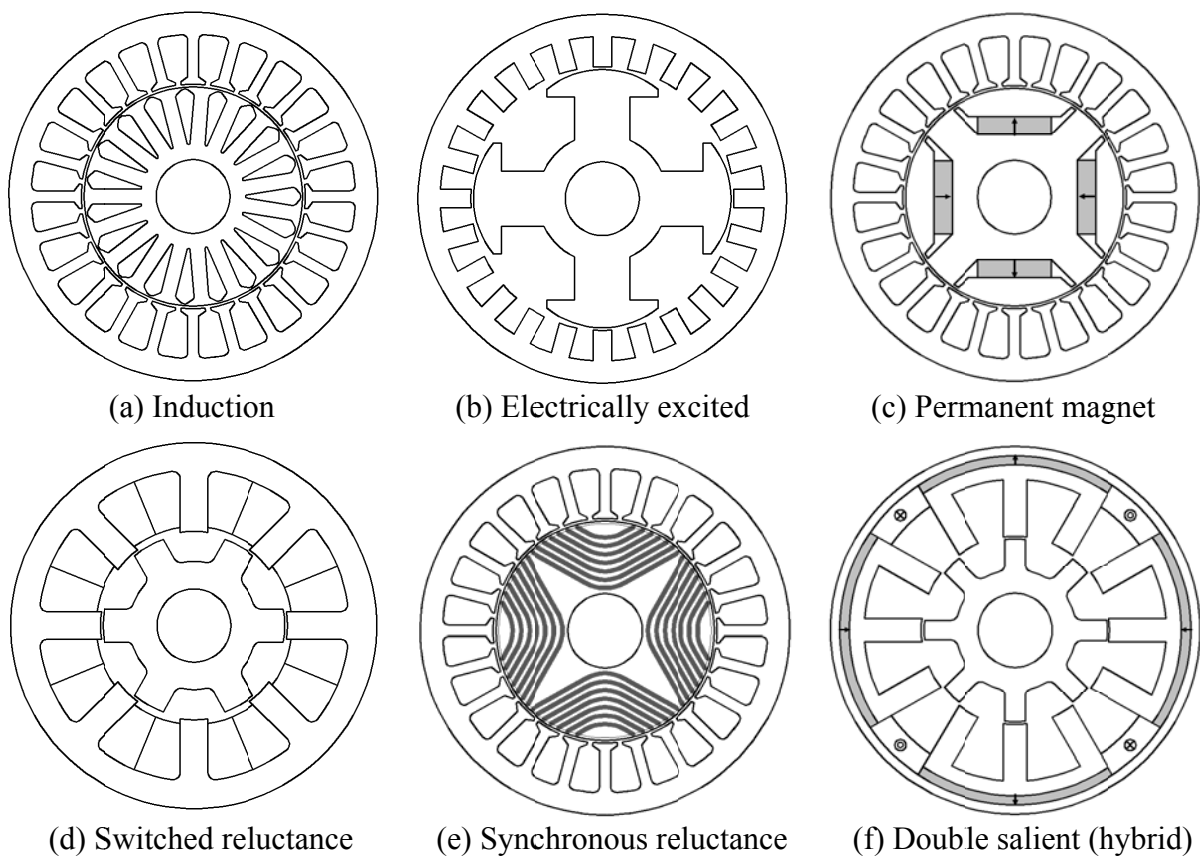


Fig. 1.3. Cross-sections of electric machine technologies.

### 1.2.1 Induction Machines

IMs are the most mature electric machine technology. IMs dominated electric drives before the development of PM machines and remained one of the most popular electric machines after the development of PM machines [51]-[56]. The major advantages of IMs are low cost, simple and robust rotor. The torque production of IMs relies on the currents induced on the rotor. In order to maintain the rotor current, a slip speed between the rotor and stator fields is necessary. If the slip speed is too high, the efficiency of IMs will be reduced due to high rotor loss. Therefore, the speed range of IMs is relative narrow. In order to extend the speed range, doubly fed IMs, in which the rotor windings are connected to a power electronic converter, are often employed. Typically, the speed ranges can extend to  $\pm 30\%$  around the synchronous speed [23] [52].

For DD applications, the machine speed is much lower due to the elimination of the gearbox and the speed varies across a large range. For example, the speed range of 3MW wind power generator is from 6 rpm to 20 rpm. It is not technically feasible to have a multi-pole low speed doubly fed IM for wind power generation without a gearbox [23]. Even for the concept of doubly fed induction generator with a one-stage gearbox, which was proposed in [21], there was no commercial implementation [53]. Therefore, IMs are currently not suitable for low speed DD applications.

### 1.2.2 Electrically Excited Machines

The majority of EE machines are used to generator power, such as steam turbine generators, hydroelectric generators, and nuclear power plants. Electrical energy is mainly generated by EE machines [60]. However, EE machines can also be used for driving applications, such as ship propulsion, pumps, and rolling mills. In recent years, EE machines have also been employed in wind turbine generators [17], [21], [22], [61], electric vehicles [62], [63], aerospace applications [64]-[66], and industrial applications [67]. In high temperature super conducting applications, nearly all the machines employed are EE machines [61], [65], [67]. Therefore, various investigations are being carried out on EE machines [68]-[73].

In EE machines, conventional distributed overlapping armature windings are usually employed. For the rotor structure, there are two types: non-salient and salient, as shown in Fig. 1.4. Non-salient pole EE machines are usually manufactured for 2 or 4 poles high speed turbine generators driven by gas or steam turbines. Salient pole EE machines are made for low speed applications with a large number of poles ( $2p > 4$ ) [60].

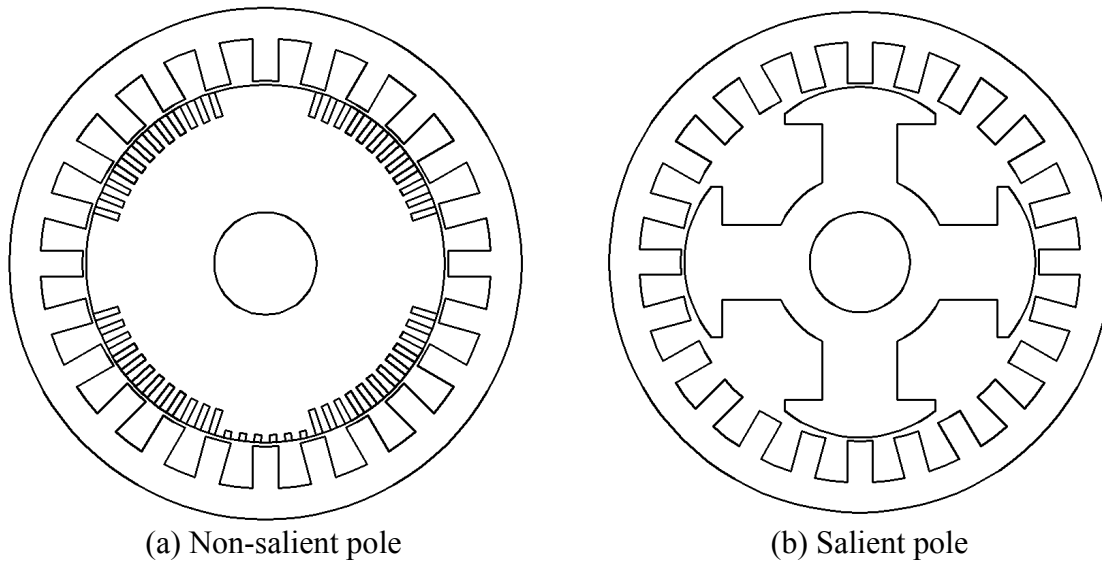


Fig. 1.4. Schematics of EE machine topologies.

The main advantages of EE machines can be summarized as:

- They are relative cheap, since there is no expensive PM material.
- There are three independent control variables, i.e.,  $d$ -axis armature current,  $q$ -axis armature current, and excitation current. Compared with PM machines, the excitation field is adjustable. Therefore, the control strategies are more flexible and particularly suitable for flux weakening.
- Unity power factor can be achieved, which benefits the power converters.

The main disadvantages of EE machines are excitation losses and devices, either a set of mechanical brushes/slip rings or a power electronics rectified exciter on the rotor.

### 1.2.3 Permanent Magnet Machines

Permanent magnet machines have developed extremely fast in last few decades, especially with the invention of high energy permanent magnet material, i.e., Neodymium Iron Baron (NdFeB), in the early 1980s [84], [85]. PM machines have been popular for various applications, such as aerospace, automotive, renewable energy, industrial and domestic applications etc [9]-[17], [21]-[51].

Due to the permanent magnets, PM machines are inherently efficient, since they are excitation copper loss free. By employing high energy PM material as well as flux focusing topologies, higher airgap flux densities, torque, and power densities can be achieved. For the same torque, PM machines can be much smaller and lighter than IM and EE machines.

The main disadvantages of PM machines are also due to the permanent magnets. First, PM machines are relatively more expensive due to the requirement for costly rare earth materials. Second, PMs have the possibility of irreversible demagnetization, which can be caused by

high temperature, vibration, or exposure to high demagnetization fields. Third, due to the fixed PM flux, flux weakening is often employed to extend the constant power speed range. However, a high demagnetizing current is required to achieve this, which results in extra copper loss in the machine and increases losses in the power electronic converters.

In order to further improve the performance, various types of PM machines have been developed specially for different applications and they are briefly summarized as follows.

- According to the flux path, they can be classified as radial-field, axial-field [25]-[28], and transverse-flux PM machines [29], [30], as shown in Fig. 1.5. Amongst them, the radial-field PM machines are the most popular due to their simple, cheap, and robust configuration.
- Based on the location of PMs, PM machines can be classified into two groups: PMs on the rotor and PMs on the stator. For topologies with PMs on the rotor, they can be further divided into four types, namely surface-mounted, surface-inset, interior-radial, and interior-circumferential, as shown in Fig. 1.6. For the machines with PMs on the stator, there are three main types, namely double salient PM machines, flux-reversal PM machines, and flux switching PM machine, as shown in Fig. 1.7 [31]-[45]. The rotors are simpler and more robust in stator PM machines, however the design of the stators tends to be more complicated. More importantly, in order to achieve equivalent torque density, higher volumes of expensive permanent magnet is required for stator PM machines than conventional rotor PM machines. Therefore, for most applications, conventional rotor PM machines are the most promising.
- Even for conventional radial-field PM machines having PMs on the rotor, they can be further classified according to the slot/pole number combination, such as integral slot, conventional fractional slot having slot number per pole per phase  $q$  being 0.5, fractional slot having slot and pole numbers being different by 1 ( $N_s = 2p \pm 1$ ), and fractional slot having slot and pole numbers being different by 2 ( $N_s = 2p \pm 2$ ), as shown in Fig. 1.8. Compared with conventional integral slot machines, fractional slot machines having  $N_s = 2p \pm 1$  or  $N_s = 2p \pm 1$  exhibit higher efficiency and torque densities, due to the significant reduction of end windings. They also have much lower cogging torque and torque ripple, due to having a much higher smallest common multiple (SCM). However, since the armature magnetomotive force (MMF) contains rich harmonics, they potentially have higher eddy current loss, iron loss, vibration and acoustic noise. For the fractional slot machines having  $N_s = 2p \pm 1$ ,

special attention should be also paid to unbalanced magnetic forces (UMF) that can occur.

- In order to achieve better mechanical integration, PM machines can have internal or external rotors.

In this thesis, the investigation is focused on conventional PM machines having radial-field and PMs on the rotor.

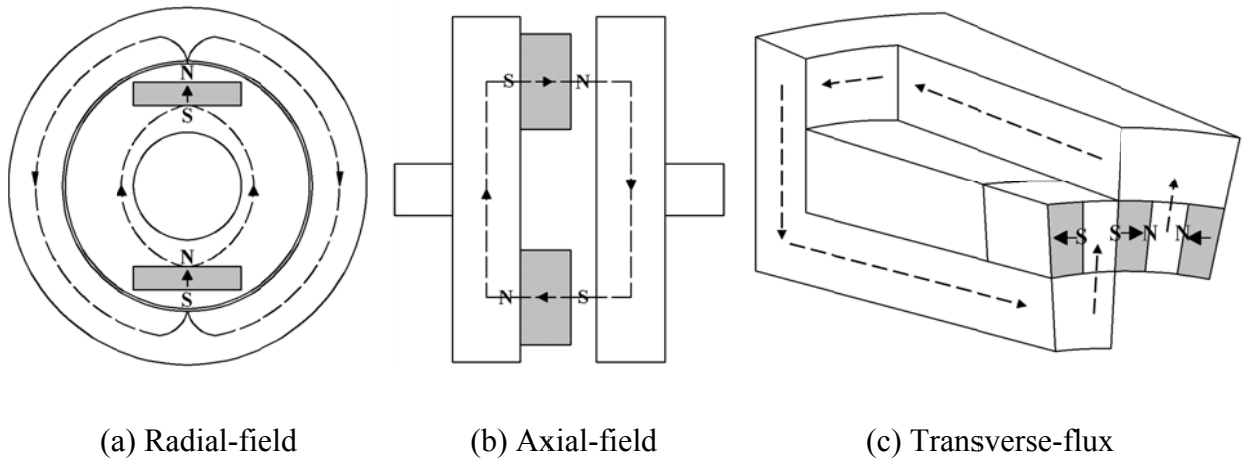
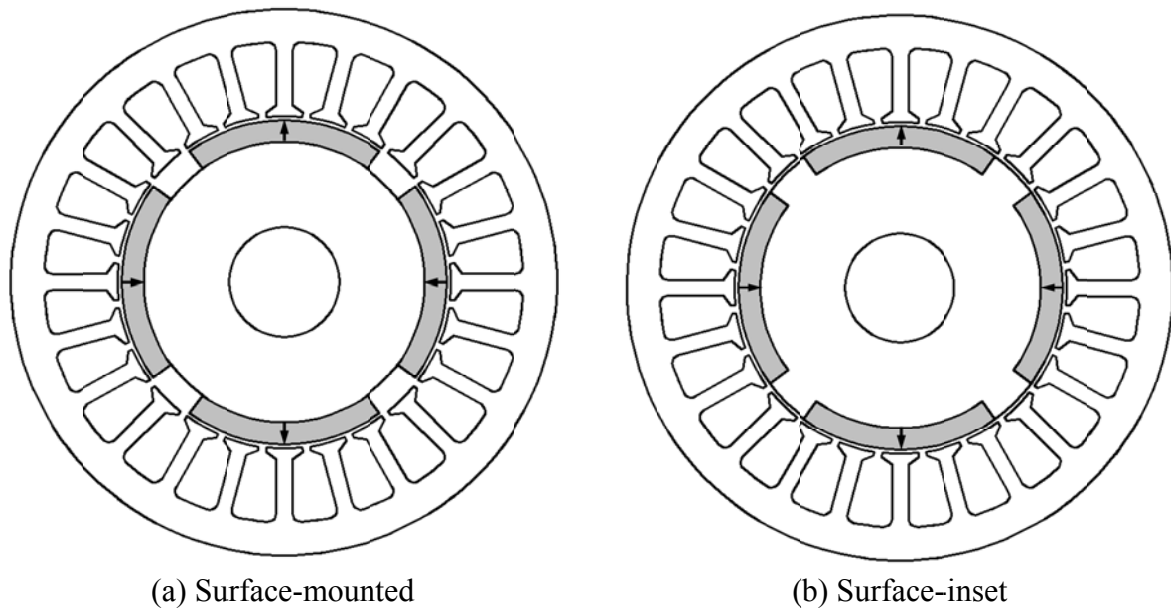


Fig. 1.5. Typical flux paths of different PM machine topologies.



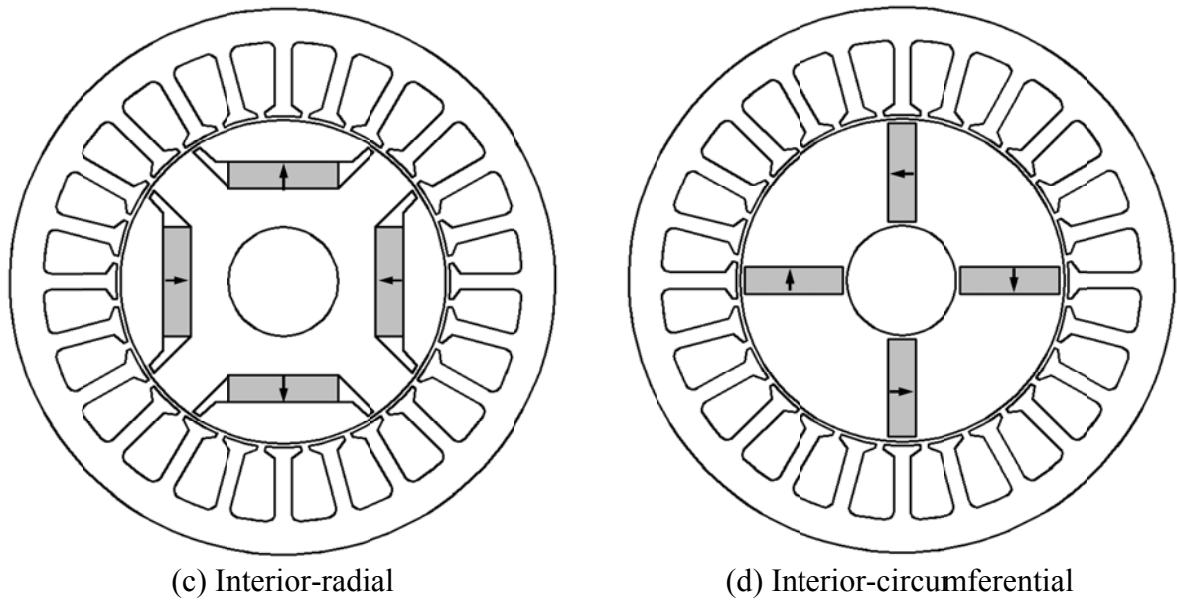


Fig. 1.6. Machines topologies with PMs on rotor.

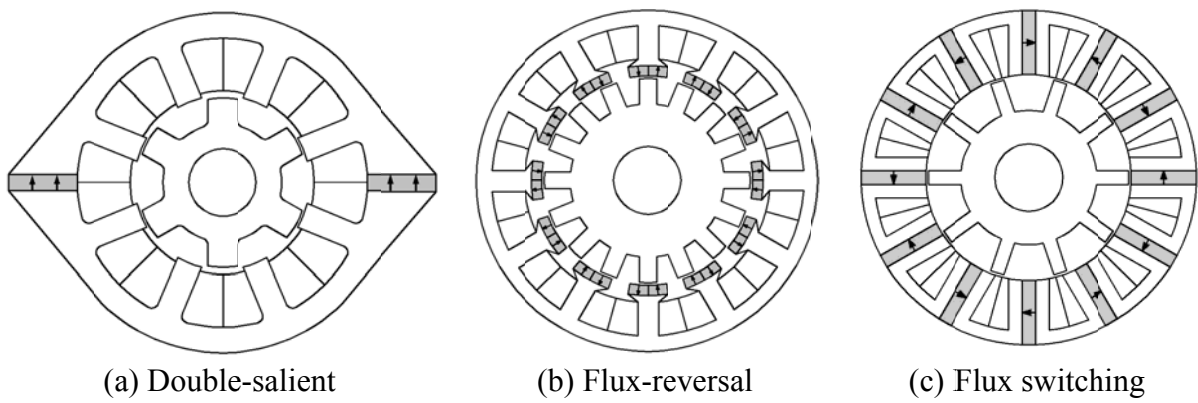
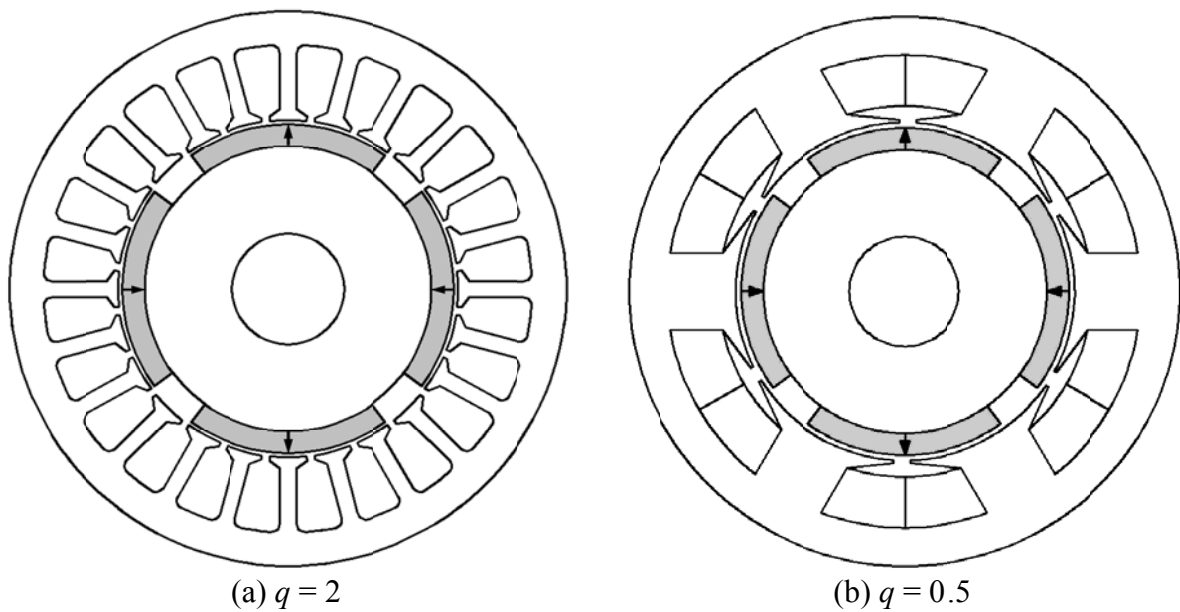


Fig. 1.7. Machines topologies with PMs on stator.



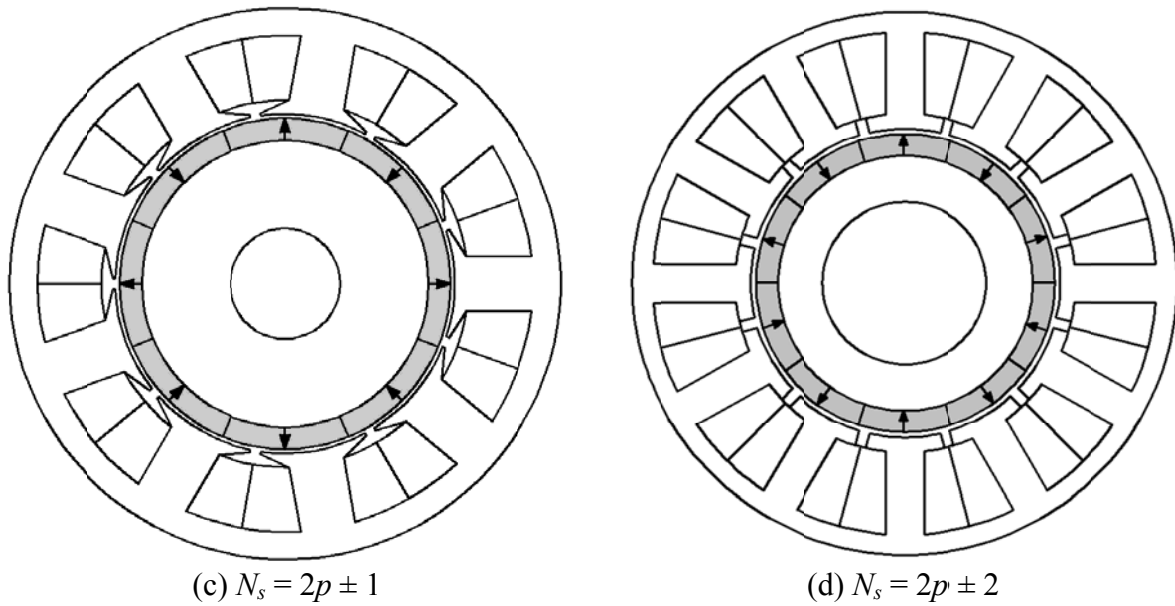


Fig. 1.8. Typical slot/pole number combinations.

#### 1.2.4 Comparison and Summary

As concluded in the preceding sections, although IM, EE and PM machines remain the main streams of electric drives, IMs are currently not suitable for low speed DD applications. Therefore, in this thesis, the comparative study is focused on EE and PM machines.

EE and PM machines have been compared on the system performance for wind power applications [21], [24], [86], [87], integrated starter and generator applications [63], and man-portable power system [88]. All of them concluded that EE machines are larger, heavier, and less efficient than PM machines.

However, the conclusions on the costs of EE and PM machines are strongly dependant on the material prices being used for cost estimation. In [21], it was concluded that PM machines were cheaper, since the costs were calculated when rare earth material prices were slightly higher than the price of copper. However, in [24] and [87], it showed that PM machines were more expensive, since the costs were calculated when rare earth material prices were much higher than the price of copper. In reality, rare earth material prices have been increasing in the last few decades and can become extreme high, such as when global supplies were limited in 2011. Therefore, it is increasingly attractive to consider less or non-rare-earth magnet machines and EE machines are a good candidate machine design in this respect.

In this thesis, EE and PM machines are quantitatively compared on their torque characteristics, both average torque and torque ripple, for the DD applications. In order to make fair comparison, both machines should be optimised first.

### 1.3 Torque Density Maximization

The optimisation of electric machines has been always one of the most important topics in machine design and was intensively discussed in literature [89]-[119]. In general, there are three ways of carrying out machine optimisation, i.e., analytical models [89]-[106], magnetic equivalent circuit (MEC) [68], [69], [107], [108], and Finite Element (FE) analysis [109]-[119]. With the development of computing devices and commercial FE software, FE analyses are increasingly popular, since it is easy to implement and does not require strong background knowledge. It is also able to simulate various conditions and consider the influence of magnetic saturation. However, although the computing speed is much faster, FE analyses are still time consuming, especially for optimisation, in which thousands of cases need to be evaluated. Therefore, it is better to use FE analyses for validation and adjustment of the design. In order to improve the computational speed while considering the influence of magnetic saturation, the MEC method is often employed. However, the accuracy of MEC largely depends on the accuracy of individual magnetic circuit components and the couplings between them. Therefore, in order to implement MEC properly, detailed knowledge on magnetic circuit modeling and the basic characteristics of magnetic field distribution is essential, which makes implementation much more difficult than using FE methods. However, both the FE and MEC methods are based on discretization, which means they have difficulties revealing the whole picture. Being different from the FE and MEC methods, the analytical method is based on modeling and optimising the geometric and electromagnetic relationships between different parts. Although the accuracy is usually compromised due to neglecting magnetic saturation, more importantly, analytical methods are able to reveal the whole picture and link the performance to the relationships between design parameters, which is extremely valuable for machine designs. Therefore, more insights and general conclusions can be obtained by using analytical methods to guide the machine design.

Most previous discussions on analytical optimisation were based on machines with an internal rotor, as this was the major configuration. In [89], instead of the conventional output equation based on the airgap diameter, the output coefficient for salient-pole EE machines was expressed for the first time as a function of the outer diameter, airgap diameter, effective axial length, magnetic loading and electric loading. The optimal airgap flux density was derived when the outer diameter, airgap diameter and number of poles were fixed. The influence of the rated phase voltage, stator slot depth, number of poles and airgap diameter on the output coefficient was investigated as well. In [90], several general sizing equations,

based on the outer diameter or the airgap diameter, were developed for electric machines. It was shown that the output torque was significantly influenced by the split ratio, i.e., the ratio of the airgap diameter to the outer diameter, and the flux density ratio, i.e., the ratio of airgap flux density to the flux density in the stator. The optimal split ratio for maximum torque per volume was derived. The influence of the flux density ratio and pole number on the optimal split ratio and maximum output was investigated as well. It showed that, when the flux density ratio was high, the optimal design would be an “iron machine”. When the flux density ratio was low, the optimal design would be a “copper machine”. The optimal split ratio and maximum output increased with the number of poles monotonously. The analytical model was also extended to cover the case having rectangular stator slots. However, the output torque coefficients in [89] and [90] have some limits. First, although it was tried, the output coefficients are not a function of the machine volume. Second, the torque coefficients were developed assuming a given airgap flux density, which is suitable for PM machines but inappropriate for EE machines, as will be shown in this thesis later. Third, the optimal quantities were derived by optimizing the stator only. However, the optimal quantities may be different when both stator and rotor are considered, especially for EE machines. Furthermore, the pole number was fixed in [89] but it is an important design parameter to be investigated.

In [91], a general power density equation was developed for radial-field machines based on the split ratio, i.e., the ratio of the airgap diameter to outer diameter, and the aspect ratio, i.e., the ratio of the effective axial length to airgap diameter. In order to cover various conditions, the waveform coefficients for various current and back EMF waveforms were calculated. The developed general power density equation was used for the comparison between IMs and double-salient machines. In [92], a general power density equation for axial field machines was developed by the same authors in the similar way and used for the comparison between conventional axial field PM machines and axial field two-stator PM machines.

The analytical optimisation of PM machines has been investigated in-depth in [93]-[103]. In [94], a simple expression of the optimal split ratio, i.e., the ratio of the rotor diameter to the outer diameter, was derived for radial-field PM machines having distributed overlapping winding, parallel teeth, and neglecting the end winding and tooth-tips. The influence of the number of poles, magnet material, and maximum flux density in the stator and rotor cores on the optimal split ratio was investigated based on the developed expression. The demagnetization issue linked with low split ratio was discussed as well. Based on [94], the influence of the split ratio on the overall cost of the machine was further investigated in [95].

In [96], the analytical model was extended to cater for high speed brushless DC motors having non-overlapping windings and a diametrically magnetized rotor. In [97], the analytical model was improved further to derive the optimal split ratio for maximum torque per volume for various PM machines, such as brushless AC or DC, overlapping or non-overlapping windings, and sinusoidal or rectangular airgap flux density distributions. The influence of tooth-tips and end windings on the optimal split ratio was investigated as well. Furthermore, in [98], the discussion focused on fractional-slot IPM machines, which have more freedom to achieve higher airgap flux density by using flux focusing configurations. Also in [98], for the first time, the flux density ratio was treated as another independent variable to be optimised in addition to the split ratio. The expressions of optimal split ratio and flux density ratio were obtained individually with one of these two variables being specified. By optimizing these two variables together, the global optimum was also derived. It showed that, mathematically, the global optimal flux density ratio was 1 for IPM machines having parallel teeth. However, it suggested that the preferred flux density ratio was around 0.5-0.7, since the torque saturated as the flux density ratio increased and the magnet usage increased significantly as well when the flux density ratio was above 0.7. The influence of slot and pole number combinations and tooth-tips on the optima was investigated as well. The analytical model developed in [99] was focused on large PM synchronous generators, which had rectangular stator slots. It showed that the optimal split ratio without any tangential stress constraint was much lower than the one with the tangential stress constraint included. However, in order to improve the estimation accuracy, an iterative correction procedure was necessary.

The analytical optimisation in [100] and [101] was focused on PM machines with an external rotor. In external rotor PM machines, first, the maximum achievable airgap flux density is limited by the split ratio of the rotor inner diameter to the outer diameter. Second, the stator slot area depended on the stator outer diameter and the diameter at the bottom of the slot, which may be linked with the inner diameter, instead of the outer diameter. Therefore, analytical models dependant on inner rotor PM machines were not applicable. The analytical torque model in [100] and [101] was developed when the inner and outer diameters were fixed and the airgap flux density was fixed to its maximum achievable value for the specific split ratio. Therefore, the developed torque was a function of the split ratio only. However, it was mathematically too complicated to analytically derive the optimal split ratio based on the developed model. The optimal split ratio was obtained alternatively by scanning. The influence of slot/pole number combinations, maximum flux densities, tooth-tips, and end-windings on the optimal split ratio was investigated as well.

A concern with the model in [100] and [101] is that it is inappropriate to fix the airgap flux density to its maximum achievable value even in external rotor PM machines, since the airgap flux density can still be independent of the split ratio when it is lower than the maximum achievable flux density. As will be shown later in this thesis, the optimal airgap flux density is lower than the maximum value for the most of the split ratio range. Therefore, in this thesis, the airgap flux density is first treated as an independent variable to find the theoretical optima. Then, the practical optima are obtained by further considering the relationship between the maximum achievable airgap flux density and the split ratio. The investigation is also extended to cater for cases when the limitation of inner diameter does not influence the optimal design. In this case, the stator slot area and hence the torque are functions of the split ratio, the flux density ratio, and the stator split ratio, and much more complicated. However, by using the proposed optimisation procedure, which will be detailed later, it is still able to analytically derive the optimal stator split ratio, split ratio, and flux density ratio and hence will provide valuable insights and aid the external rotor PM machine design. It will also be shown that, instead of the optimal split ratio, which is close to 1, the derivations of optimal flux density ratio and stator split ratio are more useful for the external rotor PM machine design.

In order to quantitatively compare the torque densities of EE and PM machines, an analytical torque model for EE machines, which considers the influence of magnetic saturation in the laminations in a simplified way, is developed in this thesis as well. Being different from the investigation in [89] and [90], the airgap flux density in EE machines is not constant but a variable, which links the rotor design to the torque and will be optimised. It will be shown later in this thesis that the optima obtained by optimising the stator only are significantly different from the optima obtained when the stator and rotor are optimised together.

#### **1.4 Torque Ripple Minimization**

Apart from optimisation of average torque, torque ripple minimization is another important issue to be addressed, since the machine is connected to the load directly in DD systems and hence the requirement to reduce the torque ripple over whole load range is much higher than the requirements of equivalent geared systems.

Being different from EE machines, even on open-circuit, PM machines have the torque ripple, i.e., cogging torque. The cogging torque is manifested by the interaction between the

rotor PM MMF and stator magnetic reluctance. It is a pulsating torque and causes vibration and acoustic noise. When PM machines are on load, the torque ripple is contributed by both the cogging torque and EM torque ripple [120].

Torque ripples can be reduced by either machine designs [120]-[182] or control methods [183]-[187]. However, most investigations on torque ripple reduction of PM machines were focused on open-circuit conditions, where the open-circuit cogging torque is the only component and the influence of magnetic saturation due to load is often neglected. The open-circuit cogging torque can be investigated by various methods, in particular by using analytical methods [121]-[126]. Consequently, various ways of reducing the open-circuit cogging torque have been developed. However, the on-load torque ripple is much more complicated than the open-circuit one. It has been shown in [164], [165], [167], [188]-[190] that the on-load torque ripple can be influenced significantly by magnetic saturation. Therefore, it is much more difficult for analytical methods. Instead, the on-load torque ripples were often investigated by FE analyses. Since the on-load PM and armature fields couple with each other, it was also significantly difficult to obtain the individual on-load torque component. Therefore, less investigations were focused on the on-load torque ripple reduction and most of them were only able to study the total on-load torque ripple.

In [120], torque ripple minimization techniques for PM machines, both brushless DC (BLDC) and brushless AC (BLAC), were systematically reviewed. On the machine design aspect, it covered machine topologies, skewing, winding types, rotor designs, and stator designs. On the control aspect, it reviewed five methods, namely programmed current waveform control, estimator and observers, commutation torque minimization, speed loop disturbance rejection, and high-speed current regulator saturation. It was concluded that the most effective ways to minimize the torque ripple were by proper machine designs.

In [121], the influence of various design parameters on open-circuit cogging torque was for the first time systematically investigated based on a general cogging torque expression. It was theoretically shown that the slot and pole number combination had a significant effect on the cogging torque and hence all the other optimal parameters utilized to minimize the cogging torque. A simple but useful guideline was obtained to indicate the “goodness” of slot and pole number combination based on their SCM. The higher the SCM, the larger the cogging torque. The optimal values for the other design parameters, such as auxiliary teeth and slots, magnet pole arc, skewing angle, and stator slot opening, were obtained as well. All the conclusions in [121] were verified again by the improved analytical cogging torque expression developed in [123]. In [122], a similar investigation was carried out based on the highest common factor

between slot and pole numbers. Most conclusions remained the same as the ones in [121], except that it was slightly extended to cover the method of pole shifting.

### 1.4.1 Rotor Shaping

One of the most widely used methods of reducing the torque ripples for various machines is rotor shaping [127]-[146].

One of the simplest ways of rotor shaping in electric machines is to change the pole arc to pole pitch ratio. In [127], the variation of open circuit cogging torque with the rotor pole arc to pole pitch ratio was calculated for the first time. In [128], the influence of the magnet shape on the open-circuit back EMF harmonics was investigated based on three magnet shapes, namely, rectangular, stepped, and trapezoidal, as show in Fig. 1.9. For a PM machine with trapezoidally shaped magnets, two different magnetization patterns, namely, parallel and radial, were further investigated in [129]. In [130], the optimal pole arc to pole pitch ratio of IPM machine was obtained for the lowest cogging torque.

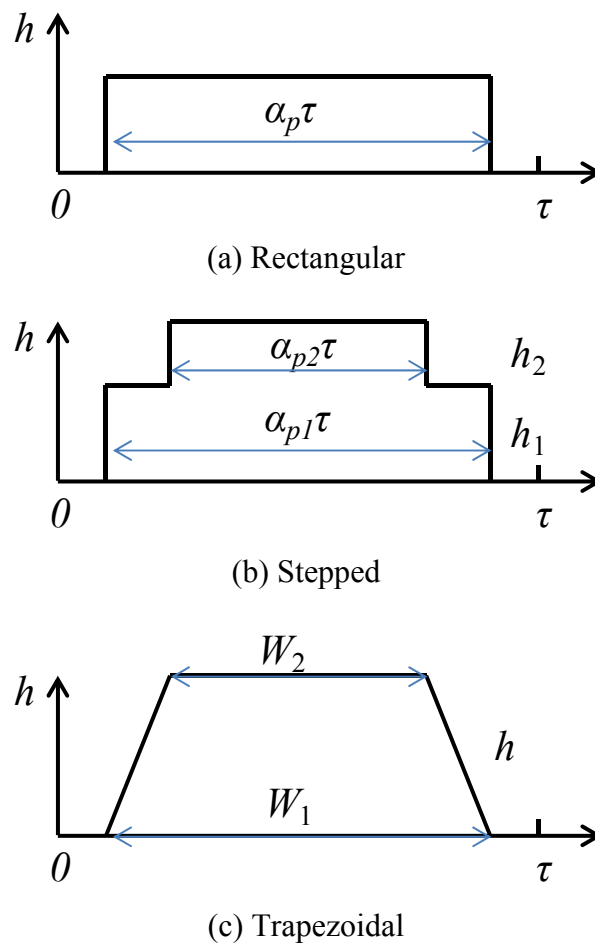
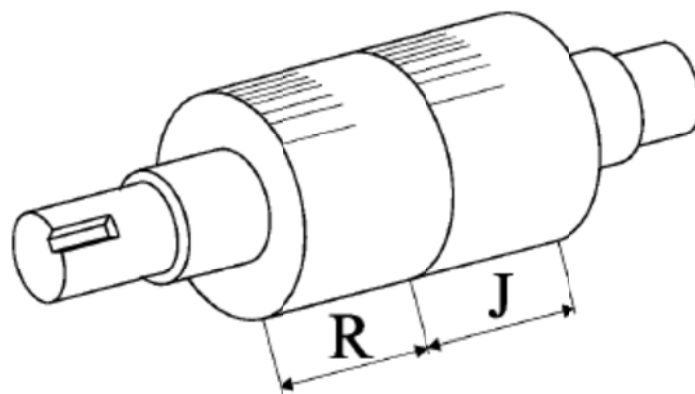
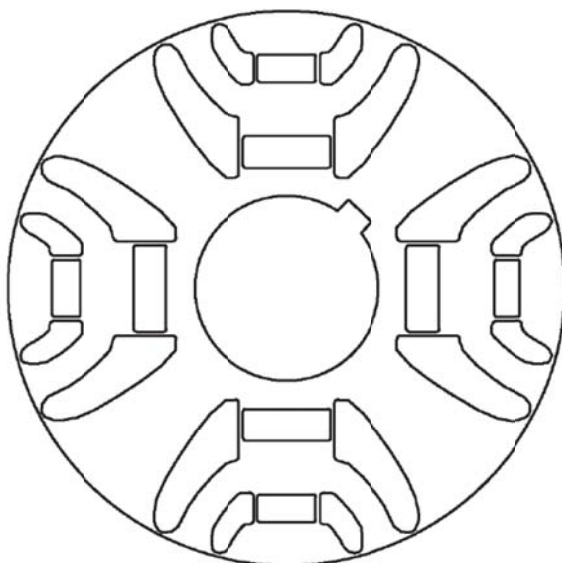


Fig. 1.9. Three magnet shapes investigated in [128].

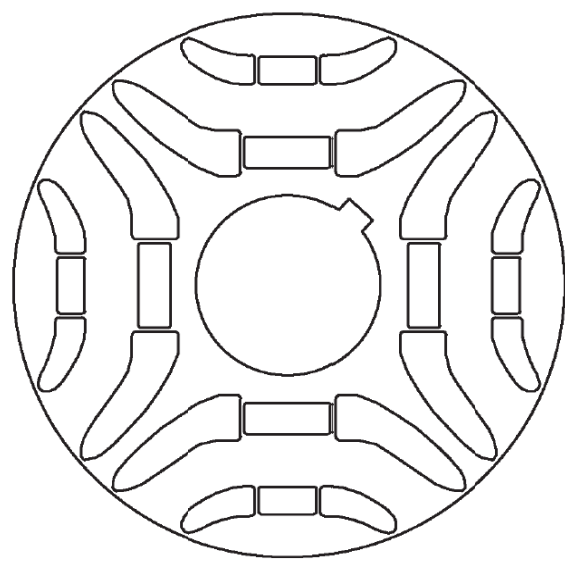
In [81], [82], and [131], the on load torque ripples were reduced by using different methods of pairing the pole arc to pole pitch ratio for different machines, as shown in Figs. 1.10-1.12. In [81], two different rotor laminations, which had different flux barrier ends and torque ripples, were paired in axial direction, as shown Fig. 1.10. Hence, low on-load torque ripple was achieved based on cancellation of the on-load torque ripples of these two parts. A similar method was also developed in [131] for SPM machines. Axial magnet pole pairs, as shown in Fig. 1.11, can consist of a variety of different axial lengths as well as pole arc widths. By selecting optimal magnet pairs, lower cogging torque, more sinusoidal back EMF, and lower on-load torque ripples can be achieved. This method also has the advantages of efficient use of magnet material and easy assembling. In [82], instead of pairing along axial direction, the different flux barrier shapes were combined within the same rotor lamination circumferentially, as shown Fig. 1.12. Again, utilizing the cancelling effect between alternative poles, a low torque ripple was obtained.



(a) Axial combination of two parts



(b) Lamination of R part



(c) Lamination of J part

Fig. 1.10. Axial pole pairing in [81].

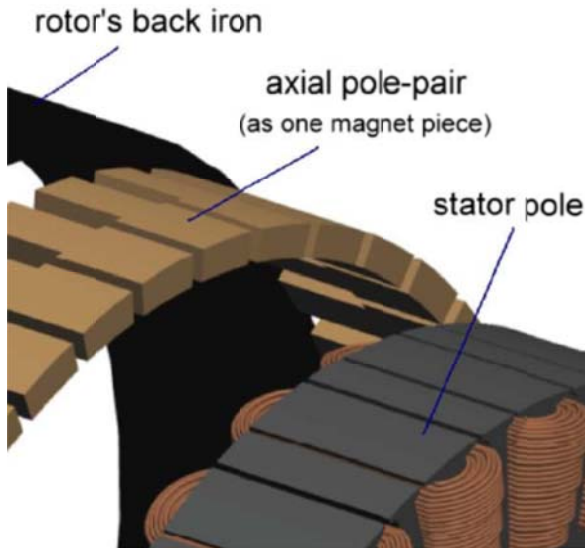


Fig. 1.11. Axial pole pairing in [131]

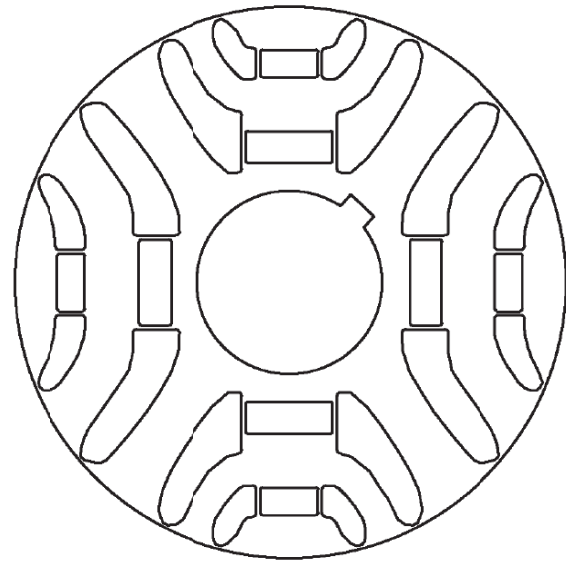
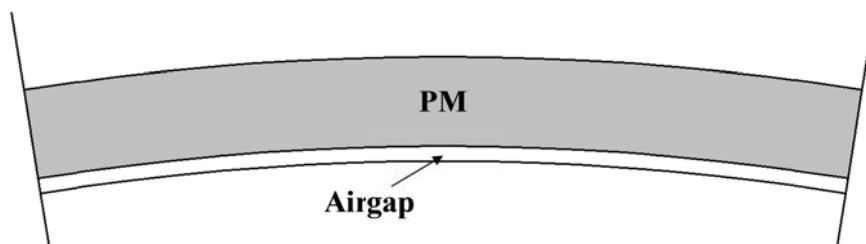


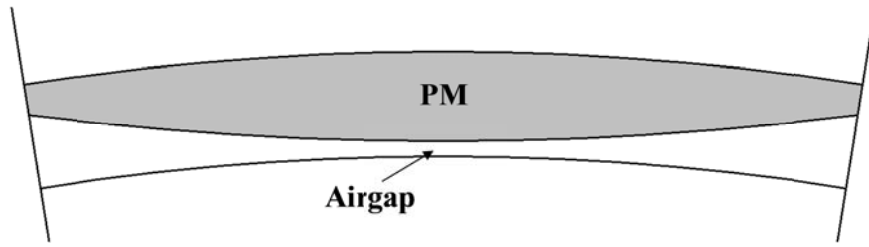
Fig. 1.12. New way of pole pairing in [82]

By optimising the pole arc to pole pitch ratio, back EMF harmonics and torque ripples can be reduced significantly. However, the rectangular rotor pole shape means that the rotor MMF harmonics remain rich. In order to reduce the MMF harmonics further, various rotor pole shapes have been proposed [132]-[139].

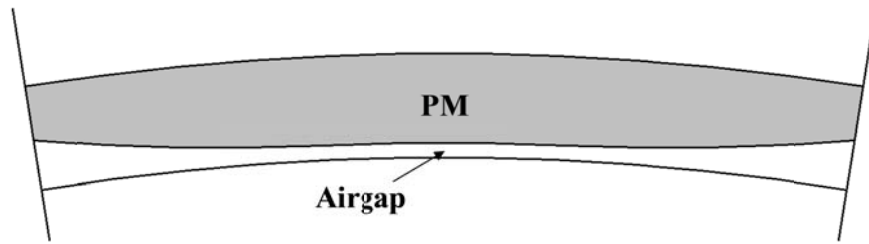
In [132], three magnet shapes, namely, tile shape, sinusoidal wave shape, and parallel top sinusoidal wave shape, were compared. As shown in Fig. 1.13, the tile shaped magnets had uniform thickness. The sinusoidal wave shape was obtained by paring off the two edges of tile shape to achieve a sinusoidal airgap flux density distribution. The parallel top sinusoidal wave magnet was developed by utilizing the third order harmonic, which only exists in phase back EMFs and does not exist in line to line back EMFs. With a parallel top sinusoidal wave shaped magnet, one part in the centre was in a concentric arc with the inner stator core surface, and the other parts were similar to that of the sinusoidal wave shaped magnet. Based on the phase back EMF expression, it was concluded that the optimal design occurred when the magnitude of the third order harmonics is 0.12 times of the magnitude of the fundamental component.



(a) Tile shape



(b) Sine wave shape



(c) Parallel top sine wave shape

Fig. 1.13. Three magnet shapes investigated in [132].

In [133], by solving Laplace's equation in the airgap, a new way of shaping the magnet to achieve sinusoidal back EMFs was obtained and given by Fig. 1.14 and (1.1).

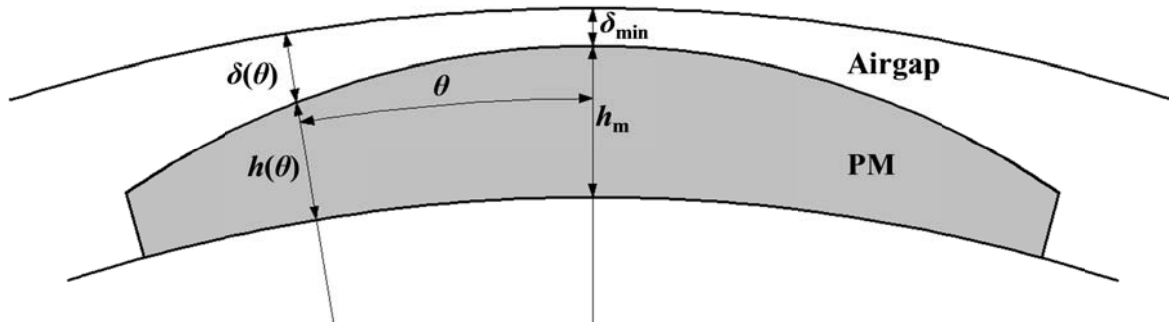


Fig. 1.14. Magnet shape, stator back iron, and airgap length variation [133].

$$\delta(\theta) = \delta_{min} / \cos(p\theta) \quad (1.1)$$

In [134], a sinusoidal parallel magnetized magnet was expressed in different way, as given by Fig. 1.15 and (1.2). It was compared with a machine having Halbach magnetized magnets, which will be reviewed later. Both methods can achieve a sinusoidal airgap flux density and negligible cogging torque.

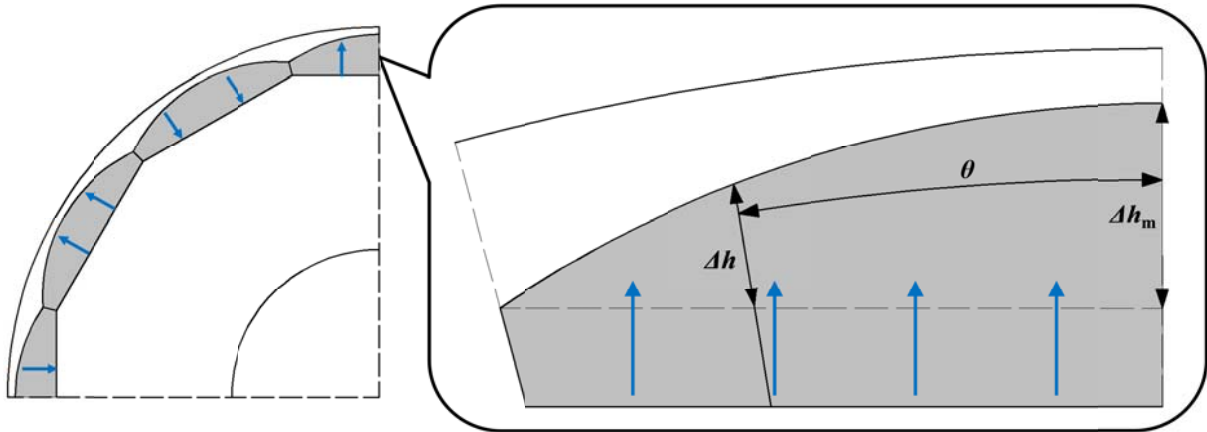


Fig. 1.15. Magnet shape, stator back iron, and airgap length variation [134].

$$\Delta h = \Delta h_m \cos(p\theta) \quad (1.2)$$

In [135], the pole shape optimisation of 6-slot 4-pole surface inset PM machine was discussed. An eccentric magnet shape, as shown in Fig. 1.16, was adopted. The eccentric distance, pole arc, and magnetic bridge were optimised.

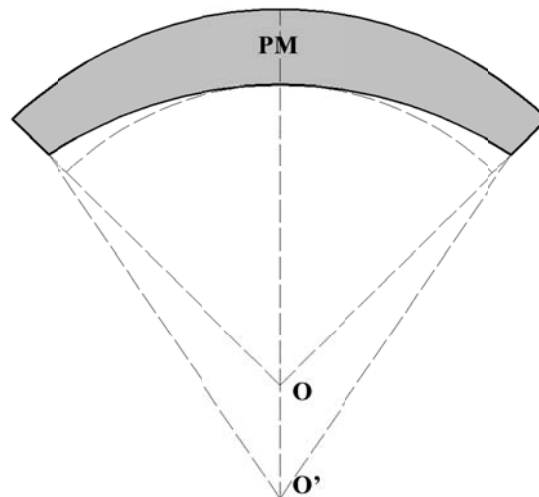


Fig. 1.16. Eccentric rotor shaping in [135].

In [136], it was concluded that, for pre-estimation, the optimal pole magnet shape for SPM machines was  $h(\theta) = h_m \cos(p\theta)$ , as shown in Fig. 1.14. However, due to the influence of circumferential flux density components and magnetic saturation, the centre-offset arc shaping method (Fig. 1.17) was developed instead of the pre-estimated shaping method. The parametric optimisation of the centre-offset arc shaped was carried out as well.

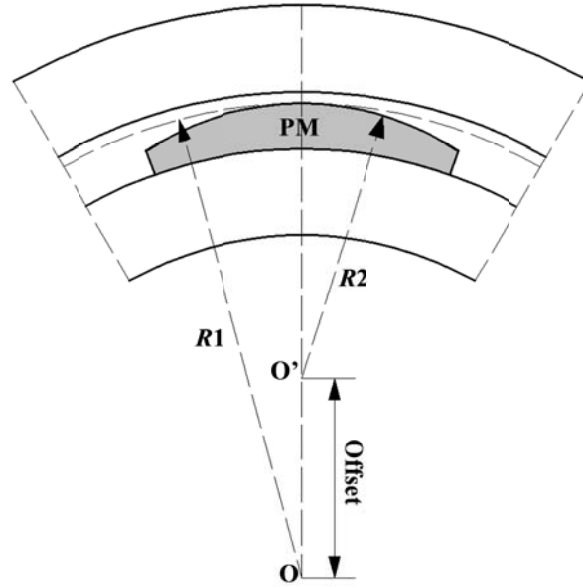


Fig. 1.17. Centre-offset arc magnet shaping in [136].

In [137], three rotor shaping methods, namely inverse cosine airgap length shape, centre-offset arc shape, and consequent poles, were investigated for IPM machines. The optima of the maximum to minimum airgap ratio for the inverse cosine airgap length shape, the pole shoe width to magnet width ratio for the centre-offset arc shape, and the soft magnetic pole shoe angle to pole pitch ratio for the consequent poles, were obtained for IPM machines.

In [138], by introducing third order harmonics into the inverse cosine airgap length shape and the sinusoidal wave magnet shape, two new magnet shaping methods were developed and given in (1.3) and (1.4). Furthermore, an optimal third order harmonic was obtained analytically, which was one sixth of the fundamental component.

$$\delta(\theta) = \frac{k\delta_{min}}{\cos(p\theta) - a_3 \cos(3p\theta)} \quad (1.3)$$

$$h(\theta) = h_m[\cos(p\theta) + a_3 \cos(3p\theta)] \quad (1.4)$$

where the  $k$  is a coefficient used to maintain the minimum airgap the same.

In [139], the work of [138] was further extended for IPM applications. Combining the inverse cosine airgap shape and the third order harmonic, the new way of rotor pole shaping for IPM machines was obtained and shown in Fig. 1.18. Again, it showed that the optimal amplitude of the third order harmonic was one sixth of the fundamental component.

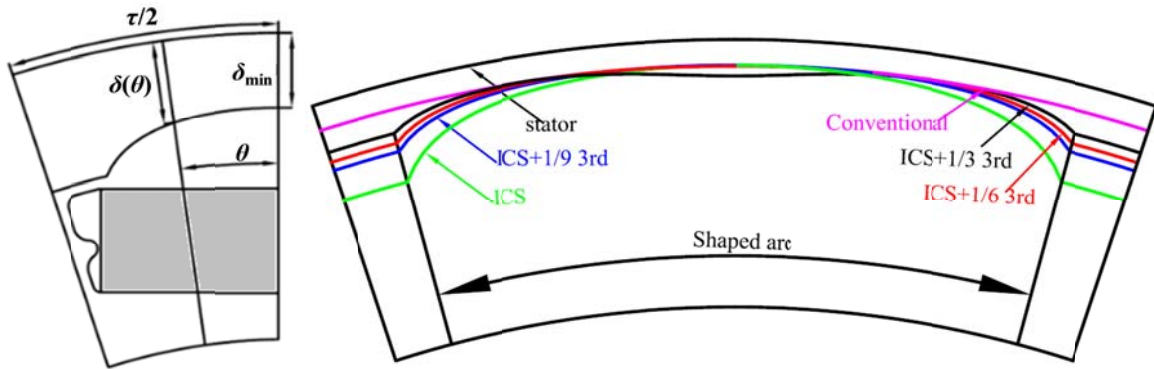
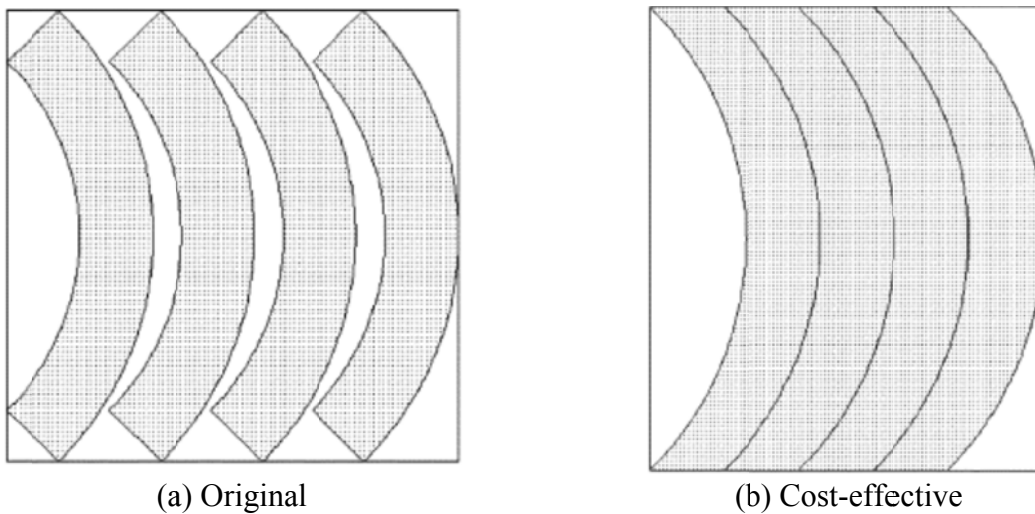
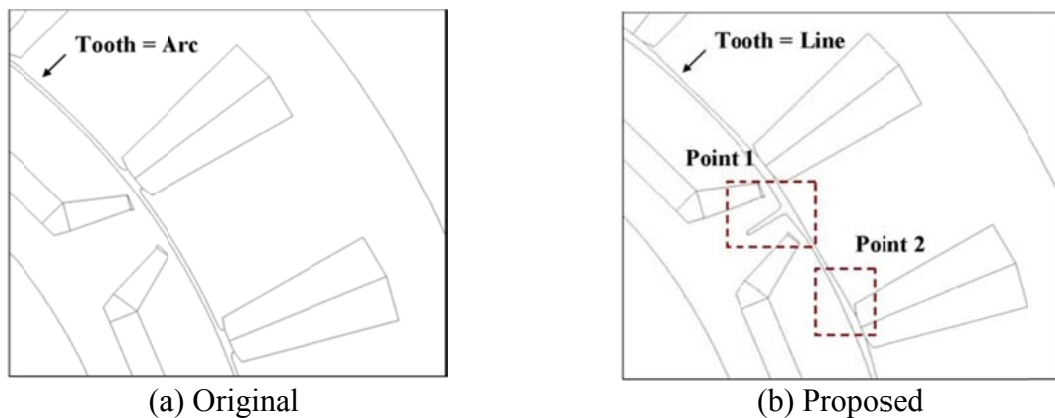


Fig. 1.18. Rotor shaping method for IPM machines in [139].

In addition to the above, a number of alternative magnet shaping methods for PM machines were reported. In [140], the magnet shape was optimised by using the Latin hypercube sampling strategy. In [141], a cost-effective rotor shaping method for SPM was proposed to reduce the cogging torque and is shown in Fig. 1.19. In [142], a new rotor shaping by introducing deep slots between the rotor poles and flattening the stator teeth, as shown in Fig. 1.20, was developed to reduce on-load torque ripples.



(a) Original (b) Cost-effective  
Fig. 1.19. Cost-effective rotor shaping for SPM developed in [141].



(a) Original (b) Proposed  
Fig. 1.20. Shaping method developed in [142] for IPM machines.

The rotor pole shaping methods of salient pole EE machines were reported in [60], [143]-[146]. As stated in [60], in salient pole EE machines, generally, the inverse cosine airgap length shape, as shown in Fig. 1.14 and (1.1), was preferred. In reality, the offset centre arc shape, as shown in Fig. 1.17(b), was often employed instead of the inverse cosine airgap length shape.

## 1.4.2 Skewing

Beside shaping the rotor, skewing either the stator or the rotor is another widely employed method of torque ripple reducing for nearly all types of electric machines [120]-[123], [147]-[173]. Skewing is also often used together with other methods to further reduce the torque ripples.

In general, there are three ways to implement skewing, namely continuous, stepped, and herringbone, as shown in Fig. 1.21. Stepped skewing was developed to simplify manufacturing [147]. Herringbone skewing was developed to reduce the axial asymmetry and the axial force [148]. In literature, some other skewing methods, although were not widely used, were also developed for especial purposes, such as examples highlighted in [25], [149], and [150].

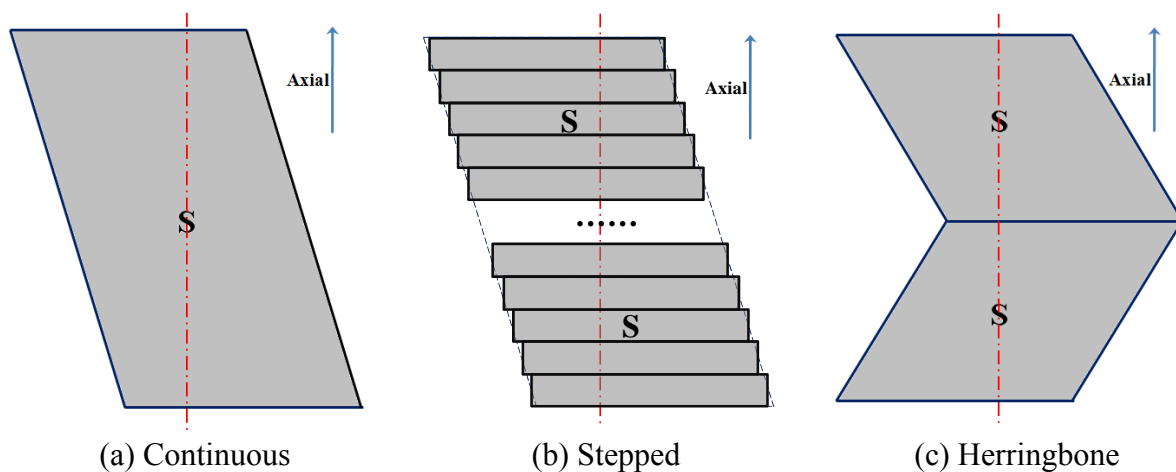


Fig. 1.21. Three ways of skewing.

Most of investigations on the influence of skewing were focused on open-circuit performance, such as cogging torque and EMF. The influence of magnetic saturation is often neglected and hence analytical methods can be employed for analyses [121]-[123], [151]-[153]. It was shown that the open-circuit performance was always improved significantly by skewing and its influence can be represented by skew factors, whilst the cogging torque can be eliminated by skewing one slot pitch, or more precisely, by one cogging torque period

[121]-[123]. In addition, skewing either the stator or the rotor had the same effect on cogging torque and EMFs.

However, the on-load torque ripples are much more difficult to analyze by analytical models due to magnetic saturation. Hence, FE methods were often employed [154]-[164]. Ideally, the 3D FE method is required for analysing the influence of skewing. However, the 3D FE method tends to be complicated and time consuming. Therefore, the 2D multi-slice method was widely used. However, it should be noticed that, using 2D multi-slice method, the end effects of skewing are not considered.

The effectiveness of skewing was examined in [164]-[168]. In [164], it was found that, in induction machines, the skewing caused axial variation of magnetic saturation. Hence, the magnetic saturation dependent parameters were different at different axial locations. However, only the inductance results were given in the paper. In [165], the influence of skewing on the magnetic field distributions of an EE machine was studied by experimental methods. By using search coils, the field distributions were calculated from the measured voltage waveforms. It was shown that, on open-circuit, a regular phase shift along axial direction can be observed due to the effects of skewing. However, when the machine was on load, not only the phase shift but also the variation of magnitude along axial direction were observed, since the armature and excitation flux densities interacted at different phase angles. Due to this, the iron loss at rotor pole face was increased by 18% when the skewing was introduced. In [166], the optimal skewing angle between PM segments for 2-step skewing was derived in terms of the lowest EMF harmonics, being half of the cogging torque period. Thus, the cogging torque was diminished by skewing. However, the test results showed that the on-load torque ripple was only reduced slightly and can be reduced more effectively when a larger skewing angle was applied. In [167], the influence of electric loading and magnetic saturation on the cogging torque and EMF was investigated. The on-load torque ripples were found to be much higher due to a much higher on-load cogging torque and richer on-load EMF harmonics under the influence of electric loading and magnetic saturation on load. Furthermore, the on-load cogging torque period became much larger than the open-circuit one and the same as on-load torque ripple period, i.e.  $60^\circ$  electrical for 3-phase machines, which caused the skewing based on open-circuit analyses less effective. However, it was mentioned that by increasing the skewing angle to the on-load torque ripple period, the on-load torque ripple could be still diminished effectively. In contrast, [168] reported for the first time that on-load torque ripples could not be always reduced by skewing. Based on the multi-slice model, it was found that the equivalent current phase advance angle for each slice under

skewing was different, which resulted in the variation of on-load torque ripple magnitude along axial direction. This axial variation of torque ripple magnitude could have caused the skewing less effective or even failed on torque ripple reduction.

However, as will be shown in chapter 3, the effectiveness of skewing largely depends on the axial variation of the torque ripple phase but less on its magnitude under skewing. Therefore, in this thesis, the influence of skewing on torque ripples in PM machines with different magnet shapes and loads are investigated, with the aims to reveal (a) why the on-load torque ripple cannot be reduced even by skewing one on-load torque ripple period; (b) when the skewing will be less effective or even fail to reduce the on-load torque ripple; (c) which torque ripple component is responsible for this; (d) whether it is only due to the influence of magnetic saturation; and (5) ways of improving the skewing when the conventional skewing method fails.

### **1.4.3 Other Methods**

In addition to rotor shaping and skewing methods, there are also a number of alternative methods to reducing torque ripple, which are briefly reviewed.

One of the methods is the combination of slot and pole numbers. Beside the open-circuit cogging torque, which has been illustrated earlier, the slot and pole number combination also largely decides the winding connections and, hence, the winding factors and torque ripples. In [174], it was shown that by using an odd slot number per pole pair in IPM machines, the torque ripple can be lower than 5% without skewing or rotor shaping. In [175], for BLDC PM machines, instead of an integral slot number per pole, one additional slot was employed, such as changing from 24-slot to 25-slot. In this way, both the cogging torque and the on load torque ripple were greatly reduced whilst maintaining a good trapezoidal back EMF waveform can still be maintained. The disadvantage of this technique was that the resultant e armature winding was unbalanced, which resulted in UMF and vibration.

In [132], [176], and [177], rotor pole shifting was employed for torque ripple reduction, as shown in Fig. 1.22. However, caution should be paid to the unbalance issues, such as UMF, vibration and noise, when using the shifting.

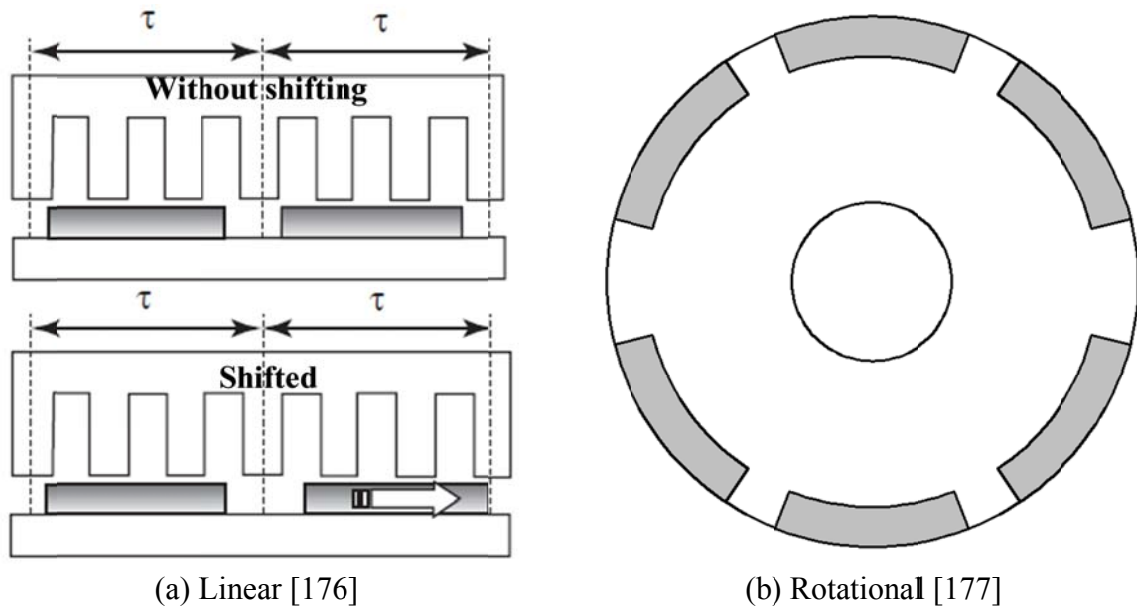


Fig. 1.22. Ways of pole shifting.

In [178]-[180], the auxiliary teeth or slots were employed to reduce the cogging torque, as shown in Fig. 1.23. The drawback of auxiliary teeth is that the slot area is reduced. For the auxiliary slots, the equivalent airgap length is increased.

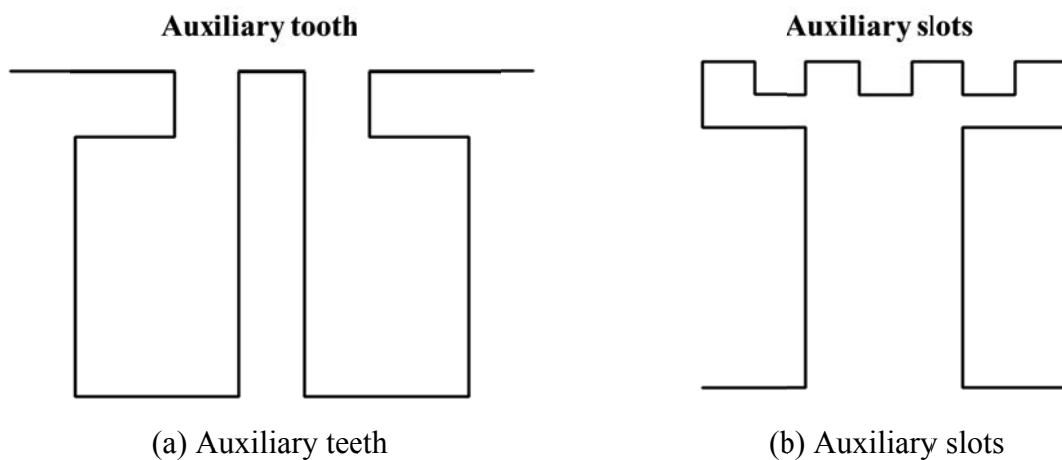


Fig. 1.23. Illustrations of auxiliary teeth and slots.

Another way of reducing torque ripple is by using Halbach magnetised rotors [181], [182], as illustrated in Fig. 1.24. Ideally sinusoidal airgap flux density and hence negligible cogging torque as well as low on-load torque ripple can be achieved. The disadvantages of Halbach magnetized machines lie in the difficulties to manufacture the rotor poles and high magnet usage.

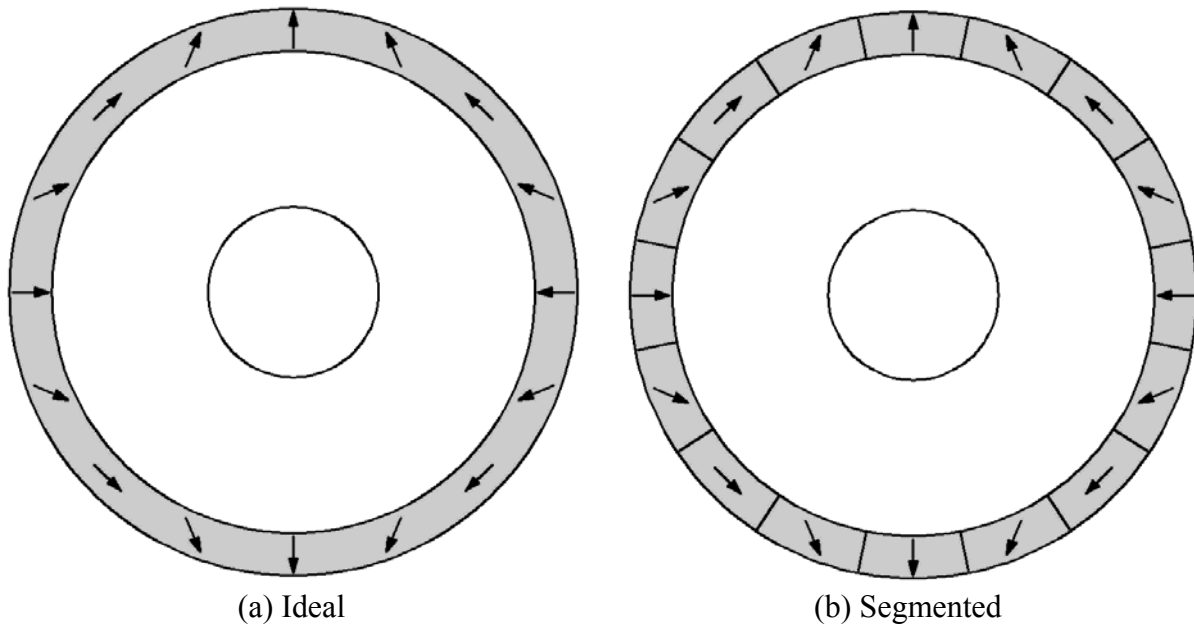


Fig. 1.24. 4-pole Halbach magnetized magnet.

For all the methods developed for torque ripple reduction, further attention should be paid to the influence of magnetic saturation on torque ripples. In [164], [165], [168], [188]-[190], it has been clearly illustrated that the torque ripples were influenced significantly by magnetic saturation. It also suggested in [189] and [190] that, in order to achieve lower torque ripple, lower magnetic saturation was preferred. Therefore, it was better to have lower electric loading, larger machine volume, larger slot opening, wider teeth, and narrower magnets.

### 1.5 On-load Torque Separation

As mentioned in the previous sections, the open-circuit cogging torque can be analysed by various methods allowing various methods of cogging torque reduction to be developed accordingly. However, this is not the case for on-load torques due to two reasons. First, the on-load torque has several components and the characteristics of each torque components are different. In terms of on-load average torque, it is contributed by the PM and reluctance torques. The PM torque is due to the interaction between the PM and armature fields. The reluctance torque is due to the interaction between the armature field and the rotor magnetic saliency. In terms of on-load torque ripple, it is contributed by on-load cogging torque and EM torque ripple. Second, due to the magnetic saturation, it is significantly difficult to have each torque component separated. In order to better understand the characteristics of on-load torque and hence improve it, the separation of the on-load torque into its individual torque components are most desirable and have been discussed in literature.

In order to separate the on-load torque, both the on-load magnetic field separation method and the torque calculation theory are essential.

It is well-known that the on-load PM and armature fields influence each other and change with magnetic saturation and cross-coupling, both the constant PM flux linkage model and the partial-coupling model [191] may result in significant inaccuracy. Hence, the frozen permeability (FP) method is often employed [167], [192]-[202], which is able to accurately separate the PM and armature fields while accounting for any magnetic saturation and cross-coupling.

For the torque calculation, the Maxwell stress tensor and virtual work principle are two of the well-known and widely used methods [203]-[211]. Based on the Maxwell stress tensor method, the torque is calculated directly from the radial and tangential flux density components. Based on the virtual work principle, the torque may be calculated from the flux linkages. It is also well known that the torques calculated by these two methods should be identical, at least theoretically, in normal finite element (FE) analyses [203]-[210] although they may be influenced by the FE mesh discretization, etc.

Therefore, for the average torque separation based on FP method, there were two ways. (1) based on the Maxwell stress tensor method, the reluctance torque is computed with the on-load armature field only and the PM torque is then calculated from the difference between the total torque and reluctance torque [208]; and (2) based on the virtual work method, the PM and reluctance torque components are calculated from the flux linkages contributed by the on-load PM or armature field only [192]-[195]. Since the torques calculated by the Maxwell stress tensor method and virtual work principle are identical in normal FE analyses, both methods are assumed to be accurate and widely employed for the torque separation in literature. However, these methods have never been validated when the FP method is employed. Therefore, in this thesis, for the first time, the average torque components separated by the Maxwell stress tensor and the virtual work principle are compared and examined when the FP method is employed.

For on-load torque ripple separation, the on-load cogging torque calculation is the most difficult challenge. Due to its complexity, methods used to calculate on-load cogging torque have only been mentioned recently in a few papers and were developed by analogy with methods used to calculate open-circuit cogging torque. The open-circuit cogging torque can be obtained by both the Maxwell stress tensor method and the virtual work principle. In [209], the on-load cogging torque was calculated as the differential of total magnetic energy stored in the machine with respect to the rotor position at constant current. The concern with this

method is that the total magnetic energy is also contributed by the armature field when the machine is on load, which means this method is inappropriate for on-load cogging torque calculation as will be shown later. In [208], nominally, the authors attempted to exclude the magnetic energy due to the armature field by replacing the total magnetic energy with the total magnetic energy less the magnetic energy stored in the coils. The concern with this method is that without using the FP method, technically, the magnetic energy was calculated by including components such as the airgap, the magnets, the rotor and stator steel and any other regions of the motor which were not part of the coils. Therefore, the magnetic energy due to the armature field is still included and hence it is inappropriate for calculation the on-load cogging torque. Based on the FP method, the on-load cogging torque was calculated by the Maxwell stress tensor with the on-load PM field only in [167], [208]. However, it was found in this thesis that the average of this calculated torque was not zero, which indicates that it cannot be the on-load cogging torque as well. Hence, none of the existing methods are accurate for calculating the on-load cogging torque.

Given the problems highlighted above, this thesis proposes a new method for on-load cogging torque calculation based on the combination of the virtual work principle and FP method. In order to implement the new method, the improved FP method is developed as well. Together with the existing methods, all the on-load cogging torque calculation methods will be examined in both linear and nonlinear cases. Furthermore, the reasons, which make the existing methods inappropriate for on-load cogging torque calculation, will be illustrated correspondingly as well.

## 1.6 Outline of Thesis

In thesis, the investigation is focused on the torque characteristics, both average torque and torque ripple, of PM and EE machines for DD applications. For the average torque investigation, analytical torque models are developed for optimisation and comparison. For torque ripple, the influence of the two most widely employed torque ripple reduction methods, i.e., skewing and rotor shaping, on both PM and EE machines is investigated and compared. In order to better understand the on-load torque, the separations of on-load torque into its components, both average torque and torque ripple, are discussed as well. The thesis is organized as follows.

**Chapter 1** reviews the background and previous work, presents the main objectives, outline, and main contributions of this thesis.

**Chapter 2** develops an analytical model of external rotor PM machines for the optimisation of torque per volume.

**Chapter 3** investigates the influence of skewing on the torque ripples of PM machines with and without rotor shaping. The ways of improving the skewing is also discussed when conventional skewing methods fail.

**Chapter 4** investigates the average torque separation of on-load torque of PM machines using frozen permeability method.

**Chapter 5** investigates the on-load cogging torque calculation in PM machines. A new on-load cogging torque calculation method is proposed based on the combination of the virtual work principle and FP method. For its implementation, an improved FP method is developed as well.

**Chapter 6** develops a simplified analytical torque model of EE machines. Based on the optimal designs, PM and EE machines are compared in terms of two torque densities, i.e., torque per volume and torque per weight.

**Chapter 7** investigates and compares the influence of rotor shaping and skewing between EE and PM machines.

**Chapter 8** makes a conclusion based on the work of this thesis and discusses the future work.

**APPENDIX A** develops an analytical model of transient response in PM machines with 3-phase symmetric short-circuit fault for investigation and design improvement.

**APPENDIX B** reports the designs of 3kW PM prototype machines.

**APPENDIX C** reports the designs of PM and EE prototype machines for the investigation of chapter 7.

**APPENDIX D** lists the publications resulted from this PhD study.

## 1.7 Major Contributions of Thesis

The major contributions of this thesis are:

- For external rotor PM machines, it reveals that the torque density is maximum when the average airgap flux density is slightly lower than the half of the maximum flux density in the stator.
- The on-load torque ripple is not always reduced by skewing. The effectiveness of skewing largely depends on the axial variation of torque ripple phase but less on its magnitude under skewing. In both linear and nonlinear cases, EM and on-load torque ripples cannot be fully eliminated by skewing one on-load torque ripple period or any other angles, except  $360^\circ$  electrical, which is impractical.
- When the FP method is employed, the average torque separation can be performed appropriately by the virtual work principle while the Maxwell stress tensor cannot.
- A new way of on-load cogging torque calculation method, which is able to avoid all the shortcomings of existing methods, is proposed based on the combination of the virtual work principle and frozen permeability method. For its implementation, an improved frozen permeability method, which makes the magnetic energy with on-load permanent magnet field only can be calculated according to the B-H curve, is also developed.
- PM machines can exhibit more than  $\sqrt{2}$  times torque densities of EE machines. For EE machines, there is an optimal pole number to maximize the torque densities and it is more advantageous for large volume applications. The optimal torque per weight designs have significantly higher split ratio and are more cost-effective than the optimal torque per volume designs.
- Rotor shaping is less effective on torque ripple reduction in EE machines than SPM machines due to asymmetric magnetic saturation caused by  $q$ -axis magnetic field. However, with skewing, EE machines still can achieve the same level torque ripple as PM machines.

## **CHAPTER 2 ANALYTICAL OPTIMISATION OF EXTERNAL ROTOR PERMANENT MAGNET MACHINES**

This chapter presents an analytical model for optimising the maximum torque per volume in external rotor PM machines, in which the maximum achievable airgap flux density depends on the split ratio of stator outer diameter to rotor outer diameter and the stator slot area is a function of split ratio, airgap flux density, and stator split ratio of stator diameter at slot bottom to stator outer diameter. The optimal split ratio, stator split ratio, and airgap flux density are derived analytically with/without considering that the maximum achievable airgap flux density is limited by the split ratio. In addition, the influence of airgap flux density distributions, slot and pole numbers, slot shapes, tooth-tips, end-windings, rotor yoke and inner diameter on the optima is discussed.

### **2.1 Introduction**

Own to high torque density and efficiency, PM machines are increasingly popular for various applications, such as electric vehicles, renewable energies, and industrial automations, and so on. Therefore, the optimisation of PM machines becomes one of the most important topics and has been intensively discussed in literature.

Most of the discussions on the optimisation have been based on the machines having internal rotor [89]-[91], [93]-[99]. In [89], the output coefficient for synchronous machines was expressed for the first time as a function of the outer diameter, airgap diameter, effective axial length, magnetic loading, and electric loading. In [90], it was shown that the output torque was significantly influenced by the split ratio, that is the ratio of airgap diameter to the outer diameter, and flux density ratio, that is the ratio of airgap flux density to the flux density in stator. The optimal split ratio for maximum torque per volume was derived and investigated for internal rotor PM machines accounting for various design features in [94], [96]-[99]. The influence of split ratio on the overall cost and thermal behavior was discussed in [95] and [116], respectively. The optimal flux density ratio was discussed and derived in [89] and [98]. The influence of PM dimensions and configurations on the design and optimisation of brushless AC machines was investigated in [117].

Meanwhile, the high-performance electric traction has been one of the most important and popular research topics. The in-wheel direct-drive by employing external rotor PM brushless machines is one of the most favorite configurations. However, external rotor PM machines

are significantly different from internal rotor PM machines in two aspects. First, in internal rotor PM machines, the maximum achievable airgap flux density is independent of the split ratio [98]. However, for external rotor PM machines, the maximum achievable airgap flux density produced by magnets is limited by the split ratio, as illustrated in Figs. 2.1 and 2.2. Fig. 2.2 is calculated by nonlinear FE analyses based on external rotor SPM machines with the remanence of magnet being 1.2T. For each split ratio, the variation of airgap flux density produced magnets with the magnet thickness is calculated. Then, the maximum achievable airgap flux density produced by magnets for different split ratio is obtained. Second, for internal rotor PM machines, the stator slot area and hence the torque density are a function of split ratio and flux density ratio. However, as will be shown later, for external rotor PM machines, the stator slot area and hence the torque density are a function of split ratio, flux density ratio, and stator split ratio (the ratio of the diameter at slot bottom to the airgap diameter). Therefore, the foregoing analytical models based on the internal rotor PM machines are not applicable to external rotor PM machines.

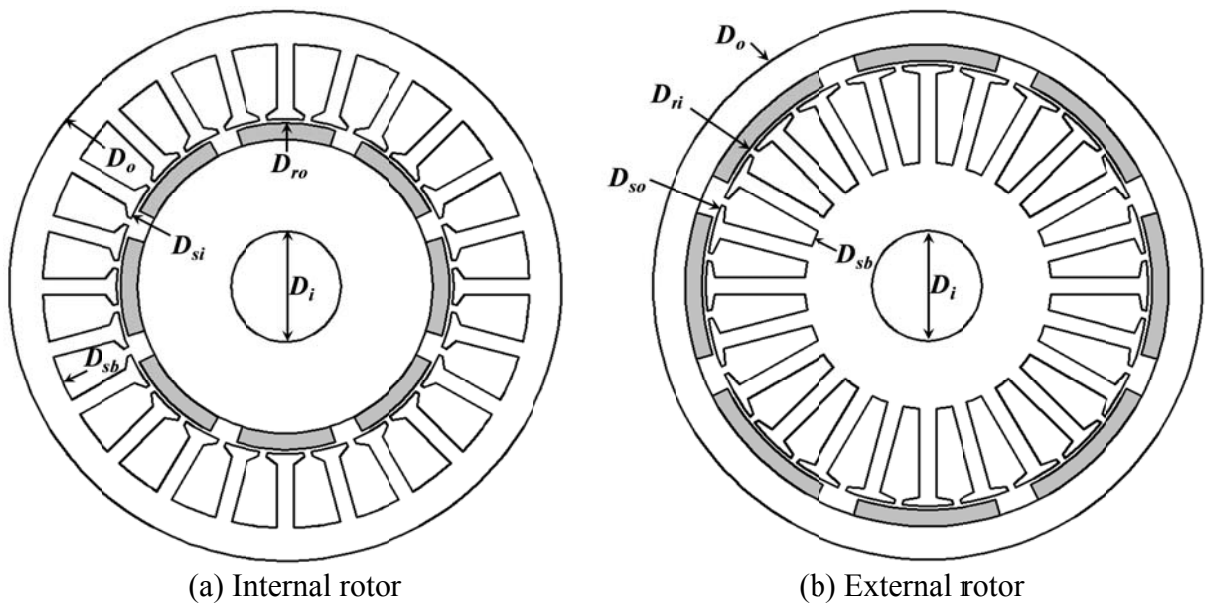


Fig. 2.1. Schematics of internal and external rotor SPM machines.

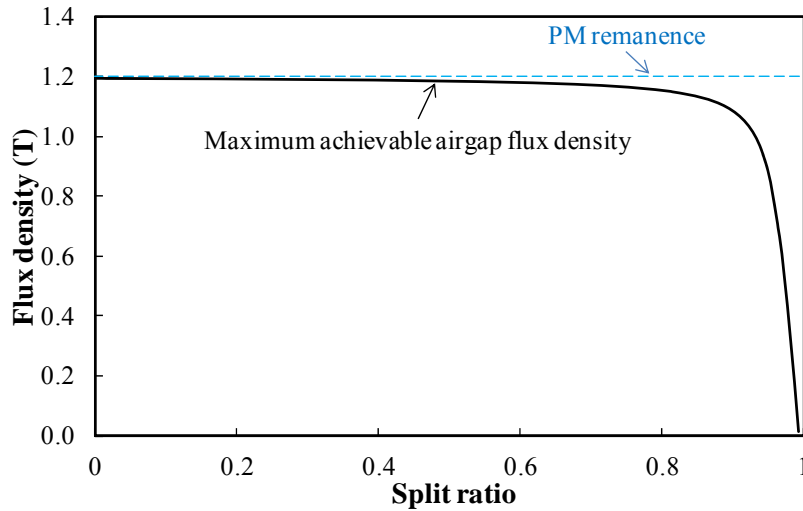


Fig. 2.2. Variation of FE predicted maximum achievable airgap flux density with split ratio in external rotor PM machines.

The optimisation of external rotor PM machines when the inner and outer diameters were fixed was reported in [100] and [101]. The analytical torque expression was developed by fixing the airgap flux density to its maximum achievable value. The stator tooth width and yoke thickness were then calculated accordingly. Therefore, the developed torque was a function of split ratio only. However, it was mathematically too complicated to analytically derive the optimal split ratio based on the developed model. Alternatively, the optimal split ratio was obtained by scanning. Although it showed that the optimal split ratio was high and close to 1, which was already well known, it failed to obtain the analytical expression of optimal split ratio. Hence, it was still unable to obtain the optimal design directly. Therefore, it was less useful for machine designs.

However, even in external rotor PM machines, it is inappropriate to fix the airgap flux density to its maximum achievable value, since the airgap flux density can still be independent of the split ratio when it is lower than the maximum achievable one. As will be shown later, the optimal airgap flux density is lower than the maximum value for most range of the split ratio. Furthermore, in this chapter, the investigation is extended to cater for the cases when the limitation of inner diameter does not influence the optimal design. In this case, the stator slot area and hence the torque are functions of split ratio, flux density ratio, and stator split ratio, which are much more complicated. However, by using the proposed optimisation procedure, as will be detailed later, it is still able to analytically derive the optimal stator split ratio, split ratio, and flux density ratio and, hence, will provide valuable insights and aid the external rotor PM machine design. It will also be shown that, instead of the optimal split ratio, which is close to 1, the derivations of optimal flux density ratio and

stator split ratio are more useful for the external rotor PM machine design.

The investigation is carried out based on general torque models. In order to illustrate the variations, numerical results are obtained based on a special example given in Table 2-I. The general torque model is developed in section 2.2. Initially, the optimal stator split ratio, split ratio, and flux density ratio are derived analytically based on the idealised machine in section 2.3. The influence of practical design considerations, such as airgap flux density distributions, slot and pole numbers, slot shapes, tooth-tips, and end-windings on the optima is investigated subsequently in section 2.4. The torque models and optima when either the rotor yoke or the inner diameter is fixed are discussed as well in sections 2.5 and 2.6, respectively. The FE and experimental validation is given in section 2.7.

Table 2-I Main parameters

Parameters	value	Parameters	value
Outer diameter $D_o$	240mm	Maximum flux density $B_m$	1.8T
Armature copper loss $p_{cua}$	23.1W	Airgap length $\delta$	0.8mm
Slot packing factor $k_{pa}$	0.37	Magnet remanance $B_r$	1.2T
Active axial length $L_{ef}$	44.1mm	Recoil permeability $\mu_r$	1.05

## 2.2 General Analytical Torque Equation

The average electromagnetic (EM) torque of PM machine, when it is under the brushless AC operation and zero d-axis current control, the airgap flux density distribution is uniform, which will be shown later in Fig. 2.7(a), and the influence of armature reaction and magnetic reluctance in the laminations is neglected, is given by

$$T_{av} = 3E_a I_a / \omega_m = 6\sqrt{2}k_{dp}L_{ef}D_\delta B_{\delta av}N_a I_a / \pi \quad (2.1)$$

where  $E_a$  is the RMS value of fundamental open-circuit phase back EMF,  $I_a$  is RMS phase current,  $\omega_m$  is the mechanical angular speed,  $D_\delta$  is the airgap diameter,  $L_{ef}$  is the effective axial length,  $B_{\delta av}$  is the average airgap flux density,  $k_{dp}$  is the winding factor, and  $N_a$  is the number of turns per phase.

It should be noticed that the influence of armature reaction usually can be neglected in small machines, where the electric loading is small. However, for large machines, where the electric loading is much bigger, the influence of armature reaction then cannot be neglected.

The magnetic reluctance in the laminations is often neglected, since the permeability of lamination is significantly higher than the permeability of the air unless the lamination is heavily saturated magnetically.

Neglecting the end-windings, the copper loss,  $p_{cua}$ , is given by

$$p_{cua} = 36(N_a I_a)^2 \rho L_{ef} / (k_{pa} A_a) \quad (2.2)$$

where  $A_a$  is the total armature slot area per machine,  $\rho$  is the conductor resistivity, and  $k_{pa}$  is the effective armature winding packing factor including the influence of slot liners (i.e., the ratio of pure copper areas to the total slot area).

By eliminating  $N_a I_a$ , the average EM torque can be given by

$$T_{av} = \frac{\sqrt{2}}{\pi} k_{dp} D_o \lambda_\delta B_m \gamma \sqrt{\frac{L_{ef} p_{cua} A_a k_{pa}}{\rho}} \quad (2.3)$$

$$\lambda_\delta = D_\delta / D_o \quad (2.4)$$

$$\gamma = B_{\delta av} / B_m \quad (2.5)$$

where  $\lambda_\delta$  is the split ratio,  $\gamma$  is the flux density ratio,  $D_o$  is the outer diameter, and  $B_m$  is the maximum flux density in the lamination.

The average EM torque equation, that is (2.3), is universal for all PM machines having either internal or external rotor. However, the special configuration of external rotor makes it different from internal rotor PM machines in several ways as follows.

For external rotor PM machines, the split ratio is defined as

$$\lambda_\delta = D_{so} / D_o \quad (2.6)$$

where  $D_{so}$  is the stator outer diameter.

The expression of stator slot area is also different. For external rotor PM machines having parallel stator teeth and neglecting the tooth-tips and slot wedges, as illustrated in Fig. 2.3(c), the stator tooth width  $b_t$  and hence the slot area  $A_s$  are given by

$$b_t = 2p\Phi_m / (L_{ef} N_s B_m) = \pi D_o \lambda_\delta B_{\delta av} / (N_s B_m) = \pi D_o \gamma \lambda_\delta / N_s \quad (2.7)$$

$$A_s = \pi D_o^2 \lambda_\delta^2 (1 - \lambda_s)(1 + \lambda_s - 2\gamma) / 4 \quad (2.8)$$

$$\lambda_s = D_{sb} / D_{so} \quad (2.9)$$

where  $\Phi_m$  is the maximum flux per pole,  $N_s$  is the slot number,  $\lambda_s$  is the stator split ratio, and

$D_{sb}$  is the diameter at slot bottom.

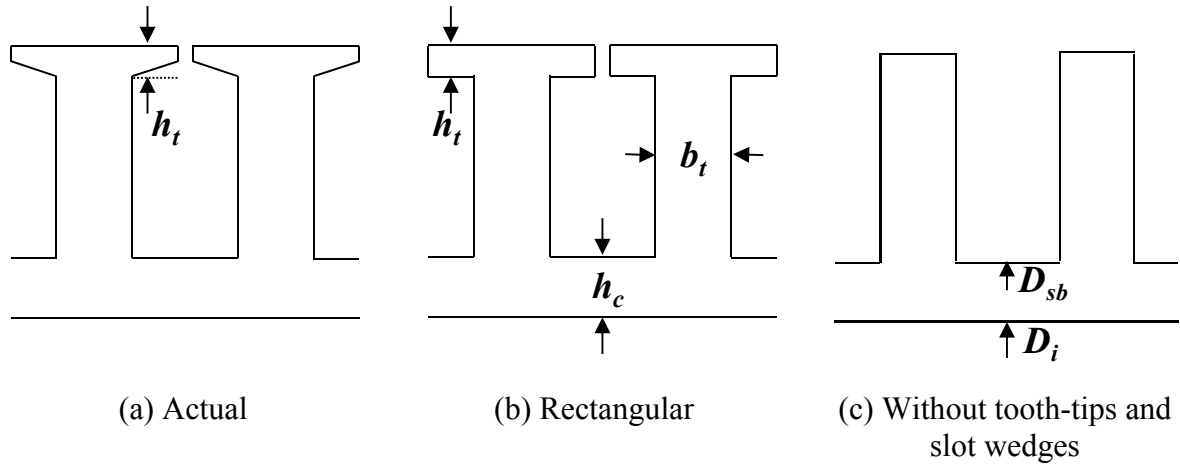


Fig. 2.3. Alternative stator tooth-tip shapes.

It can be seen that the slot area of external rotor PM machines depends on the split ratio, flux density ratio, and stator split ratio, which is significantly different from the one of internal rotor PM machines.

By submitting (2.8) into (2.3), the average EM torque for external rotor PM machines can be obtained as

$$T_{av} = C_1 \cdot \lambda_\delta^2 \gamma \sqrt{(1 - \lambda_s)(1 + \lambda_s - 2\gamma)} \quad (2.10)$$

$$C_1 = \sqrt{L_{ef} p_{cua} k_{pa} / (2\pi\rho) k_{ap} D_o^2 B_m} \quad (2.11)$$

Another difference is that in external rotor PM machines, the maximum achievable airgap flux density depends on the split ratio, which makes the analyses even more complicated.

### 2.3 Optimal Stator Split Ratio, Flux Density Ratio, and Split Ratio

In order to cope with the difficulties mentioned earlier and derive the optimal values analytically, a three-step optimisation procedure is proposed:

Step-1: the stator slot area is maximised by optimising the stator split ratio, since the stator split ratio is the only independent design parameter.

Step-2: based on Step-1, the ideal optimal flux density ratio and split ratio are further obtained assuming that the flux density ratio is independent of the split ratio.

Step-3: based on Step-2, the analytical torque model is developed and simplified for the optimisation accounting for the extra relationship between the flux density ratio and split ratio.

As will be shown later, based on the proposed three-step optimisation procedure, the relationships are decoupled one by one and then the optima can be derived analytically. Furthermore, the investigation of Step-2 helps to confine the ranges of flux density ratio and split ratio, and then simplify the analytical model in Step-3 significantly. The difference between Step-2 and Step-3 also reveals the influence of this extra relationship on the optimal design.

### 2.3.1 Optimal Stator Split Ratio for Specific Flux Density Ratio

For the given split ratio and flux density ratio, the slot area increases when the stator split ratio starts to decrease from 1, as shown in Fig. 2.4. Since the stator tooth width is fixed in this case, geometrically, the slot area reaches the maximum when the adjacent stator teeth just touch each other, as shown in Fig. 2.4(c). By differentiating (2.8), the optimal stator split ratio to maximize the slot area can be obtained as

$$\lambda_{sop} = \gamma \quad (2.12)$$

It can be seen that the optimal stator split ratio only depends on the flux density ratio. This is due to that, when the flux density ratio is given, the stator tooth width changes proportionally to the airgap diameter.

Based on the optimal stator split ratio in (2.12), the slot area and average EM torque can be then obtained as

$$A_a = \pi D_o^2 \lambda_\delta^2 (1 - \gamma)^2 / 4 \quad (2.13)$$

$$T_{av} = C_1 \cdot \lambda_\delta^2 \gamma (1 - \gamma) \quad (2.14)$$

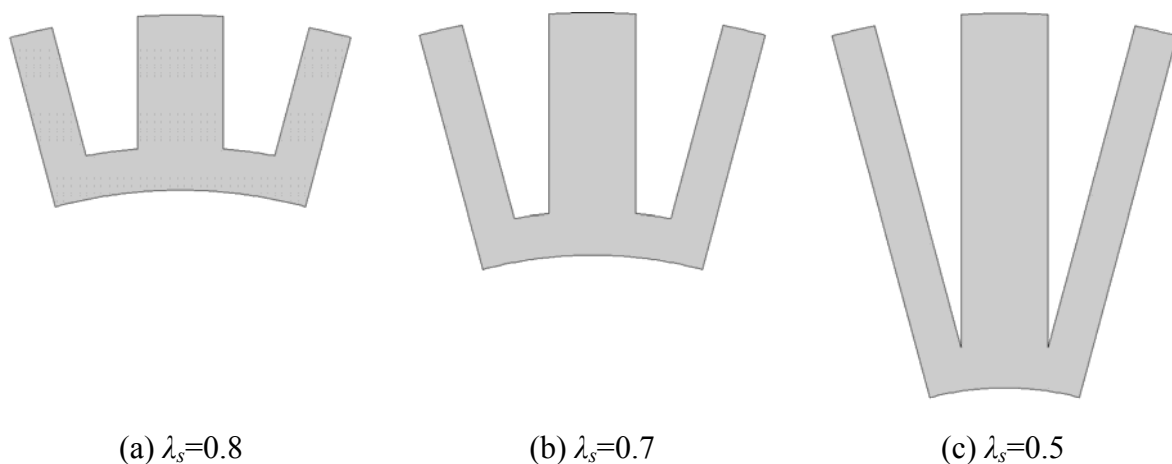


Fig. 2.4. Variation of slot area with stator split ratio when  $\gamma=0.5$ , teeth are parallel, and tooth-tips are neglected

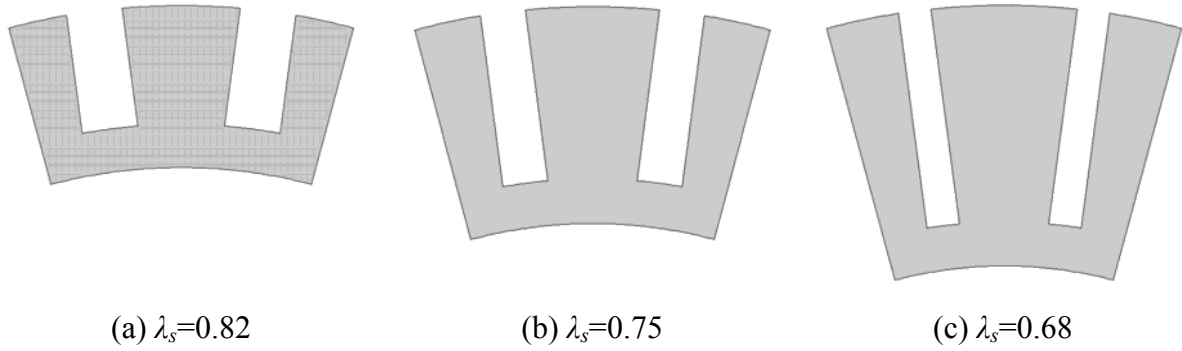


Fig. 2.5. Variation of slot area with stator split ratio when  $\gamma=0.5$ , slots are parallel (which will be investigated in section 2.4.3), and tooth-tips are neglected.

### 2.3.2 Optimal Split Ratio and Flux Density Ratio

Based on the optimal stator split ratio, the torque becomes a function of the split ratio and flux density ratio, as shown in (2.14). Mathematically, the optimal flux density ratio and split ratio can be derived independently and individually, since there is no term of  $\gamma\lambda_\delta$ .

On the other hand, as shown in Fig. 2.2, the maximum achievable airgap flux density depends on the split ratio. However, the airgap flux density can be free to vary in wide range except when the split ratio is close to 1.

In order to account for the influence of this extra relationship between airgap flux density and split ratio, the Step 2 and Step 3 mentioned in the foregoing are employed.

Assuming that the airgap flux density is independent of the split ratio, the ideal optimal flux density ratio to maximize the torque can be obtained from (2.14) as

$$\gamma_{op} = 0.5 \quad (2.15)$$

Ideally, the average EM torque is maximum when the average airgap flux density is half of the flux density in the stator. Combined with (2.12), for this ideal stator, the tooth width is half of the tooth pitch and slot depth is half of the airgap radius, as shown in Fig. 2.4(c).

It can be seen from Fig. 2.2 that this ideal optimal flux density ratio can be achieved for the most range of split ratio except when the split ratio is very close to 1.

In contrast, the optimal flux density ratio for internal rotor PM machines is 1 [98], which is twice of the external rotor one and may not be easily achieved even using flux focusing configuration.

Based on the optimal stator split ratio in (2.12) and the ideal optimal flux density ratio in (2.15), the torque is given as

$$T_{av} = C_1 \cdot \lambda_\delta^2 / 4 \quad (2.16)$$

In this case, the torque is proportional to the square of split ratio. One is contributed by the airgap diameter and the other one is because of the armature MMF. Apparently, the torque is higher when the split ratio increases.

However, when the split ratio approaches 1, the maximum achievable airgap flux density ratio reduces rapidly. When the flux density ratio is lower than 0.5, (2.16) no longer holds. Therefore, it is necessary to revise the torque model for the optimisation when the flux density ratio is lower than 0.5 and depends on the split ratio.

In this case, the split ratio is close to 1 and its variation is very limited whereas the flux density ratio changes significantly from 0 to 0.5. Hence, the variation of torque is largely due to the flux density ratio rather than the split ratio. Therefore, the derivation of the optimal flux density ratio is more useful than the optimal split ratio.

Since the flux density ratio is lower than 0.5, the investigation can be based on the surface-mounted configuration, where the relationship between the flux density ratio and split ratio is given by

$$\lambda_\delta = \frac{1 - \beta_\delta - \mu_r \beta_\delta \gamma / (\gamma_r - \gamma)}{1 + \pi \gamma / (2p)} \quad (2.17)$$

$$\beta_\delta = 2\delta / D_o \quad (2.18)$$

$$\gamma_r = B_r / B_m \quad (2.19)$$

where  $p$  is the number of pole pairs,  $\delta$  is the airgap length,  $B_r$  is the magnet remanence, and  $\mu_r$  is the relative permeability of magnet.

Combining (2.14) with (2.17), the torque performance over the whole range of flux density ratio and split ratio can be obtained, as shown in Fig. 2.6. However, it is mathematically complicated to derive the optima based on (2.17).

On the other hand, based on (2.15) and Fig. 2.6, it can be seen that the torque peaks when the flux density ratio is slightly lower than its ideal optimal value, that is 0.5.  $\gamma_r - \gamma$  can then be approximated by  $\gamma_r - 0.45$ . Combined with  $\beta_\delta \ll 1$ , (2.17) can be simplified as

$$\lambda_\delta = \frac{(1 - \beta_\delta)(1 - k_1 \gamma)}{1 + k_2 \gamma} \approx \frac{1 - \beta_\delta}{(1 + k_1 \gamma)(1 + k_2 \gamma)} \approx \frac{1 - \beta_\delta}{1 + (k_1 + k_2) \gamma} \quad (2.20)$$

$$k_1 = \frac{\mu_r \beta_\delta}{(1 - \beta_\delta)(\gamma_r - 0.45)} \quad (2.21)$$

$$k_2 = \pi/(2p) \quad (2.22)$$

By eliminating the split ratio in (2.14), the torque can be expressed as

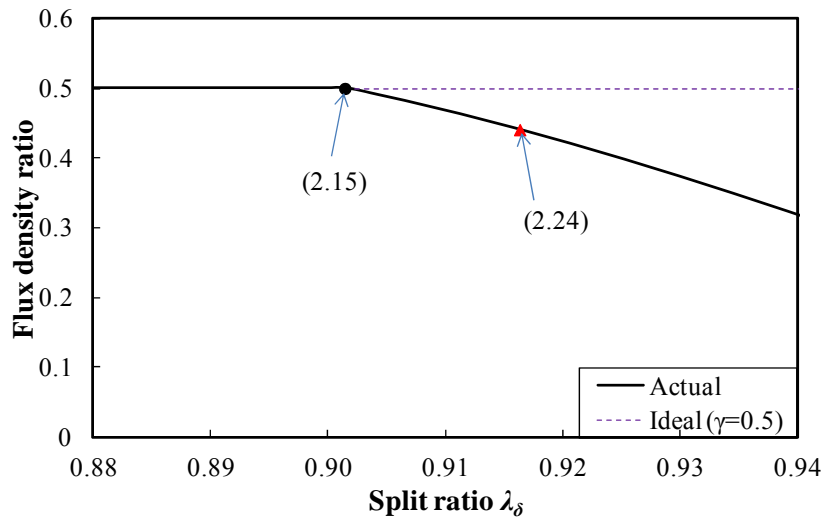
$$T_{av} = C_1 \frac{(1 - \beta_\delta)^2 \gamma (1 - \gamma)}{[1 + (k_1 + k_2) \gamma]^2} \quad (2.23)$$

Therefore, the simplified actual optimal flux density ratio accounting for the extra limitation on the flux density ratio because of the split ratio can be derived as:

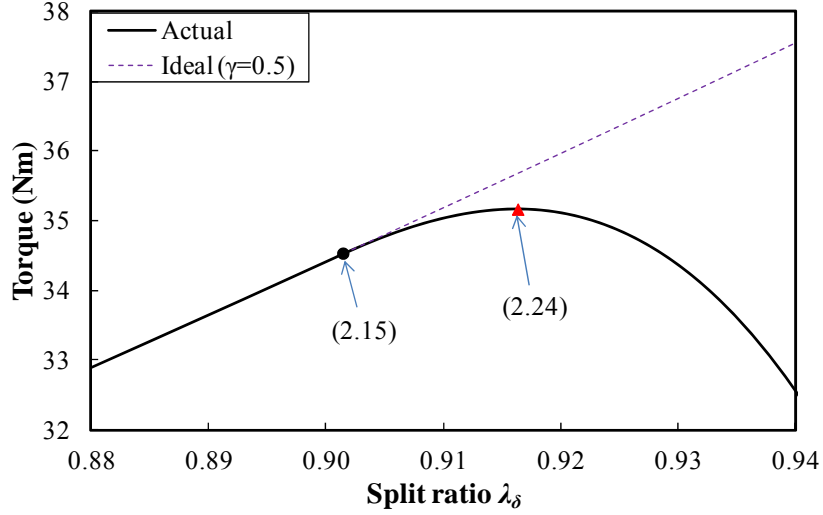
$$\gamma_{op} = 1/(2 + k_1 + k_2) \quad (2.24)$$

Compared with the ideal optimal flux density ratio given by (2.15), the actual optimal flux density ratio given by (2.24) is slightly lower, because of the influence of magnet and rotor yoke. Since, mathematically, (2.24) is derived including the maximum achievable torque of (2.15), it suggests that (2.24) is the overall optimal flux density ratio. Based on (2.20) and (2.24), the optimal split ratio can be obtained easily.

The variation of torque and flux density ratio with split ratio is given in Fig. 2.6. The black dot represents the maximum achievable torque based on (2.15) in actual design. The red triangle represents the torque based on (2.24). It confirms that the design based on (2.24) is the overall optimal.



(a) Flux density ratio



(b) Average torque

Fig. 2.6. Variation of average EM torque and flux density ratio with  $\lambda_\delta$  ( $2p=20$ ).

## 2.4 Practical Design Considerations

In previous sections, the torque expression and optima are derived based on an idealized PM machine. In this section, the influence of practical design considerations, such as airgap flux density distribution, slot and pole numbers, slot shapes, tooth-tips, and end-windings on the optima and torque is investigated.

### 2.4.1 Influence of Airgap Flux Density Distribution

In the actual machines, the airgap flux density distribution may be far away from uniform. However, the foregoing analytical model and conclusions are equally applicable based on the following two updates.

(a) The general torque equation can be given as:

$$T_{av} = \frac{3\pi}{2\sqrt{2}} k_{dp} k_\phi L_{ef} D_\delta B_{\delta av} N_a I_a \quad (2.25)$$

$$k_\phi = \frac{\Phi_1}{\Phi_m} = \frac{\Phi_1}{\pi D_\delta B_{\delta av} L_{ef} / (2p)} \quad (2.26)$$

where  $k_\phi$  is the flux ratio of airgap flux density distribution, and  $\Phi_1$  is the magnitude of fundamental flux component per pole.

(b) The relationship between the flux density ratio and split ratio, (2.17), is updated due to that the magnet thickness is determined by the maximum of airgap flux density ( $B_{\delta m}$ ) rather than the average airgap flux density ( $B_{\delta av}$ )

$$\lambda_\delta = \frac{1 - \beta_\delta - \mu_r \beta_\delta k_m \gamma / (\gamma_r - k_m \gamma)}{1 + \pi \gamma / (2p)} \quad (2.27)$$

$$k_m = B_{\delta m} / B_{\delta av} \quad (2.28)$$

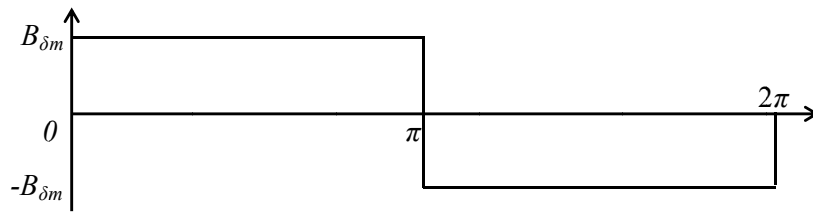
where  $k_m$  is the magnitude ratio of airgap flux density distribution.

All the other expressions, such as copper loss and stator slot area, remain the same as the ones given in section 2.2.

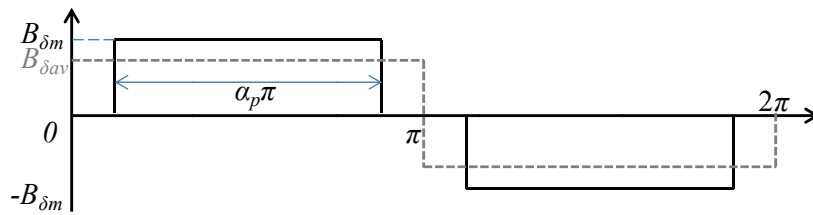
By way of example, typical airgap flux density distributions and their  $k_\phi$  and  $k_m$  are summarized in Table 2-II and Fig. 2.7.

Table 2-II Airgap flux density distributions and coefficients

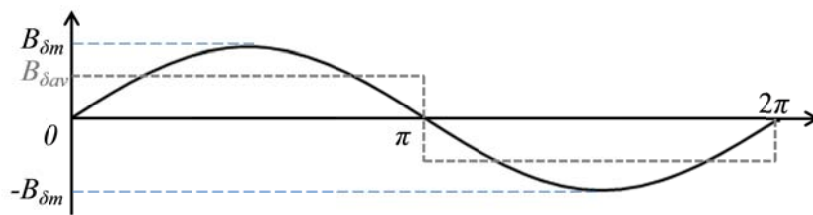
Waveform	$k_\phi$	$k_m$
Fig. 2.7(a)	$8/\pi^2$	1
Fig. 2.7(b)	$\frac{8}{\alpha_p \pi^2} \sin\left(\frac{\alpha_p \pi}{2}\right)$	$1/\alpha_p$
Fig. 2.7(c)	1	$\pi/2$



(a) Uniform (full pitched)



(b) Uniform (short pitched)



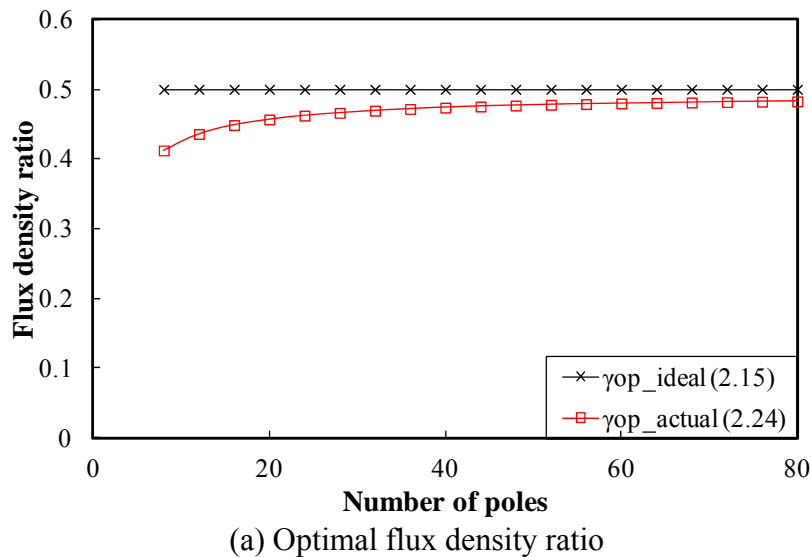
(c) Sinusoidal

Fig. 2.7. Typical airgap flux density distributions.

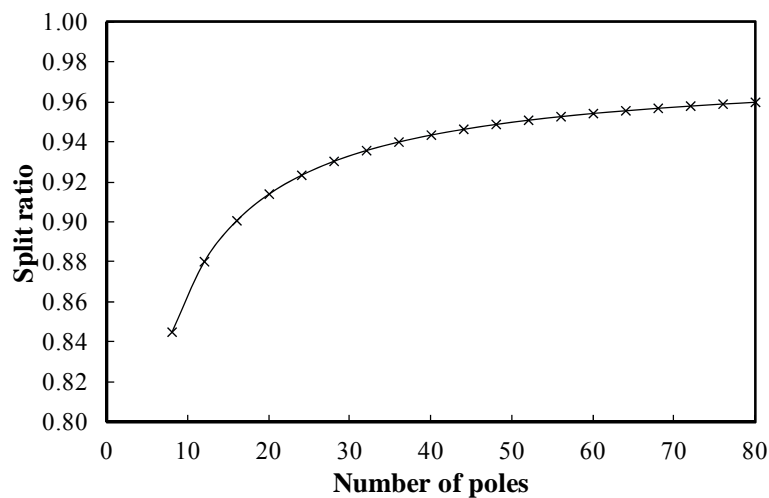
### 2.4.2 Influence of Slot and Pole Numbers

The pole and slot numbers determine the winding configuration and stator yoke, which influence the optimal split ratio of internal rotor PM machines [98]. However, as shown earlier, in external rotor PM machines, the slot area is only influenced by the rotor yoke but not by the stator yoke when there is no constraint on the inner diameter. Therefore, the optimal split ratio and flux density ratio for external rotor PM machines is only influenced by the number of poles.

As can be seen from Fig. 2.8, when the number of poles increases, the actual optimal flux density ratio increases and is closer to its ideal value, that is 0.5. The optimal split ratio increases as well, since the rotor yoke is thinner. The variation of optimal flux density ratio and split ratio is lower when the number of poles is higher.



(a) Optimal flux density ratio



(b) Optimal split ratio based on (2.24)

Fig. 2.8. Variation of optimal flux density ratio and split ratio with  $2p$ .

### 2.4.3 Influence of Slot Shape

For some applications, the parallel stator slots, as shown in Fig. 2.9(b), are often employed to ease the manufacturing and repairing process of armature windings. In this case, the stator slot area is given as

$$A_a = \pi D_o^2 \lambda_\delta^2 (1 - \lambda_s)(\lambda_s - \gamma)/2 \quad (2.29)$$

Consequently, the optimal stator split ratio and corresponding maximum slot area can be obtained as

$$\lambda_{sop} = (1 + \gamma)/2 \quad (2.30)$$

$$A_a = \pi D_o^2 \lambda_\delta^2 (1 - \gamma)^2/8 \quad (2.31)$$

Compared with the optimal values having parallel teeth in (2.12) and (2.13), it can be seen that, for the same split ratio and flux density ratio, the optimal stator split ratio is higher whereas the maximum stator slot area is halved when the machine has parallel slots, which can also be seen from Fig. 2.9. Therefore, the optimal flux density ratio and split ratio remain the same as foregoing whereas the maximum torque having parallel slots is  $1/\sqrt{2}$  of the one having parallel teeth.

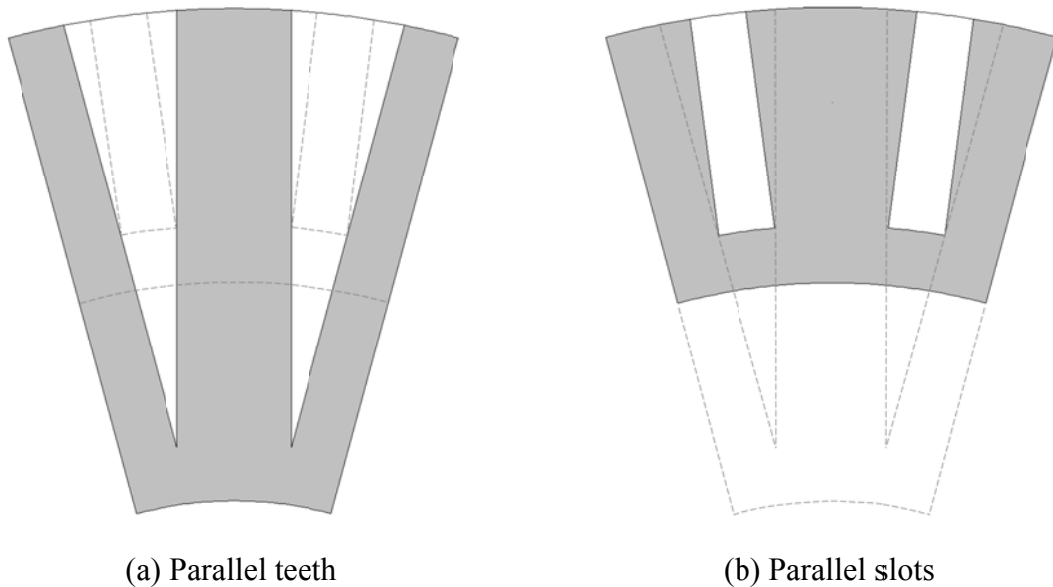


Fig. 2.9. Optimal stator cross-sections with parallel teeth or parallel slots, without tooth-tips when  $\gamma=0.5$  (dash lines represent the other design).

#### 2.4.4 Influence of Tooth-tips and Slot Wedges

In the actual machines, the tooth-tips and slot wedges are often employed to reduce the influence of slot opening. Although there are various shapes of tooth-tips and slot wedges, they can be treated equivalently by using the rectangular shape including the influence of slot wedges, as illustrated in Fig. 2.3(a) and (b). The stator slot area accounting for the tooth-tips is given by

$$A_a = \pi D_o^2 \lambda_\delta^2 (1 - \beta_t - \lambda_s)(1 - \beta_t + \lambda_s - 2\gamma)/4 \quad (2.32)$$

$$\beta_t = 2h_t/D_{so} \quad (2.33)$$

where  $h_t$  is the equivalent height including the tooth-tips and slot wedges.

Since the optimal split ratio for external rotor PM machines will be close to 1,  $\beta_t$  can be approximated by the tooth-tip ratio  $2h_t/D_o$ .

Based on (2.32), the same optimal stator split ratio can be obtained as (2.12), since the tooth-tip does not influence the tooth width. However, the maximum stator slot area is reduced and given by

$$A_a = \pi D_o^2 \lambda_\delta^2 (1 - \beta_t - \gamma)^2/4 \quad (2.34)$$

Consequently, the ideal optimal flux density ratio assuming the flux density ratio is independent of split ratio becomes

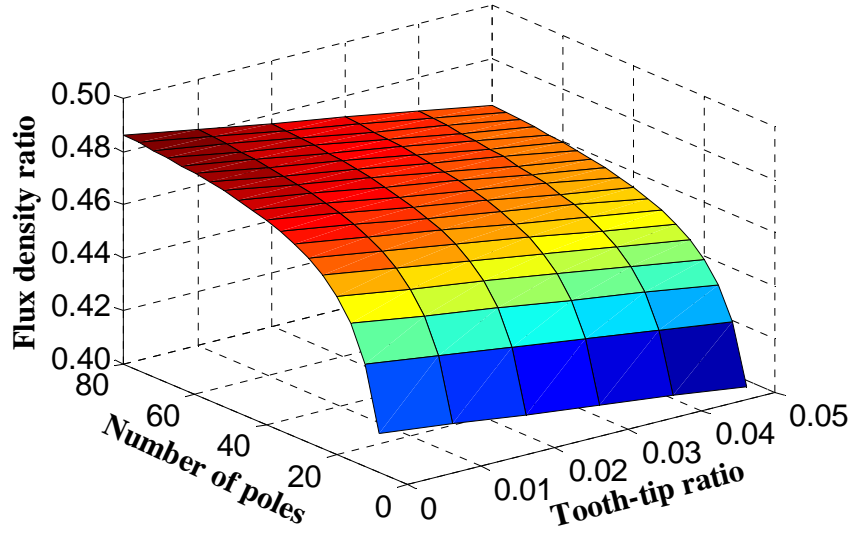
$$\gamma_{op} = (1 - \beta_t)/2 \quad (2.35)$$

The actual optimal flux density ratio considering the relationship between flux density and split ratio is given by

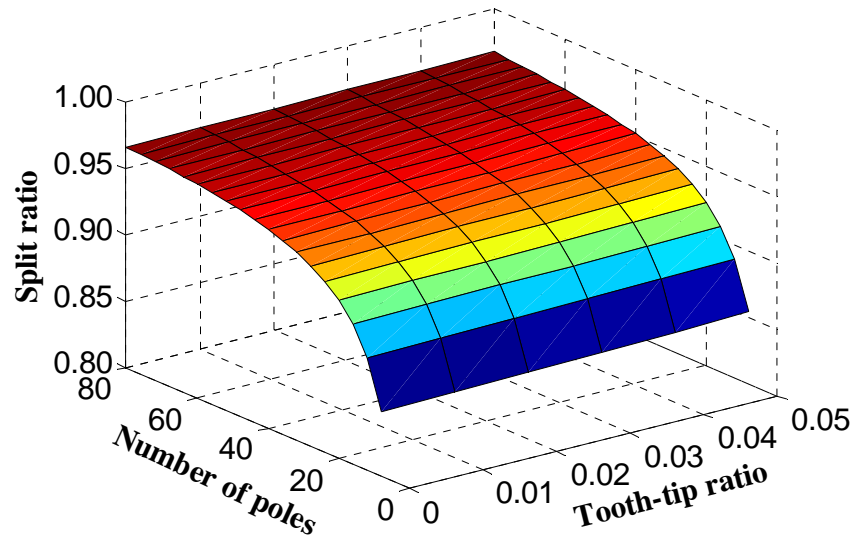
$$\gamma_{op} = \frac{1 - \beta_t}{2 + (k_1 + k_2)(1 - \beta_t)} \quad (2.36)$$

The optimal split ratio can be obtained correspondingly based on (2.20) and (2.36).

The influence of tooth-tips on the optima is given in Fig. 2.10. It can be seen that the optimal flux density ratio reduces almost linearly with the tooth-tip ratio, especially when the machine has high number of poles. However, the influence of tooth-tips on the optimal split ratio is negligible.



(a) Optimal flux density ratio by (2.36)



(b) Optimal split ratio

Fig. 2.10. Variation of actual optimal split ratio and flux density ratio with tooth-tip ratio.

#### 2.4.5 Influence of End-windings

The copper loss and the average torque accounting for the end-windings can be rewritten as

$$p_{cua} = 36(N_a I_a)^2 \rho (L_{ef} + L_{aend}) / (k_{pa} A_a) \quad (2.37)$$

$$T_{av} = \frac{\pi}{4} \sqrt{\frac{p_{cua} k_{pa} A_a}{2\rho (L_{ef} + L_{aend})}} k_{dp} k_{\phi} L_{ef} D_{\delta} B_{\delta av} \quad (2.38)$$

where  $L_{aend}$  is the average end-windings length of armature winding.

The end-windings length largely depends on the slot/pole number combination and winding

configurations, such as overlapping or non-overlapping windings. It is also significantly affected by the manufacturing. Its influence is important only when the ratio of pole pitch to the effective axial length is high. Therefore, instead of being predicted analytically based on assumptions, which is complicated and not necessarily accurate, the end-winding length can be treated as a constant depending on the slot/pole number combination and winding configurations. Since the end-winding only affects the constant  $C_1$ , the optima remain the same as foregoing.

## 2.5 Optimisation with Fixed Rotor Yoke Thickness

For the majority of machine designs, the rotor yoke varies correspondingly with the number of poles and flux density ratio to avoid heavy magnetic saturation. However, when the pole number keeps increasing, the rotor yoke becomes too thin to support the rotor. Therefore, in this case, it is better to fix the rotor yoke thickness for the mechanical consideration.

When the rotor yoke thickness is fixed, the relationship between the flux density ratio and split ratio becomes

$$\lambda_\delta \approx \frac{1 - \beta_\delta - \beta_{ry}}{1 + k_1\gamma} \quad (2.39)$$

$$\beta_{ry} = 2h_{ry}/D_o \quad (2.40)$$

where  $\beta_{ry}$  is the rotor yoke ratio and  $h_{ry}$  is the thickness of rotor yoke.

Therefore, the actual optimal flux density ratio is changed slightly into

$$\gamma_{op} = 1/(2 + k_1) \quad (2.41)$$

All the other analytical models and optima remain the same as the ones in sections 2.2 and 2.3.

## 2.6 Optimisation with Fixed Inner Diameter

The foregoing investigation is carried out without any constraint on the inner diameter. Therefore, the stator yoke and, hence, the slot number have no influence on the optimal designs. However, the inner diameter  $D_i$  may also be fixed because of the mechanical requirement.

Since the optimal stator split ratio of the machines having parallel teeth is much lower than

the one having parallel slots, the investigation with the fixed inner diameter is carried out on the one having parallel teeth. In this case, the slot area is given as

$$A_a = \pi D_o^2 (\lambda_\delta - \lambda_0 - k_{sb} \lambda_\delta \gamma) (\lambda_\delta + \lambda_0 + k_{sb} \lambda_\delta \gamma - 2 \lambda_\delta \gamma) / 4 \quad (2.42)$$

$$\lambda_0 = D_i / D_o \quad (2.43)$$

where  $\lambda_0$  is the constant representing the ratio of the inner diameter to the outer diameter, and  $k_{sb}$  is the stator yoke coefficient and given as:

$$k_{sb} = \pi / (2p) \text{ when stator yoke is half of pole pitch} \quad (2.44)$$

$$k_{sb} = \pi / N_s \text{ when stator yoke is half of tooth width} \quad (2.45)$$

where  $N_s$  is the slot number.

It should be noticed that only when  $\lambda_0$  is higher than 0.5, it is then able to influence the optimal design.

Assuming the flux density ratio is independent of split ratio, the ideal optimal flux density ratio can be derived as:

$$\gamma_{op} = \frac{k_3 - \sqrt{k_3^2 - 32k_{sb}(2 - k_{sb})(\lambda_\delta^2 - \lambda_0^2)}}{8\lambda_\delta k_{sb}(2 - k_{sb})} \quad (2.46)$$

$$k_3 = 3[2(\lambda_\delta - \lambda_0) + 2k_{sb}\lambda_0] \quad (2.47)$$

Based on (2.1), (2.17), and (2.42), the analytical torque expression considering the relationship between flux density and split ratio can also be developed. Although the optimal flux density ratio and split ratio can be derived analytically, it is mathematically complicated. Alternatively, they can be obtained easily by scanning.

The variation of actual optimal split ratio and flux density ratio with the inner diameter ratio is shown in Fig. 2.11. When the number of poles is low, the influence of stator yoke is higher. Therefore, when the inner diameter ratio  $\lambda_0$  increases, the optimal flux density ratio reduces to have thinner stator yoke. Consequently, the optimal split ratio increases. When the number of poles is high, the optimal flux density ratio firstly increases and then decreases with  $\lambda_0$ . It can be explained as follows.

When the pole number is high and  $\lambda_0$  is low, the influence of stator yoke can be neglected and, hence, (2.46) can be further simplified as

$$\gamma_{op} = \frac{1}{3} + \frac{\lambda_0}{3\lambda_\delta} \quad (2.48)$$

In this case, the optimal flux density increases with  $\lambda_0$  and can be higher than 0.5.

When  $\lambda_0$  keeps increasing, the influence of stator yoke is higher and cannot be neglected even when the pole number is high. Therefore, being similar with the case when the number of pole is low, the optimal flux density decreases with  $\lambda_0$ .

However, since the influence of stator yoke is greatly reduced, both the optimal flux density ratio and split ratio change modestly with  $\lambda_0$  when the pole number is high, as shown in Fig. 2.11.

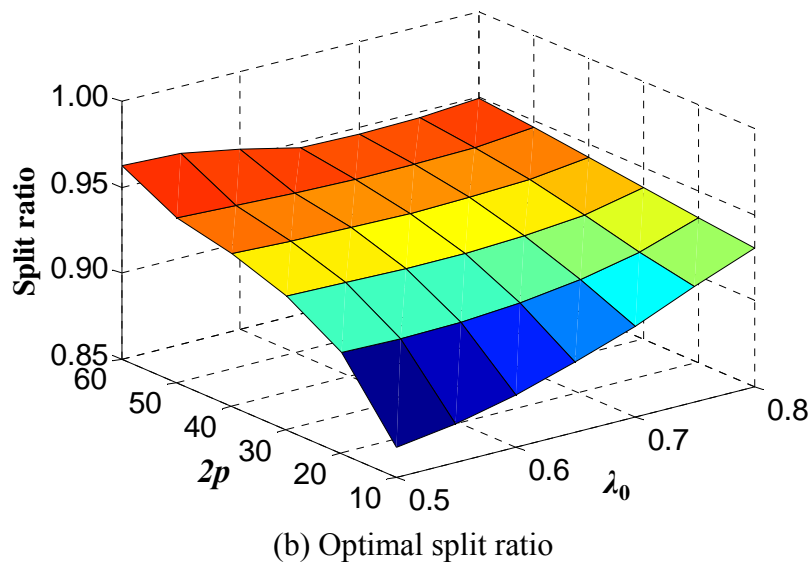
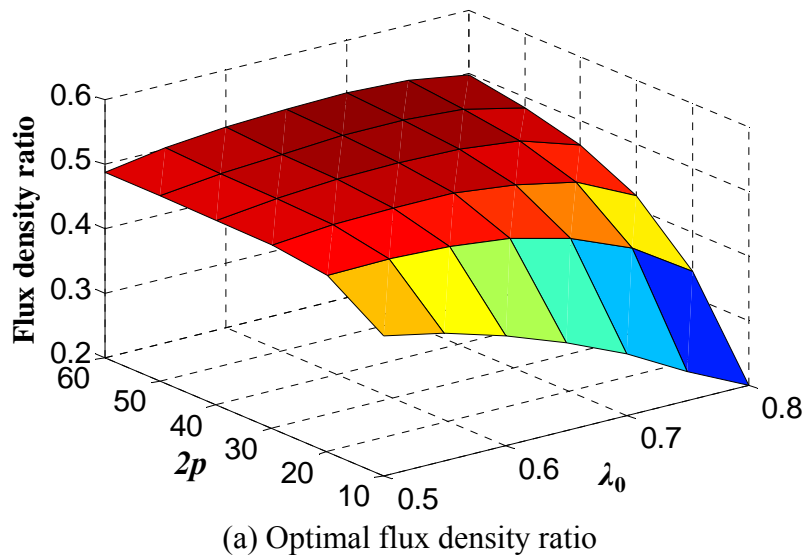


Fig. 2.11. Variation of optimal flux density ratio and split ratio with inner diameter ratio  $\lambda_0$ .

## 2.7 Verification by FEA and Measurements

In order to verify the foregoing analytical models and investigation, the FE analyses and experimental measurements have been carried out on a 54-slot/60-pole external rotor PM machine with its outer diameter, inner diameter, and rotor yoke thickness fixed as 240mm, 160mm, and 3.1mm, respectively, whereas the tooth-tip height is 4mm and the end-winding length is 8.5mm. The other parameters are detailed in Table 2-I.

The variation of analytical and FE calculated flux density ratios and output torques with the split ratio is shown Fig. 2.12. For each specific split ratio, the optimal design is obtained by the analytical analysis. Based on the analytically predicted dimensions, the 2-D FE model of the optimal design is created and the FE calculated results are obtained by nonlinear FE analyses. Although the analytically predicted torque is slightly higher than the FE calculated torque because of the assumptions as well as the magnetic saturation, it can be seen that the analytically predicted torque varies with the split ratio in the same way as the FE calculated torque. More importantly, the FE calculated torque peaks at the same optimal split ratio predicted analytically and the optimal flux density ratio is slightly lower than 0.5 as predicted analytically.

Based on the optimisation shown in Fig. 2.12, the prototype is built and measured. The permanent magnet thickness for the optimal flux density ratio and split ratio is 2.73mm. However, the PM thickness is increased slightly to 3mm to ease the manufacturing with almost the same output torque, as shown in Fig. 2.12(b). Correspondingly, the tooth width is 5.7mm and the stator yoke is 2.9mm. The stator and rotor of the prototype machine are shown in Fig. 2.13. The measured and FE predicted open-circuit back-EMF waveforms are shown in Fig. 2.14. The measured average torque is 27.9Nm, which confirms the analytically predicted torque (29.6Nm) and the FE calculated torque (29.1Nm).

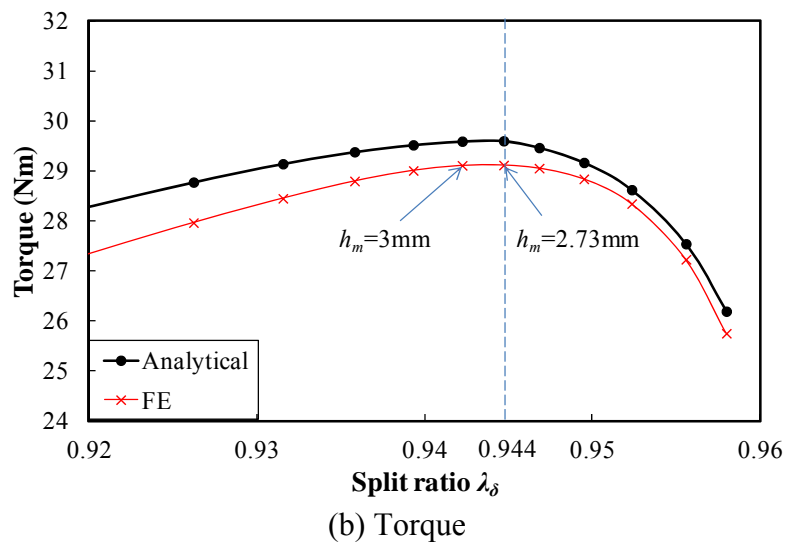
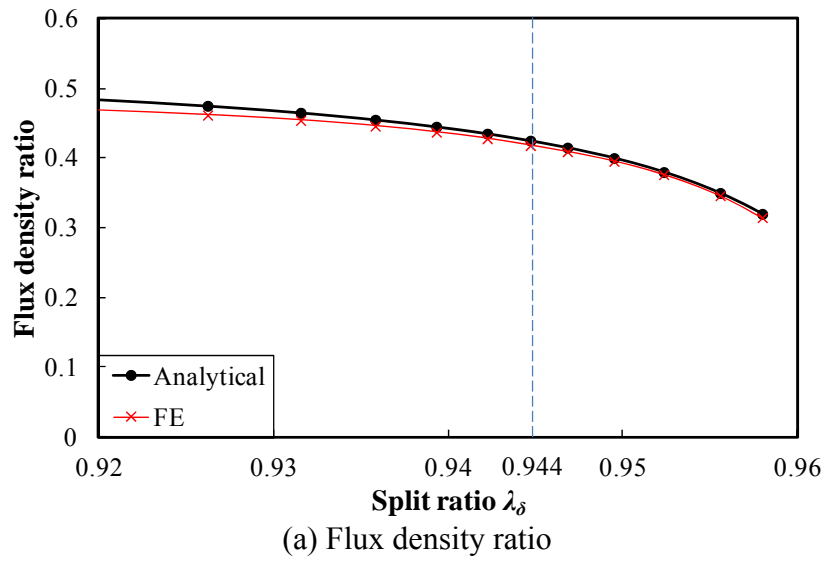


Fig. 2.12. Variation of analytically and FE predicted flux density ratios and torques with split ratio of 54-slot/60-pole machine.



(a) Stator with windings



(b) Rotor and hub

Fig. 2.13. Prototype 54-slot/60-pole external rotor PM machine.

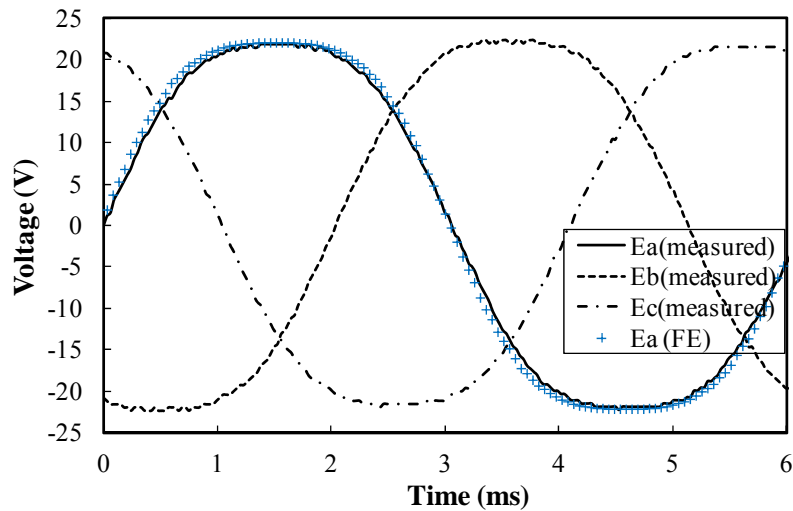


Fig. 2.14. Measured and FE predicted open-circuit back-EMF waveforms of 54-slot/60-pole prototype machine at 325rpm.

## 2.8 Summary

The analytical optimisation of maximum torque density for external rotor PM machines has been investigated with/without fixing the rotor yoke or inner diameter. The optimal stator split ratio, split ratio, and flux density ratio have been derived analytically and verified by both FEA and measurements. The differences between the internal and external rotor PM machines are highlighted. The influence of airgap flux density distributions, slot and pole numbers, slot shapes, tooth-tips, and end-windings with/without fixing the rotor yoke or inner diameter has been systematically investigated. All the investigation, especially the optimal stator split ratio, split ratio, and flux density ratio, provides valuable insights and aids the external rotor PM machine design.

# **CHAPTER 3    INVESTIGATION OF TORQUE RIPPLE IN PERMANENT MAGNET SYNCHRONOUS MACHINE WITH SKEWING**

This chapter investigates the influence of skewing on torque ripples, including EM torque ripple and cogging torque, in PM machines. It is found that the effectiveness of skewing largely depends on the axial variation of torque ripple phase but less on its magnitude under skewing. It is further found that, in both linear and nonlinear cases, the EM and on-load torque ripples cannot be fully eliminated by skewing one on-load torque ripple period or any other angles, except  $360^\circ$  electrical, which is impractical. Furthermore, an improved way of skewing by optimising both the skewing angle and current phase advance angle is proposed to reduce the torque ripple when the conventional skewing fails.

## **3.1 Introduction**

Due to high torque density and efficiency, PM machines are popular for many applications. It is essential to reduce the torque ripples for low vibration and acoustic noise, especially for high-performance applications, such as electrical power steering, servo motors, and direct-drive wind power generators.

Various studies have been carried out on the analysis and reduction of torque ripples, which include cogging torque and EM torque ripple [120]. The torque ripples can be reduced by either machine designs [127]-[182] or control methods [183]-[187], one of the most widely used methods being the skewing, which is also often employed together with other methods to further reduce the torque ripple. The investigation on the effectiveness of skewing may be divided into open-circuit and load conditions.

Most of the investigation on the influence of skewing was focused on the open-circuit performance, such as cogging torque and EMF. The influence of magnetic saturation is often neglected and, hence, analytical methods can be employed for analysis. It was shown that the open-circuit performance was always improved significantly by skewing, and its influence can be represented by a skew factor [121], [123], [153], while the cogging torque can be eliminated by skewing one slot pitch, or more precisely, by one cogging torque period [121]-[123]. In addition, skewing either the stator or the rotor had the same effect on the cogging torque and the EMF [121]-[123], [151]-[153].

However, the on-load torque ripples are much more difficult to analyse by analytical

models due to magnetic saturation [188]-[190]. Hence, FE methods [154]-[163] were often employed. The 3-D FE method is required for analysing the influence of skewing. However, it is usually complicated and time consuming. Therefore, the 2-D multi-slice method was widely used [156]-[162].

The effectiveness of skewing on load was examined in [164]-[168]. In [164], it was found that the skewing caused the axial variation of magnetic saturation. Hence, the magnetic-saturation-dependent parameters were different in different slices. However, only the result of inductance was given. In [166], the optimal skewing angle between PM segments for 2-step skewing was derived in terms of the lowest EMF harmonics, being half of the cogging torque period. Thus, the cogging torque was diminished by skewing. However, its test results showed that the on-load torque ripple was only slightly reduced and can be reduced more effectively when a larger skewing angle was applied. In [167], the influence of electric loading and magnetic saturation on the cogging torque and the EMF was investigated. The on-load torque ripples were found to be much higher due to higher cogging torque and richer EMF harmonics under the influence of electric loading and magnetic saturation on load. Furthermore, the on-load cogging torque period became much larger than the open-circuit one and the same as on-load torque ripple period, i.e.,  $60^\circ$  electrical for three-phase machines, which caused the skewing based on the open-circuit analysis less effective. However, it was mentioned that, by increasing the skewing angle to the on-load torque ripple period, the on-load torque ripple could be still diminished effectively. In contrast, Islam *et al.* [168] reported for the first time that the on-load torque ripple could not be always reduced by skewing. Based on the multi-slice model, it was found that the equivalent current phase advance angle for each slice under skewing was different, which resulted in the variation of on-load torque ripple magnitude along axial direction. This axial variation of torque ripple magnitude could have caused skewing to be less effective or even fail on torque ripple reduction. However, as will be shown in this chapter, the effectiveness of skewing largely depends on the axial variation of torque ripple phase but less on its magnitude under skewing.

Therefore, in this chapter, the influence of skewing on the torque ripples in PM machines with different magnet shapes and loads is investigated, with the aims to reveal:

- (1) why the on-load torque ripple cannot be reduced even by skewing one on-load torque ripple period;
- (2) when the skewing is less effective or even fail to reduce the on-load torque ripple;
- (3) which torque ripple component is responsible for this;
- (4) whether it is only due to the influence of magnetic saturation; and

(5) ways of improving the skewing when the conventional one fails.

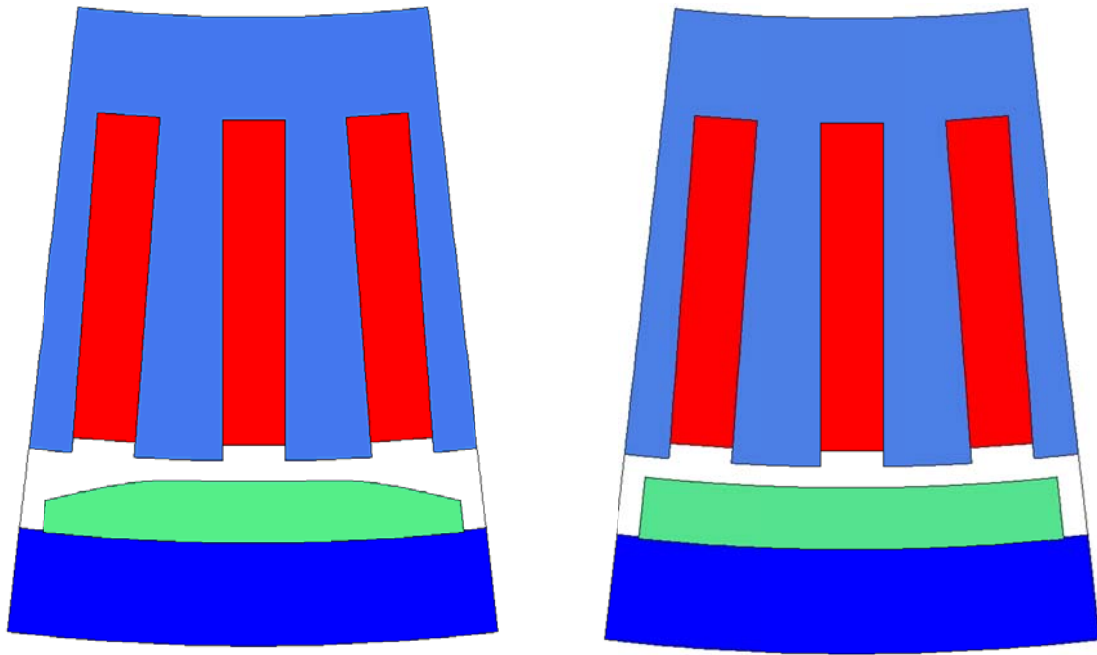
The chapter is organized as follows. In section 3.2, two prototype machines with/without magnet shaping are described. In section 3.3, the torque waveforms and ripples with/without skewing by one on-load torque ripple period are presented. The mechanism and effectiveness of skewing on torque ripple reduction at open-circuit, half load, and full load are investigated in section 3.4. The influence of skewing steps is given in section 3.5. The effectiveness of skewing with different skewing angles under non-linear and linear cases is further investigated in sections 3.6 and 3.7, respectively. The ways of improving the skewing are discussed in section 3.8. The 3-D FE verification is given in section 3.9.

## 3.2 Prototype Machines

The investigation is carried out on SPM machines. To achieve the stringent torque ripple requirement, the magnet is shaped as illustrated in Fig. 3.1(a). It is referred to as M1. For the comparative study, another machine with uniform magnet thickness, which is the same as the maximum thickness of M1 and having identical magnet width as that of M1, is investigated as well and referred to as M2. The other parameters of these two machines are the same and given in Table 3.I.

Three operation conditions, i.e., open-circuit, half load, and full load, are investigated. Without skewing, on half load, the phase current  $I_a$  is 60A RMS while  $I_a=120A$  RMS when it is on full load. The current phase advance angle on-load  $\beta$  is referred to the negative q-axis and is optimised for maximum torque per current. As shown in Fig. 3.2, the average torque peaks when  $\beta$  is  $-12^\circ$  electrical and  $-14^\circ$  electrical for half load and full load, respectively, which is due to the influence of magnetic saturation. The magnetic saturation will result in an equivalent magnet saliency, and the PM flux linkage will be higher when the  $d$ -axis current is negative.

The torque waveforms without skewing are shown in Figs. 3.4 and 3.5. Without magnet shaping, the cogging torque and on-load torque ripples of M2 are much higher and have the similar pattern, which indicates that the on-load torque ripple is dominated by the cogging torque. With the magnet shaping, the cogging torque and on-load torque ripples of M1 are significantly reduced. However, skewing is required for the purpose of addressing the potential manufacturing tolerances and further reduction of torque ripples.



(a) Shaped magnet (M1)

(b) Uniform magnet (M2)

Fig. 3.1. Cross-sections of two PM machines.

Table 3-I Main parameters

Parameters	value	Parameters	value
Slot number	84	Airgap length	2mm
Pole number	28	Effective axial length	110mm
Magnet thickness	6 mm	Rotor outer diameter	426mm
Remanence	1.17 T	Stator outer diameter	390mm
Coercive force	891 kA/m	Number of turns per phase	420

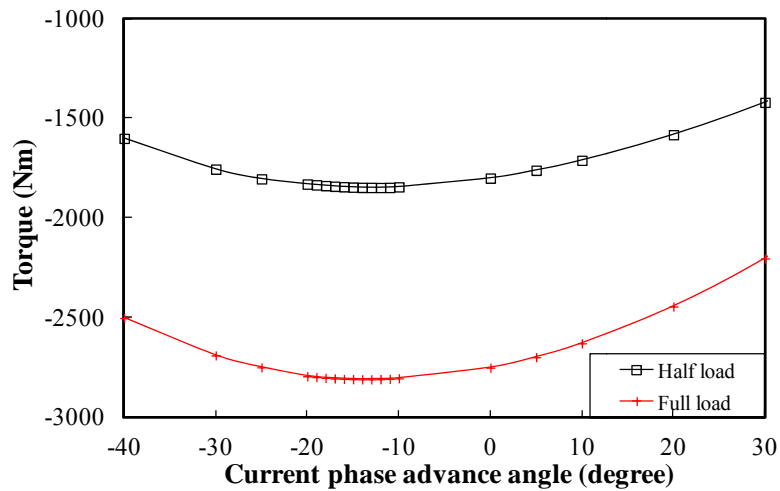


Fig. 3.2. Variation of average torques of M1 with  $\beta$ .

### 3.3 Torque Waveforms and Ripples with/without Skewing by One On-load Torque Ripple Period

For the conventional skewing, the skewing angle  $\theta_{sk}$  is usually chosen to be equal to one torque ripple period. Hence, for the on-load torque ripple in three-phase PM machine,  $\theta_{sk}$  is  $60^\circ$  electrical. Furthermore, since the cogging torque period is  $60^\circ/k$  electrical ( $k=1, 2, 3\dots$ ), both the on-load torque ripple and cogging torque are expected to be eliminated when  $\theta_{sk}$  is  $60^\circ$  electrical.

Ideally, the 3-D FE method is required in analysing the influence of skewing, especially for the flux fringing effects at the stator ends and the axial flux component. The end effect is important in the machine with high pole pitch to effective axial length ratio. For the prototype machines in Table 3-I, it is negligible. Therefore, instead of the 3-D FE method, which is usually complicated and time consuming, the torque waveforms with/without skewing are calculated firstly based on the multi-slice model [156]-[162] using OPERA FE software. The 3-D verification based on magnetostatic FE analyses is given for the typical designs, such as without skewing, with conventional skewing, and with the improved skewing.

In multi-slice model, the skewed rotor is represented by discrete slices as the step skewing. The rotor in each slice is rotated forwards or backwards circumferentially with an angle, which depends on the slice number ( $N$ ) and the skewing angle. In this chapter, the continuous skewing is approximated by 20 slices. The magnet distributions of 2-slice and  $N$ -slice models are illustrated in Fig. 3.3. All the slices share the same non-skewed stator and, hence, the same current, and are solved simultaneously. The resultant instant torque is calculated from the summation of all slices with due consideration of their phase shifts. As shown in Fig. 3.3, for each slice along the axial direction, the magnet centre line is shifted from the original centre of the magnet pole. This causes the axial variations of both torque waveform shifting and the equivalent current phase advance angle for each slice. As will be shown later, the axial variation of equivalent current phase advance angle significantly influences the effectiveness of skewing.

The torque waveforms and torque ripple spectra with and without skewing by one on-load torque ripple period are shown in Figs. 3.4 and 3.5. The torque ripple spectra are obtained based on that the fundamental period is  $60^\circ$  electrical. In order to scale the torque ripple and for better presentation, the torque ripple magnitude spectra are represented in per unit (p.u.) values, where the base value is the average torque at full load, i.e., 2807Nm.

It can be seen that, for both machines, only the cogging torques, but none of on-load torque ripples, are eliminated by skewing. It is noticed that the half load torque ripples are reduced

but not eliminated. However, for the full load torque ripple, the two machines behave in different ways. The full load torque ripple of M2 is reduced as expected. However, the full load torque ripple of M1 is even increased after skewing. Thus, it indicates that the skewing does not always reduce the on-load torque ripple, especially when the cogging torque is low and electric loading is high, as will be highlighted further in details in the following sections.

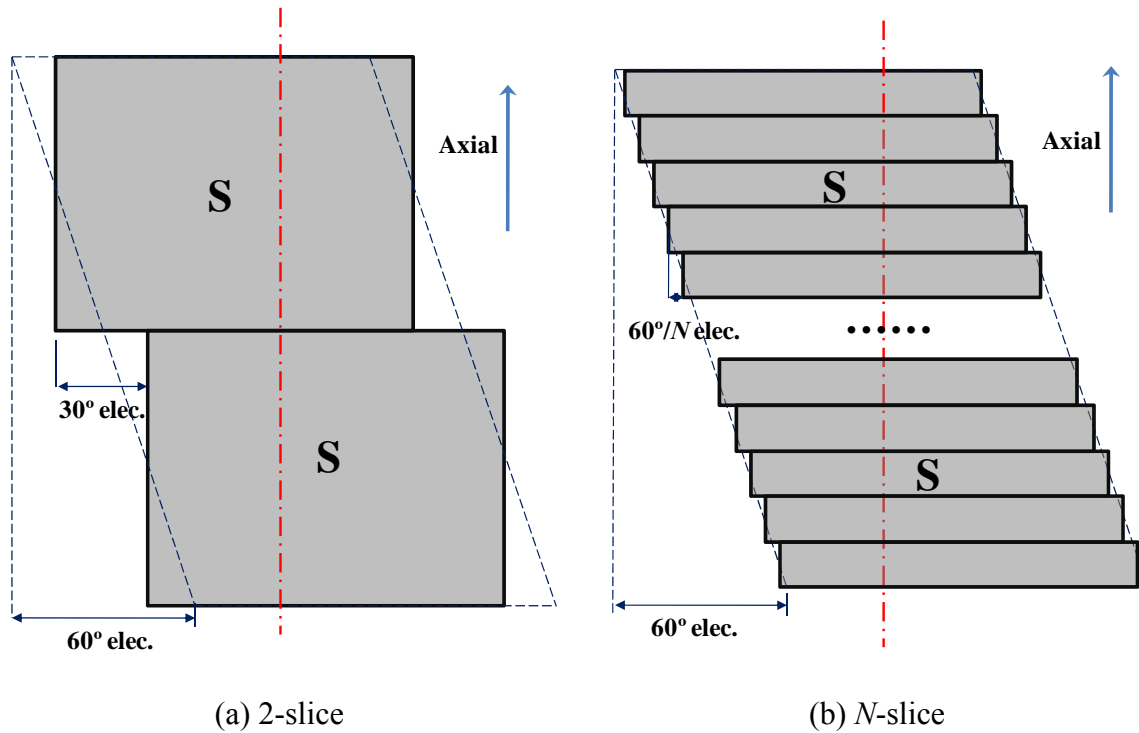
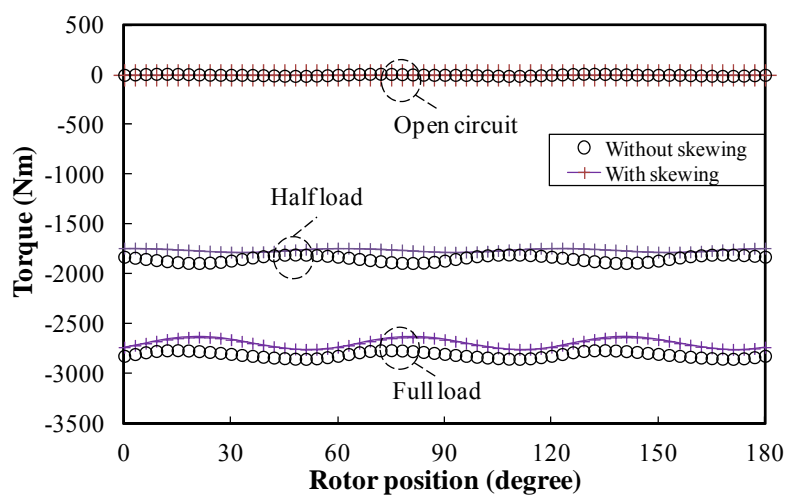
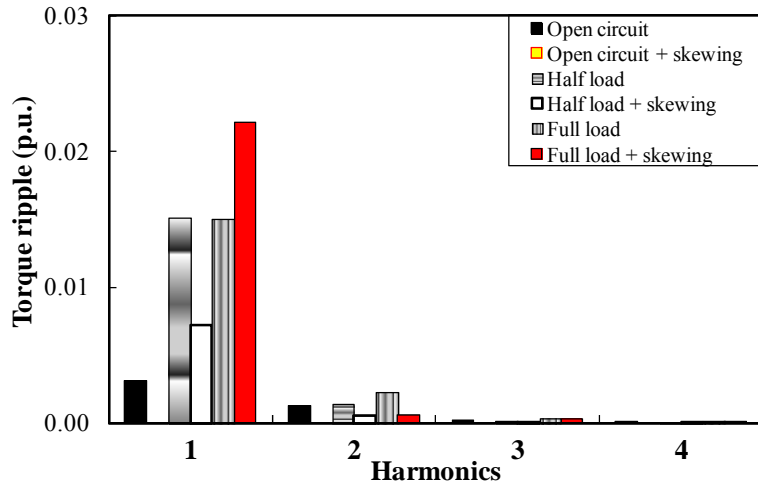


Fig. 3.3. Magnet arrangements along axial direction when  $\theta_{sk}=60^\circ$ .

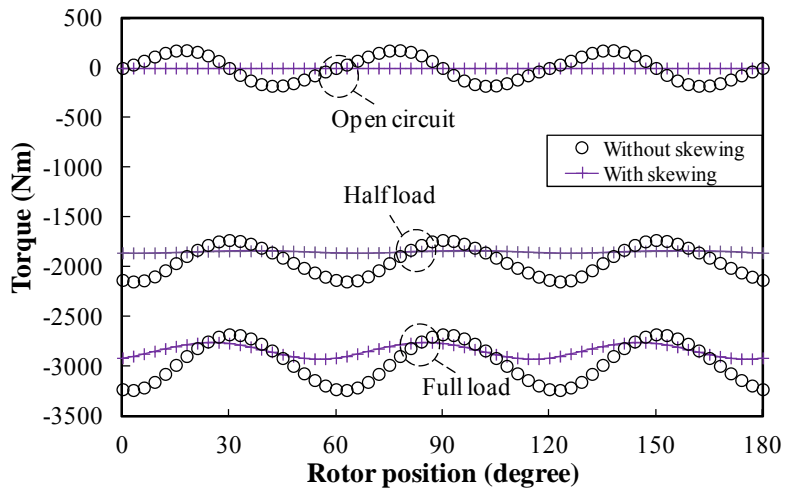


(a) Torque waveforms

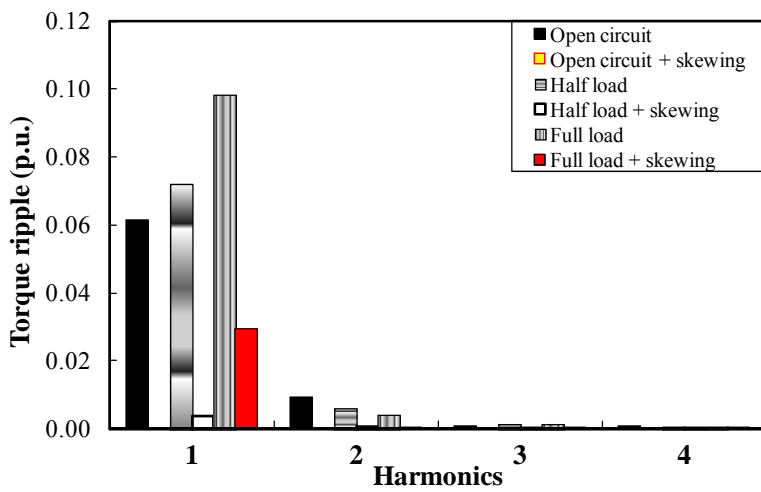


(b) Torque ripple spectra (base value=2807Nm)

Fig. 3.4. Torque performance for M1 when  $\theta_{sk}=60^\circ$ .



(a) Torque waveforms



(b) Torque ripple spectra (base value=2807Nm)

Fig. 3.5. Torque performance for M2 when  $\theta_{sk}=60^\circ$ .

### 3.4 Mechanism and Effectiveness of Skewing

In order to explain the variation of resultant torque ripple after skewing, it is desirable to examine the torque components contributed by each slice. As shown in Fig. 3.3, skewing results in different rotor shifting in each slice, which has two effects. First, the torque waveform of each slice is retarded or advanced compared with the middle slice. As will be shown later, this phase shifting is the key to torque harmonic cancellation and reduction. Second, since all the slices share the same unskewed stator and hence current, the equivalent current phase advance angle for each slice is different. It is also true for the equivalent current phase advance angle when the stator is skewed instead of a rotor. As will be shown later, this axial variation of equivalent current phase advance angle causes the axial variations of magnetic saturation and EM torque ripple, which makes the skewing less effective or even failed. According to the distribution in Fig. 3.3,  $\beta$  and  $\theta_0$ , which represent the equivalent current phase advance angle and the torque waveform shifting for each slice, respectively, can be obtained. Therefore, the overall torque can be calculated accounting for the axial variation of  $\beta$  and  $\theta_0$  after skewing as follows

$$T_{sk} = \frac{1}{\theta_{sk}} \int_{-\theta_{sk}/2}^{\theta_{sk}/2} T_{(\beta=\beta_0+\theta, \theta_0=-\theta)} d\theta \quad (3.1)$$

where  $T_{sk}$  and  $\beta_0$  are the resultant torque and the overall current phase advance angle with skewing and  $T_{(\beta, \theta_0)}$  is the torque without skewing when its current phase advance angle is  $\beta$  and the torque waveform shifting is  $\theta_0$ .

It also should be noticed that, after skewing  $60^\circ$ , the range of equivalent current phase advance angle varies from  $\beta_0 - 30^\circ$  to  $\beta_0 + 30^\circ$ . Although  $\beta_0 < 0^\circ$ , the equivalent current phase advance angle for some slices can be positive, i.e., flux enhancing, especially for SPM machines, in which  $\beta_0$  is usually small.

In order to clearly illustrate the influence of skewing, the explanations are based on 2-slice skewing and  $\theta_{sk} = 60^\circ$ . With  $T_1$  and  $T_2$  representing the torque components of two slices, respectively, the overall torque with 2-slice skewing is given as:

$$T_{sk} = (T_1 + T_2)/2 \quad (3.2)$$

$$T_1 = T_{(\beta=\beta_0-15^\circ, \theta_0=15^\circ)} \quad (3.3)$$

$$T_2 = T_{(\beta=\beta_0+15^\circ, \theta_0=-15^\circ)} \quad (3.4)$$

### 3.4.1 Open-circuit

On open-circuit, since the electric loading is zero, the influence of saturation due to armature reaction does not exist and the EM torque ripple is zero.  $T_1$  and  $T_2$  have the same waveform (cogging torque). After skewing,  $T_1$  and  $T_2$  are antiphase in terms of the fundamental torque ripple, as illustrated in Fig. 3.6. Hence, the fundamental torque ripple is eliminated in  $T_{sk}$ , while all the other harmonics remain. Mathematically, it can be concluded that only  $kN$ -order cogging torque harmonics remain after  $N$ -step skewing. By using continuous skewing, the cogging torque is eliminated, as shown in Figs. 3.4 and 3.5.

It can also be concluded that the mechanism of skewing for reducing the torque ripples is the cancellation of harmonics based on the waveform shifting, which is due to the geometric shifting. However, in order to eliminate the torque ripple by skewing, it requires that all slices have the same torque waveform and the phase difference between the torque components of different slices is only due to the geometric shifting introduced by skewing.

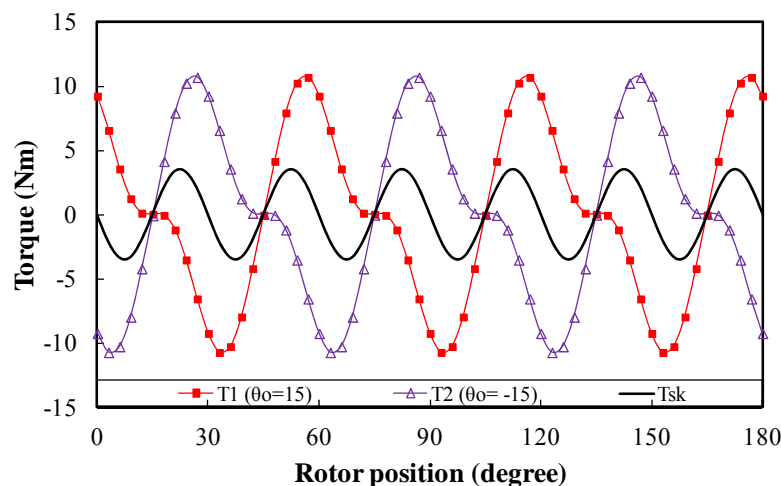


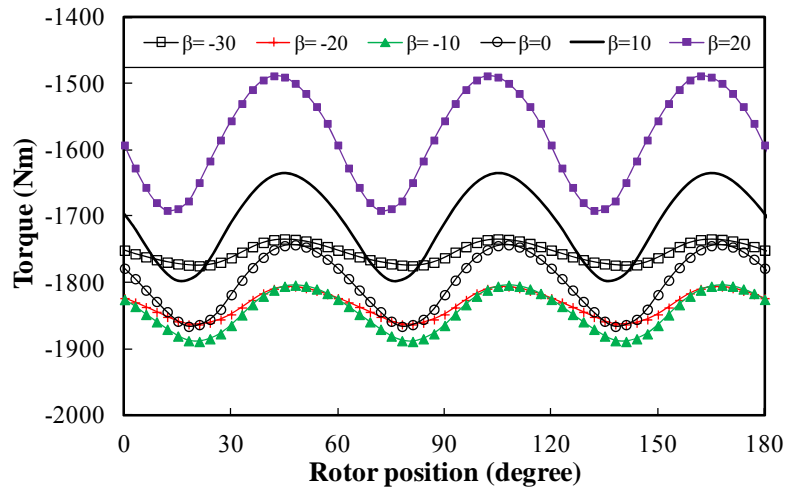
Fig. 3.6. Torque components of M1 based on 2-slice skewing when it is open circuit and  $\theta_{sk} = 60^\circ$ .

### 3.4.2 Half-load

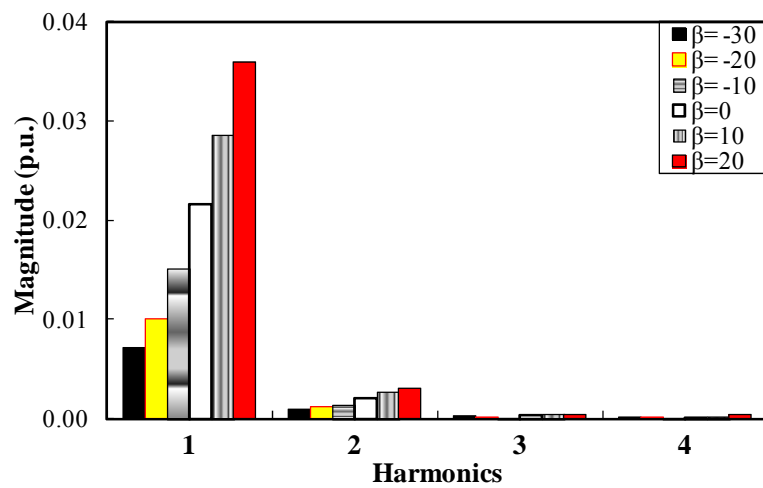
On half load, the armature current and, hence, EM torque ripple are not zero. As shown in Fig. 3.7(a)-(c), without skewing, the on-load torque ripple, especially its magnitude, changes with  $\beta$ .

After skewing, since the phase variation of torque ripple with  $\beta$  is modest, the torque ripples of  $T_1$  and  $T_2$  can partially cancel each other. Hence, the half load torque ripple is still reduced by skewing as shown in Fig. 3.7(d), although the torque ripple magnitude varies significantly with  $\beta$ .  $T_0$  represents the torque without skewing. However, different from the

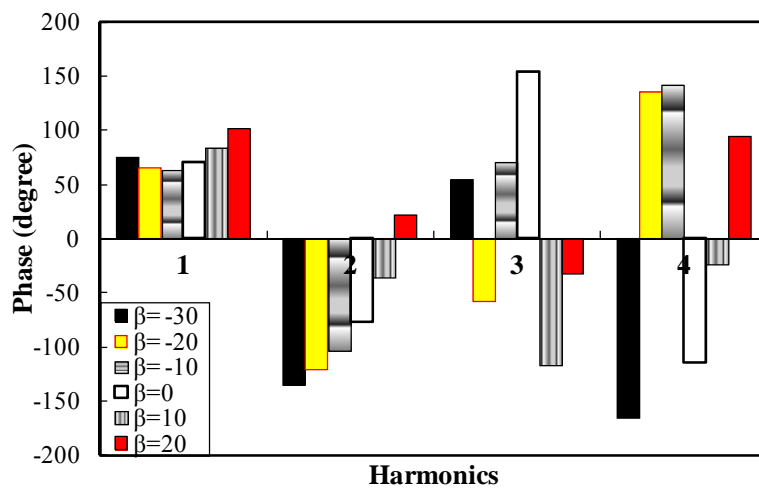
open-circuit one, the half load torque ripple, even its fundamental, cannot be eliminated by skewing, due to the extra variation of the on-load torque ripple, both magnitude and phase, with  $\beta$ .



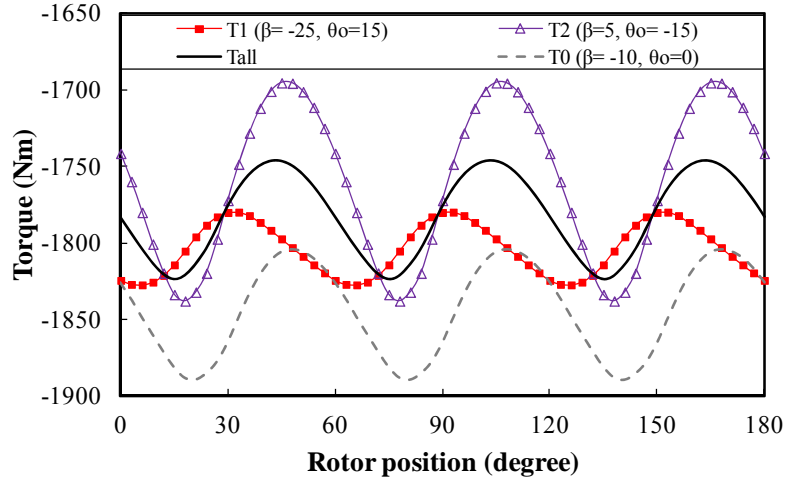
(a) Torque waveforms without skewing



(b) Torque ripple magnitude spectra without skewing (base value = 2807Nm)



(c) Torque ripple phase spectra without skewing



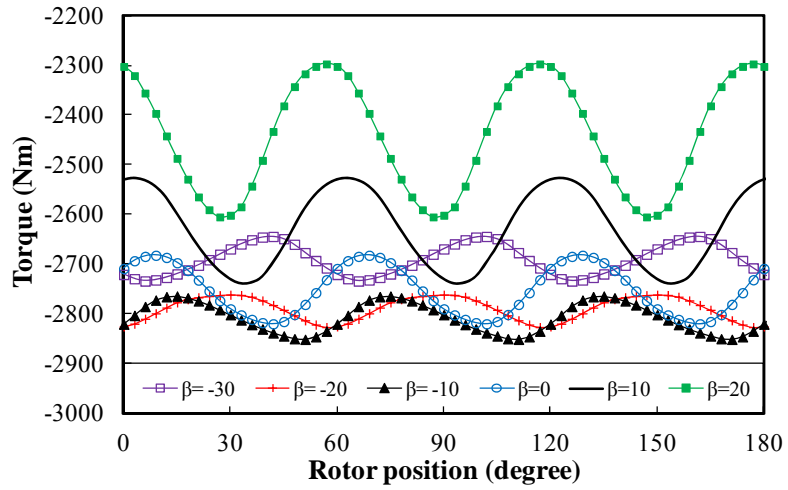
(d) Torque components based on 2-slice skewing and  $\theta_{sk} = 60^\circ$

Fig. 3.7. Torque waveforms of M1 when  $I_a = 60A$ .

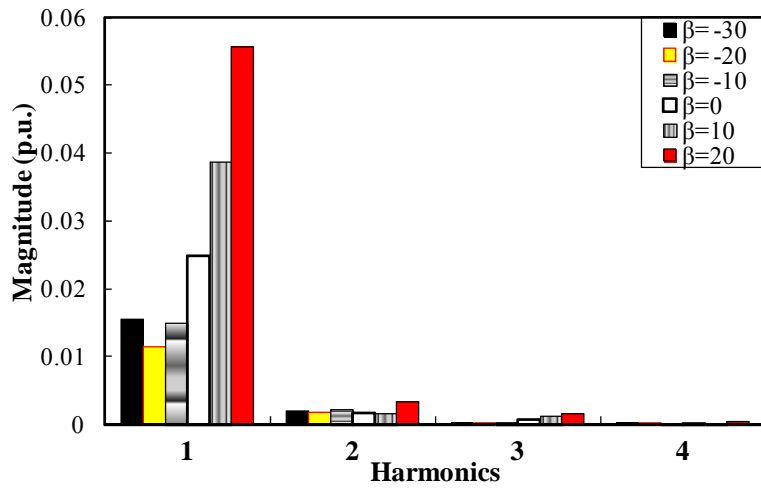
### 3.4.3 Full-load

On full load, since the magnetic saturation due to armature reaction and EM torque ripple are much higher, the on-load torque ripple without skewing changes significantly with  $\beta$ , as shown in Fig. 3.8(a)-(c). It is worth noticing that the torque ripples are almost antiphase when  $\beta$  changes by  $30^\circ$ , e.g., the torque ripples when  $\beta = -30^\circ$  and  $\beta = 0^\circ$ . The torque ripple magnitude changes as well, especially when  $\beta > 0^\circ$ , where the magnetic saturation is heavier due to flux enhancing.

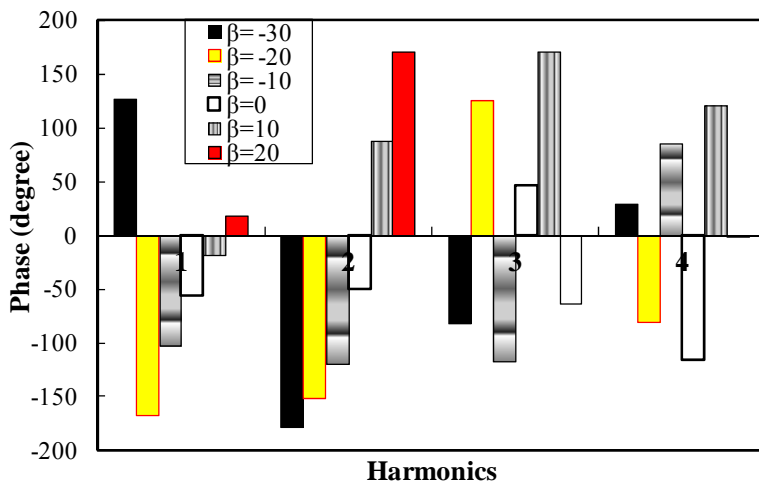
After skewing, due to the significantly extra phase shifting caused by axial variation of  $\beta$  and, hence, magnetic saturation, the torque ripples of  $T_1$  and  $T_2$  are not antiphase but almost in-phase. Thus, there is no cancelling but additive effect. Furthermore, since the ripple of  $T_2$  is much higher than  $T_0$ , the full load torque ripple is not eliminated but increased by skewing, as shown Fig. 3.8(d).



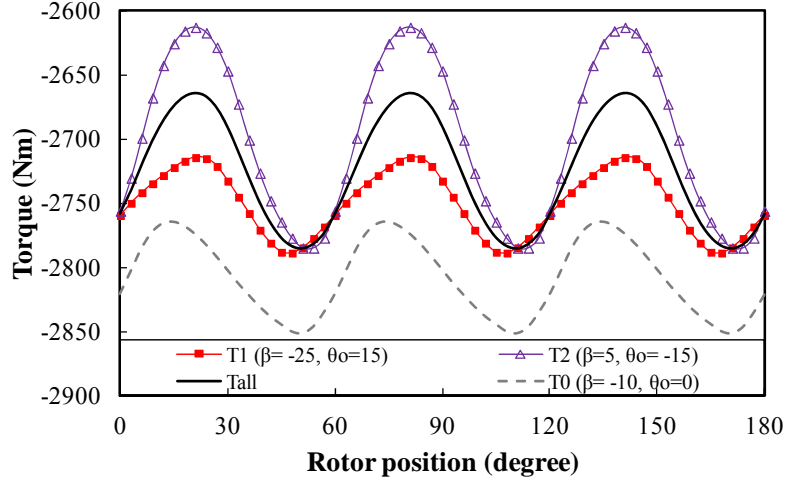
(a) Torque waveforms without skewing



(b) Torque ripple magnitude spectra without skewing (base value=2807Nm)



(c) Torque ripple phase spectra without skewing



(d) Torque components based on 2-slice skewing and  $\theta_{sk} = 60^\circ$

Fig. 3.8. Torque waveforms of M1 when  $I_a = 120A$ .

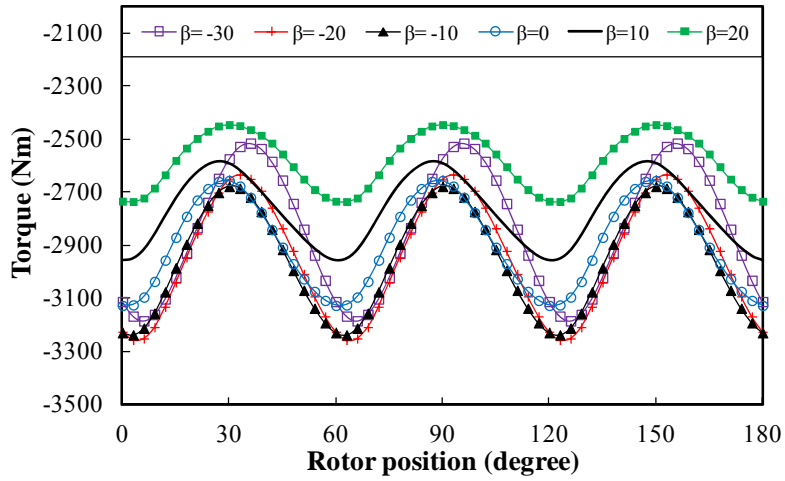
### 3.4.4 Comparison between M1 and M2

Therefore, it is useful to examine the case when cogging torque is high, such as M2. Due to the high cogging torque, the phase of full load torque ripple without skewing varies with the current phase advance angle modestly, as shown in Fig. 3.9(c). Hence, after skewing, the full load torque ripple is reduced, as shown in Fig. 3.5. However, the full load torque ripple is also not eliminated by skewing, due to the extra torque ripple variation with  $\beta$ .

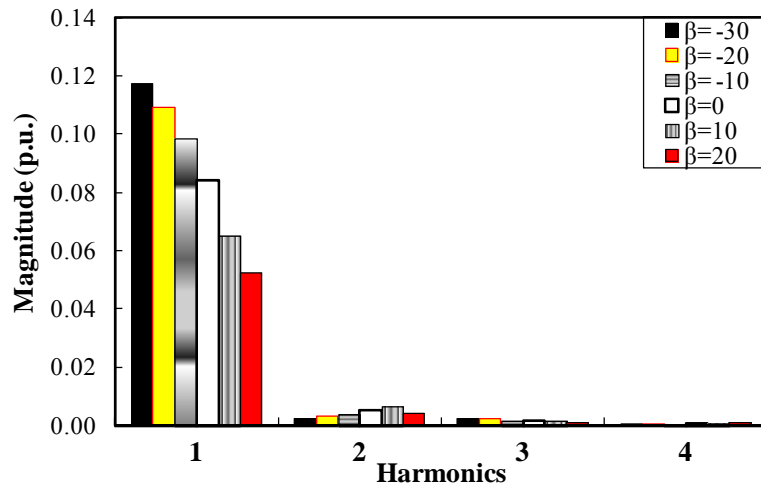
Furthermore, compared Fig. 3.9(b) with Fig. 3.8(b), it can be seen that without skewing, the fundamental torque ripples of M1 and M2 change with  $\beta$  by almost the same amount. For example, when  $\beta$  changes from  $-30^\circ$  to  $20^\circ$ , the changes of fundamental torque ripples of M1 and M2 are about 0.067 p.u. (190Nm), noticing that for M1, the phase of fundamental torque ripple when  $\beta = -30^\circ$  is opposite with the others, as shown in Fig. 3.8(c) and, thus, its magnitude in Fig. 3.8(b) is equivalent to negative. Therefore, the variation of on-load torque ripple with  $\beta$  is mainly due to the EM torque ripple, and the variations of the EM torque ripples of M1 and M2 with  $\beta$  are similar.

Furthermore, after skewing, the resultant fundamental torque ripples of M1 and M2 are almost at the same level, which is  $\sim 0.0249$  p.u. (70Nm) as shown in Figs. 3.5(b) and 3.4(b).

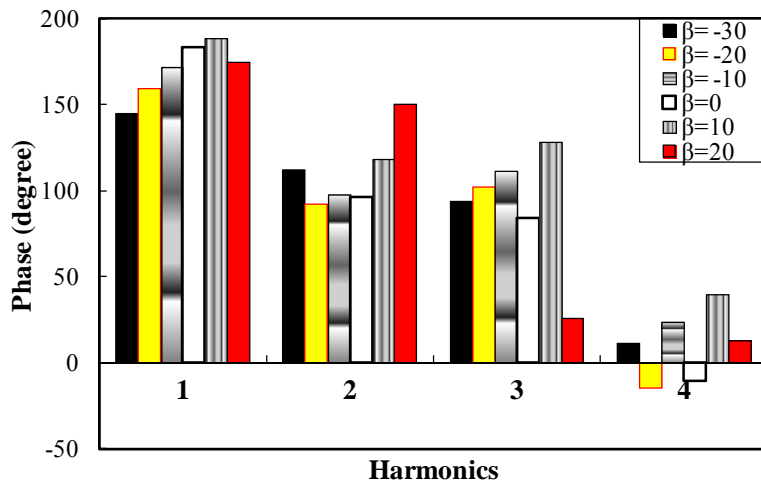
These two similarities, both with and without skewing, strongly support that, the same as M1, the full load EM torque ripple of M2 is also increased by skewing. Therefore, the on-load torque ripple reduction by skewing in M2 is only due to the effective reduction of its remarkable cogging torque, while the skewing still fails to reduce the EM torque ripple at full load.



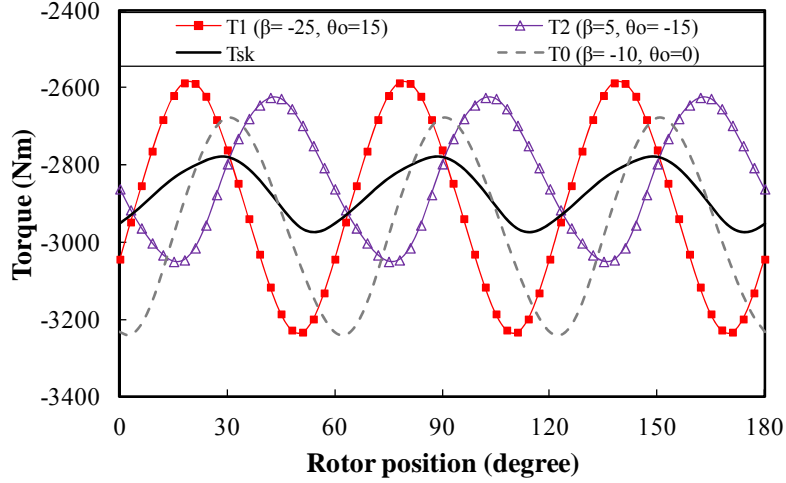
(a) Torque waveforms without skewing



(b) Torque ripple magnitude spectra without skewing (base value=2807Nm)



(c) Torque ripple phase spectra without skewing



(d) Torque components based on 2-slice skewing and  $\theta_{sk} = 60^\circ$

Fig. 3.9. Torque waveforms of M2 when  $I_a = 120A$ .

### 3.4.5 Summary

Based on the foregoing investigations, it can be concluded that the effectiveness of skewing on the torque ripple reduction largely depends on the axial variation of torque ripple phase but less on the magnitude under skewing.

By skewing one on-load torque ripple period, the cogging torque is eliminated. However, the EM torque ripple and, hence, on-load torque ripple cannot be eliminated since the EM torque ripple varies with  $\beta$ .

After skewing, the EM torque ripple may be reduced or even increased, depending on the electric loading. Therefore, when the cogging torque is higher, skewing on the on-load torque ripple reduction is more effective. In contrast, when the electric loading is high, where the magnetic saturation due to armature reaction is more significant and the EM torque ripple is higher, skewing is less effective. The on-load torque ripple can be even increased by skewing, especially when the cogging torque is low and electric loading is high.

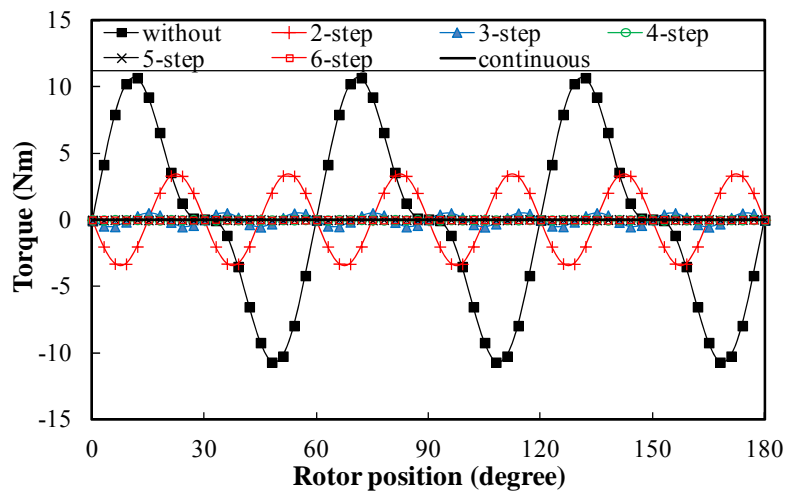
### 3.5 Influence of Step Skewing Number on Torque Ripple

For the sake of manufacturing and reducing the cost, step skewing is widely employed as an alternative to continuous skewing. The PM arrangements for different step numbers are illustrated in Fig. 3.3. The variation of torque waveforms and torque ripples of M1 with different numbers of skewing steps when  $\theta_{sk} = 60^\circ$  is shown in Fig. 3.10.

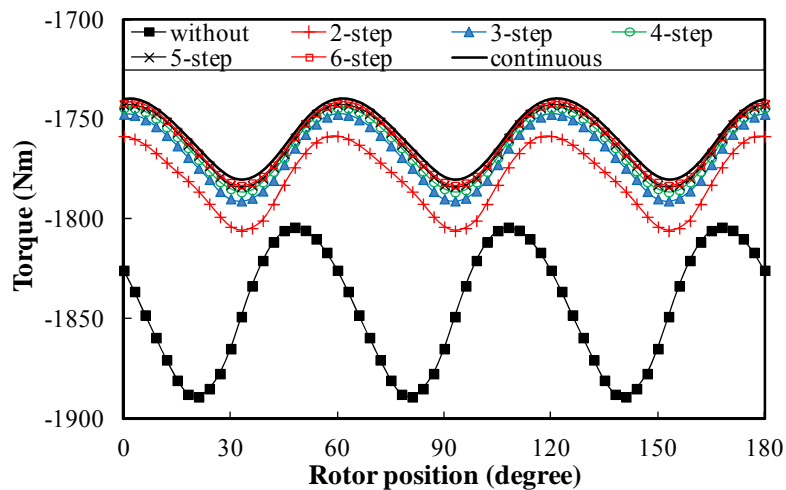
It can be seen that for all the cases, 3-step skewing achieves almost the same level of the torque ripple as the continuous skewing while its PM segment number is low. It also has been

mathematically concluded earlier in this chapter that the 3-step skewing is able to eliminate the fundamental and second harmonics of cogging torque, which are dominant. Therefore, the 3-step skewing is the most promising alternative for the continuous skewing in low cost applications.

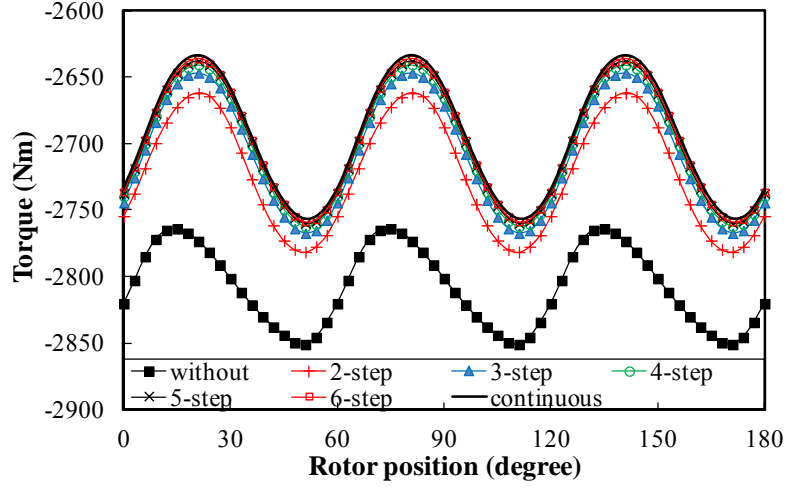
On the other hand, regardless of the number of skewing steps, the difference between the influence of step skewing and continuous skewing on the torque is negligible, since the step skewing is the approximate way of the continuous skewing and, hence, it is based on the same mechanism as illustrated earlier for the continuous skewing.



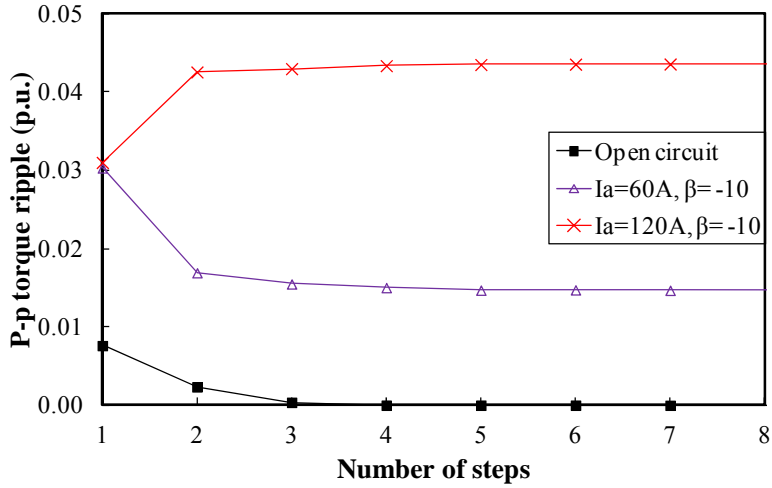
(a) Torque waveforms on open circuit



(b) Torque waveforms when  $I_a = 60A$  and  $\beta = -10^\circ$



(c) Torque waveforms when  $I_a = 120\text{A}$  and  $\beta = -10^\circ$



(d) Torque ripple variation with number of steps (base value= $2807\text{Nm}$ )

Fig. 3.10. Torque waveforms and torque ripple of M1 with step skewing when  $\theta_{sk} = 60^\circ$ .

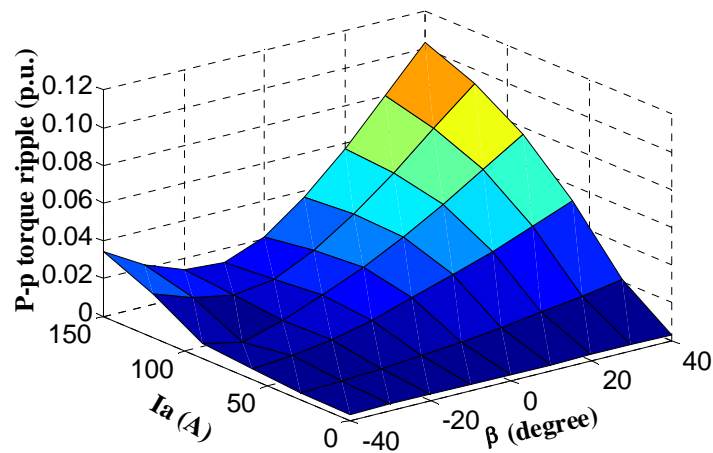
### 3.6 Effectiveness of Skewing with Different Skewing Angles

It has been shown in the foregoing sections that the on-load torque ripple cannot be eliminated or can even be increased by skewing one no-load torque ripple period. Thus, it is necessary to examine the effectiveness of skewing on torque ripple elimination with different skewing angles.

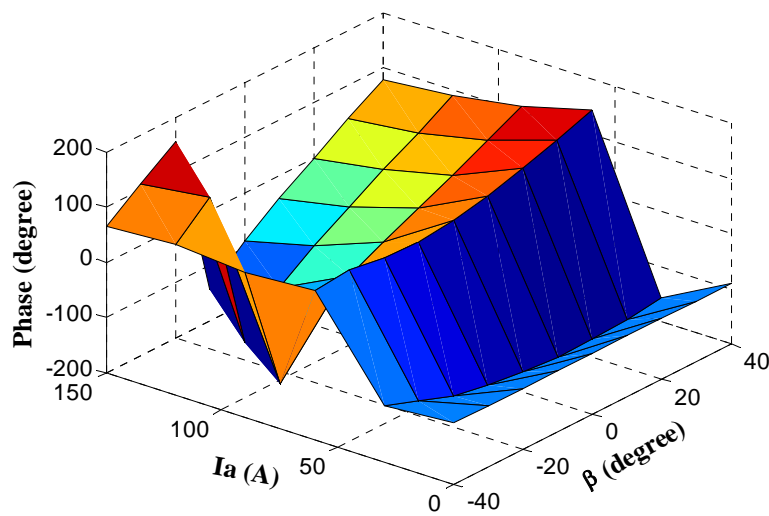
As indicated by (3.1), the larger skewing angle will result in wider range of the equivalent current phase advance angle and, hence, electric loadings. Therefore, the influence of electric loading on the on-load torque ripple of M1 without skewing is investigated and shown in Fig. 3.11. It can be seen that both the phase and magnitude of the torque ripple change more significantly when either  $I_a$  or  $\beta$  is higher, since the magnetic saturation is heavier. Therefore, in terms of the lower on-load torque ripple, it is desirable to have lower magnetic saturation.

The torque variations with different skewing angles of M1 based on the continuous skewing are shown in Fig. 3.12. It can be seen that skewing is less effective when the electric loading is higher. On open circuit, the cogging torque is eliminated by skewing when  $\theta_{sk}$  is  $k \times 60^\circ$ . However, the on-load torque ripples cannot be eliminated when  $\theta_{sk}$  is  $k \times 60^\circ$ . The half load torque ripple is reduced by skewing but less effective than the open-circuit one. Furthermore, the full load torque ripple is even increased by skewing when  $30^\circ < \theta_{sk} < 240^\circ$ . It can be reduced effectively only when  $\theta_{sk}$  is higher than  $300^\circ$  while its average torque is reduced by more than 82%.

It is also worth noticing that the on-load torque ripple cannot be fully eliminated by the skewing unless the skewing angle is  $360^\circ$  electrical, which is impractical, since the average torque will be zero, as shown in Fig. 3.12(b).

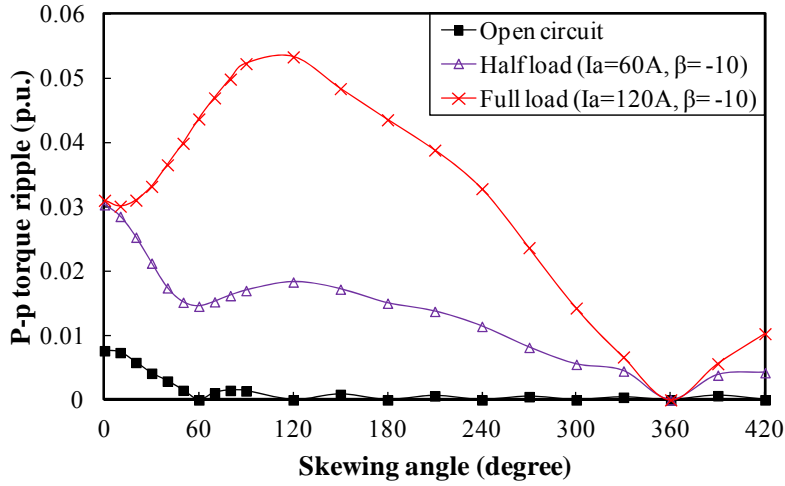


(a) Magnitude (base value=2807Nm)

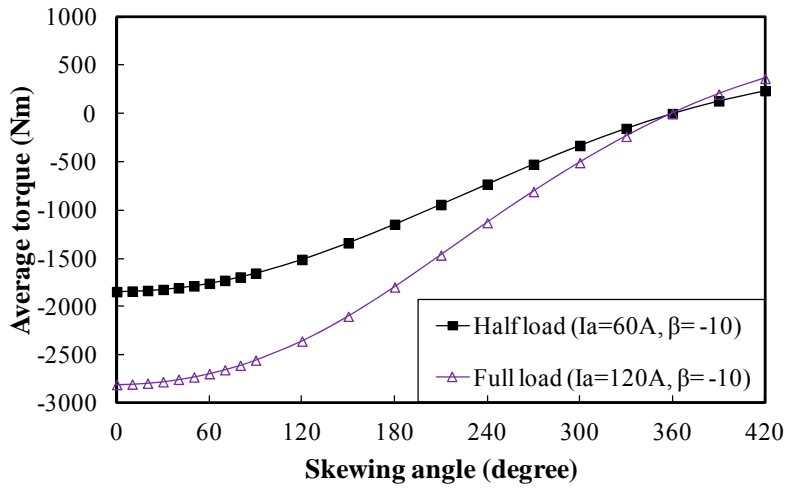


(b) Phase

Fig. 3.11. Variations of torque ripple fundamental component with electric loading of M1 without skewing.



(b) Peak-peak torque ripple



(b) Average torque

Fig. 3.12. Torque variation with skewing angle of M1.

### 3.7 Effectiveness of Skewing Under Linear Case

It has been shown in the previous sections that, in nonlinear cases, it is impractical to eliminate the on-load torque ripple by skewing, since the axial variation of magnetic saturation and  $\beta$  introduced by skewing cause the variation of on-load torque ripple, especially the EM torque ripple, of each slice. It is necessary to find out whether it is only due to the influence of magnetic saturation on load. Therefore, further investigation based on linear models is carried out.

#### 3.7.1 Analytical Analysis

Since, in linear cases, the PM field and cogging torque are independent of loads, the on-load torque ripple can be obtained analytically.

For the prototype SPM machines, the reluctance torque is zero and EM torque is only due to the mutual torque, which is produced by the interaction between PM and armature fields. In order to ease the illustration, only the fundamental, fifth, and seventh PM flux linkage components are considered. Hence, the phase flux linkage due to the PM field can be given as

$$\psi_a = \psi_1 \cos(\omega t) + \psi_5 \cos(5\omega t + \theta_5) + \psi_7 \cos(7\omega t + \theta_7) \quad (3.5)$$

where  $\psi_1$ ,  $\psi_5$ ,  $\psi_7$ ,  $\theta_5$ , and  $\theta_7$  are the magnitudes and phase angles of fundamental, fifth, and seventh flux linkage components, respectively, and  $\omega$  is the electrical angular speed.

The ideal sinusoidal phase current is given as

$$i_a = -\sqrt{2}I_a \sin(\omega t + \beta) \quad (3.6)$$

For the three-phase balanced PM machines, the on-load torque without skewing can be obtained as

$$T = T_{av} + T_6(m) + T_c = T_{av} + T_6(5) + T_6(7) + T_c \quad (3.7)$$

$$T_{av} = 1.5p\sqrt{2}I_a\psi_1 \cos(\beta) \quad (3.8)$$

$$T_6(5) = -1.5p\sqrt{2}I_a(5\psi_5) \cos(6\omega t + \theta_5 + \beta) \quad (3.9)$$

$$T_6(7) = 1.5p\sqrt{2}I_a(7\psi_7) \cos(6\omega t + \theta_7 - \beta) \quad (3.10)$$

$$T_c = \Sigma T_c(k) \cos(6k\omega t + \theta_{ck}) \quad (3.11)$$

where  $T_{av}$  and  $T_6(m)$  are average torque and the sixth harmonic of the mutual torque, respectively.  $T_6(5)$  and  $T_6(7)$  are the sixth torque ripple components contributed by  $\psi_5$  and  $\psi_7$ , respectively.  $T_c$  is the cogging torque without skewing.  $T_c(k)$  and  $\theta_{ck}$  are the magnitude and phase of  $k$ th order cogging torque harmonics, respectively.

It can be seen that the EM torque ripples change with  $\beta$  even for the linear cases, which indicates that the EM torque ripples cannot be eliminated by skewing one on-load torque ripple period.

After skewed by  $\theta_{sk}$ , the on-load torque is given as

$$T_{sk} = k_{avsk}T_{av} + k_{5sk}T_6(5) + k_{7sk}T_6(7) + \Sigma k_{cksk}T_c(k) \cos(6k\omega t + \theta_{ck}) \quad (3.12)$$

$$k_{avsk} = \sin(\theta_{sk}/2) / (\theta_{sk}/2) \quad (3.13)$$

$$k_{5sk} = \sin(5\theta_{sk}/2) / (5\theta_{sk}/2) \quad (3.14)$$

$$k_{7sk} = \sin(7\theta_{sk}/2) / (7\theta_{sk}/2) \quad (3.15)$$

$$k_{cksk} = \sin(k3\theta_{sk}) / (k3\theta_{sk}) \quad (3.16)$$

where  $k_{avsk}$ ,  $k_{5sk}$ , and  $k_{7sk}$  are the skew factors for the average torque and sixth order torque ripples due to  $\psi_5$  and  $\psi_7$ , respectively.  $k_{cksk}$  is the skew factor for  $k$ th-order cogging torque harmonics.

It can be seen that the influence of skewing on the mutual torque and cogging torque can be represented by the skew factors [121], [123], [153]. Based on their expressions, the variations of skew factors with skewing angle are shown in Fig. 3.13. Although only the variation of  $k_{c1}$  is illustrated, it can be seen from (3.16) that the cogging torque is eliminated by skewing  $k \times 60^\circ$ , since the skew factors for all cogging torque components are zero. However, neither  $T_6(5)$  nor  $T_6(7)$  is eliminated by skewing  $k \times 60^\circ$ .

It also shows that the optimal skewing angles to eliminate  $T_6(5)$  or  $T_6(7)$  are different, since  $T_6(5)$  and  $T_6(7)$  vary with the current phase advance angle in different ways, as shown in (3.9) and (3.10). In order to eliminate  $T_6(5)$  and  $T_6(7)$  simultaneously, the skewing angle must be  $360^\circ$  electrical.

Theoretically, except  $360^\circ$  electrical,  $T_6(m)$  can also be eliminated when  $T_6(5)$  and  $T_6(7)$  cancel each other, as shown in Fig. 3.14, where  $\theta_7 = 0^\circ$  and the peak-peak mutual torque ripple without skewing is 1 p.u.. However, it can be seen that these optimal skewing angles, where  $T_6(5)$  and  $T_6(7)$  cancel each other, change significantly with  $\psi_5/\psi_7$ ,  $\theta_5$ , and  $\beta$ . It can also be deduced that these optimal skewing angles cannot eliminate other torque ripple components, such as 12th mutual torque ripple components produced by eleventh and thirteenth flux linkages. Therefore, in general, the EM torque ripple can only be eliminated when the skewing angle is  $360^\circ$  electrical.

Furthermore, it is worth noticing that except  $360^\circ$  electrical, the optimal skewing angles, by which  $T_6(5)$  and  $T_6(7)$  cancel each other, are different from the optimal skewing angles for eliminating the cogging torque.

Therefore, the on-load torque ripple can be fully eliminated only when the skewing angle is  $360^\circ$  electrical. However, it is impractical, since the average torque will also be zero, as shown in Fig. 3.13.

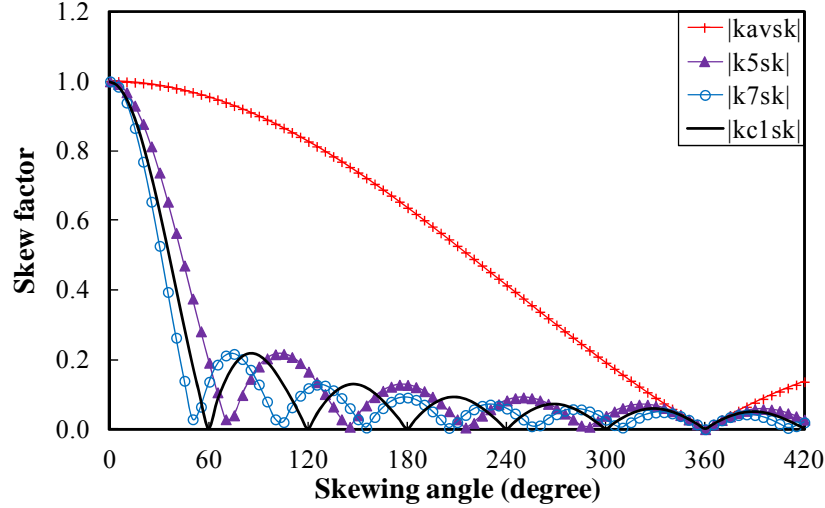


Fig. 3.13. Variations of skewing factors with  $\theta_{sk}$ .

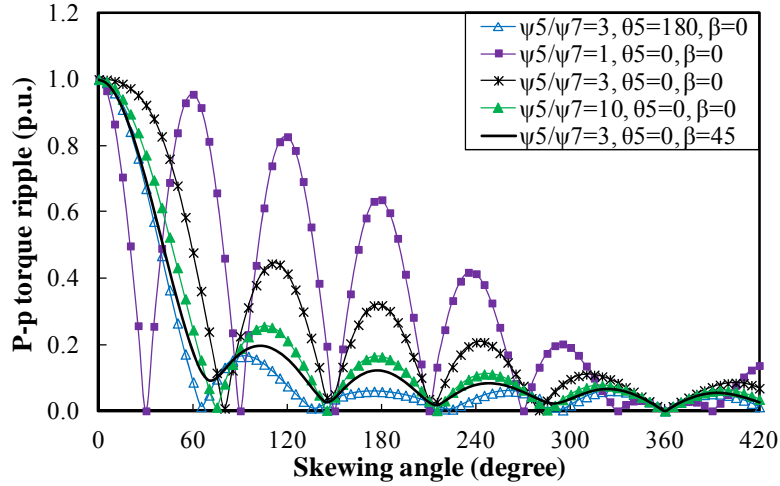


Fig. 3.14. Variation of peak-peak mutual torque ripple with  $\theta_{sk}$ .

### 3.7.2 FE results

The foregoing results and conclusions based on analytical analyses are general and applicable to any three-phase PM machines. For example, the torque ripple variations with different skewing angles are obtained based on the linear model of M1, in which the relative permeability of the stator core and rotor yoke is set to 5000, and shown in Fig. 3.15. For the linear model of M1 without skewing, i.e.,  $\theta_{sk} = 0^\circ$ ,  $\psi_5/\psi_7$  is 5.95 and, hence,  $T_6(5)$  is much higher than  $T_6(7)$ . It can also be noticed from Fig. 3.13 that the cogging torque is much lower than the half and full load torque ripples. Therefore, the on-load torque ripples are dominated by  $T_6(5)$ .

As referred to Fig. 3.13, after skewing, the cogging torque follows the envelope of  $|k_{csk}|$  and the half-load and full-load torque ripple variations with skewing angle have the similar envelope with  $|k_{5sk}|$ , since they are dominated by  $T_6(5)$ .

It is worth noticing that the cogging torque is eliminated when the skewing angle is  $k \times 60^\circ$ . However, neither the half- or full-load torque ripples are fully eliminated in these cases. The on-load torque ripples can be eliminated only when the skewing angle is  $360^\circ$  electrical. However, as mentioned earlier, the average torque will also be zero. Therefore, it can be concluded that it is impractical to fully eliminate the on-load torque ripple by skewing even in linear cases.

Compared Fig. 3.15 with Fig. 3.12, it can be seen that the effectiveness of skewing is influenced significantly by the magnetic saturation. Without the magnetic saturation, although it is impractical to fully eliminate the on-load torque ripple due to the variation of EM torque ripple with the current phase advance angle, the on-load torque is still reduced effectively after skewing. However, with magnetic saturation, which aggravates the variation of EM torque ripple with the equivalent current phase advance angle, the on-load torque ripple can even be increased by skewing. Therefore, it is desirable to design the machine to have lower magnetic saturation in order to reduce the on-load torque ripple by skewing.

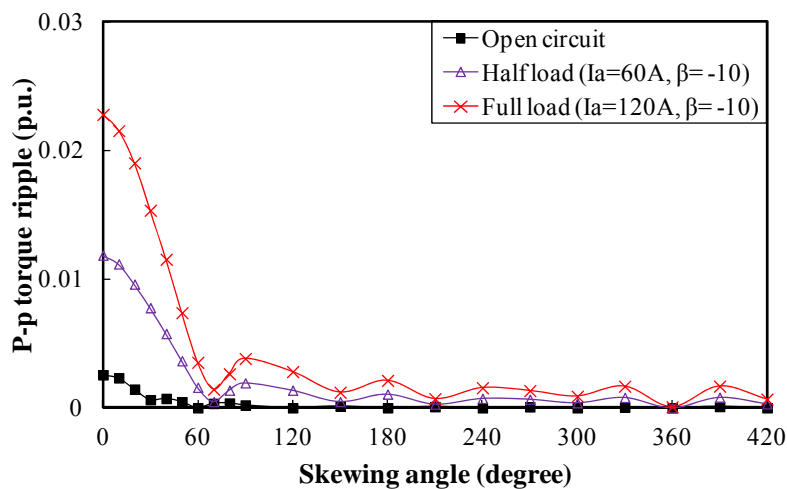


Fig. 3.15. Peak-peak torque ripple variation of M1 ( $\mu = 5000$ ) with  $\theta_{sk}$  (base value=2807Nm).

### 3.8 Improved Method

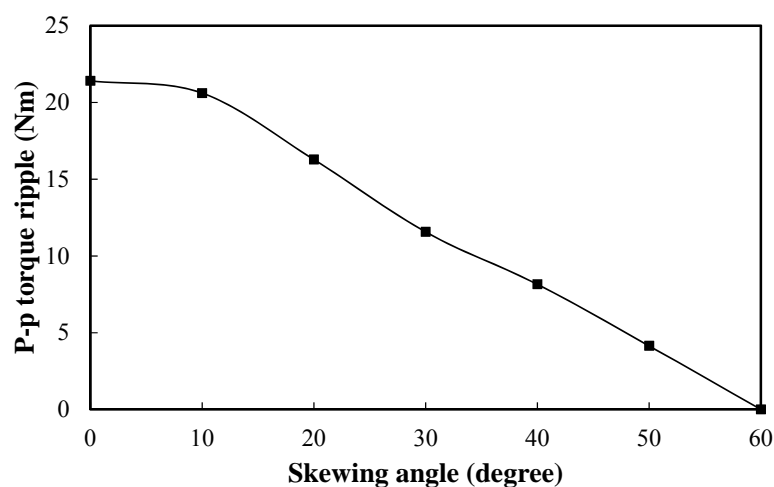
In order to meet the stringent torque ripple requirement over whole load range, it is necessary and important to find ways of improving the skewing and avoiding the increase of torque ripple.

Based on the foregoing analyses, the guideline is to appropriately reduce the magnetic saturation. The magnetic saturation can be alleviated by either reducing armature current or increasing the tooth width and stator yoke. However, all of them will result in lower torque,

which means the machine volume and cost should be increased to meet the same average torque.

Actually, without reducing current or increasing machine volume, the magnetic saturation also depends on the range of current phase advance angle  $\beta$ , which varies from  $\beta_0 - \theta_{sk}/2$  to  $\beta_0 + \theta_{sk}/2$  at different axial positions in the machine with skewing. The variation of on-load torque ripple with different  $\beta_0$  and  $\theta_{sk}$  is shown in Fig. 3.16. It can be seen that when it is on half load, it prefers larger negative current phase advance angle and larger skewing angle to have lower torque ripple. When it is on full load, the torque ripple is minimum when  $\beta_0 = -20^\circ$  and  $\theta_{sk} = 0^\circ$ . For the current phase advance angle, it can be controlled independently for different loads. However, for the skewing angle, since it is shared by all the load conditions, the trade-off between the torque ripples at different loads is necessary.

According to Fig. 3.16, the optimal skewing angle for this machine can be  $10^\circ$ . As shown in Table 3-II, for the machine without skewing, the on-load torque ripples are higher than the requirement although its cogging torque requirement is satisfied. The conventional skewing is then employed for the purpose of eliminating all the torque ripples. However, only the cogging torque is eliminated. The half load torque ripple is reduced while the full load torque ripple is even increased. Hence, it fails to achieve the torque ripple requirement over whole load range. Therefore, the improved skewing, where both  $\beta_0$  and  $\theta_{sk}$  are optimised, is employed. Compared with the conventional skewing, although the open-circuit and half load torque ripples are slightly higher, they are still sufficient to meet the requirement. The full load torque ripple is now reduced further to fully meet the stringent torque ripple requirement. Furthermore, high average torques are achieved as well due to smaller skewing angle.



(a) Open-circuit

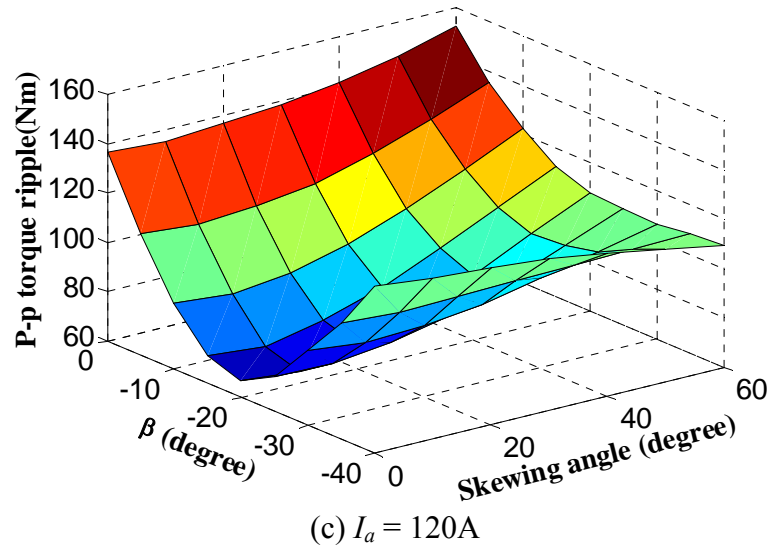
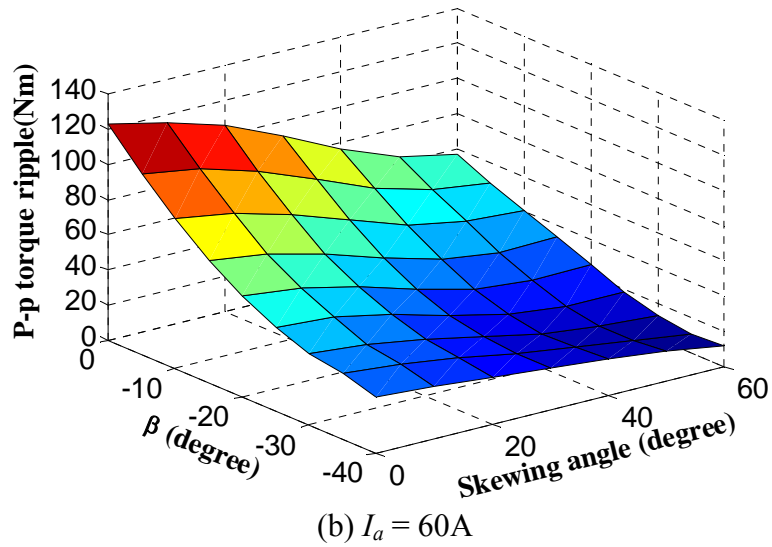


Fig. 3.16. Variation of torque ripple with current phase advance angle  $\beta$  and skewing angle of M1 having continuous skewing.

Table 3-II Comparison of torques and torque ripples by different continuous skewing methods based on M1

		Without skewing	Conventional skewing	Improved skewing
$\theta_{sk}$	$^\circ$	0	60	10
Open circuit ( $I_a=0A$ )				
P-p ripple	Nm	21.4 (0.38%)	0 (0%)	20.6 (0.36%)
Half load ( $I_a=60A$ )				
$\beta_0$	$^\circ$	-10	-10	-20

Average	Nm	-1844	-1759	-1829
P-p ripple	Nm	85.0 (1.51%)	40.7 (0.75%)	53.4 (0.95%)
Full load ( $I_a=120A$ )				
$\beta_0$	°	-10	-10	-20
Average	Nm	-2807	-2694	-2783
P-p ripple	Nm	87.0 (1.55%)	122.5 (2.27%)	64.7 (1.15%)

### 3.9 3-D FE Verification

In order to verify the 2-D FE analyses based on multi-slice method, 3-D FE analyses, where all the skewing effects including end effects are included, are carried out. Since the 3-step achieves almost the same level of torque ripple as the continuous skewing while it makes the 3-D modelling significantly easier, the 3-D FE analyses are based on 3-step skewing. The 3-D models of different skewing methods are shown in Fig. 3.17. The 3-D FE analyses are carried out by using JMAG, where the magnetic properties of the laminations in axial direction are degraded in order to take account of the stacking factor.

The 2-D and 3-D predicted full load torque waveforms with/without skewing are given in Fig. 3.18. It can be seen that the 3-D predicted torques are slightly different from the 2-D predicted ones, since the end effect and other 3-D effects are included. However, the 3-D results confirm the 2-D analyses on the variation of torque ripple with/without skewing. The full load torque ripple is increased when the conventional skewing ( $\beta_0 = -10^\circ$  and  $\theta_{sk} = 60^\circ$ ) is used. However, by using the improved skewing ( $\beta_0 = -20^\circ$  and  $\theta_{sk} = 10^\circ$ ), the full load torque ripple is reduced.

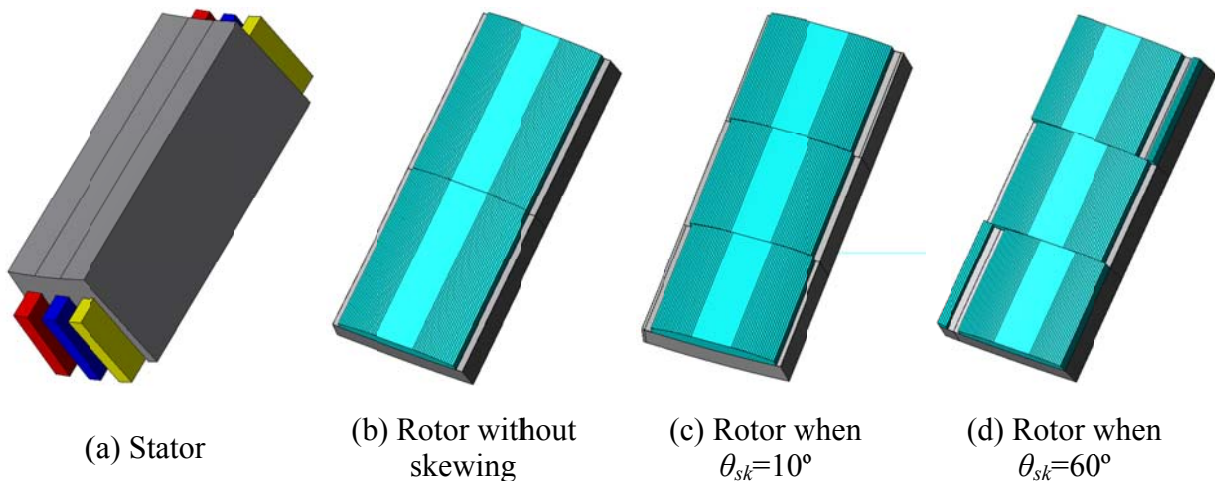


Fig. 3.17. 3-D FE models of different skewing methods.

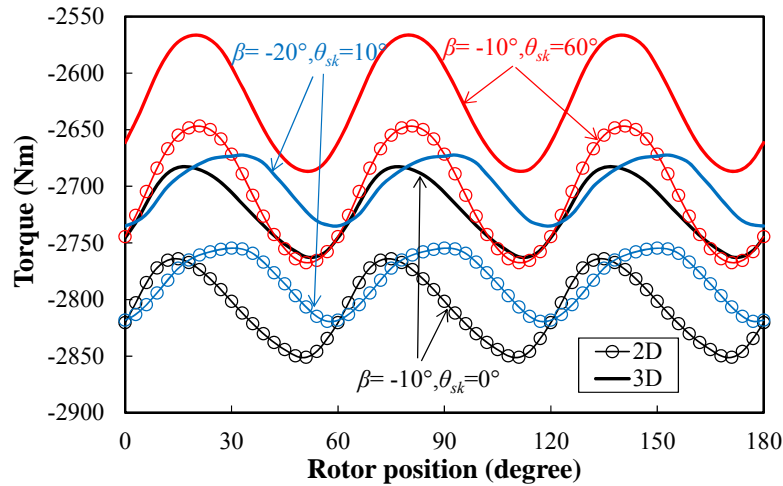


Fig. 3.18. 2-D and 3-D predicted torque waveforms of M1 with/without 3-step skewing when  $I_a = 120\text{A}$ .

### 3.10 Summary

The effectiveness of skewing on torque ripple reduction of PM machines has been investigated with/without magnet shaping under different electric loadings and skewing angles, for both linear and nonlinear cases. It is found that the effectiveness of skewing largely depends on the axial variation of torque ripple phase but less on its magnitude under skewing. Although the cogging torque can be fully eliminated by skewing, it is impractical to fully eliminate the on-load torque ripple by skewing even in linear cases. With magnetic saturation, which aggravates the variation of EM torque ripple with equivalent current phase advance angle, the on-load torque ripple can even be increased by skewing. The improved skewing method has been developed based on optimizing the skewing angle and the current phase advance angle together.

Although the investigation is carried out the SPM machines, the conclusions are also applicable to the IPM machines, where the influence of armature field and magnetic saturation is more significant.

## **CHAPTER 4 AVERAGE TORQUE SEPARATION IN PERMANENT MAGNET SYNCHRONOUS MACHINES USING FROZEN PERMEABILITY**

This chapter investigates the average torque separation in PM synchronous machines. In order to accurately separate the PM and armature fields and, hence, the torque components accounting for the magnetic saturation and cross-coupling, the frozen permeability (FP) method is often employed, while the torque can be calculated by different methods, such as Maxwell stress tensor and virtual work principle. Although these two methods result in identical torques in normal FE analyses when appropriate FE meshes are used, the average torques calculated by these two methods are found to be different when the FP method is employed due to the influence of equivalent rotational magnetic saliency in the stator, which causes a part of PM torque being improperly attributed to the reluctance torque when Maxwell stress tensor method is employed. However, by using the virtual work principle, this is eliminated, and, hence, the average torque components can still be appropriately separated and analysed.

### **4.1 Introduction**

Due to high torque density and efficiency, PM machines are popular in various applications, such as electrical vehicles, power generations, aerospace, and industrial applications [9]-[16] [212]-[217].

It is well-known that the average torque in PM machines is contributed by two components: the PM and reluctance torques. The PM torque is due to the interaction between the PM and armature fields, whilst the reluctance torque is due to the interaction between the armature field and the rotor magnetic saliency. The separation of average torque into its PM and reluctance components will provide valuable insights for PM machine design and optimisation.

For the torque calculation, the Maxwell stress tensor and virtual work principle are two most well-known and widely used methods [203]-[211]. Based on the Maxwell stress tensor method, the torque is calculated directly from the radial and tangential flux density components. Based on the virtual work principle, the torque may be calculated from the flux linkages. It is also well-known that the torques calculated by these two methods should be identical, at least theoretically, in normal FE analyses [203]-[210] although they may be

influenced by the FE mesh discretization, etc.

However, for the average torque separation, the flux density or flux linkage components due to on-load PM or armature field are required. Three methods have been reported in the existing literature for the average torque separation [191]-[194]: (1) the constant PM flux linkage model; (2) the partial-coupling model [191], in which the PM flux linkage varies with the  $q$ -axis current only; and (3) the FP FE method. Since the PM and armature fields influence each other and change with the magnetic saturation and cross-coupling, both the constant PM flux linkage model and the partial-coupling model may result in significant inaccuracy. Hence, the FP method is often employed [192]-[202], in order to accurately separate the PM and armature fields and, hence, the torque components accounting for the magnetic saturation and cross-coupling.

Based on the FP method, there are two ways of average torque separation: (1) based on the Maxwell stress tensor method, the reluctance torque is computed with the on-load armature field only and the PM torque is then calculated from the difference between the total torque and reluctance torque [208]; and (2) based on the virtual work method, the PM and reluctance torque components are calculated from the flux linkages contributed by the on-load PM or armature field only [192]-[202]. Since the torques calculated by the Maxwell stress tensor method and virtual work principle are identical in normal FE analyses, both methods are assumed to be accurate and widely employed for the torque separation in the literature. However, none of them has been validated when the FP method is employed. Therefore, in this chapter, for the first time, the average torque components separated by the Maxwell stress tensor and virtual work principle are compared and examined when the FP method is employed. It is found that the average torque components predicted by these two methods are different. When the FP method is employed, the average torque separation can be performed appropriately by virtual work principle while the Maxwell stress tensor cannot.

The investigation is carried out on an inset PM prototype machine, which is described in section 4.2. The FP method is illustrated and the on-load field components are separated and analysed in section 4.3. The Maxwell stress tensor method and the virtual work principle are firstly examined and compared in normal FE analyses for the total torque calculation in section 4.4 and further investigated in section 4.5 for the average torque separation when the FP method is employed. The cause for the torque discrepancy is explained in section 4.5 as well. Finally, the variation of average torque components is obtained and analysed in section 4.6.

## 4.2 Prototype Machine

In order to reveal the influence of magnetic saturation and cross-coupling, as well as the variation of PM and reluctance torque components, the investigations are carried out on an inset PM prototype machine, whose cross-section and parameters are given in Table 4-I and Fig. 4.1. All the simulations are carried out by the commercial FE software OPERA. The phase current is ideal sinusoidal and the current phase advance angle  $\beta$  is referred to the positive  $q$ -axis. When  $0^\circ < \beta < 90^\circ$ , the  $q$ -axis current is positive and the  $d$ -axis current is negative.

Table 4-I Main parameters

Parameters	value	Parameters	value
Outer diameter	106mm	Rated current (peak)	4A
Stator inner diameter	62mm	Number of turns per phase	152
Airgap length	0.75 mm	Magnet thickness	18.2mm
Axial length	30mm	Remanence	1.17T
Slot number	18	Coercive force	-891 kA/m
Pole number	6		

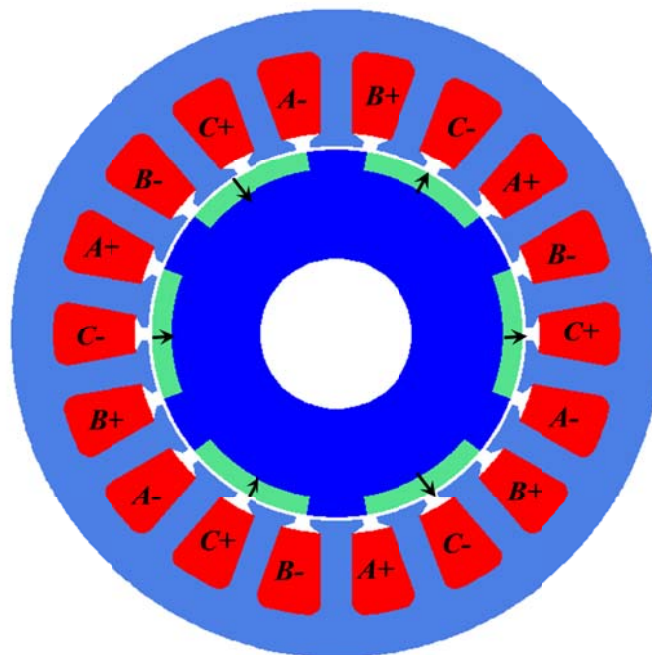


Fig. 4.1. Cross-section of inset PM machine.

### 4.3 Frozen Permeability Method

#### 4.3.1 Principle and Procedure

The FP method has been widely used to investigate the issues related with magnetic saturation and cross-coupling [192]-[202]. When using the FP method, the armature current is constant, which means that the total rotating excitation is constant and the variation of flux density at different rotor positions is due to the variation of permeability. Therefore, the analyses are based on the apparent permeability instead of the incremental permeability. Its principle is illustrated and compared with the conventional method in Fig. 4.2.

Without using the FP method, with the PM excitation ( $H_{PM}$ ) only, i.e., open-circuit, the resultant flux density is  $B_{PM}$  (point B). With the armature excitation ( $H_i$ ) only, the resultant flux density is  $B_i$  (point C). When it is on load (point A), the PM machine is excited by both PM and current, i.e.,  $H_{all} = H_{PM} + H_i$ . However, the resultant flux density  $B_{all}$  is lower than  $B_{PM} + B_i$ . The on-load PM and armature field components cannot be decomposed.

In the FP method, the on-load permeability  $\mu_{all}$  is first obtained and stored by solving the on-load model (point A). Then, two linear analyses, represented by the points D and E, can be solved further based on  $\mu_{all}$ : with either the PM or armature excitation only to obtain  $B(FP,PM)$  or  $B(FP,i)$ , respectively. Since the nonlinear problem has been transformed into the linear one by freezing the permeability as  $\mu_{all}$ ,  $B_{all} = B(FP,PM) + B(FP,i)$ . Therefore, the on-load PM and armature field components are decomposed. Furthermore, since  $\mu_{all}$  varies according to the operation point, the influence of magnetic saturation and cross-coupling is also included.

Based on the principle of FP method, the procedure in the FE computation is summarized in Fig. 4.3. First, the nonlinear FE model with all excitations (PM and current), referred to as the whole model, is solved. Second, the permeability of the whole model, referred to as on-load permeability, in each element and each step, is saved and frozen. Finally, the on-load PM or armature field component is obtained by solving the linear FE model based on the on-load permeability, with either PM or armature excitation only, respectively.

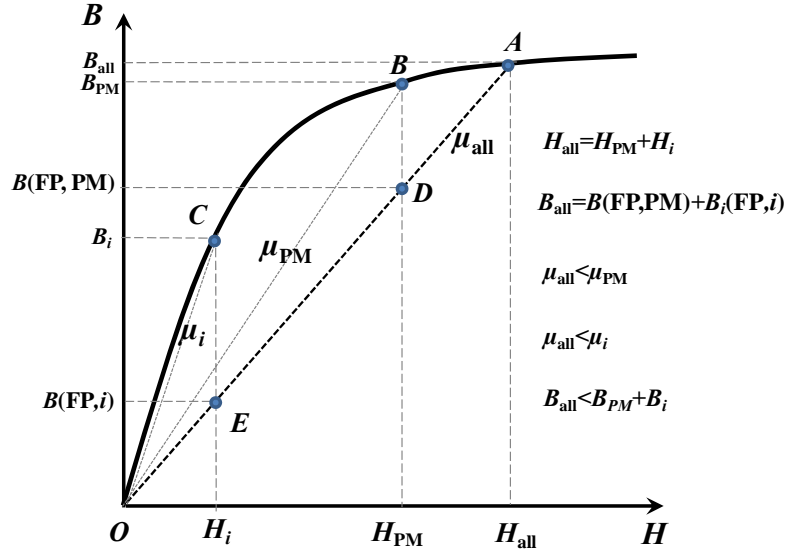


Fig. 4.2. Principle of frozen permeability method.

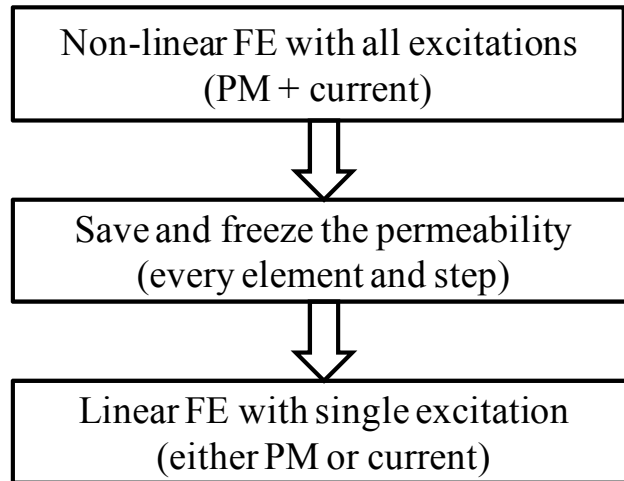


Fig. 4.3. Procedure of frozen permeability method.

### 4.3.2 Field Distributions

By using the FP method, the on-load PM and armature field components can be obtained. For example, the on-load field distributions when the peak phase current  $I_{ap}$  is 4A,  $\beta = 0^\circ$ , and rotor position  $\theta$  is  $0^\circ$  (electrical), are shown in Fig. 4.4.

It can be seen that the on-load field and permeability distributions are neither symmetrical with  $d$ -axis nor with  $q$ -axis due to the influence of armature field [Fig. 4.4(a) and (b)]. Therefore, the on-load PM field [Fig. 4.4(c)] is asymmetric with  $d$ -axis and has  $q$ -axis flux linkage, although the PM excitation is aligned with the  $d$ -axis. It is also true for the on-load armature field. Although only  $q$ -axis current is applied, the on-load armature field [Fig. 4.4(d)] is asymmetric with  $q$ -axis and has  $d$ -axis flux linkage.

For further illustration of on-load field decomposition, the radial and tangential flux density components along the middle of airgap in Fig. 4.4 are obtained and shown in Fig. 4.5. It can be seen that, for each point, the flux densities in the whole model (PM and current) is the same as the mathematic summation of the two flux density components, with either the on-load PM or armature field only, respectively. This is also true for any other rotor position and load condition, as will be shown later.

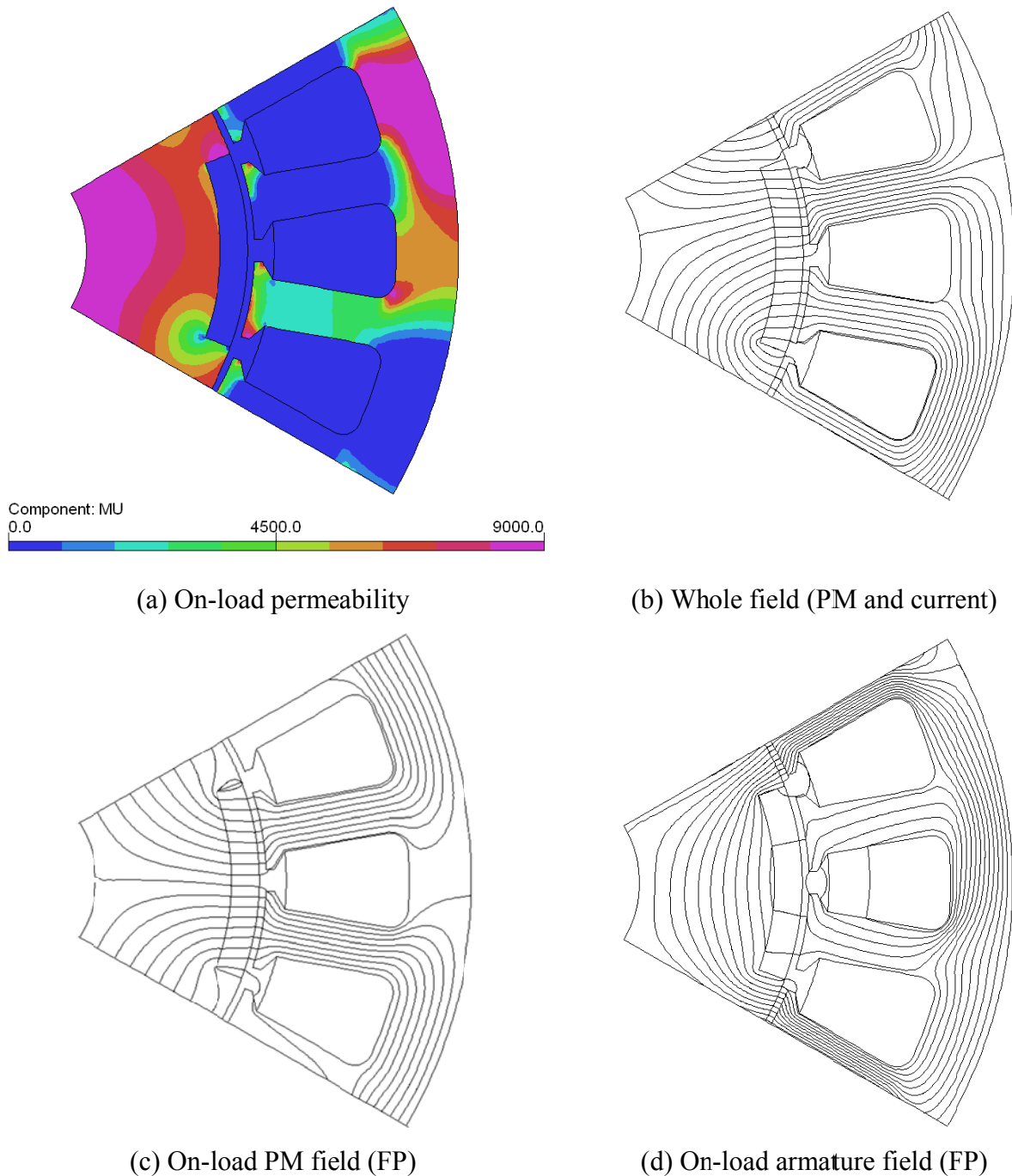
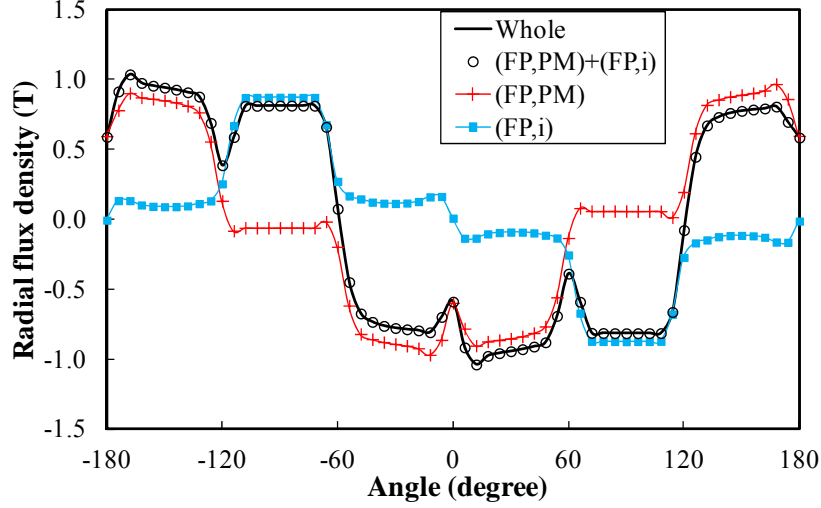
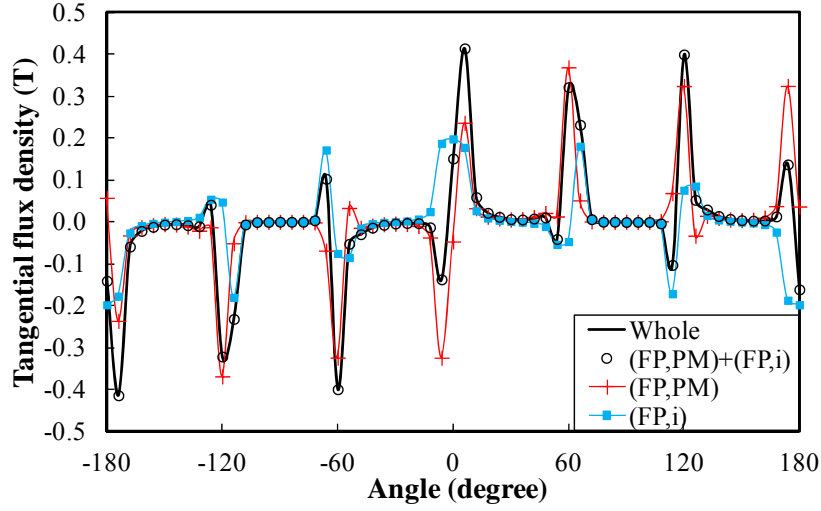


Fig. 4.4. On-load field distributions when  $I_{ap} = 4A$ ,  $\beta = 0^\circ$ , and  $\theta = 0^\circ$ .



(a) Radial flux density components



(b) Tangential flux density components

Fig. 4.5. Flux density components in middle of airgap when  $I_{ap} = 4A$ ,  $\beta = 0^\circ$ , and  $\theta = 0^\circ$ .

### 4.3.3 Flux Linkage Results

Based on the foregoing investigation, the complete flux linkage model should be given by [192], [193]

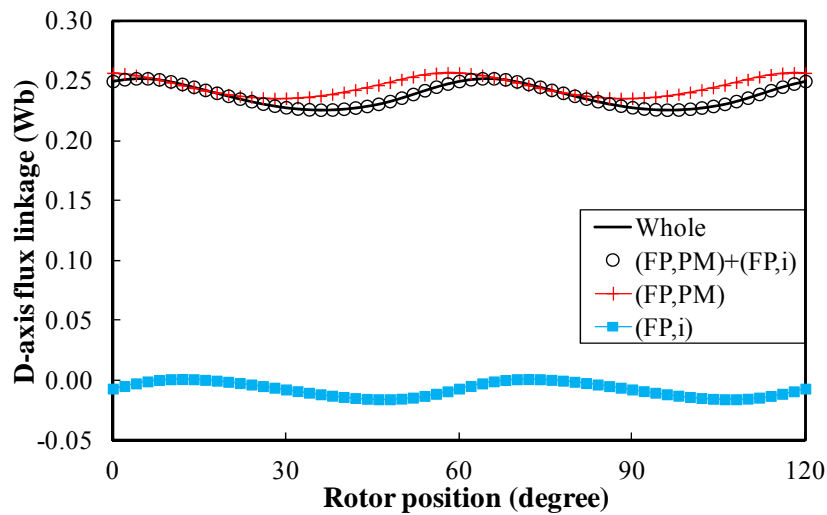
$$\psi_d = \psi_d(\text{PM}) + \psi_d(i) = \psi_d(\text{PM}) + L_{dd}I_d + L_{dq}I_q \quad (4.1)$$

$$\psi_q = \psi_q(\text{PM}) + \psi_q(i) = \psi_q(\text{PM}) + L_{dq}I_d + L_{qq}I_q \quad (4.2)$$

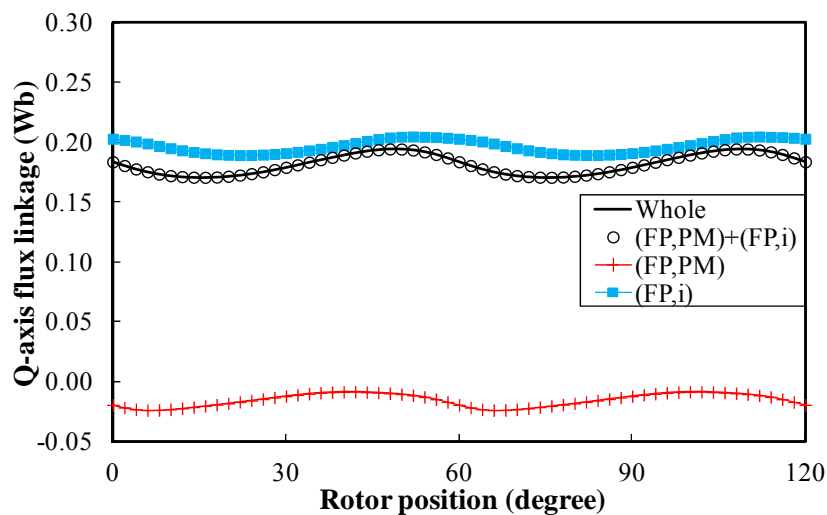
where  $\psi_d$  and  $\psi_q$  are the total  $d$ - and  $q$ -axis flux linkages, respectively.  $\psi_d(\text{PM})$  and  $\psi_q(\text{PM})$  are the  $d$ - and  $q$ -axis flux linkages due to on-load PM field, respectively.  $\psi_d(i)$  and  $\psi_q(i)$   $d$ - and  $q$ -axis flux linkages due to on-load armature field, respectively.  $I_d$  and  $I_q$  are  $d$ - and  $q$ -axis

currents, respectively.  $L_{dd}$ ,  $L_{qq}$ , and  $L_{dq}$  are  $d$ - and  $q$ -axis self and mutual inductances, respectively.

The variation of flux linkage components with rotor position is shown in Fig. 4.6. It can be seen more clearly that not only the instantaneous  $\psi_q(\text{PM})$  but also its average is not zero. The average of  $\psi_d(i)$  is also not zero, although only  $q$ -axis current is applied. These are due to the influence of cross-coupling, which has been illustrated in Fig. 4.4.



(a)  $D$ -axis flux linkages

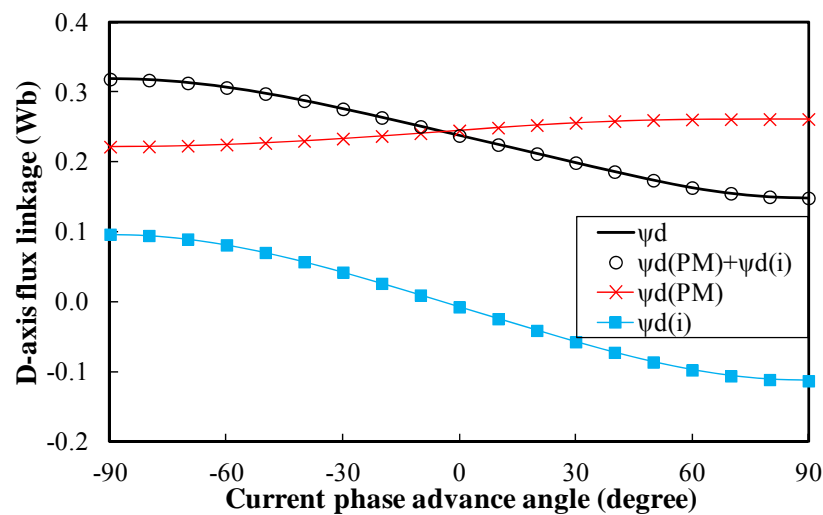


(b)  $Q$ -axis flux linkages

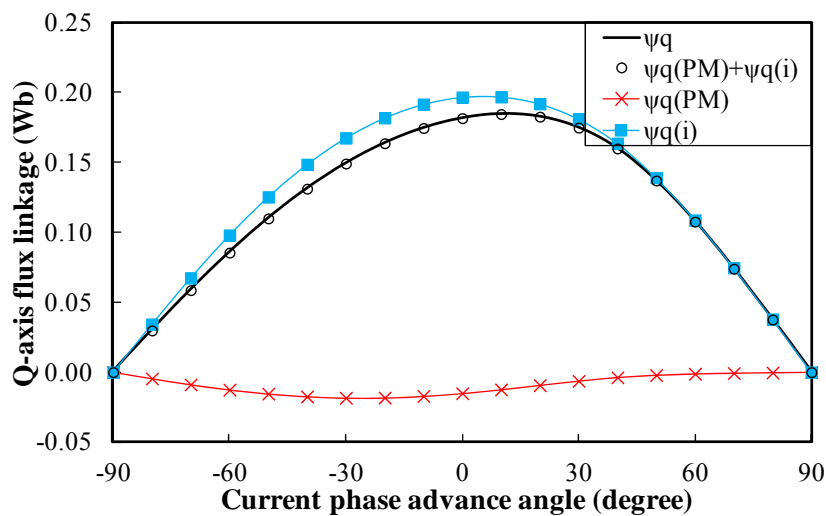
Fig. 4.6. Variation of flux linkages with rotor position when  $I_{ap} = 4\text{A}$  and  $\beta = 0^\circ$ .

The variation of average flux linkages and inductances with  $\beta$  is shown in Fig. 4.7. The influence of magnetic saturation is represented by  $\psi_d(\text{PM})$ ,  $L_{dd}$ , and  $L_{qq}$ . When  $\beta = -90^\circ$ ,  $I_d$  is positive maximum. The  $d$ -axis magnetic saturation is the heaviest due to maximum flux

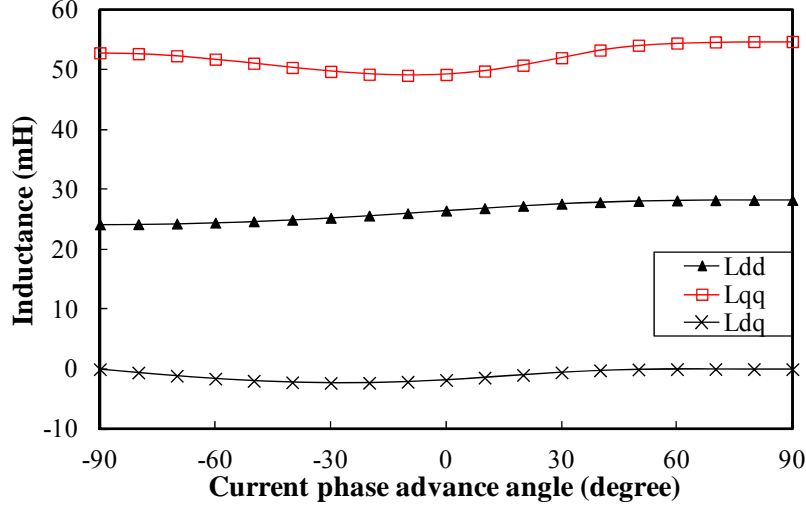
enhancing. Hence,  $\psi_d(\text{PM})$  and  $L_{dd}$  are minimum. When  $\beta = 0^\circ$ ,  $I_d$  is zero and  $I_q$  is maximum. The magnetic saturation is modest along the  $d$ -axis but the heaviest along the  $q$ -axis. Therefore,  $\psi_d(\text{PM})$  and  $L_{dd}$  are higher while  $L_{qq}$  is the lowest. When  $\beta = 90^\circ$ ,  $I_d$  is negative maximum and the magnetic saturation along  $d$ -axis is the lowest due to maximum flux weakening. Therefore,  $\psi_d(\text{PM})$  and  $L_{dd}$  are maximum. The influence of cross-coupling is represented by  $\psi_q(\text{PM})$  and  $L_{dq}$ . The cross-coupling is zero and hence  $\psi_q(\text{PM})$  and  $L_{dq}$  are zero when  $\beta = \pm 90^\circ$  since  $I_q$  is zero. Although  $I_q$  is maximum when  $\beta = 0^\circ$ , the cross-coupling is the heaviest and hence  $\psi_q(\text{PM})$  and  $L_{dq}$  reach the peak at  $\beta = -30^\circ$  since it is aggravated by the magnetic saturation. Therefore, the on-load PM and armature field components can be decomposed by the FP method accounting for the influence of saturation and cross-coupling. Hence, it is possible to separate the total torque into its PM and reluctance components based on FP method.



(a) D-axis flux linkages



(b) Q-axis flux linkages



(c) Inductances

Fig. 4.7. Variation of average flux linkages and inductance with  $\beta$  when  $I_{ap} = 4A$ .

#### 4.4 Torque Calculation Methods

For the torque calculation, the Maxwell stress tensor and virtual work principle are two most well-known and widely used methods [203]-[211]. Based on the Maxwell stress tensor method, the torque is calculated from an integral directly from the flux density components

$$T_{mw} = \frac{L_{ef}}{\mu_0} \int_0^{2\pi} r^2 B_n B_t d\theta_m \quad (4.3)$$

where  $\mu_0$  is the permeability of free space,  $L_{ef}$  is the effective axial length,  $r$  is the radius of integration path,  $B_n$  and  $B_t$  are the normal and tangential flux density components, respectively, and  $\theta_m$  is the rotor position in mechanical angle.

Based on the virtual work principle, the torque is obtained from the energy conservation law. For an open conservative lossless system, the torque is given as [208], [209]

$$T_{vir} = \frac{\partial W'_m}{\partial \theta_m} = \frac{\partial W_{in}}{\partial \theta_m} - \frac{\partial W_m}{\partial \theta_m} = T_{in} - \frac{\partial W_m}{\partial \theta_m} \quad (4.4)$$

where  $W'_m$  is the magnetic co-energy,  $W_{in}$  and  $T_{in}$  are the input energy and corresponding torque, and  $W_m$  is the stored magnetic energy in the machine.

The calculation of  $W_m$  is detailed in Appendix 4.8 and for electrical machines,  $T_{in}$  can be calculated as [218]-[221]

$$T_{in} = \frac{3}{2} p (I_d \frac{d\psi_d}{d\theta} + I_q \frac{d\psi_q}{d\theta} + \psi_d I_q - \psi_q I_d) \quad (4.5)$$

In this chapter, the torque obtained by OPERA is based on the Maxwell stress tensor method and the torque based on virtual work principle is calculated through flux linkage results as shown in (4.4) and (4.5). It is well-known that these two methods are identical for torque calculation in normal FE simulations [203]-[210], although attention should be paid to the mesh discretization. For example, the instantaneous torque waveforms based on the Maxwell stress tensor method and virtual work principle are obtained and shown in Fig. 4.8. It can be seen that the torque results based on these two methods are the same, as expected, which also indicates that the mesh discretization is appropriate and hence its influence is negligible.

Furthermore, for (4.4) and (4.5), it can be noticed that  $\partial W_m/\partial\theta_m$ ,  $\psi_d/d\theta$ , and  $\psi_q/d\theta$  have no contribution to the average torque, since the magnetic field repeats every cycle. Hence, for the average torque, it can also be calculated by the classical  $dq0$  model as:

$$T_{dq0} = 1.5p(\psi_d I_q - \psi_q I_d) \quad (4.6)$$

Without the derivative operation and calculation of magnetic energy, (4.6) is much simpler and more widely used than (4.4) and (4.5) for the average torque calculation. It also has been validated in various machines on the average torque calculation even when the machine is heavily saturated or the winding layout is far from sinusoidal [210], [222]-[224]. The drawback of (4.6) is that it cannot be used for the instantaneous torque and torque ripple computation, as shown in Fig. 4.8. However, it does not influence the average torque separation.

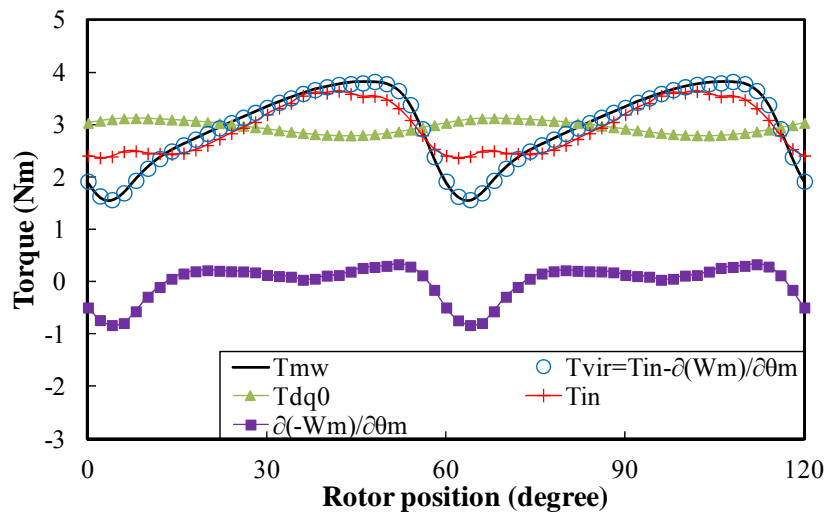


Fig. 4.8. Torque waveforms when  $I_{ap} = 4.0A$  and  $\beta = -30^\circ$ .

#### 4.5 Average Torque Separation Based on Frozen Permeability Method

As stated foregoing, in order to separate the on-load PM and armature fields and, hence, the average torque components accurately, the FP method are often employed. The same as normal simulations, when the FP is applied, two torque results can be obtained from every FE solution, based on the Maxwell stress tensor method or virtual work principle, respectively. Therefore, there are two possible ways of the average torque separation, which are summarized in Fig. 4.9 and Table 4-II.

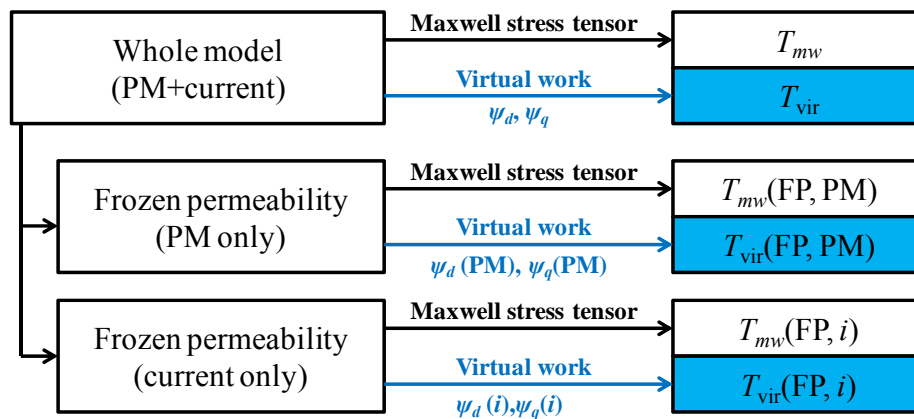


Fig. 4.9. Relationships between FE solutions and torque results.

Table 4-II On-load average torque separation and components

	Maxwell stress tensor	Virtual work
Total torque	$T_{mw}$	$T_{vir}$
Reluctance torque	$T_{mw}(FP, i)$	$T_{vir}(FP, i)$
PM torque	$T_{mw} - T_{mw}(FP, i)$	$T_{vir}(PM)$ or $T_{vir} - T_{vir}(FP, i)$
On-load PM field	$T_{mw}(FP, PM)$	$T_{vir}(FP, PM)$

The torque separation in [208] is based on the Maxwell stress tensor method. The reluctance torque is computed with the on-load armature field only by (4.7). The PM torque is then calculated as the difference between the total torque and the reluctance torque by (4.8). The output torque with on-load PM field only is the on-load cogging torque as given in (4.9).

$$T_{mw}(\text{rel}) = T_{mw}(FP, i) = \frac{L_{ef}}{\mu_0} \int_0^{2\pi} r^2 B_n(i) B_t(i) d\theta_m \quad (4.7)$$

$$T_{mw}(\text{PM}) = T_{mw} - T_{mw}(\text{FP}, i) \quad (4.8)$$

$$T_{mw}(\text{FP}, \text{PM}) = \frac{L_{ef}}{\mu_0} \int_0^{2\pi} r^2 B_n(\text{PM}) B_t(\text{PM}) d\theta_m \quad (4.9)$$

where  $B_n(i)$  and  $B_t(i)$  are the normal and tangential flux density components due to the on-load armature field only, and  $B_n(\text{PM})$  and  $B_t(\text{PM})$  are the normal and tangential flux density components due to the on-load PM field only.

The average torque separations in [192]-[195] are based on the virtual work principle. Since only the average torque is concerned, the torque components are estimated by (4.10)-(4.12) based on the classical  $dq0$  model. In order to identify the calculation method and the related torque components, (4.10)-(4.12) are labeled as  $T_{\text{vir}}(\text{rel})$ ,  $T_{\text{vir}}(\text{PM})$ , and  $T_{\text{vir}}(\text{FP}, \text{PM})$ , respectively.

$$T_{\text{vir}}(\text{rel}) = T_{\text{vir}}(\text{FP}, i) = 1.5p[\psi_d(i)I_q - \psi_q(i)I_d] \quad (4.10)$$

$$T_{\text{vir}}(\text{PM}) = 1.5p[\psi_d(\text{PM})I_q - \psi_q(\text{PM})I_d] = T_{\text{vir}} - T_{\text{vir}}(\text{FP}, i) \quad (4.11)$$

$$T_{\text{vir}}(\text{FP}, \text{PM}) = 0 \quad (4.12)$$

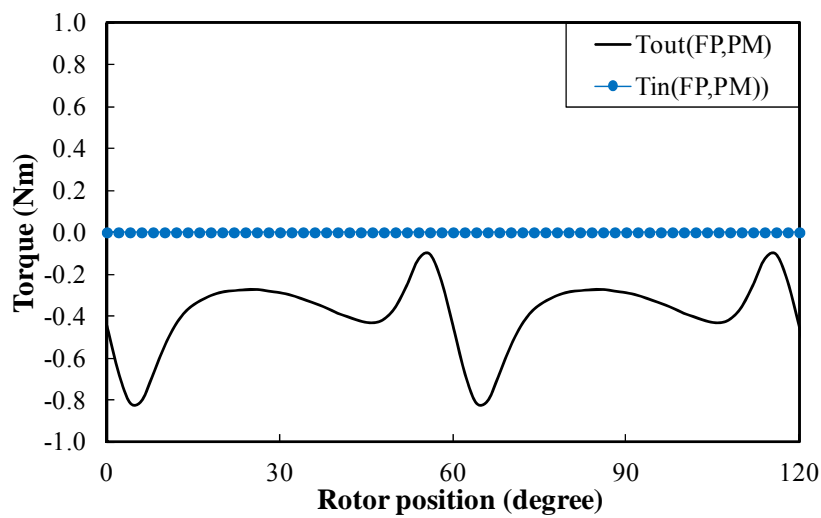
However, it should be noticed that (4.10)-(4.12) are different from the actual reluctance torque, the PM torque and the on-load cogging torque, respectively, since the torque ripples are inaccurate. Therefore, (4.10)-(4.12) is only suitable for the average torque evaluation but not for the torque waveform and torque ripples.

By way of example, when with the on-load PM field only, the torque predicted by (4.12) is always zero. The average torque is zero, since the phase current and input power are zero. The predicted torque ripple is zero due to that the variation of stored magnetic energy, which results in the on-load cogging torque, is excluded in (12).

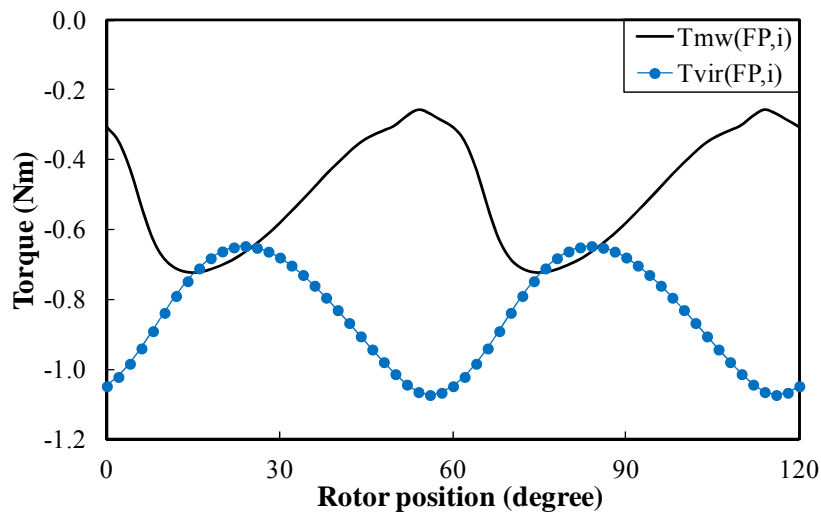
However, neither the Maxwell stress tensor method nor the virtual work principle has been verified in literature when the FP is employed. Therefore, it is important and necessary to examine and compare these two ways of torque separation when the FP is employed.

As can be seen from Figs. 4.10 and 4.11, when the FP method is applied, the average torques calculated by the Maxwell stress tensor or virtual work methods are different. With the on-load PM field only, the average of  $T_{mw}(\text{FP}, \text{PM})$  based on the Maxwell stress tensor method is always lower than the average of  $T_{\text{vir}}(\text{FP}, \text{PM})$ , which is zero and based on the virtual work principle. With the on-load armature field only, the average of  $T_{mw}(\text{FP}, i)$  based

on the Maxwell stress tensor method is always higher than the average of  $T_{vir}(FP,i)$  based on the virtual work principle. Hence, it is important to find out what causes the discrepancy of average torque and which one performs the average torque separation properly. For these purposes, the torque results with on-load PM field only are utilized due to its unique features: the phase current is zero and the torque is manifested by the PM only, which is similar with the open circuit one. Therefore, the average of resultant torque, i.e., on-load cogging torque, must be zero. Hence, it can be concluded that the Maxwell stress tensor method cannot provide the torque calculation properly when the FP method is applied since its calculated average torque is not zero with the on-load PM field excitation only.



(a) Related torque with on-load PM field (FP) only



(b) Related torque with on-load armature field (FP) only

Fig. 4.10. Torque results based on Maxwell stress tensor and virtual work principle when  $I_{ap} = 4.0A$  and  $\beta = -30^\circ$ .

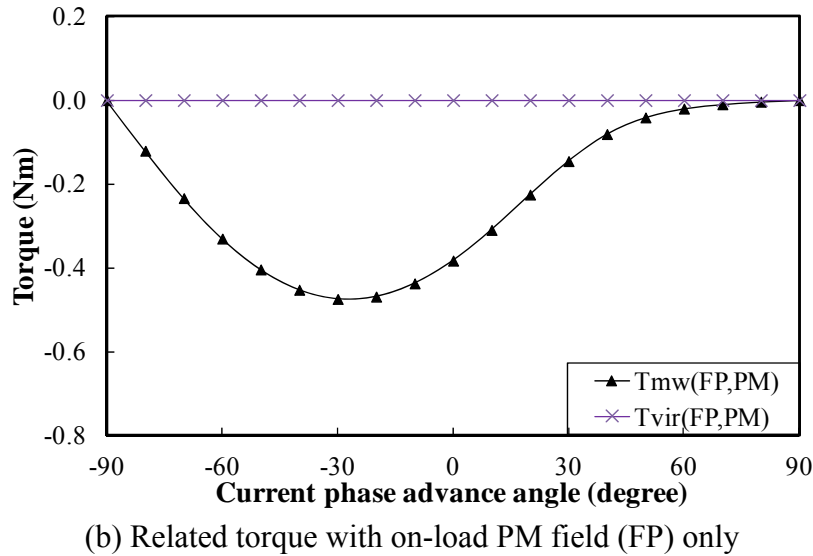
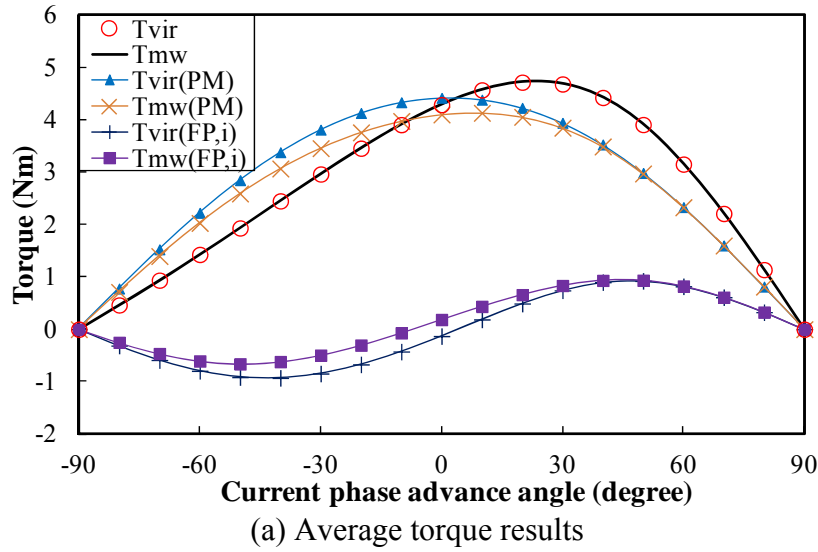


Fig. 4.11. Variation of average torque and separated torque components with current phase advance angle based on Maxwell stress tensor and virtual work principle.

However, it is also important to find out that why the average of  $T_{mw}(FP,PM)$  is nonzero. In order to aid the analyses, the results with on-load PM field only are compared with the open-circuit one in Figs. 4.12-4.14. In Figs. 4.12 and 4.13, the permeability distributions at two representative rotor positions, i.e.,  $\theta = 0^\circ$  and  $\theta = 30^\circ$ , are illustrated, respectively. When it is on open-circuit, the torque is zero at both rotor positions due to the symmetrical permeability distribution as shown in Figs. 4.12 and 4.14. However, the on-load permeability distribution is asymmetric with the PM due to the influence of armature field, both in the rotor and stator, as shown in Fig. 4.13. In other words, there is an equivalent magnetic saliency in the stator as well. Therefore, when the on-load PM field is applied, the nonzero torque is produced due to the interaction between PM and equivalent rotational magnetic saliency in the stator. It can be seen from Fig. 4.13, for both rotor positions, there will be a negative torque on the rotor.

Furthermore, since the armature field rotates synchronously with the rotor, the equivalent magnetic saliency in the stator rotates synchronously with the rotor as well. For this prototype, the PM excitation is always in advance of the high permeance region in the stator. Therefore, the average torque per cycle with on-load PM field only is negative, as shown in Fig. 4.14. The mechanism of “produced” torque is the same as the reluctance torque.

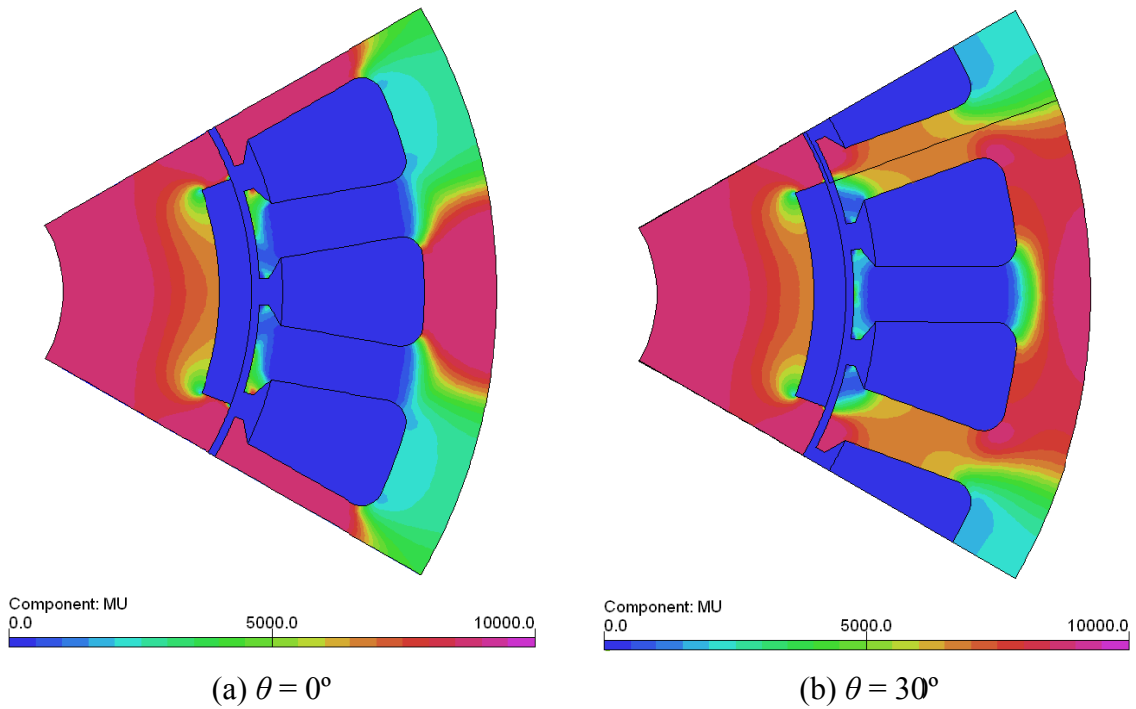


Fig. 4.12. Permeability distributions on open circuit.

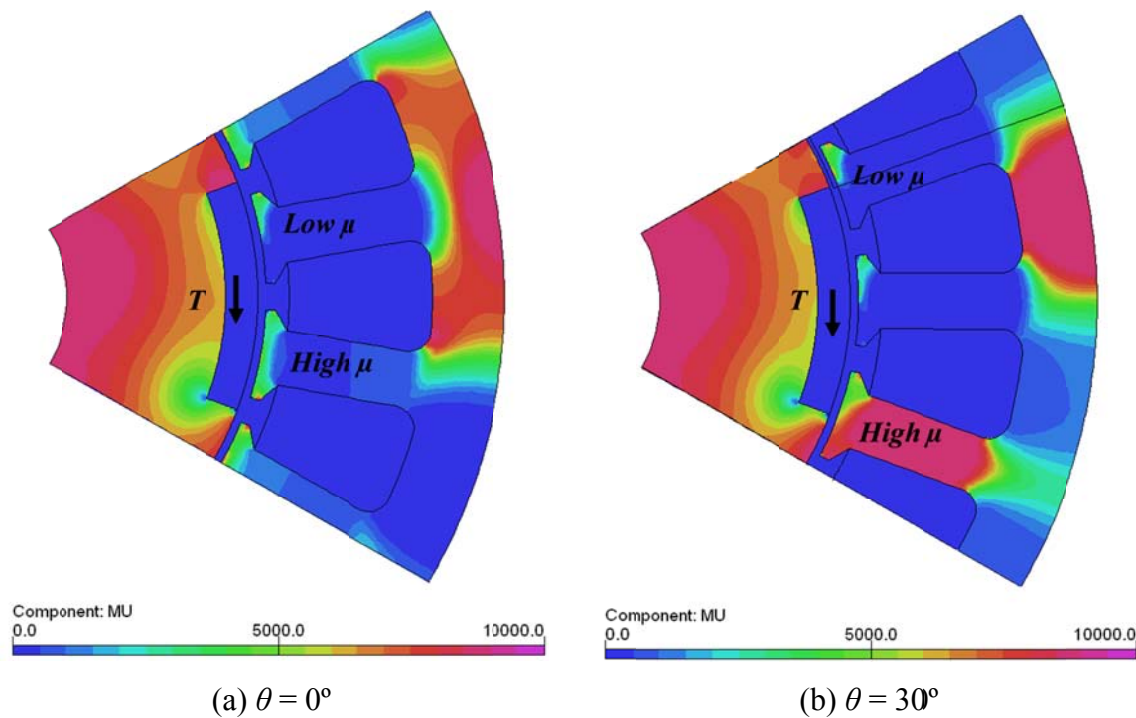


Fig. 4.13. Permeability distributions on load when  $I_{ap} = 4.0A$  and  $\beta = -30^\circ$ .

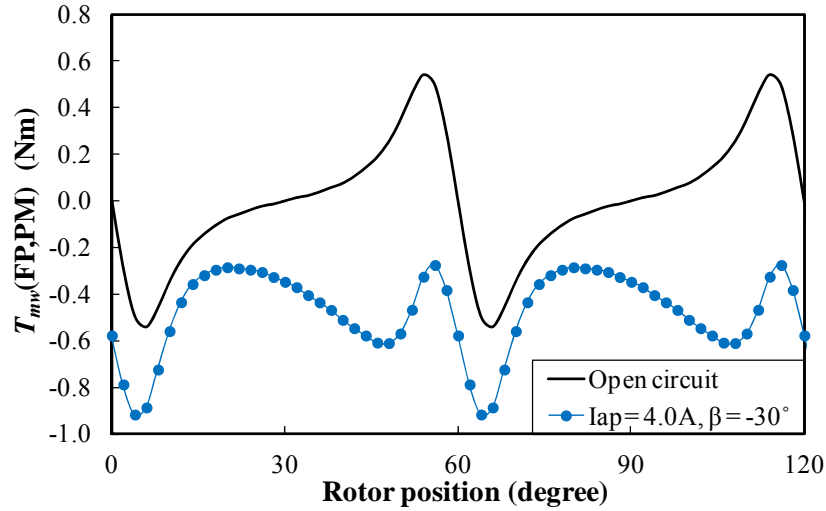


Fig. 4.14. Torque waveforms based on Maxwell stress tensor.

The nonzero average torque of  $T_{mw}(FP,PM)$  can also be explained based on the on-load PM flux linkage results. As can be seen from Fig. 4.15, on open-circuit, the average of  $\psi_q(PM)$  per cycle is zero, due to the fact that there is no equivalent rotational magnetic saliency in the stator. However, when it is on load, the average  $\psi_q(PM)$  per cycle is negative due to the equivalent rotational stator saliency. By reacting with positive  $\psi_d(PM)$ , the negative average  $\psi_q(PM)$  results in the negative average of  $T_{mw}(FP,PM)$ , as shown Fig. 4.11(b).

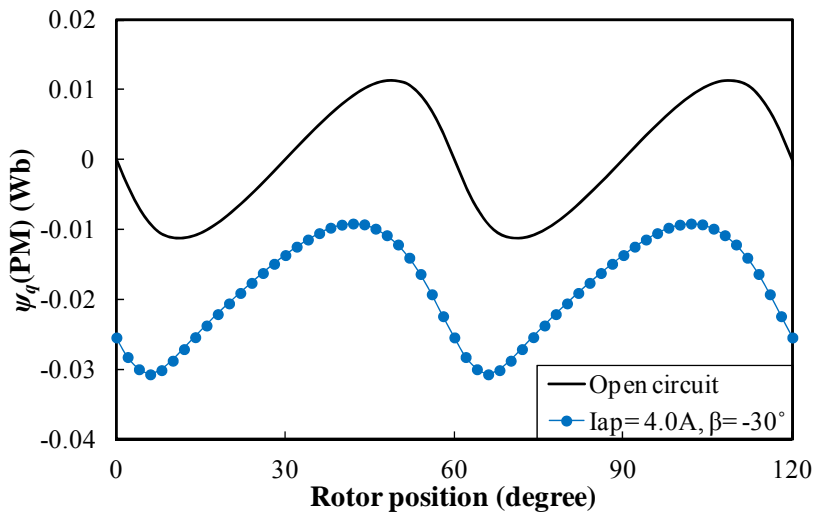


Fig. 4.15. Flux linkages results.

Alternatively, it may be explained that when the on-load armature field is applied, this equivalent rotational magnetic saliency will react with the armature field and produce an extra torque component. Since the high permeance region in the stator is always in advance of the armature excitation in this prototype machine,  $T_{mw}(FP,i)$  is always higher than  $T_{vir}(FP,i)$ , as shown Fig. 4.11(a). Similarly, when it is a generator, it can be predicted that

$T_{mw}(\text{FP,PM})$  will be higher than  $T_{vir}(\text{FP,PM})$ , which is zero and  $T_{mw}(\text{FP},i)$  will be lower than  $T_{vir}(\text{FP},i)$ . According to Fig. 4.11, it also can be seen that the influence of equivalent rotational magnetic saliency in the stator changes similarly with the cross-coupling: it reaches the peak when  $\beta = -30^\circ$  and vanishes when  $\beta = \pm 90^\circ$ .

Since the on-load permeability distribution and hence the equivalent rotational magnetic saliency in the stator is a result of the interaction between PM and armature fields, the relevant torque, whose average torque is nonzero, should be a part of the PM torque. However, when using the Maxwell stress tensor method for the torque calculation with the FP method, the relevant torque due to the equivalent rotational magnetic saliency in the stator is included in  $T_{mw}(\text{FP,PM})$  and  $T_{mw}(\text{FP},i)$ . It is a fundamental limit for the torque calculation based on the combination of the Maxwell stress tensor and FP method. Therefore, neither  $T_{mw}(\text{FP},i)$  is the reluctance torque nor  $T_{mw}(\text{FP,PM})$  is the on-load cogging torque.

By using the virtual work principle, the improper torque attribution is eliminated and, hence, the average torque calculations and separations are still performed properly as given in (4.10)-(4.12).

#### 4.6 Variation of Average Torque Components

Based on the magnetic model in (4.1) and (4.2), the on-load torque is further divided as follows

$$T_{\text{PM}} = T_{\text{PM}}(d) + T_{\text{PM}}(q) \quad (4.13)$$

$$T_{\text{PM}}(d) = 1.5p\psi_d(\text{PM})I_q \quad (4.14)$$

$$T_{\text{PM}}(q) = -1.5p\psi_q(\text{PM})I_d \quad (4.15)$$

$$T_r = T_r(d - q) + T_r(dq) \quad (4.16)$$

$$T_r(d - q) = 1.5p(L_{dd} - L_{qq})I_dI_q \quad (4.17)$$

$$T_r(dq) = 1.5pL_{dq}(I_d^2 - I_q^2) \quad (4.18)$$

where  $T_{\text{PM}}$ ,  $T_{\text{PM}}(d)$ , and  $T_{\text{PM}}(q)$  are the average PM torque and its components due to  $\psi_d(\text{PM})$  and  $\psi_q(\text{PM})$ , respectively; and  $T_r$ ,  $T_r(d-q)$ , and  $T_r(dq)$  are the average reluctance torque and its components due to the self-inductances and mutual inductance, respectively.

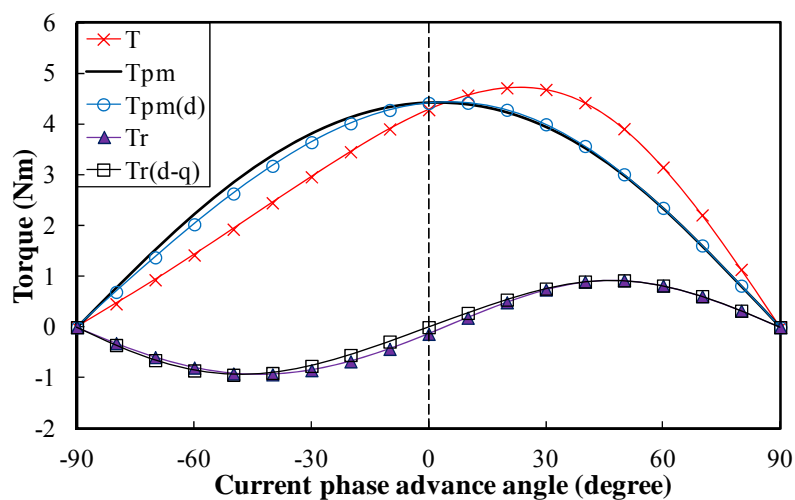
The variation of average torque components with the current phase advance angle is shown in Fig. 4.16. Together with the flux linkages and inductances in Fig. 4.7, the variation can be

explained as follows.

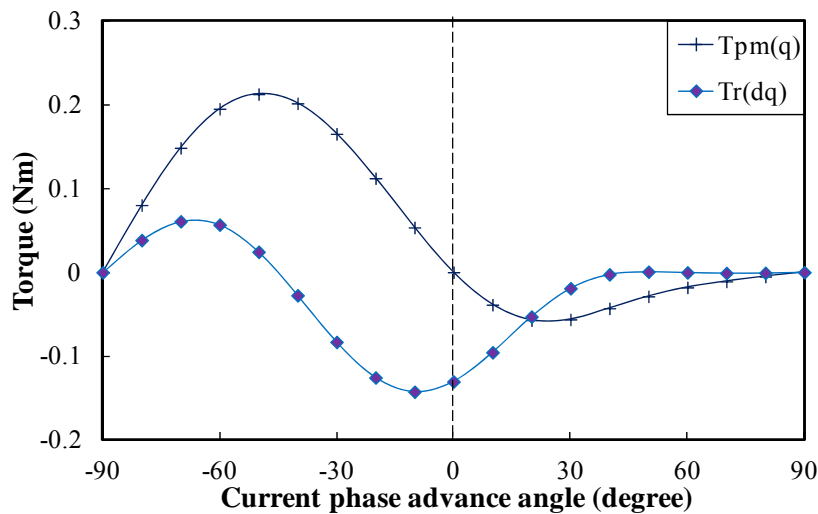
$T_{PM}(d)$  and  $T_r(d-q)$  are influenced by the magnetic saturation. Since  $\psi_d(\text{PM})$  and  $L_{dd}$  increase with  $\beta$ , the positive  $\beta$  will result in higher  $T_{PM}(d)$  and lower  $|T_r(d-q)|$  than the negative  $\beta$ , for example,  $T_{PM}(d)$  at  $\beta = 30^\circ$  is higher than  $T_{PM}(d)$  at  $\beta = -30^\circ$ .  $T_{PM}(d)$  reaches the peak at  $\beta = 10^\circ$ .

$T_{PM}(q)$  and  $T_r(dq)$  depend on the cross-coupling. Since  $\psi_q(\text{PM}) < 0$ ,  $T_{PM}(q)$  is higher than zero when  $\beta < 0^\circ$  and lower than zero when  $\beta > 0^\circ$ .  $T_{PM}(q)$  reaches the peak when  $\beta = -50^\circ$ , due to  $\psi_q(\text{PM})$  being at maximum when  $\beta = -30^\circ$  and  $I_d$  being at maximum when  $\beta = -90^\circ$ .  $T_r(dq)$  peaks when  $\beta = -10^\circ$ , since  $L_{dq}$  is maximum when  $\beta = -30^\circ$  while  $I_q^2 - I_d^2$  peaks when  $\beta = 0^\circ$ .

When  $\beta = 0^\circ$ ,  $T_{PM}(q)$  and  $T_r(d-q)$  are zero. However, due to the cross-coupling,  $T_r(dq)$  and hence  $T_r$  are less than zero. Therefore, the total torque is lower than the PM torque.



(a) Main torque components



(b) Torque components due to cross-coupling

Fig. 4.16. Variation of average torque components.

## 4.7 Summary

The average torque separation based on the Maxwell stress tensor method and the virtual work principle, respectively, have been investigated in this chapter when the FP method is employed. It is found that these two methods result in different average torques when the FP method is employed. This discrepancy is due to the influence of equivalent rotational magnetic saliency in the stator, which is a result of interaction of PM and armature fields and causes the improper torque attribution when the Maxwell stress tensor method is used. The average torque components can still be appropriately separated and analysed by using the virtual work principle when the FP method is employed.

The average torque calculation and separation in association with the FP method can provide valuable insights for the machine design and optimisation. The discussions and conclusions are equally applicable to any other type of electrical machines.

## 4.8 Appendix

The magnetic energy in the machine is calculated according to the material properties as [207], [208], [225]

$$W_m = \int w_m dV = \iint_0^B HdBdV \quad (4.19)$$

For the nonmagnetic regions, such as air and copper, the magnetic energy density  $w_m$  becomes

$$w_{air} = B^2/(2\mu_0) \quad (4.20)$$

For the soft magnetic regions, such as iron, the magnetic energy density  $w_m$  is calculated as

$$w_{iron} = \int_0^B HdB \quad (4.21)$$

In the hard-magnet regions  $w_m$  is

$$w_{PM} = (B_p - B_r)^2/2\mu_0\mu_{rp} + B_t^2/2\mu_0\mu_{rt} \quad (4.22)$$

where  $B_r$ ,  $B_p$ , and  $B_t$  are the remanence, parallel, and tangential flux densities, respectively; and  $\mu_{rp}$ , and  $\mu_{rt}$  are the relative recoil permeability on parallel and tangential directions.

## **CHAPTER 5 ON-LOAD COGGING TORQUE CALCULATION IN PERMENENT MAGNET MACHINES**

This chapter investigates the on-load cogging torque calculation in permanent magnet machines. Vast majority of existing methods for calculating the cogging torque, no matter whether analytical or numerical methods, neglect the influence of load, or are inappropriate in considering the influence of load. Without using the frozen permeability method, the torque calculated by the virtual work principle includes the magnetic energy due to the armature field. When using the frozen permeability method, the resultant torque based on the Maxwell stress tensor with the on-load permanent magnet field only has nonzero average torque and, hence, is not the on-load cogging torque. A new on-load cogging torque calculation method is proposed in this chapter based on the combination of the virtual work principle and frozen permeability method. For its implementation, an improved frozen permeability method, which makes the magnetic energy with on-load permanent magnet field only can be calculated according to the B-H curve, is also developed. By using the new method, all the shortcomings of existing methods can be avoided and, hence, the on-load cogging torque can be calculated appropriately in both linear and nonlinear cases.

### **5.1 Introduction**

Due to high torque density and efficiency, PM machines are popular for many applications. However, one of the drawbacks is the cogging torque, which is manifested by the interaction between the rotor PM magnetomotive force and stator magnetic reluctance. It is merely a pulsating torque and causes vibration and acoustic noise. However, for high-performance applications, such as electrical power steering, servo motors, and direct-drive wind power generators, smooth torque is required over a whole load range. The minimization of torque ripple is usually a major design goal and has been carried out extensively in literature [120]-[182]. Most of them were focused on the open-circuit, where the open-circuit cogging torque is the only component and the influence of magnetic saturation due to load is often neglected. The open-circuit cogging torque can be obtained by various methods, such as the Maxwell stress tensor method and virtual work principle. Therefore, the open-circuit cogging torque can be investigated, and then, various methods can be developed to reduce it. However, the on-load torque ripple is much more complicated than the open-circuit one. The on-load torque has several components while the on-load PM and armature fields couple each other.

It has also been shown in [188]-[190] that the on-load torque ripple can be influenced significantly by the magnetic saturation. Therefore, the most investigation was only able to study the total on-load torque ripple but unable to look into each individual on-load torque component. With the increasing importance of on-load torque ripple, it is strongly desirable to find the ways of separating the on-load PM and armature fields and, hence, the on-load torque components. Therefore, the FP method was developed and widely used [167], [203]-[211]. By using the FP method, the on-load PM and armature fields and, hence, the on-load back EMF can be obtained. However, the calculation of on-load cogging torque remains the most difficult challenge.

Due to its complexity, the on-load cogging torque calculation methods, developed by analogy with the open-circuit ones, have only been mentioned recently in a few papers. The on-load cogging torque was calculated as the differential of total magnetic energy stored in the machine with respect to the rotor position at constant current in [209]. However, the total magnetic energy is also contributed by the armature field when the machine is on load, which will be shown later; this method is inappropriate for on-load cogging torque calculation. In [208], nominally, it tried to exclude the magnetic energy due to the armature field by replacing the total magnetic energy with the total magnetic energy less the magnetic energy stored in the coils. However, without using the FP FE method, technically, the magnetic energy was calculated by including the components such as airgap, magnets, rotor and stator steel, and any other motor regions being not parts of the coils. Therefore, the magnetic energy due to the armature field is still included, and hence, it is inappropriate for the on-load cogging torque calculation. In order to separate the on-load PM and armature fields, the FP method was often employed. Based on the FP method, the on-load cogging torque was calculated by the Maxwell stress tensor with the on-load PM field only in [167] and [208]. However, it was found in last chapter that the average of this calculated torque was not zero, which indicates that it cannot be the on-load cogging torque as well. Hence, none of the existing methods is accurate for the on-load cogging torque calculation.

Therefore, in this chapter, a new method for on-load cogging torque calculation is proposed based on the combination of virtual work principle and FP method. In order to implement the new method, the improved FP method is developed as well and detailed in section 5.5. Together with the existing ones, all the methods will be examined in both linear and nonlinear cases in sections 5.6 and 5.7, respectively. Furthermore, the reasons, which make the existing methods inappropriate for on-load cogging torque calculation, will be illustrated correspondingly as well.

## 5.2 Prototype Machine

In order to reveal the influence of magnetic saturation and cross-coupling, as well as the variation of PM and reluctance torque components, the investigations are carried out on an inset PM prototype machine, whose cross-section and parameters are given in Table 4-I and Fig. 4.1. All the simulations are carried out by the commercial FE software OPERA with ideal sinusoidal phase current. The current phase advance angle  $\beta$  is referred to the positive  $q$ -axis. When  $0^\circ < \beta < 90^\circ$ , the  $q$ -axis current is positive and the  $d$ -axis current is negative.

## 5.3 Open-circuit Cogging Torque Calculation Methods

Since all the on-load cogging torque calculation methods mentioned in literature are developed by analogy with the open-circuit ones, as will be shown later, it is necessary to review the calculation methods of open-circuit cogging torque.

When it is on open-circuit, the machine is excited by PM only. The cogging torque is manifested by the interaction between the rotor PM magnetomotive force and stator magnetic reluctance. Based on the virtual work principle, it can be obtained as [121]-[123]

$$T_c(\text{open}) = -\partial W_m / \partial \theta_m |_{i=0} \quad (5.1)$$

where  $W_m$  is the total magnetic energy stored in the machine, and  $\theta_m$  is the rotor position in mechanical angle.

The open-circuit cogging torque can also be calculated based on the Maxwell stress tensor as [121]-[123]

$$T_c(\text{open}) = \frac{L_{ef}}{\mu_0} \int_0^{2\pi} r^2 B_n(\text{open}) B_t(\text{open}) d\theta_m \quad (5.2)$$

where  $\mu_0$  is the permeability of free air space.  $L_{ef}$  is the effective axial length.  $r$  is the radius of integration path.  $B_n(\text{open})$  and  $B_t(\text{open})$  are the normal and tangential airgap flux density components on open-circuit, respectively.

It is well-known and has been shown in chapter 4 that these two methods are identical, at least theoretically, for torque calculation [203]-[210], although they may be influenced by the FE mesh discretization, etc.

## 5.4 Existing On-load Cogging Torque Calculation Methods

Different from the open-circuit one, the on-load cogging torque can be influenced

significantly by the electric loading and magnetic saturation. Furthermore, since the on-load PM and armature fields are coupled each other, most investigation is only able to study the total on-load torque ripple [188]-[190] and the on-load cogging torque calculation is much more complicated. However, in order to separate and investigate the on-load torque ripple components, the method of on-load cogging torque calculation is strongly desirable.

Several candidate methods for on-load cogging torque calculation have been mentioned in literature. They are all developed by analogy with the open-circuit ones, i.e., (5.1) and (5.2), and can be summarized as follows.

#### 5.4.1 Virtual Work Methods without Using FP Technique

By analogy with (5.1), it is mentioned in [209] that the on-load cogging torque can be calculated as the derivative of the total magnetic energy with respect to the rotor position at constant current

$$T_c(\text{load}) = -\partial W_m / \partial \theta_m |_{i=ct} \quad (5.3)$$

However, as will be shown later, it is inappropriate since the total magnetic energy is also contributed by the armature field when the machine is on load.

In [208], the on-load cogging torque is calculated in a slightly different way as

$$T_c(\text{load}) = -\partial W_{mlc} / \partial \theta_m |_{i=ct} \quad (5.4)$$

where  $W_{mlc}$  is the magnetic energy stored in the system less the magnetic energy stored in the coils and includes components as airgap, magnets, rotor and stator steel, and any other motor regions, which are not parts of the coils.

From the definition of  $W_{mlc}$ , it can be seen that the attempt is to exclude the influence of magnetic energy due to armature field. However, without using the FP method, technically, it is impossible to separate the magnetic energy due to the armature field, since the on-load PM and armature fields exist in every region and are coupled each other. Hence, it is also inappropriate.

#### 5.4.2 Maxwell Stress Tensor Methods with FP Technique

By analogy with (5.2), it is mentioned in [167] and [208] that the on-load cogging torque can be computed by the Maxwell stress tensor with the on-load PM field only as

$$T_c(\text{load}) = T_{mw}(\text{FP, PM}) = \frac{L_{ef}}{\mu_0} r^2 \int_0^{2\pi} B_n(\text{FP, PM}) B_t(\text{FP, PM}) d\theta_m \quad (5.5)$$

where  $T_{mw}(\text{FP, PM})$  is the calculated torque based on the Maxwell stress tensor with on-load PM field only.  $B_n(\text{FP, PM})$  and  $B_t(\text{FP, PM})$  are the normal and tangential airgap flux density components due to the on-load PM field only.

In order to obtain the on-load PM field and implement (5.5), the FP method is often employed. The principle of conventional FP method [192]-[202] has been illustrated in Fig. 4.2 and 4.3.

By using the FP method, the on-load PM field and, hence,  $T_{mw}(\text{FP, PM})$  can be obtained. However, it has been shown in chapter 4 that  $T_{mw}(\text{FP, PM})$  had nonzero average torque in nonlinear cases and, hence, cannot be exactly the on-load cogging torque.

## 5.5 Proposed On-load Cogging Torque Calculation Method

### 5.5.1 Proposed Method

Since none of the existing methods is accurate for the on-load cogging torque calculation, a new on-load cogging torque calculation method is strongly desirable. By analogy with (5.2), theoretically, it can be developed by combining the FP method with virtual work principle as

$$T_c(\text{load}) = -\partial W_m(\text{FP, PM}) / \partial \theta_m |_{i=ct} \quad (5.6)$$

where  $W_m(\text{FP, PM})$  is the total magnetic energy with on-load PM field only.

However, since the magnetic energy with on-load PM field only cannot be calculated according to the B-H curve in the conventional FP method, as explained later, a new FP method is required for the implementation of (5.6).

### 5.5.2 Improved FP Method

For this purpose, an improved FP method is developed and illustrated in Figs. 5.1 and 5.2. Different from the conventional FP method, in the improved FP method, the third step is replaced by solving nonlinear FE models with the nonlinear iteration number being 1. By this special setting, the following benefits can be obtained and illustrated by comparing the on-load PM field distributions obtained by these two methods.

As shown in Fig. 5.3(c) and (d), in the improved FP method, the on-load PM flux density distribution is still calculated from the on-load permeability distribution, and, hence, the same

as the one obtained by the conventional FP method. It can also be seen that due to the influence of electric loading, the on-load PM flux density distribution is different from the open-circuit one [Fig. 5.3(b)].

However, the resultant permeability distributions with on-load PM field only by these two FP methods are different. In the conventional FP method, the resultant permeability distribution remains the same as the on-load one, due to that the third step is carried out by solving linear FE models. Together with its flux density result, it can be represented equivalently by the point D in Fig. 5.1. However, due to the linearization, in the post-process, the magnetic energy will be calculated according to the linear B-H curve, whose permeability is  $\mu_{all}$ , and represented equivalently by the hatched triangle in Fig. 5.4(a). Consequently, the magnetic energy in the iron parts will be significantly overestimated. As shown in Fig. 5.5, the calculated magnetic energy in the iron parts with on-load PM field only is even higher than the one with the whole field under flux enhancing. It also confirms that, in this case, the magnetic energy results in the iron parts with on-load PM field only calculated by  $\int HdB$  (solid line in Fig. 5.5) or  $HB/2$  (circles in Fig. 5.5) are the same.

In contrast, by using the improved FP method, the permeability will be updated according to B-H curve based on the on-load PM flux density distribution, and, hence, different from the on-load one, as shown in Fig. 5.3(a) and (d). Together with its flux density result, it is represented equivalently by the point F in Fig. 5.1. Therefore, the magnetic energy with on-load PM field only can still be calculated properly according to the B-H curve and represented equivalently by the hatched area in Fig. 5.4(b), which is significantly smaller than the one by conventional FP method (Figs. 5.4 and 5.5). It can also be seen that, by using the improved FP method, the calculated magnetic energy in the iron parts with on-load PM field only is smaller than the one with the whole field under flux enhancing (dashed line in Fig. 5.5) as expected. Furthermore, due to the nonlinearity of B-H curve, it is expected the calculated magnetic energy result in the iron parts by  $\int HdB$  (blue line with triangle markers in Fig. 5.5) is much lower than the one by  $HB/2$  (red line with cross markers in Fig. 5.5).

Therefore, by using the improved FP method, the on-load PM flux density distribution can still be obtained in the same way as the conventional FP method, which means the torque calculated by the Maxwell stress tensor method remains the same. However, the improper magnetic energy calculation in the conventional FP method has been overcome. Hence, the on-load cogging torque computation based on the combination of the FP method with the virtual work principle, i.e., (5.6), can be implemented.

Based on (5.6), it can be seen that the average of resultant torque is inherently zero.

Meanwhile, since it is calculated based on the on-load PM field only, the magnet energy due to armature field is excluded while the influence of electric loading and magnetic saturation is still included.

Including the proposed one (method d), all the candidate on-load cogging torque calculation methods are summarized in Table 5-I and will be examined in both linear and nonlinear cases in the sections 5.6 and 5.7.

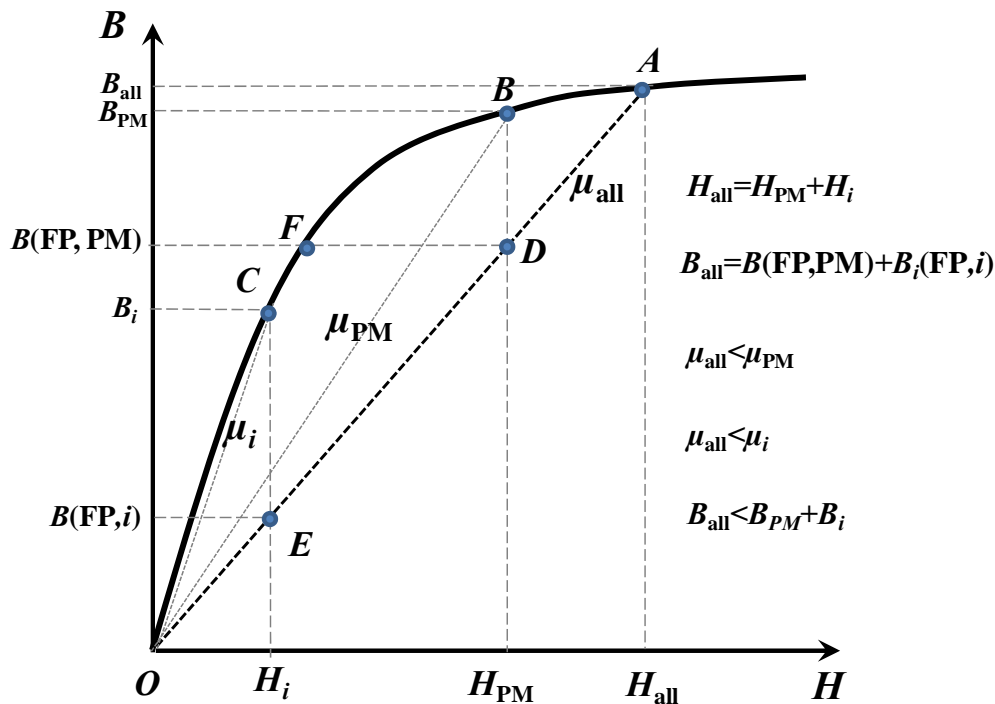


Fig. 5.1. Principle of frozen permeability method.

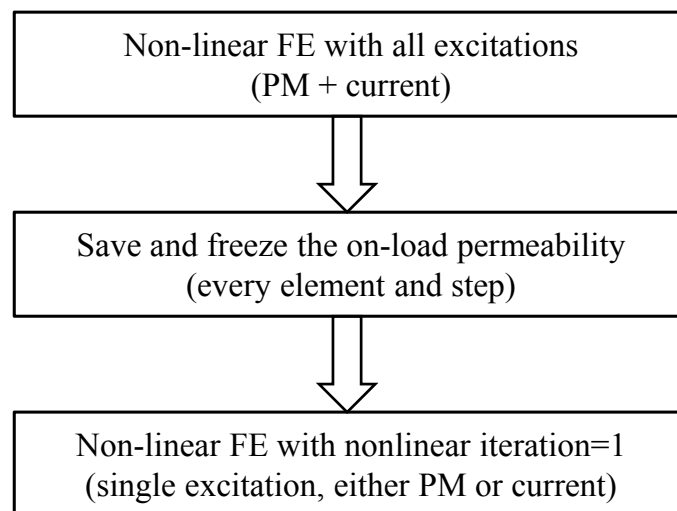
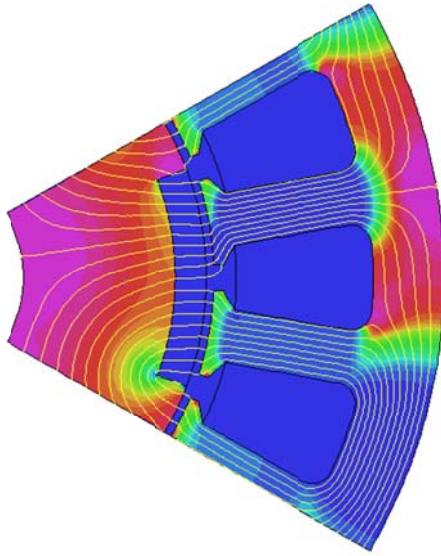
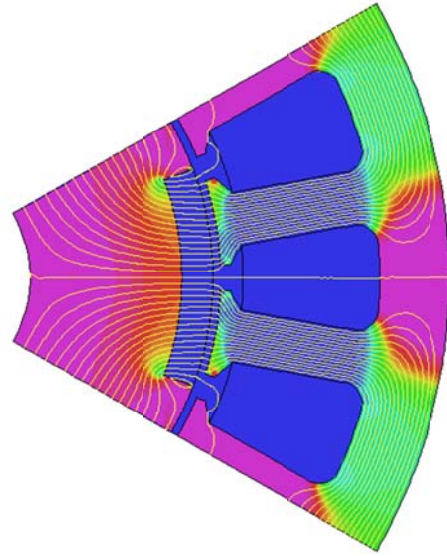


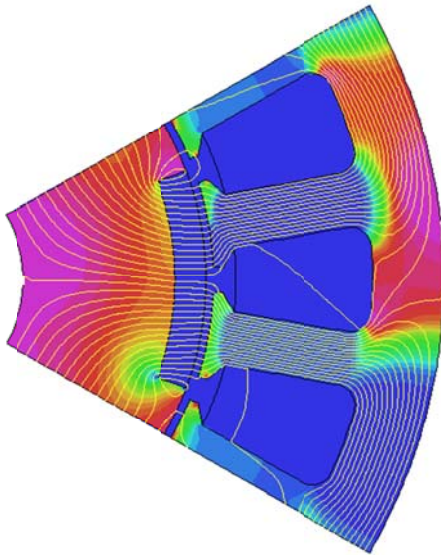
Fig. 5.2. Implementation procedure of improved FP method for each rotor position.



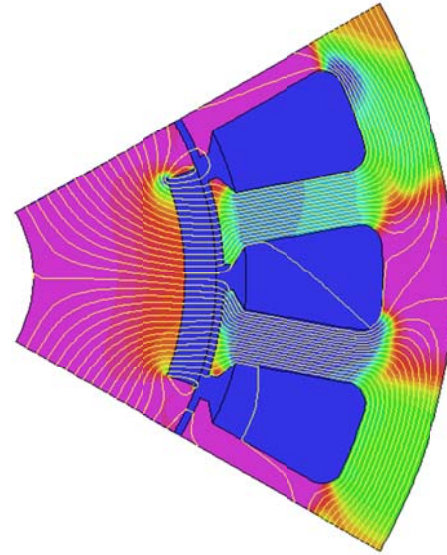
(a) Whole field  $I_{ap} = 4A$ ,  $\beta = 30^\circ$



(b) Open circuit

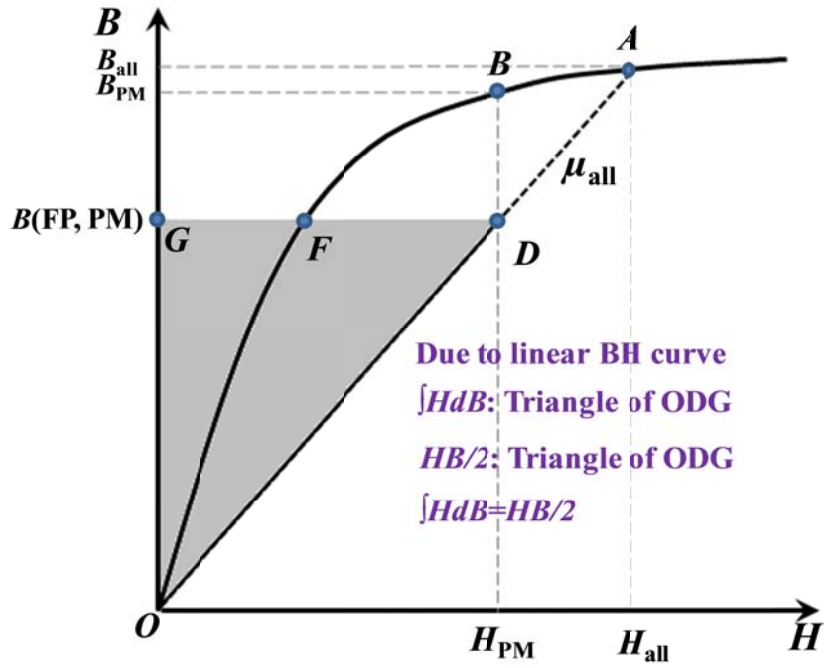


(c) On-load PM field  $I_{ap} = 4A$ ,  $\beta = 30^\circ$   
(conventional FP)

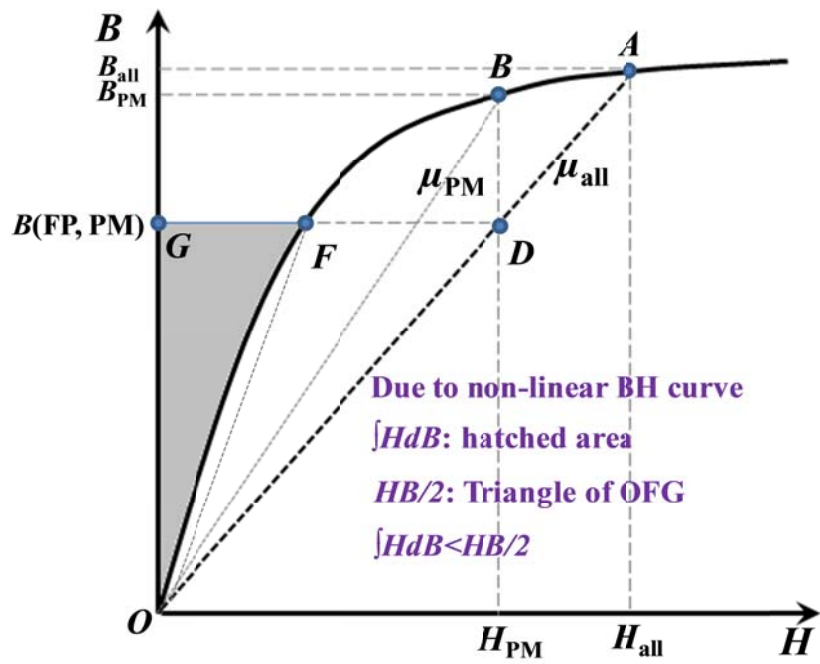


(d) On-load PM field  $I_{ap} = 4A$ ,  $\beta = 30^\circ$   
(improved FP)

Fig. 5.3. Field distributions when  $\theta=0^\circ$  (line represents equal potential distribution and color represents permeability distribution).



(a) Conventional FP method



(b) Improved FP method

Fig. 5.4. Equivalent magnetic energy areas of two FP methods.

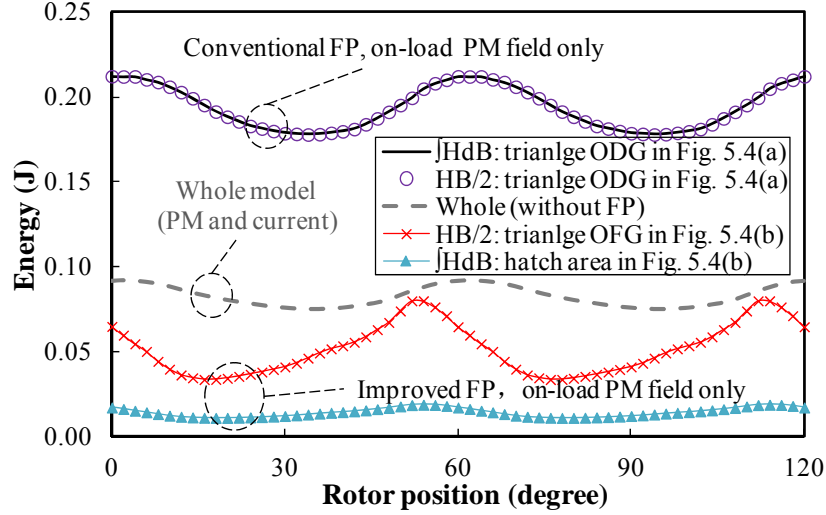


Fig. 5.5. Magnetic energy results in iron parts when  $I_{ap} = 4A$  and  $\beta = -30^\circ$ .

Table 5-I Candidate methods for on-load cogging torque calculation

Methods	Expression	Method involved (equation)
a	$-\partial W_m / \partial \theta_m  _{i=ct}$	Virtual work principle (5.3)
b	$-\partial W_{mlc} / \partial \theta_m  _{i=ct}$	Virtual work principle (5.4)
c	$T_{mw}(FP, PM)$	Maxwell stress tensor, FP (5.5)
d	$-\partial W_m(FP, PM) / \partial \theta_m  _{i=ct}$	Virtual work principle (5.6)

## 5.6 Linear Cases

All the candidate methods are first examined in linear cases, where the on-load permeability, PM field distribution, and, hence, the on-load cogging torque are the same as the open-circuit ones.

Furthermore, in linear cases, since the permeability remains unchanged, the superposition principle holds and it inherently has the same effect as the FP method. In order to equivalently simulate the on-load field components and aid the investigation, the torque and magnetic energy results under three operation conditions, i.e., open circuit (PM only), load current only (without PM), and whole model (current and PM), are calculated.

In linear cases, since they are the same as (5.1) and (5.2), respectively, both (5.5) and (5.6) can be used for the on-load cogging torque calculation, as shown in Fig. 5.6. It also indicates that the mesh is appropriate, and, hence, its influence is negligible.

However, as shown in Fig. 5.7, the torque calculated by (5.3) is significantly different from

the cogging torque shown in Fig. 5.6. It is due to the fact that the total magnetic energy is also contributed by the armature field when it is on load. In linear cases, the relationship between the magnetic energy variations can be derived as follows.

Based on the virtual work principle, the total torque and its on-load torque components can be given as

$$T = 1.5p[(I_d d\psi_d + I_q d\psi_q)/d\theta + \psi_d I_q - \psi_q I_d] - \partial W_m / \partial \theta_m |_{i=ct} \quad (5.7)$$

$$T_c = -\partial W_m(\text{FP, PM}) / \partial \theta_m |_{i=ct} \quad (5.8)$$

$$T_r = 1.5p[I_d \frac{d\psi_d(i)}{d\theta} + I_q \frac{d\psi_q(i)}{d\theta} + \psi_d(i) I_q - \psi_q(i) I_d] - \partial W_m(\text{FP, } i) / \partial \theta_m |_{i=ct} \quad (5.9)$$

$$T_{\text{PM}} = 1.5p[I_d d\psi_d(\text{PM})/d\theta + I_q d\psi_q(\text{PM})/d\theta + \psi_d(\text{PM}) I_q - \psi_q(\text{PM}) I_d] \quad (5.10)$$

where  $T$  is the total torque;  $T_r$  is the reluctance torque component;  $T_{\text{PM}}$  is the PM torque component;  $\psi_d$  and  $\psi_q$  are total d- and q-axis flux linkages, respectively;  $\psi_d(\text{PM})$  and  $\psi_q(\text{PM})$  are the d- and q-axis flux linkages due to on-load PM field, respectively.  $\psi_d(i)$  and  $\psi_q(i)$  are d- and q-axis flux linkages due to on-load armature field, respectively;  $I_d$  and  $I_q$  are d- and q-axis currents, respectively; and  $W_m(\text{FP, } i)$  is the system magnetic energy with armature excitation only.

Since the torque and flux linkage relationships are:

$$T = T_c + T_r + T_{\text{PM}} \quad (5.11)$$

$$\psi_d = \psi_d(\text{PM}) + \psi_d(i) \quad (5.12)$$

$$\psi_q = \psi_q(\text{PM}) + \psi_q(i) \quad (5.13)$$

In linear case, the relationship between the magnetic energy variations is:

$$\frac{\partial W_m}{\partial \theta_m} = \frac{\partial W_m(\text{FP, PM})}{\partial \theta_m} + \frac{\partial W_m(\text{FP, } i)}{\partial \theta_m} \quad (5.14)$$

The magnetic energy relationship is also confirmed by the FE results in Fig. 5.7. However,  $W_m(\text{FP, } i)$  is due to the armature field, and, hence, should be excluded for the cogging torque calculation. Therefore, equation (5.3) should be discarded.

Although, by the definition, it is aimed to exclude the magnetic energy due to armature field, the torque calculated by equation (5.4) is still different from the cogging torque, as shown in Fig. 5.7. It is due to the factor that without using FP method, technically, it is

impossible to separate the on-load armature field, and, hence, the relevant magnetic energy just by selecting different components. Hence, (5.4) should be discarded as well.

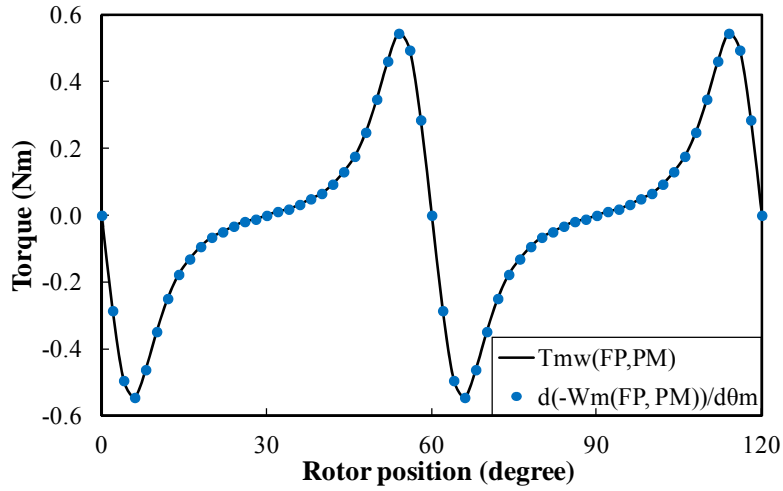


Fig. 5.6. Torque results based on (5.5) and (5.6) in linear cases.

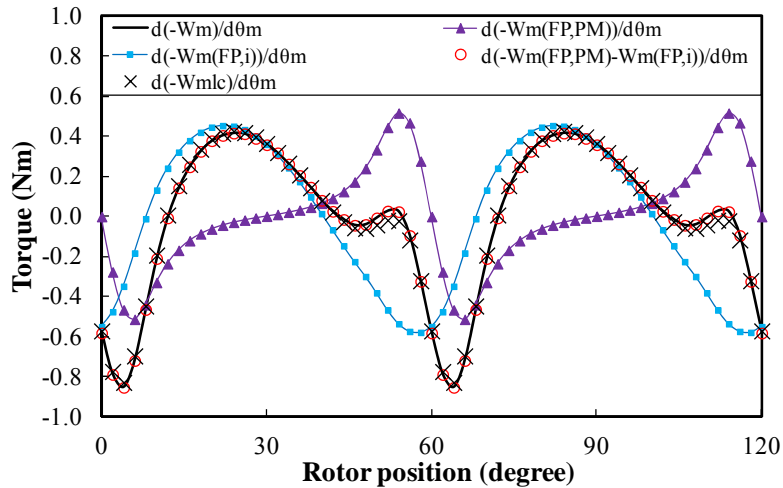


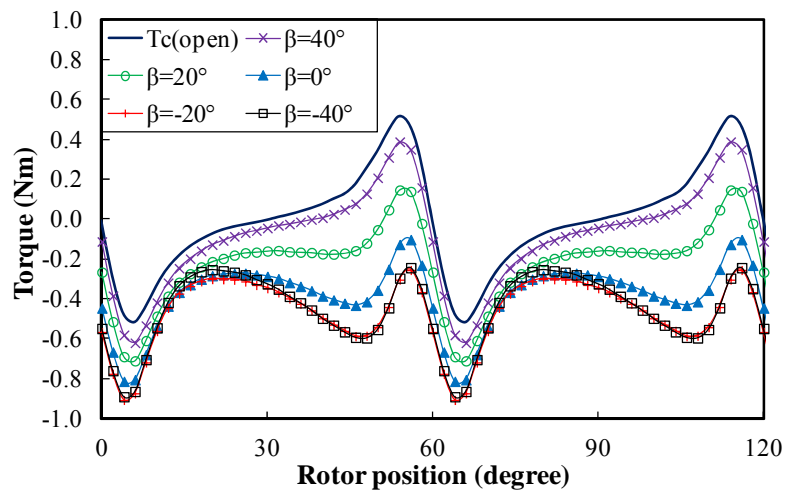
Fig. 5.7. Torque results based on magnetic energy variation in linear cases when  $I_{ap} = 4A$  and  $\beta = -30^\circ$ .

## 5.7 Nonlinear Cases

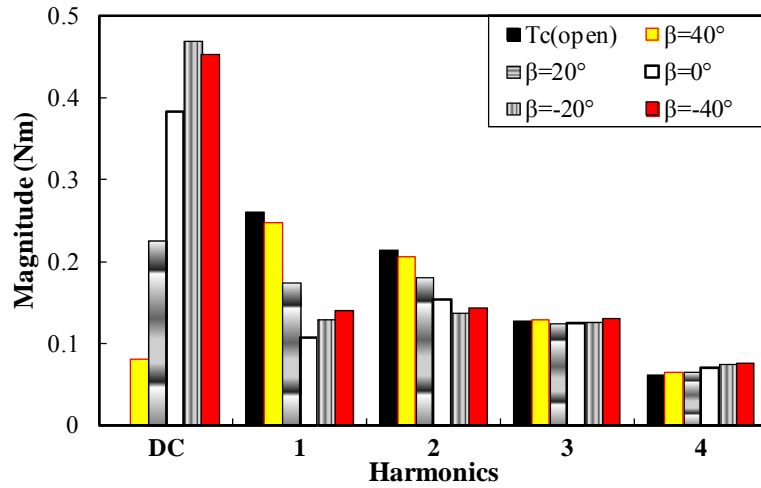
Different from the linear cases, the actual PM machines can be influenced significantly by the magnetic saturation as mentioned earlier. Meanwhile, in order to separate the on-load PM and armature fields, the FP method is often employed. Therefore, it is necessary to examine (5.5) and (5.6) further in nonlinear cases when the FP method is employed.

Using the improved FP method, the FE results based on (5.5) and (5.6) are obtained and shown in Figs. 5.8 and 5.9, where the torque spectra are obtained based on that the

fundamental period is  $60^\circ$  electrical. It can be seen that when the FP method is employed, the torque results calculated by (5.5) and (5.6) are significantly different from each other. Furthermore, it is worth noticing that average of the resultant torque by (5.5),  $T_{mw}(\text{FP,PM})$ , is nonzero. Hence, it can be concluded that (5.5), which is based on the Maxwell stress tensor method, cannot performance the on-load cogging torque calculation properly when the FP method is applied. In chapter 4, the reason for the nonzero average of  $T_{mw}(\text{FP,PM})$  has been explained, e.g., a part of PM torque is improperly attributed to the reluctance torque due to the influence of equivalent rotational magnetic saliency in the stator. In contrast, by using (5.6), which is developed from the virtual work principle, the improper torque attribution is inherently eliminated while the influence of electric load and magnetic saturation is still fully included. Hence, the on-load cogging torque can still be obtained properly and shown in Fig. 5.9. It can be seen that the on-load cogging torque varies with the electric loading and is different from the open-circuit one. When  $\beta < 0^\circ$ , the magnetic saturation is heavier due to the flux enhancing and, hence, has higher influence. Therefore, the on-load cogging torque waveform is much different from the open-circuit one. When  $\beta > 0^\circ$ , the magnetic saturation is lighter due to the flux weakening and has less influence. Hence, the on-load cogging torque waveform is closer to the open-circuit one.

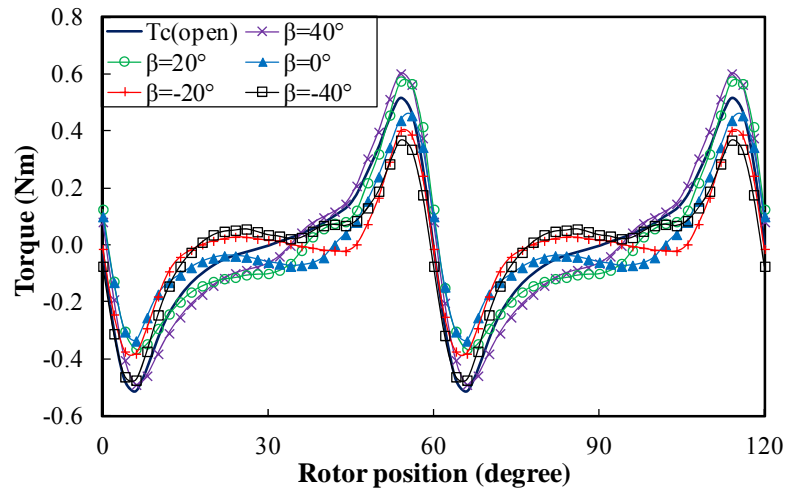


(a) Waveform

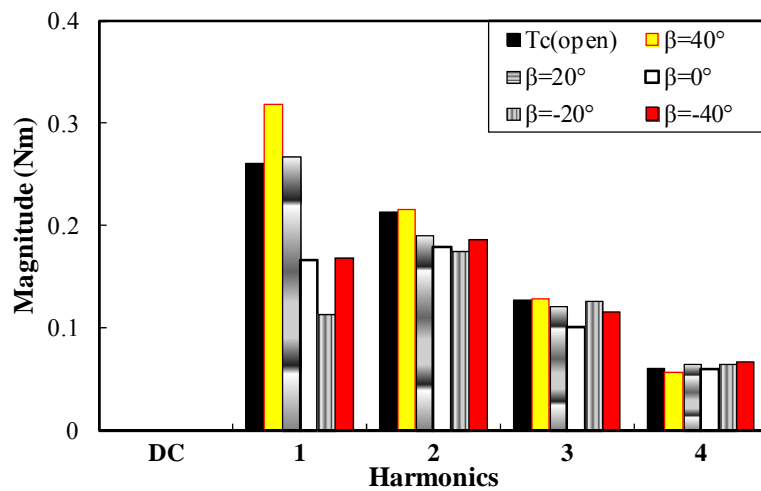


(b) Spectra

Fig. 5.8. Calculated torque results by (5.5), based on Maxwell stress tensor, when  $I_{ap} = 4.0A$ .



(a) Waveform



(b) Spectra

Fig. 5.9. Calculated torque results by (5.6), based on virtual work principle, when  $I_{ap} = 4.0A$ .

## **5.8 Summary**

The on-load cogging torque calculation in PM machines has been investigated in this chapter. A new on-load cogging torque calculation method has been proposed based on the virtual work principle in conjunction with the FP method to avoid the improprieties of the existing methods. For its implementation, an improved FP method, which makes the magnetic energy with on-load PM field only can be calculated according B-H curve, has also been developed. Based on the FE results, the new on-load cogging torque calculation method has been shown to be effective in both linear and nonlinear cases.

# CHAPTER 6 ANALYTICAL OPTIMISATION AND COMPARISON OF TORQUE DENSITIES BETWEEN ELECTRICALLY EXCITED AND PERMANENT MAGNET MACHINES

This chapter reports the simplified analytical optimisation and comparison of two torque densities, i.e., torque per volume ( $T/V$ ) and torque per weight ( $T/G$ ), between PM and EE machines for low speed applications when they have the same overall size and copper loss. Both machines are optimised analytically and individually. The optimal split ratio and flux density ratio are derived. The influence of pole number and machine size is investigated as well. The analytical models and analyses are verified by both FE analyses and experiments. It shows that PM machines can exhibit more than  $\sqrt{2}$  times torque densities of EE machines. For EE machines, there is an optimal pole number to maximize the torque densities and large volume applications are preferred. The comparison also shows that the optimal  $T/G$  designs have significantly higher split ratio than the optimal  $T/V$  designs to balance torque and weight.

## 6.1 Introduction

Electrically excited and permanent magnet machines are two most widely employed electrical machines in various applications, such as traction vehicles, renewable energies, and industrial automations. With recent significant increase in the price of rare-earth magnets, it becomes increasingly attractive to consider less or non-rare-earth magnet machines. EE machine is clearly one of potential replacement candidates.

Some comparative studies have been made between EE and PM machines. In [21], [24], [86], [87] the comparison is on the system performance for wind power applications. In [88], they are compared in terms of system mass and efficiency for the man-portable power system using the genetic algorithm (GA). In this paper, their torque densities will be quantitatively compared when they have the same overall size and copper loss. For fair comparison, it is necessary to optimise the machines first.

The optimisation of electric machines is always one of the most important topics and has been discussed intensively by analytical and FE analyses [89]-[119]. Compared with the FE methods, the analytical methods are more general and insightful.

Instead of the conventional output equation based on the airgap diameter, in [89], the output coefficient for synchronous machines was expressed for the first time as a function of

the outer diameter. In [90], several sizing equations for electrical machines were developed. It was shown that the output torque was significantly influenced by the split ratio and flux density ratio. The optimal split ratio was derived analytically while the influence of flux density ratio was investigated as well. However, the output torque coefficients in [89] and [90] have some limits. First, it is less meaningful when they are not a function of the machine volume  $D_o^2 L_{ef}$ . Second, the torque coefficients were developed assuming the given airgap flux density, which will be shown later in this chapter that it is inappropriate for EE machines. Third, the optimal quantities were derived by optimizing the stator only. However, the optimal quantities may be different when both stator and rotor are considered, especially for EE machines. Furthermore, the pole number was fixed in [90] but it is an important design parameter to be investigated.

The optimisation of PM machines has been investigated in-depth in [93]-[103]. In [94]-[97], the optimal split ratio of radial-field PM machines having internal rotor, parallel-side stator teeth, and full-pitch magnets in terms of torque per volume was obtained analytically. In [98], the optimal flux density ratio was further obtained analytically based on IPM machines. The optimisation of large PM synchronous generators having rectangular stator slots with or without considering the tangential stress constraint was discussed in [99]. In [100] and [101], the optimisation of PM machines having external rotor was investigated analytically. The modeling and optimisation of axial field PM machine was reported in [103] and [226] while for the radial-flux toroidally wound PM machines, it was reported in [227].

This chapter reports the simplified analytical optimisation and comparison of EE and PM machines in terms of two torque densities, torque per volume ( $T/V$ ) and torque per weight ( $T/G$ ), for low speed applications when they have the same machine size, copper loss and semi-closed rectangular slots and stator windings, which will be detailed in section 6.2. In order to study the influence of machine size, two sets of dimensions will be investigated. Based on the general torque equation in section 6.2, PM and EE machines are optimised individually in terms of  $T/V$  in sections 6.3 and 6.4, respectively. Be different from the investigation in [89] and [90], the airgap flux density in EE machines is not given but a variable, which links the rotor design to the torque and is going to be optimised as well. Based on the optimal designs, PM and EE machines are compared in terms of  $T/V$  for different machine sizes when the number of poles varies in section 6.5. In Section 6.6, PM and EE machines are optimised and compared in terms of  $T/G$  for different machine sizes and number of poles. Further comparison between the optimal  $T/V$  designs and the optimal  $T/G$

designs is given in Section 6.7. The analytical analyses are verified by both the FE analyses and the experiments. The FE verification is presented together with the analytical predictions of the optimal designs while the experimental verification is given in section 6.8.

## 6.2 General Torque Equation

For fair comparison, EE and PM machines have the same machine size and stator configuration, which is full-pitch distributed overlapping armature windings and rectangular semi-closed stator slots. Since the loss is dominated by copper loss in low speed applications, the comparison is based on that EE and PM machines have the same copper loss. For EE machines, the field windings have rectangular cross-sections as well, as illustrated in Fig. 6.1. The other parameters are detailed in Table 6-I. In order to study the influence of machine size, two sets of dimensions, D1 and D2 shown in Table 6-I, will be investigated and compared. The armature winding's packing factor is set as high as the field windings in the large machine, since both windings are usually pre-formed in large machines. The flux leakage coefficients in  $T/V$  designs or large machines are higher, which is due to the deeper slots.

The average EM torque when the machine is under the brushless AC operation with zero  $d$ -axis armature current control (hence unit internal power factor), and the airgap flux density distribution is rectangular as shown in Fig. 2.5(b), is given by:

$$T_{av} = 3\pi\alpha_p k_\phi L_{ef} D_\delta B_{\delta av} N_a I_a / (2\sqrt{2}) \quad (6.1)$$

$$k_\phi = \frac{\Phi_1}{\Phi_m} = \frac{8}{\alpha_p \pi^2} \sin\left(\frac{\alpha_p \pi}{2}\right) \quad (6.2)$$

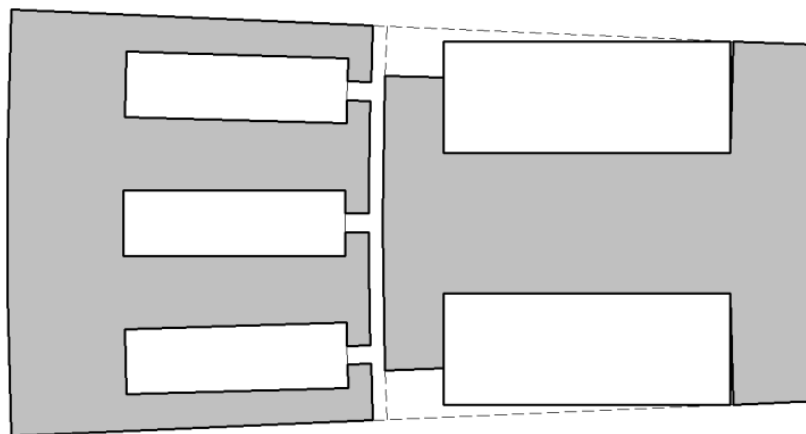


Fig. 6.1. Cross-section of EE machine.

Table 6-I Main parameters

Profile dimension set	D1	D2
Pole arc to pole pitch ratio $\alpha_p$	0.75	
Maximum $B$ in the laminations $B_m$	1.4T	
Conductor resistivity $\rho$	$1.724 \cdot 10^{-8} \Omega\text{m}$	
Pole shoe height of EE machines $h_{ps}$	$0.1\tau$	
Outer diameter $D_o$	420mm	2500mm
Active axial length $L_{ef}$	110mm	1100mm
Airgap length $\delta$	2mm	4mm
Total copper loss $p_{cu}$	300W	25kW
Armature winding packing factor $k_{pa}$	0.45	0.7
Field winding packing factor $k_{pf}$	0.7	0.7
Tooth tip height $h_o$	4mm	8mm
For $T/V$ designs		
Stator flux leakage coefficient $\sigma_s$	1.08	1.35
Rotor flux leakage coefficient $\sigma_r$	1.08	1.3
For $T/G$ designs		
Stator flux leakage coefficient $\sigma_s$	1.08	1.15
Rotor flux leakage coefficient $\sigma_r$	1.05	1.1

The relationship between the armature copper loss and  $N_a I_a$  accounting for the end-winding is given in (2.37).

The minimum stator tooth width, stator yoke thickness, and hence the total stator slot area can be obtained according to the geometric and magnetic relationships by

$$b_t = \frac{\sigma_s \alpha_p \gamma \pi D_o \lambda_\delta}{N_s} \quad (6.3)$$

$$h_{sc} = \frac{\sigma_s \alpha_p \gamma \pi D_o \lambda_\delta}{4p} \quad (6.4)$$

$$A_a = \frac{\pi D_o^2 \lambda_\delta}{2} \left(1 - \beta_s - \lambda_\delta - \frac{\pi \sigma_s \alpha_p \gamma \lambda_\delta}{2p}\right) (1 - \sigma_s \alpha_p \gamma) \quad (6.5)$$

$$\lambda_\delta = D_\delta / D_o \quad (6.6)$$

$$\gamma = B_{\delta av} / B_m \quad (6.7)$$

$$\beta_s = 2h_o / D_o \quad (6.8)$$

By eliminating  $N_a I_a$  and  $A_a$  in (6.1), the general torque equation, which is applicable for both PM and EE machines, can be obtained as

$$T_{av} = \frac{\pi D_o^2 B_m \alpha_p k_\phi L_{ef} \lambda_\delta \gamma}{8} \sqrt{\frac{\pi p_{cua} k_{pa} \lambda_\delta (1 - \sigma_s \alpha_p \gamma)}{\rho (L_{ef} + L_{aend})} \left(1 - \beta_s - \lambda_\delta - \frac{\pi \sigma_s \alpha_p \gamma \lambda_\delta}{2p}\right)} \quad (6.9)$$

It can be seen that the output torque is a function of  $\lambda_\delta$ ,  $\gamma$ , and  $2p$  when  $D_o$ ,  $L_{ef}$ , and  $p_{cua}$  are fixed. In the following sections, the optimal  $\lambda_\delta$ ,  $\gamma$ , and maximum torque density will be derived analytically while the influence of  $2p$  and machine size is investigated as well.

For most applications, a higher torque is desired when the machine size is fixed. Therefore, PM and EE machines are optimised and compared in terms of maximum torque per volume ( $T/V$ ) first.

### 6.3 Maximum Torque Per Volume of PM Machines

For PM machines, the open-circuit field is established by PMs. They are excitation copper loss free. The equivalent airgap length, which is the sum of the mechanical airgap and the PM thickness, is much larger, since the permeability of PM is close to the air. Therefore, the MMF drops in the iron parts is negligible and can be easily compensated by slightly increasing the magnet thickness, although it is also important to consider the cost. By using SPM or IPM configurations without influencing the airgap diameter, they are able to achieve a wider range of  $B_{\delta av}$  and  $\gamma$ . Therefore, for PM machines,  $\gamma$  and  $\lambda_\delta$  are two independent variables and (6.9) is sufficient for the torque calculation and optimisation.

Based on (6.9), the torque variation with the split ratio and flux density ratio is obtained and shown in Fig. 6.2. It can be seen that there is an optimal combination of the split ratio and flux density ratio to maximize the torque.

When  $\gamma$  is given, the optimal split ratio  $\lambda_{\delta op}$  to maximize the torque is derived by letting  $\partial T_{av} / \partial \lambda_\delta = 0$  as

$$\lambda_{\delta op} = \frac{3}{4} \frac{1 - \beta_s}{[1 + \pi \sigma_s \alpha_p \gamma / (2p)]} \quad (6.10)$$

Since  $\beta_s$ ,  $\sigma_s$ , and  $\alpha_p$  are constant,  $\lambda_{\delta op}$  simply depends on  $\gamma$  and  $2p$ . As shown in Fig. 6.3, when either  $\gamma$  is higher or  $2p$  is lower,  $\lambda_{\delta op}$  is lower, since the stator yoke is thicker. However, when  $2p$  is higher, the influence of  $\gamma$  on  $\lambda_{\delta op}$  is less.

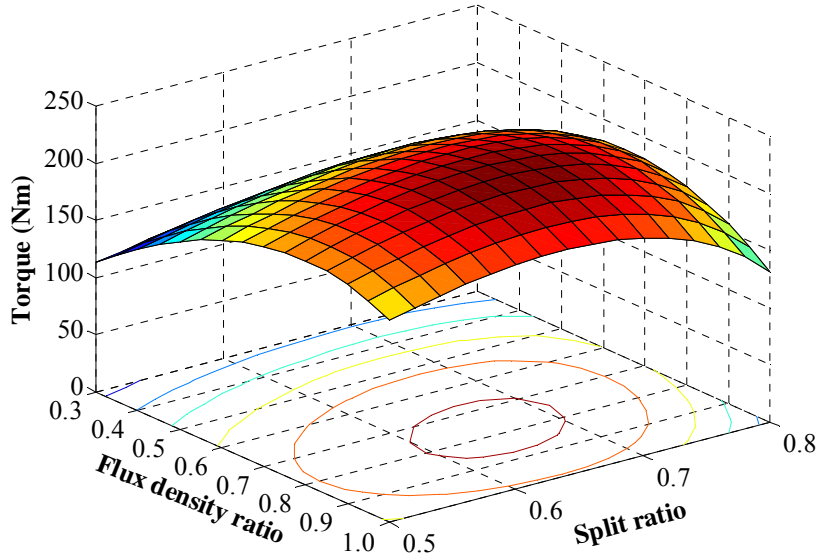


Fig. 6.2. Torque variation of PM machines with split ratio and flux density ratio when  $2p = 16$  and size is D1.

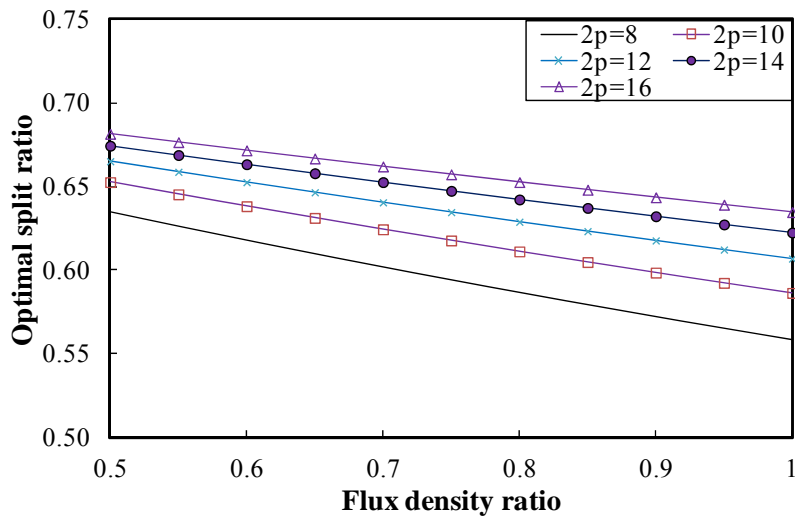


Fig. 6.3.  $\lambda_{\delta op}$  variations of PM machines with flux density ratio and number of poles when size is D1.

In the similar way, by letting  $\partial T_{av} / \partial \gamma = 0$ , the optimal flux density ratio  $\gamma_{op}$  for maximum torque when  $\lambda_{\delta}$  is given can be obtained as

$$\gamma_{op} = \frac{1}{8\sigma_s\alpha_p\pi\lambda_\delta} \left\{ \begin{array}{l} 3[2p(1 - \beta_s - \lambda_\delta) + \pi\lambda_\delta] - \\ \sqrt{9[2p(1 - \beta_s - \lambda_\delta) + \pi\lambda_\delta]^2 - 64p\pi\lambda_\delta(1 - \beta_s - \lambda_\delta)} \end{array} \right\} \quad (6.11)$$

The influence of  $\lambda_\delta$  and  $2p$  on  $\gamma_{op}$  is illustrated in Fig. 6.4. Either lower  $2p$  or higher  $\lambda_\delta$  will result in larger  $\gamma_{op}$ , since the stator yoke is thicker. It also shows that for the optimal designs, whose  $\lambda_\delta < 0.75$ , their  $\gamma_{op}$  is high and varies modestly.

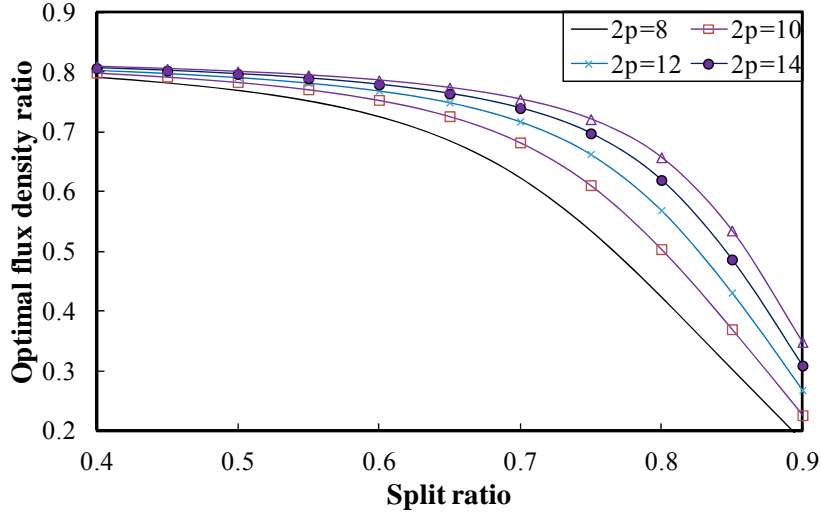


Fig. 6.4.  $\gamma_{op}$  variations of PM machines with split ratio when size is  $D1$ .

The global optimal designs can be obtained by letting both  $\partial T_{av}/\partial\lambda_\delta=0$  and  $\partial T_{av}/\partial\gamma=0$ :

$$\gamma_{op} = \frac{4p}{\alpha_p(6p + \pi)} \quad (6.12)$$

$$\lambda_{\delta op} = \frac{(1 - \beta_s)(6p + \pi)}{4(2p + \pi)} \quad (6.13)$$

The performance of global optimal PM designs is shown in Figs. 5.8-5.13. It can be seen that the optimal split ratio, flux density ratio and hence torque increase when the number of poles is higher, since the stator yoke is thinner.

Due to the assumption of constant flux leakage coefficients, which is for the sake of simplicity and understanding, the predicted torque increases monotonously with the pole number. Actually, when the pole number is higher, the inter-pole leakage increases and the stator slots are deeper and narrower. Therefore, the flux leakages and hence flux leakage constants will increase. Consequently, the torque will be lower. However, by updating the

leakage constants in Table 6-I, the analytical models are still applicable.

## 6.4 Maximum Torque per Volume of EE Machines

### 6.4.1 Torque Equation

For EE machines, being different from PM machines, the open-circuit airgap flux density is produced by the field windings. Therefore, EE machines have both armature copper loss and excitation copper loss. With the armature copper given in (2.37), the relationship between the excitation copper loss and excitation MMF is given by

$$p_{cuf} = 4(N_f I_f)^2 \rho (L_{ef} + L_{fend}) / (k_{pf} A_f) \quad (6.14)$$

It should be noticed that  $N_f I_f$  is proportional to  $2p$  when the airgap flux density produced by the field windings remains the same.

In addition to the loss, the field windings usually require more space than the PMs as well. Assuming that the flux density ratio and split ratio are given, the rotor dimensions and field winding area per machine can be obtained based on the geometric and magnetic relationships as

$$b_p = \sigma_r \alpha_p \gamma \pi D_o \lambda_\delta / (2p) \quad (6.15)$$

$$A_f = \pi (D_o \lambda_\delta)^2 (\lambda_r - \sigma_r \alpha_p \gamma) (1 - \beta_r - \lambda_r) / 2 \quad (6.16)$$

$$\beta_r = 2(\delta + h_{ps}) / (D_o \lambda_\delta) \quad (6.17)$$

$$\lambda_r = D_{ry} / D_\delta \quad (6.18)$$

It can be seen from (6.14) and (6.16) that there is a relationship between the field winding area and airgap flux density: magnetically, higher field winding area results in higher airgap flux density while geometrically higher airgap flux density results in lower field winding area. Being different from PM machines, it also shows that the field winding area and hence the airgap flux density is a function of the split ratio. Therefore, for EE machines, the flux density ratio is not an independent variable. The range of flux density ratio depends on the split ratio.

Furthermore, another difference between PM and EE machines is the influence of MMF drops in the stator and rotor. As mentioned foregoing, for PM machines, the influence of the MMF drops in the stator and rotor is negligible. However, for EE machines, the influence of

the MMF drops in the stator and rotor is much higher, since the equivalent airgap is simply the mechanical airgap and much smaller than the one of PM machines. Meanwhile, the field winding area is proportional to the square of excitation MMF as shown in (6.14). Hence, the MMF drops in the stator and rotor will result in a significant increase of the field winding area and, hence, affect the machine design. Therefore, for EE machines, it is important and necessary to consider the MMF drops in the stator and rotor.

In the actual EE machines, the MMF drops in stator and rotor are complicated. However, a simplified method is suggested here to approximate the influence by using an average relative permeability  $\mu$  and an equivalent airgap length  $\delta'$

$$\delta' = \delta + (1 - \lambda_\delta \lambda_r) D_o / \mu \quad (6.19)$$

Based on (5.14), the expression of  $B_{\delta av}$  can be obtained magnetically by

$$B_{\delta av} = \frac{\mu_0 N_f I_f}{2p\delta'} = \frac{\mu_0}{2p\delta'} \sqrt{\frac{p_{cu f} A_f k_{pf}}{4\rho(L_{ef} + L_{fend})}} \quad (6.20)$$

By eliminating  $B_{\delta av}$  and  $N_a I_a$  in (6.1), the torque equation of EE machines is given as:

$$T_{av} = \frac{\pi \alpha_p k_\phi D_o \lambda_\delta}{16\sqrt{2} \rho p \delta'} \sqrt{\frac{k_{pa} k_{pf} L_{ef}^2 p_{cua} A_a p_{cu f} A_f}{(L_{ef} + L_{aend})(L_{ef} + L_{fend})}} \quad (6.21)$$

## 6.4.2 Optimisation

In order to maximize the torque of EE machines, the special optimisation procedure is developed as follows to solve the challenges mentioned foregoing one by one.

As can be seen from (6.21), the torque of EE machines is the function of both the armature and excitation copper losses. The portions of these two copper losses should be optimised first to maximize the torque when the total copper loss  $p_{cu}$  is fixed due to the efficient and cooling requirements.

When the total copper loss is given, the output torque is rewritten as

$$T_{av} = \frac{\pi \alpha_p k_\phi D_o \lambda_\delta}{16\sqrt{2} \rho p \delta'} \sqrt{\frac{k_{pa} k_{pf} L_{ef}^2 p_{cua} A_a (p_{cu} - p_{cua}) A_f}{(L_{ef} + L_{aend})(L_{ef} + L_{fend})}} \quad (6.22)$$

Therefore, the optimal combination of the two copper losses to achieve the maximum torque is

$$p_{cua} = p_{cuf} = p_{cu}/2 \quad (6.23)$$

Electromagnetically, it can be explained that the armature field and rotor field contribute equally to the torque. Therefore, when the excitation copper loss equals the armature copper loss, the output torque is the maximum.

In reality, it should be fully aware that the loss in the rotor and the loss in the stator have significantly different thermal impacts, since the cooling conditions in the rotor and stator are different.

Compared EE machines with PM machines, since PM machines are excitation copper loss free, PM machines can achieve much higher torque, at least  $\sqrt{2}$  times, than EE machines when they have the same size and total copper loss.

However, in order to emphasize the differences due to the rotor, all maximum torque results given in this chapter are obtained when they have the same armature copper loss, which means the total copper loss of EE machines is twice of the one of PM machines.

The second step is to solve the relationship between the field winding area and airgap flux density to obtain the maximum achievable flux density ratio  $\gamma_m$ .

In order to achieve higher  $\gamma$ , the EE rotor needs to be optimised first. It can be seen from (6.16) that  $A_f$  depends on  $\lambda_r$  when  $\gamma$  and  $\lambda_\delta$  are given. As shown in Fig. 6.5, there is an optimal value of rotor split ratio  $\lambda_{rop}$  to maximize  $A_f$ . For the optimal design, which can provide  $\gamma_m$ , the rotor split ratio is the optimal while (6.14), (6.16), and (6.20) are met as well. Therefore, in order to derive  $\gamma_m$ ,  $\lambda_{rop}$  should be obtained first.

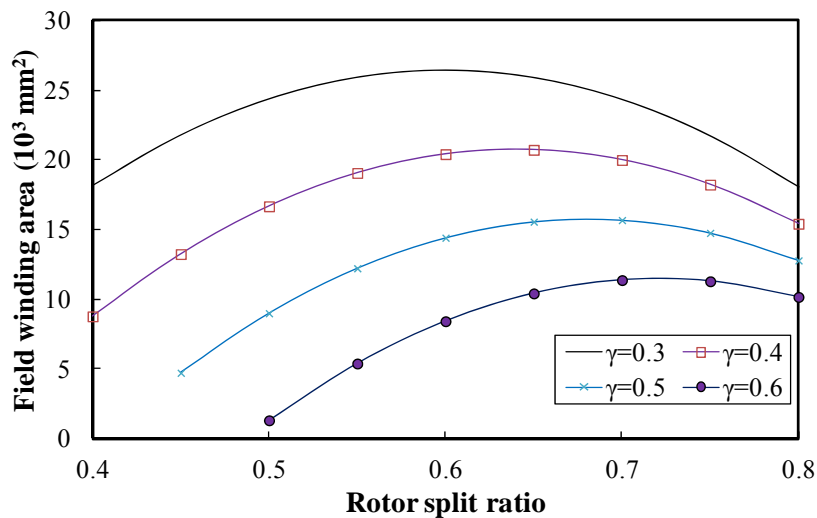


Fig. 6.5.  $A_f$  Variation with  $\lambda_r$  of EE machines when  $\lambda_\delta=0.75$ ,  $2p = 20$ , and size is  $DI$ .

By letting  $\partial A_f / \partial \lambda_r = 0$ , the optimal rotor split ratio  $\lambda_{rop}$  and hence maximum field winding area  $A_{fm}$  can be obtained as

$$\lambda_{rop} = (1 - \beta_r + \sigma_r \alpha_p \gamma) / 2 \quad (6.24)$$

$$A_{fm} = \pi D_\delta^2 (1 - \beta_r - \sigma_r \alpha_p \gamma) / 8 \quad (6.25)$$

Based on the maximized field winding area given in (6.25), the maximum achievable flux density can be obtained when (6.14) and (6.20) are met as

$$\gamma_m = \frac{(1 - \beta_r)}{k_3 + \sigma_r \alpha_p} \quad (6.26)$$

$$k_3 = \frac{2p\delta' B_m}{\mu_0 D_o \lambda_\delta} \sqrt{\frac{32\rho(L_{ef} + L_{fend})}{\pi p_{cu} k_{pf}}} \quad (6.27)$$

For the optimal  $T/V$  designs, the machine space is most effectively utilized to achieve higher torque. Therefore, in this case, the equivalent airgap length  $\delta'$  can be approximated as

$$\delta' \approx \begin{cases} \delta + (1 - 0.4)D_o/\mu & \text{(small machines)} \\ \delta + (1 - 0.5)D_o/\mu & \text{(large machines)} \end{cases} \quad (6.28)$$

It can be seen from (6.26) that, in EE machines, the maximum achievable flux density ratio is a function of the split ratio and number of poles. The variation of maximum achievable flux density ratio with the split ratio and number of poles is shown in Fig. 6.6. It shows that  $\gamma_m$  increases when  $\lambda_\delta$  is larger, since more rotor space is available. When  $2p$  increases,  $\gamma_m$  decreases, since  $B_{\delta av}$  is inverse proportional to  $2p$  as shown in (6.20). Therefore, for this purpose, lower  $2p$  is preferred. However, on the other hand, lower  $2p$  results in longer end windings, thicker yokes, and, consequently, lower MMFs and torque. Therefore, for EE machines, it can be predicted that there will be an optimal  $2p$  to maximize the torque.

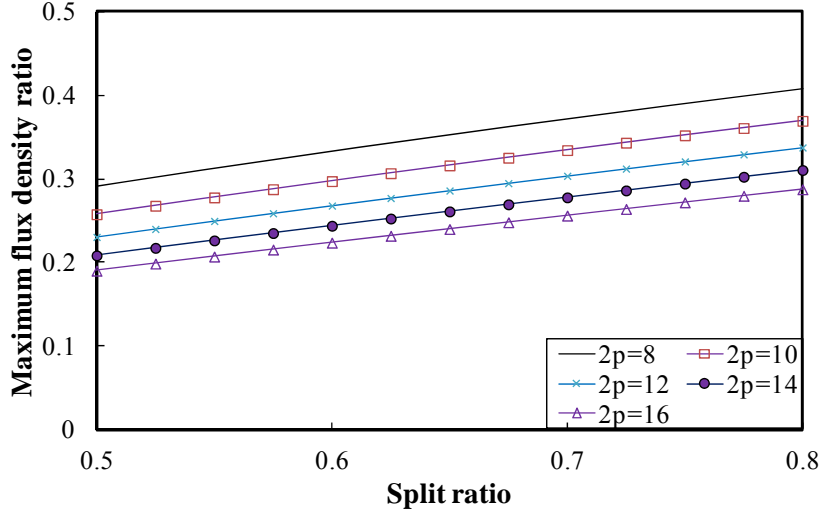


Fig. 6.6.  $\gamma_m$  variation with split ratio and number of poles of EE machines when size is  $DI$ .

By so far, the maximum achievable flux density ratio in EE machines has been obtained. In order to obtain the maximum torque, another further step is needed to select the optimal flux density ratio for EE machines based on (6.11) and (6.26). There are two cases.

Case 1: the maximum achievable flux density ratio given by (6.26) is higher than the one given by (6.11), which means that the optimal flux density ratio of (6.11) can be achieved. Therefore, the optimal flux density ratio is the one given by (6.11), which is the same as PM machines, and the torque of EE machine can be calculated by (6.9).

Case 2: the maximum achievable flux density ratio given by (6.26) is lower than the one given by (6.11), which means that the optimal flux density ratio of (6.11) cannot be achieved. Hence, the maximum torque is calculated according to (6.26) and is lower than the torque predicted by (6.9) and (6.11).

Based on (6.21), (6.23), and (6.26), the torque expression of the Case 2 can be obtained as

$$T_{av}^2 = \frac{\pi^3 (k_\phi D_o^2 B_m L_{ef})^2 p_{cua} k_{pa} \lambda_\delta^3 \left[ \frac{(1 - \beta_r) \lambda_\delta}{k_4 + k_\sigma \lambda_\delta} \right]^2 \left[ 1 - \frac{(1 - \beta_r) \lambda_\delta}{k_4 + k_\sigma \lambda_\delta} \right] \left[ 1 - \beta_s - \lambda_\delta - \frac{\pi (1 - \beta_r) \lambda_\delta^2}{2p (b + k_\sigma \lambda_\delta)} \right]}{64 \rho (L_{ef} + L_{aend})} \quad (6.29)$$

$$k_4 = \frac{k_3 \lambda_\delta}{\sigma_s \alpha_p} = \frac{2p \delta' B_m}{\sigma_s \mu_0 D_o \alpha_p} \sqrt{\frac{32 \rho (L_{ef} + L_{fend})}{\pi p_{cuf} k_{pf}}} \quad (6.30)$$

$$k_\sigma = \sigma_r / \sigma_s \quad (6.31)$$

Since  $k_\sigma \approx 1$ ,  $\beta_r \ll 1$ , and  $\lambda_\delta < 1$ , hence,  $(k_\sigma - 1 + \beta_r) \lambda_\delta \approx 0$ . Therefore, (6.29) can be simplified as:

$$T_{av}^2 \propto \frac{\lambda_\delta^5}{(b + k_\sigma \lambda_\delta)^3} \left[ 1 - \beta_s - \lambda_\delta - \frac{\pi (1 - \beta_r) \lambda_\delta^2}{2p (b + k_\sigma \lambda_\delta)} \right] \quad (6.32)$$

Based on the foregoing models, the variation of output torque in EE machines with the split ratio can be obtained and shown in Fig. 6.7. When the split ratio increases, although the higher flux density ratio can be achieved, the stator slot area and, hence, armature MMF will be reduced. Therefore, there is an optimal split ratio to maximize the torque of EE machines as well. Since the maximum achievable flux density ratio given by (6.26) is lower than the one given by (6.11), which will be shown later, the optimal split ratio should be obtained from (6.29). Mathematically, three optimal values can be derived from (6.32). However, only one of them is the actual optimal split ratio, which is a real number and between 0.5-1.

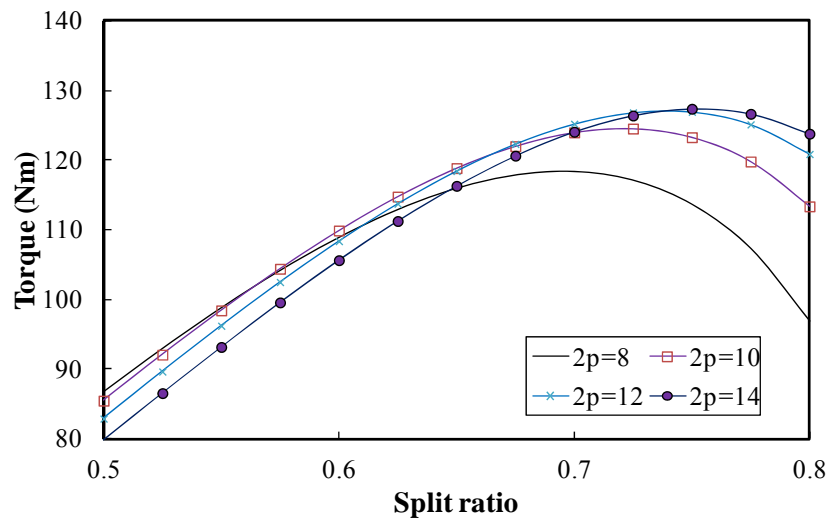


Fig. 6.7. Torque variation with split ratio and pole number of EE machines when size is  $DI$ .

## 6.5 Comparison on Maximum Torque per Volume

With both machines being optimised in terms of  $T/V$  individually, the performance of EE and PM designs are compared in Figs. 6.8-6.13 when they have the same armature copper loss.

It shows that for both machines, when  $2p$  increases,  $\lambda_{\delta op}$  increases, since the stator yoke is thinner. However, EE machines have higher  $\lambda_{\delta op}$  due to that their  $\gamma$  is lower. When  $2p$  increases,  $\gamma$  of EE machines decreases while PM machines can maintain  $\gamma_{op}$ . Consequently,

EE machines have lower torque even when they have the same armature copper loss as PM machines. Therefore, when EE and PM machines have the same total copper losses, the armature copper loss of PM machine is doubled and, hence, their torque can be increased by  $\sqrt{2}$  times. In other words, PM machines can exhibit higher torque, at least  $\sqrt{2}$  times, than EE machines when they have the same total copper loss.

It also shows that the pole number influences PM and EE machines in significantly different ways. For PM machines, their torque increases monotonically with  $2p$  when the flux leakage is assumed to be constant. However, for EE machines, the torque increases first and then decreases. There is an optimal  $2p$  for EE machines to maximize torque. It is due to the compromise between the influence of yokes, end windings, and airgap flux density.

Compared the torque difference between EE and PM machines having different machine size, it shows that the differences between EE and PM machines is much less when the size is  $D2$ . It is due to that, for larger machines, the electric load is higher. EE machines are then able to achieve higher maximum airgap flux density and, hence, the torque difference between EE and PM machines is less. Therefore, EE machines prefer large volume applications.

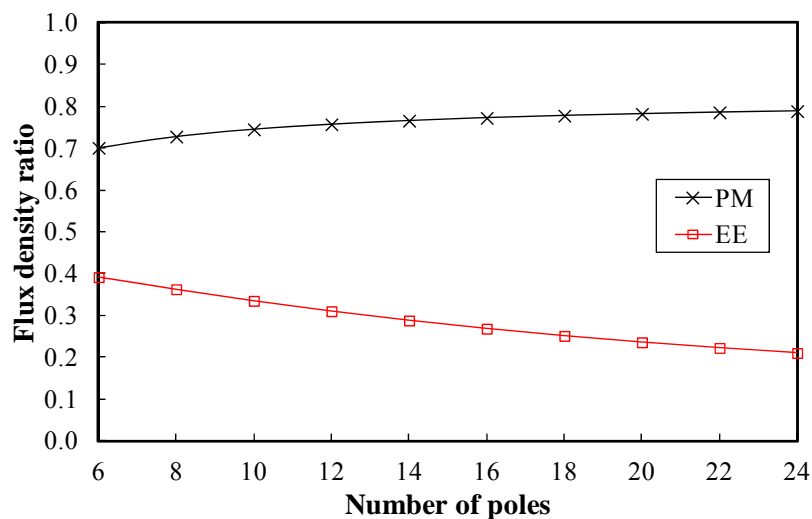


Fig. 6.8. Variation of  $\gamma$  with  $2p$  in  $D1$  for max.  $T/V$ .

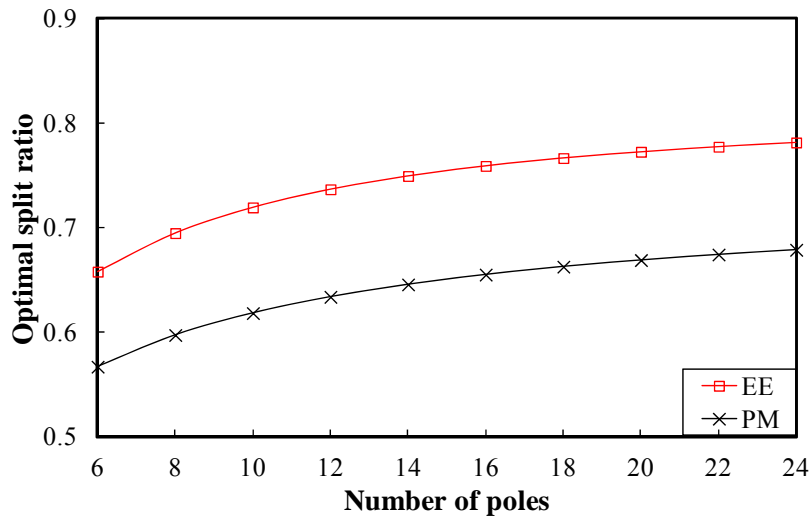


Fig. 6.9. Variation of  $\lambda_{\delta op}$  with  $2p$  in  $D1$  for max.  $T/V$ .

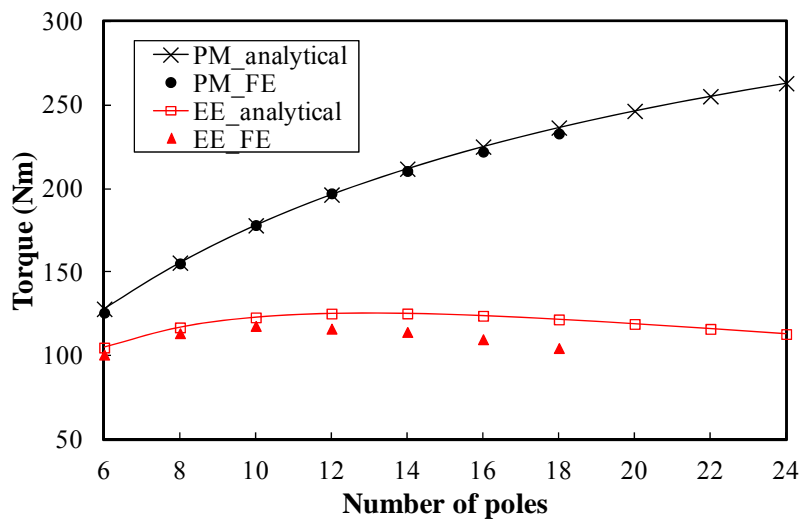


Fig. 6.10. Variation of torque with  $2p$  in  $D1$  for max.  $T/V$ .

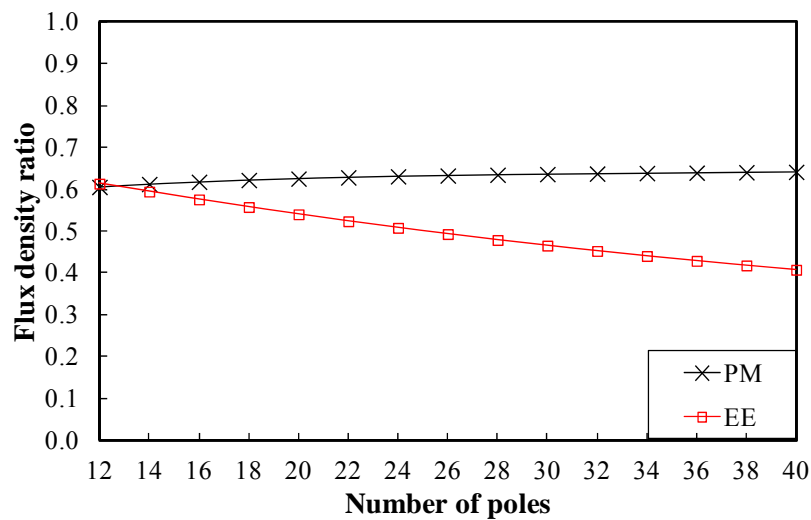


Fig. 6.11. Variation of  $\gamma$  with  $2p$  in  $D2$  for max.  $T/V$ .

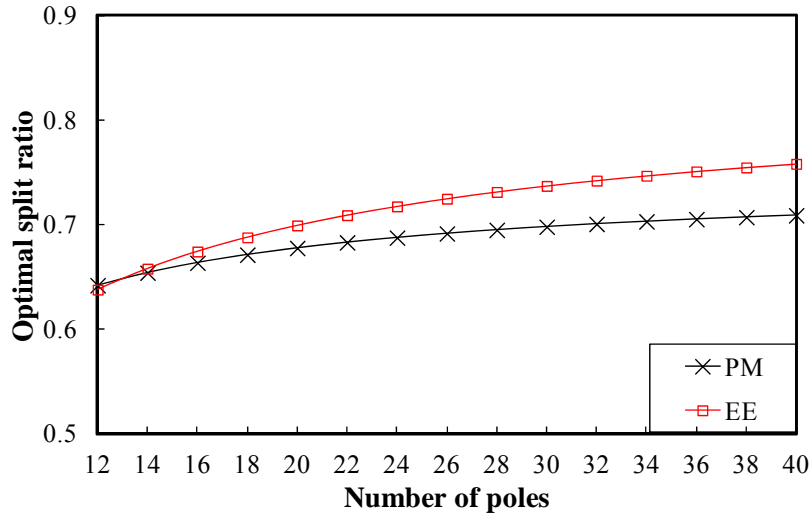


Fig. 6.12. Variation of  $\lambda_{\delta op}$  with  $2p$  in  $D2$  for max.  $T/V$ .

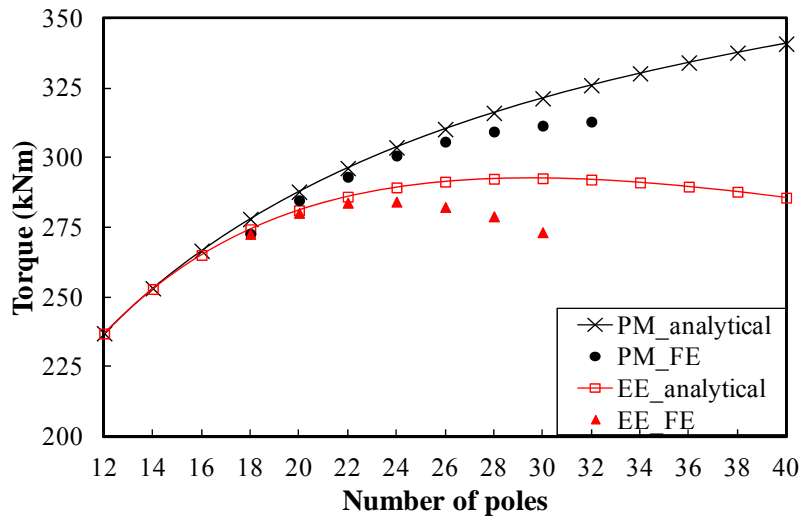


Fig. 6.13. Variation of torque with  $2p$  in  $D2$  for max.  $T/V$ .

## 6.6 Optimisation of Maximum Torque per Weight

The foregoing optimisation is aimed for maximization of  $T/V$ . As can be seen foregoing, the higher torque results in heavier machines, although the machine volume is fixed. However, for some applications, such as wind power generation, they prefer higher torque per weight ( $T/G$ ), since the mass on the top influences system performance significantly. Therefore, it is also important to discuss the optimisation in terms of  $T/G$ .

### 6.6.1 Analytical Model

The torque expression (6.9) is adequate for the investigation, since  $T/G$  is meaningless when the EE rotor is unable to provide required  $B_{\delta av}$ . The torque per weight is calculated as

the ratio between average output torque of the weight of active materials, i.e., copper, PM, stator core, and rotor core.

### 6.6.2 Optimisation

According to (6.9), the relationship between the torque and weight can be given simply as

$$\frac{T_{av}}{G} \propto \frac{\lambda_{\delta} \sqrt{A_a}}{G_a + G_{sc} + G_r} = \frac{\lambda_{\delta}}{k_{aG} \sqrt{A_a} + (G_{sc} + G_r) / \sqrt{A_a}} \quad (6.33)$$

As will be shown later, the variation of  $\lambda_{\delta}$  is modest and hence assumed as constant. Therefore, the simplified design principle of maximum torque per weight can be obtained by letting  $\partial(T_{av}/G)/\partial A_a=0$  as:

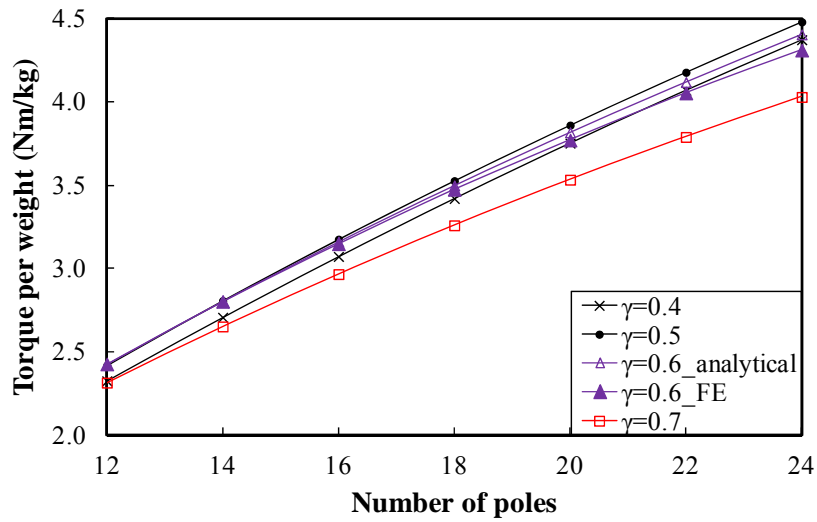
$$G_{aop} = k_{aG} A_{aop} = (G_{sc} + G_r) \quad (6.34)$$

In other words,  $T/G$  peaks when the armature winding weight equals with the total weight of other parts.

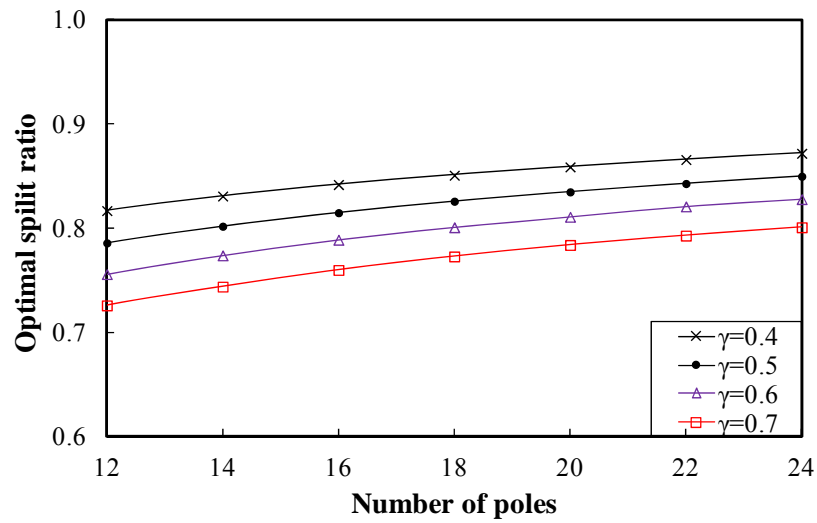
### 6.6.3 Results and Comparison

The optima of the maximum  $T/G$  PM machines are shown in Fig. 6.14.  $T/G$  and  $\lambda_{\delta op}$  increase when the pole number is higher, since the yokes are thinner. When  $\gamma$  is higher, the rotor and stator laminations are heavier. It needs more armature winding area to balance the weight. Hence,  $\lambda_{\delta op}$  is lower.  $T/G$  peaks when  $\gamma=0.5$ , since the further increase of  $\gamma$  results in much thicker magnets and, hence, lower  $T/G$ .

The optima of the maximum  $T/G$  EE machines are shown in Fig. 6.15, which are significantly different from PM machines. For EE machines, when the number of poles increases, their yokes and end windings decrease while the field winding area increases.  $G_{sc} + G_r$  decreases first and then increases. Hence,  $T/G$  increases first and then decreases. There will be an optimal pole number to maximize  $T/G$ . When the pole number is low,  $\lambda_{\delta op}$  increases modestly. However, when the pole number increases further,  $\lambda_{\delta op}$  is forced to increase sharply, since the field windings require significantly more space. Consequently,  $T/G$  decreases rapidly. When  $\gamma$  is higher, the sharp increase of  $\lambda_{\delta op}$  happens at lower pole number. The higher  $\gamma$  also results in lower maximum  $T/G$ , since the rotor is heavier.

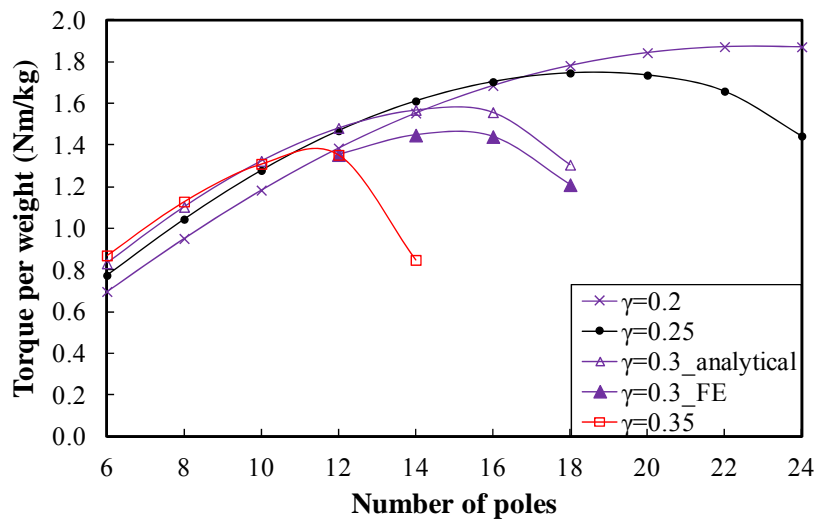


(a) Torque per weight  $T/G$

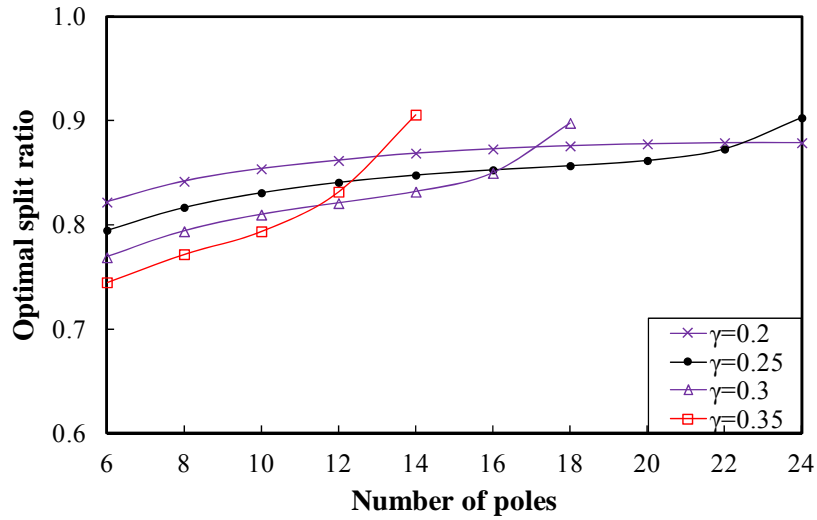


(b) Optimal split ratio

Fig. 6.14. Optimal  $T/G$  designs of PM machines when size is  $D1$ .



(a) Torque per weight  $T/G$



(b) Optimal split ratio

Fig. 6.15. Optimal  $T/G$  designs of EE machines when size is  $D1$ .

The optimal  $T/G$  designs of PM and EE machines are compared in Figs. 6.16 and 6.17. It shows that PM machines have higher  $T/G$  than EE machines even when their armature copper losses are the same. Therefore, when they have the same total copper loss, PM machines are able to exhibit  $\sqrt{2}$  times torque per weight than EE machines. It can also be seen that the differences between PM and EE machines in  $D2$  are less than the ones in  $D1$ , which suggests again that EE machines prefer large volume applications.

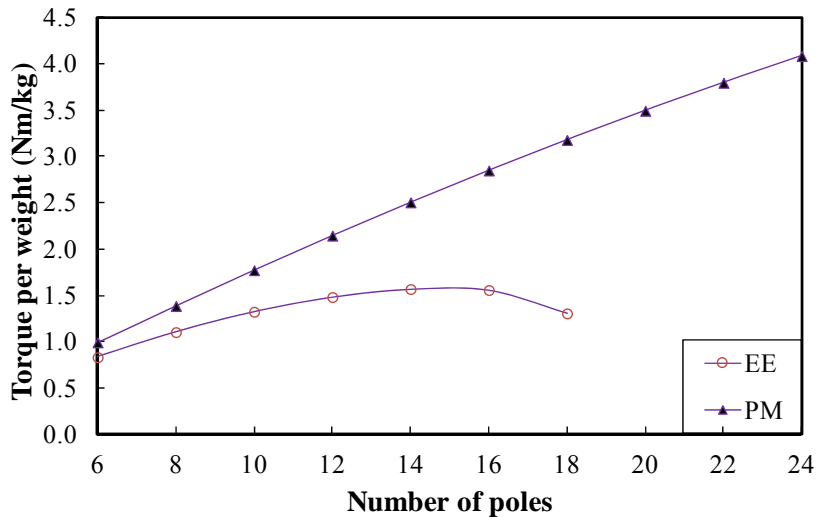


Fig. 6.16. Comparison of optimal  $T/G$  designs when  $\gamma = 0.3$  and size is  $D1$ .

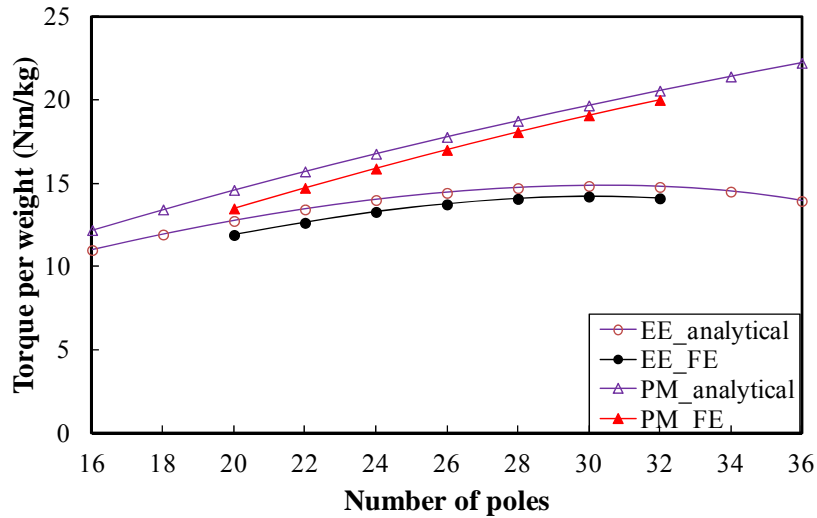


Fig. 6.17. Comparison of optimal  $T/G$  designs when  $\gamma=0.6$  and size is D2.

### 6.7 Max. $T/V$ versus Max. $T/G$

The optimal designs in terms of two torque densities,  $T/V$  and  $T/G$ , are compared in Fig. 6.18 and Table 6-II. It can be seen that the different criteria have led to the entirely different design principles and outcomes.

For the maximum  $T/V$  designs, they make most use of the space to achieve higher torque, while for the maximum  $T/G$  designs, they are the optimal balances between the torque and weight. The most remarkable difference is that  $\lambda_{\delta op}$  for the maximum  $T/G$  is more than 20% higher than the one for the maximum  $T/V$ , as illustrated in Fig. 6.18.

By way of example, four designs are detailed and compared in Table 6-II and Fig. 6.19. the torques of  $T/V$  designs are 20% and 16% higher than the  $T/G$  designs for PM and EE machines, respectively, while the  $T/V$  designs are 77% and 74% heavier for PM and EE machines, respectively. In total, the  $T/G$  designs of PM and EE machines exhibit 47% and 45% higher torque per weight, respectively.

It also suggests that the  $T/V$  designs are heavier and more expensive than the  $T/G$  designs. Although the  $T/V$  designs exhibit higher torque, their torque per weight and torque per cost are significantly lower than the  $T/G$  designs. Therefore, for the weight- and cost-sensitive applications, such as wind power generation, the  $T/G$  designs are more suitable. Furthermore, it indicates that the power factors of  $T/V$  designs are lower than  $T/G$  designs, since the slot leakage inductance increases significantly due to the deeper slots. This makes  $T/G$  designs even more promising than  $T/V$  designs.

Furthermore, higher flux density ratio is demanded for the  $T/V$  designs than the  $T/G$

designs. As shown in Fig. 6.14, PM machines have maximum  $T/G$  when  $\gamma = 0.5$ , which is lower than  $\gamma_{op}$  for  $T/V$  designs given in (6.13), Figs. 6.8, and 6.11. For EE machines, it can be seen from Fig. 6.15 that their optimal flux density ratio for  $T/G$  designs is even lower.

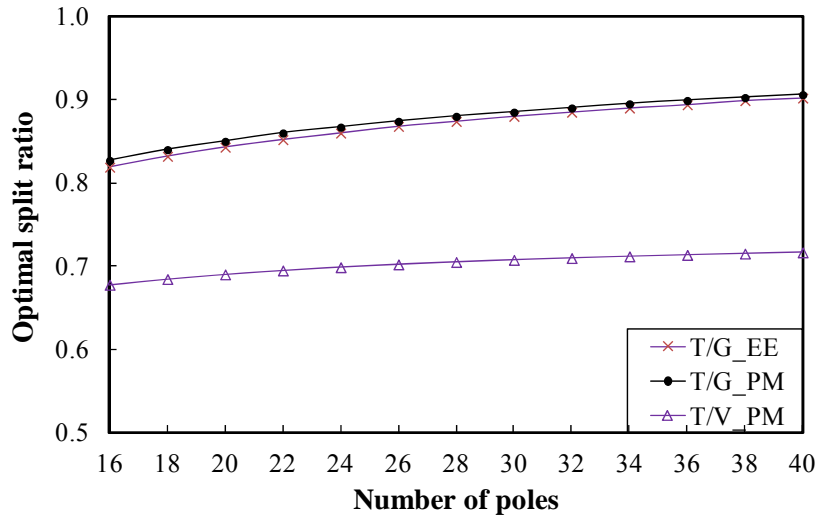


Fig. 6.18. Comparison of optimal split ratios for  $T/V$  and  $T/G$  designs when  $\gamma = 0.5$  and size is  $D2$ .

Table 6-II Comparison of four designs with same armature copper loss)

Design	PM_T/V	PM_T/G	EE_T/V	EE_T/G
Machine size	$D2$			
Flux density ratio	0.5			
Number of poles	24			
Torque (kNm)	288.30	239.05	288.30	247.15
Split ratio	0.698	0.867	0.698	0.860
Total weight (Ton)	25.22	14.19	29.33	16.82
$T/G$ (Nm/kg)	11.42	16.84	9.82	14.68
Total cost (k€)	106.77	57.10	111.27	57.54
T/cost (Nm/€)	2.70	4.18	2.59	4.29
Power factor	0.88	0.96	0.87	0.92
Material price (€/kg)	Copper: 8.5, PM: 40, Lamination: 1.25			

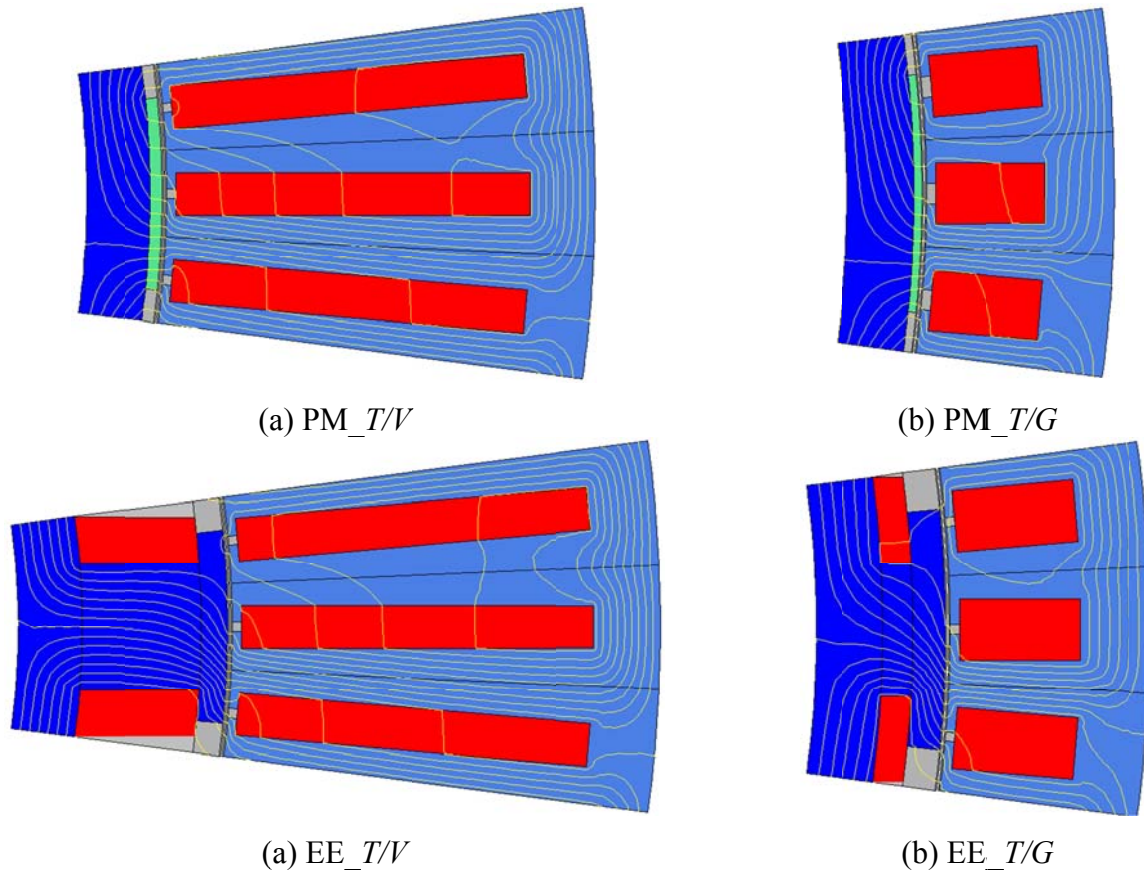


Fig. 6.19. Cross-sections of four designs in Table 6-II.

## 6.8 FE and Experimental Verifications

The analytical models and analyses are verified by both FE analyses and experiments.

The FE verification is carried out by 2-D non-linear analyses using the commercial FE software OPERA. As can be seen from Figs. 6.10, 6.13, 6.14, and 6.17, the analytical and FE predicted torques agree well.

The experimental verification is carried out on a smaller scale EE prototype machine, which is optimised with the conditions listed in Table 6-III. The variation of average torque with the split ratio, which is shown in Fig. 6.20 and validated by FE results, is obtained based on the analytical model in section 6.4.

Table 6-III Summary of main parameters of prototype machine

Outer diameter $D_o$	100mm
Active axial length $L_{ef}$	50mm
Total copper loss $p_{cu}$	50W

Pole arc to pole pitch ratio $\alpha_p$	0.75
Maximum $B$ in the laminations $B_m$	1.4T
Pole shoe height of EE machines $h_{ps}$	$0.075\tau$
Airgap length $\delta$	0.5mm
Armature winding packing factor $k_{pa}$	0.35
Field winding packing factor $k_{pf}$	0.6
Tooth tip height $h_o$	2mm
Stator flux leakage coefficient $\sigma_s$	1.05
Rotor flux leakage coefficient $\sigma_r$	1.02

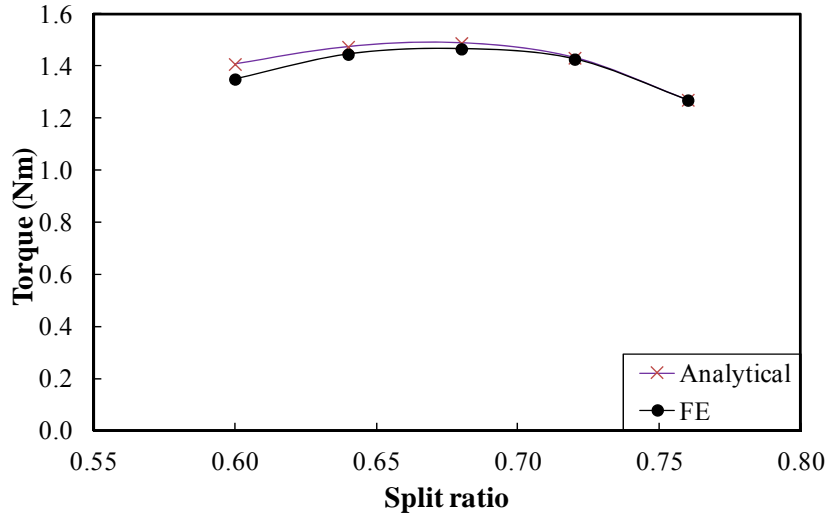


Fig. 6.20. Average torque variation with split ratio with conditions listed in Table 6-III.

Based on the optimal design, whose split ratio is 0.68, the EE prototype machine is made and shown in Fig. 6.21. When the machine is on full load, the armature phase current is 3.18A rms and the field current is 3.57A. The FE and measured open-circuit back EMF and cogging torque waveforms are shown in Figs. 6.22 and 6.23, respectively. Ideally, the full-load torque waveform, which is shown in Fig. 6.24, should be measured. However, a three-phase controller is required to generate the phase currents according to the rotor position. Instead, the torque waveforms when the armature and field currents are fixed and the stator is at different positions are measured based on the method developed in [228] and shown in Fig. 6.25. The torque waveforms are far away from sinusoidal, which is due to the high torque

ripple as shown in Fig. 6.24. In addition, the peak torques with different field and armature currents are measured and shown in Fig. 6.26. It can be seen in Figs. 6.22, 6.23, 6.25, and 6.26 that the FE and measured results at different loads agree well.



Fig. 6.21. Stator and rotor of EE prototype machine..

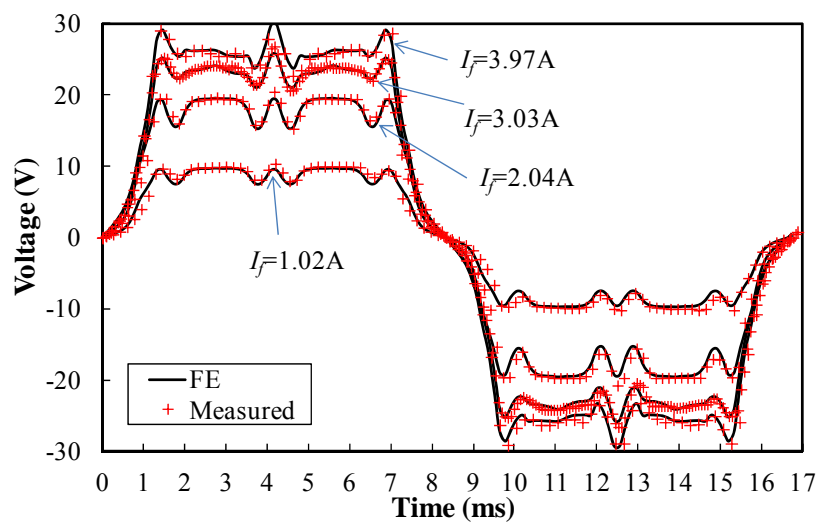


Fig. 6.22. FE predicted and measured EMF waveforms with different excitations of EE prototype machine at 1200 rpm.

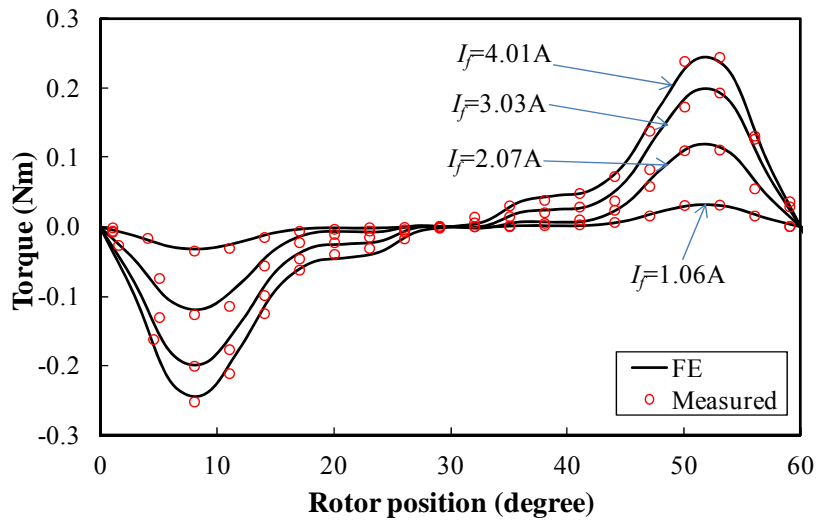


Fig. 6.23. FE predicted and measured cogging torque waveforms of EE prototype machine.

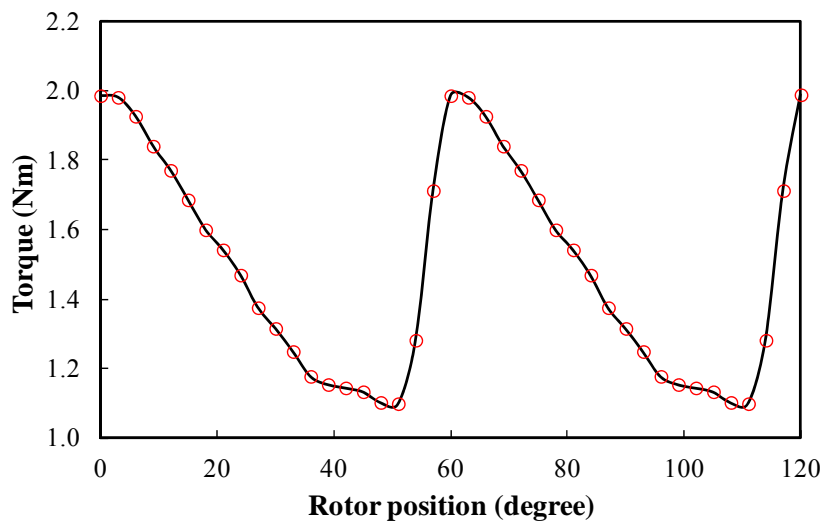


Fig. 6.24. Full-load torque waveform of EE prototype machine when  $p_{cua} = p_{cuf} = 25\text{W}$  ( $I_a = 3.18\text{A rms}$ ,  $I_f = 3.57\text{A}$ ).

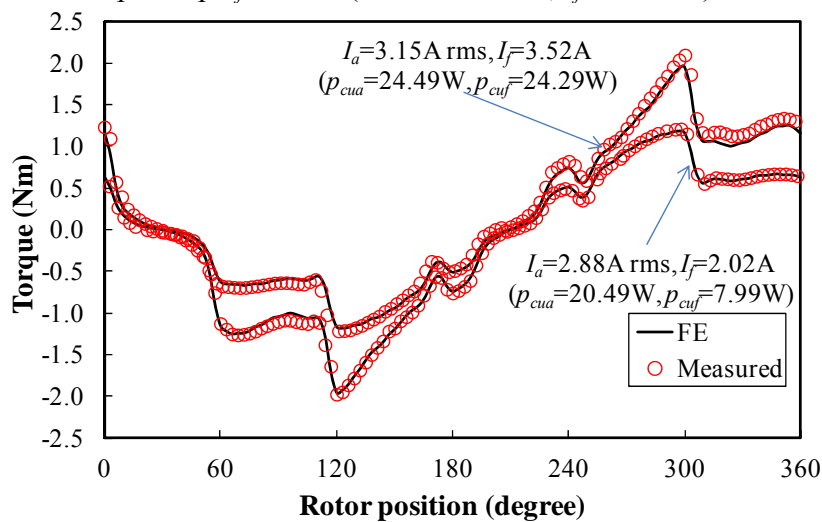


Fig. 6.25. FE predicted and measured torque waveforms of EE prototype machine.

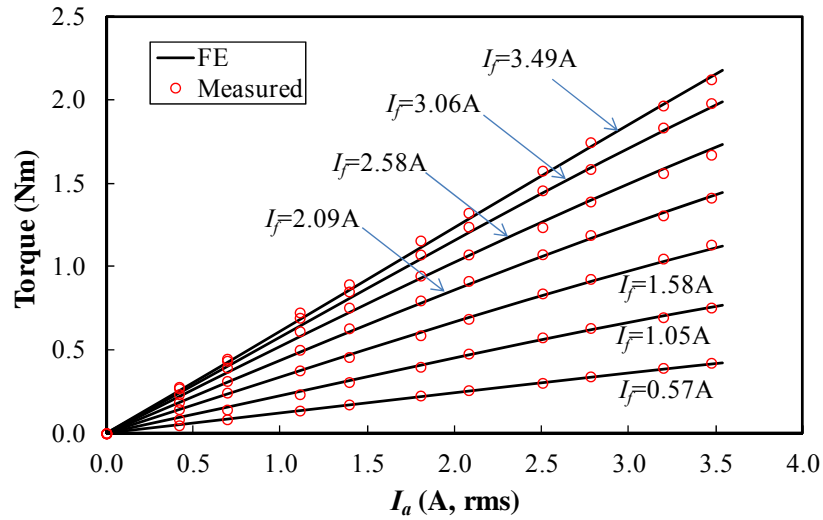


Fig. 6.26. FE predicted and measured peak torques (rotor position is  $120^\circ$  in Fig. 6.25) of EE prototype machine.

## 6.9 Summary

In this paper, the optimisation and comparison between EE and PM machines in terms of maximum  $T/V$  and maximum  $T/G$  have been investigated. The optimal split ratio and flux density ratio have been derived analytically. The influence of pole number and machine size has been analyzed as well to aid the machine designs.

The results show that PM machines can exhibit more than  $\sqrt{2}$  times torque densities of EE machines when they have the same total copper loss. The optimal  $T/G$  designs have significantly higher split ratio than the optimal  $T/V$  designs and more suitable for weight- and cost-sensitive applications. For EE machines, they have an optimal number of poles to maximize the torque densities and prefer large volume applications

# **CHAPTER 7 COMPARATIVE INVESTIGATION ON INFLUENCE OF ROTOR SHAPING AND SKEWING BETWEEN ELECTRICALLY EXCITED AND PERMANENT MAGNET MACHINES**

In this chapter, the influence of rotor shaping and skewing on EE machines is investigated and compared with PM machines. In addition to the conventional inverse cosine airgap length and offset centre arc rotor shaping methods, the effectiveness of rotor shaping utilizing the third order harmonic on EE machines is also examined and compared with PM machines. The influence of skewing on the EE machines with and without rotor shaping is further investigated and compared with PM machines as well. It is shown that the average torque of the EE machine having the inverse cosine airgap length shape is only slightly lower than the one of PM machine with rotor shaping utilizing the third order harmonic. It can barely improve the average torque further by utilizing the third order harmonic in rotor shaping of EE machines. Due to the asymmetric magnetic saturation, the rotor shaping is less effective on torque ripple reduction in EE machines than SPM machines. However, using the rotor skewing, EE machines can still achieve the same low torque ripple as PM machines.

## **7.1 Introduction**

EE and PM machines are two most widely employed electrical machines for various applications, such as traction vehicles, renewable energies, and industrial automations. With the increase of rare-earth magnets' price, it becomes increasingly attractive to consider less or non-rare-earth magnet machines. EE machine is clearly one of potential replacement candidates.

Meanwhile, for high performance applications, the electric machines should be able to deliver a high and smooth torque. In chapter 6, the torque densities of EE and PM machines have been quantitatively compared. However, the torque ripple minimization is another important issue to be addressed. For the torque ripple minimization, skewing and rotor shaping are the two most widely used methods [120]-[173].

For the rotor shaping of EE machines, the inverse cosine airgap length shaping method, as shown in Fig. 1.14 and (1.1), was preferred. In reality, the offset centre arc shaping method, as shown in Fig. 1.17(b), was always employed [60]. Meanwhile, for PM machines, except these two methods, there were several other shaping methods developed [132]-[139]. For

example, the torque density can be improved while the torque ripple remained low when the inverse cosine airgap length with the third order harmonic shaping method was employed. However, the effectiveness of these rotor shaping methods on the torque ripple reduction in EE machines has not been examined.

For the skewing, it has been shown in chapter 2 that, for PM machines, the torque ripple is not always reduced by skewing, especially when the torque ripple is reduced significantly by the rotor shaping already. However, the effectiveness of skewing on the torque ripple reduction in EE machines with shaped rotor has not been discussed.

Therefore, in this chapter, the influence of rotor shaping and skewing on EE machines is investigated and compared with PM machines. First, the effectiveness of various rotor shaping methods, such as the inverse cosine airgap length, the offset centre arc, and the rotor shaping methods utilizing the third order harmonic, on the torque ripple reduction of EE machines is investigated and compared with PM machines. Second, the influence of skewing on EE machines with or without rotor shaping is investigated and compared with PM machines as well.

## 7.2 EE and PM Prototype Machines

The comparative investigation is carried out between salient pole EE and SPM prototype machines. All the prototype machines have the same stator except the axial length, which is listed in Table 7-I. In order to ease the comparison, EE machines are slightly longer and larger than SPM machines to have the same average full load torque while neither the rotor shaping nor the skewing is applied. The detailed development of EE and PM machines is given in Appendix C.

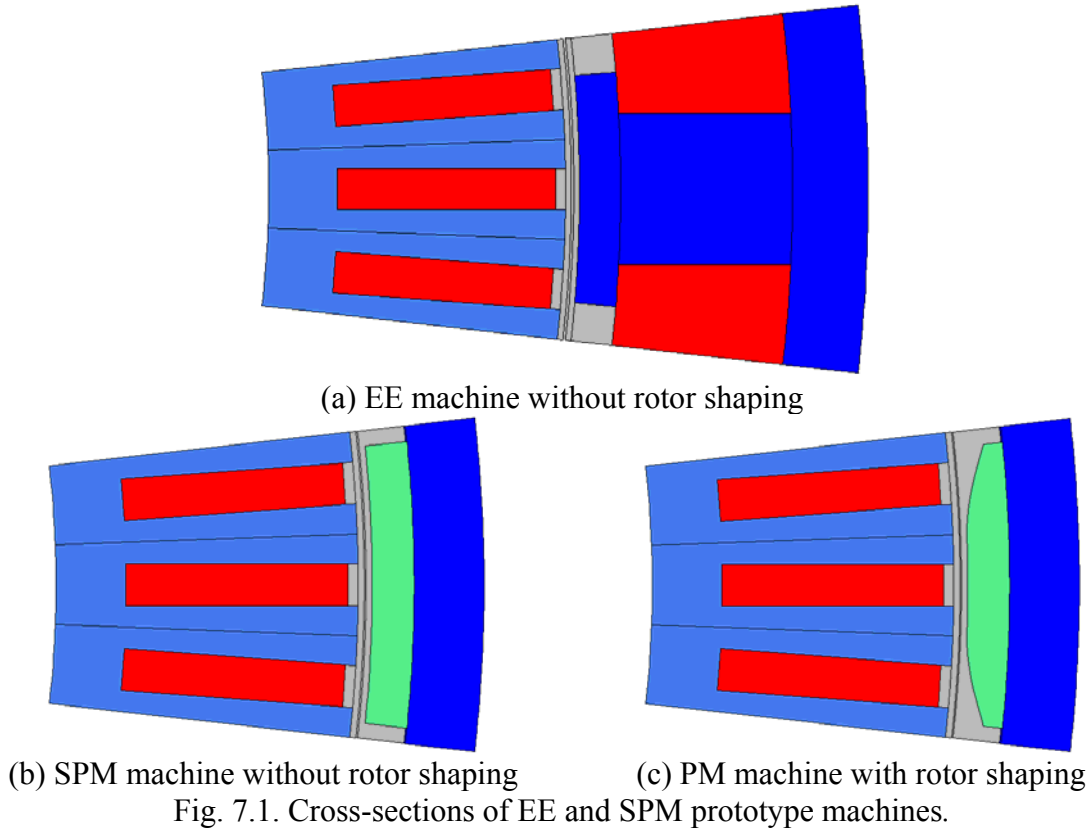
Without rotor shaping, the cross-section and main parameters of the EE prototype machine are given in Table 7-I and Fig. 7.1(a). Since EE machines have both armature and excitation copper losses, the maximum current density is fixed as the lowest value with liquid cooling, i.e., 10 A/mm<sup>2</sup>. The packing factor of field windings is selected as 0.6, which is higher than the packing factor of armature winding (0.42), since they are concentrate-wound. Two operation conditions, i.e., half load and full load, are investigated. On full load, the phase armature current  $I_a$  is 19 A RMS and the field current  $I_f$  is 17A DC. On half load, both the armature and field copper losses are halved to maintain the lowest total copper loss, i.e.,  $I_a = 13.4A$  and  $I_f = 12A$ . The optimal current phase advanced angles  $\beta$ , which is referred to the negative  $q$ -axis, for the maximum torques at half and full loads are 0° and -6° electrical,

respectively.

The cross-section and main parameters of PM prototype machines are given in Table 7-I and Fig. 7.1(b) and (c). Three operation conditions, i.e., open-circuit, half load, and full load, are investigated. On full load, the phase armature current  $I_a$  is 19 A RMS, which is the same as the EE prototype machines. On half load, the armature current is halved, i.e.,  $I_a = 9.5A$ . The optimal current phase advanced angles  $\beta$  for the maximum torques at half and full loads are  $-1.5^\circ$  and  $-3^\circ$  electrical, respectively. The SPM machine with rotor shaping is developed based on the cosine magnet shape utilizing the third order harmonic, which is shown in (1.4) and has been proved to be better than the cosine one [138]. The detailed optimisation of magnet shape is given in Appendix C.

Table 7-I Main parameters of prototype machines

Shared parameters			
Parameters	value	Parameters	value
Number of slots	84	Number of poles	28
Stator outer diameter	390 mm	Airgap length	2 mm
Number of turns per phase	420	Rated armature current	19 A RMS
Slot opening	6 mm	Slot depth	31.7 mm
Stator yoke	10 mm		
Parameters of EE machines			
Rotor outer diameter	478 mm	Effective axial length	119 mm
Rated field current	17A DC	Pole shoe height	6 mm
Pole arc to pole pitch ratio	0.75	Rotor pole body height	25 mm
Rotor pole body width	22 mm	Rotor yoke thickness	11 mm
Parameters of SPM machines			
Rotor outer diameter	426mm	Effective axial length	110 mm
Magnet thickness	6 mm	Remanence	1.17 T
Coercive force	891 kA/m		



### 7.3 Influence of Rotor Shaping

#### 7.3.1 EE Machines with Different Rotor Shapes

For the rotor shaping of EE machines, conventionally, the inverse cosine airgap length shape, which is shown in Fig. 1.14 and (1.1), and the offset centre arc shape are often employed [60]. The schematic of the offset centre arc rotor shaping for external rotor EE machines is illustrated in Fig. 7.2. Since the inverse cosine airgap length shape with the third order harmonic, which is shown in (1.3) and Fig. 1.18, has been proved to be better than the conventional inverse cosine airgap length shape in IPM machines [139]. The effectiveness of this method in EE machines is investigated. Furthermore, as shown in chapter 6, in EE machines, the equivalent magnetic reluctance in the laminations is not negligible. Therefore, the fourth rotor shaping method, which is based on the inverse cosine airgap length shape with the third order harmonic by adding an equivalent airgap length  $\delta_{ad}$  to represent the influence of magnetic reluctance in the lamination, is developed as well and given as

$$\delta(\theta) = \frac{k'(\delta_{min} + \delta_{ad})}{\cos(p\theta) - a_3 \cos(3p\theta)} - \delta_{ad} \quad (7.1)$$

where  $k'$  is a constant to keep the minimum airgap length the same.

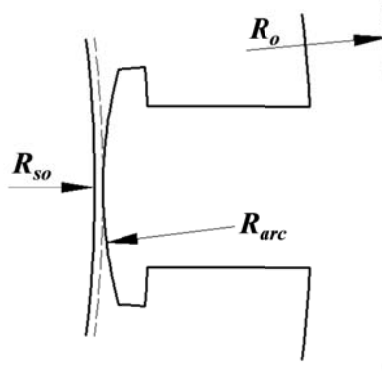


Fig. 7.2. Schematic of offset centre arc rotor shaping for external rotor EE machines.

The effectiveness of different rotor shaping methods on EE machines is investigated based on the full load torque, which is shown in Figs. 7.3-7.5.

For the offset centre arc rotor shaping, as shown in Fig. 7.3, the average torque keeps reducing when  $R_{arc}$  decreases, since the average airgap length is larger. However, the torque ripple becomes stable at the lowest level when  $R_{arc}$  is smaller than 50mm.

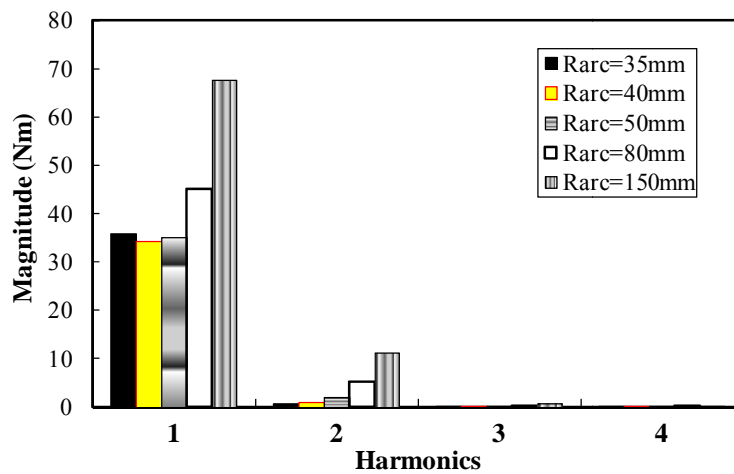
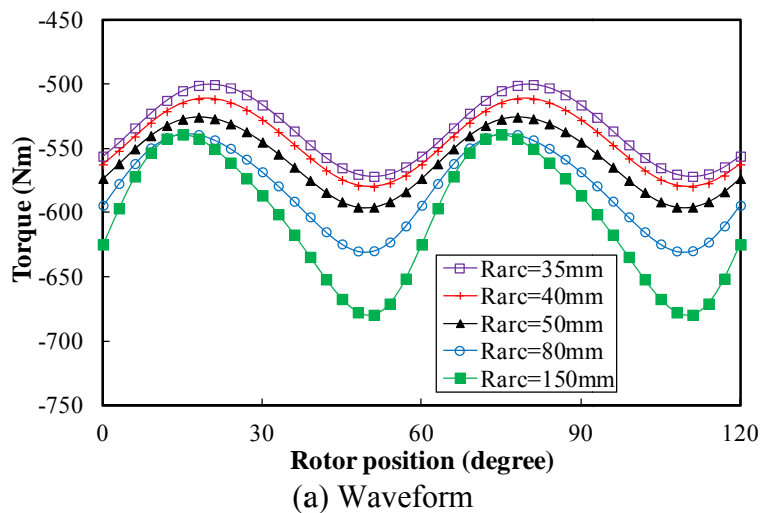


Fig. 7.3. Torque variation with rotor arc radius using offset centre arc rotor shape when  $I_a = 19A$ ,  $I_f = 12A$ , and  $\beta = -6^\circ$ .

For the inverse cosine airgap length shaping utilizing the third order harmonic, as shown in Fig. 7.4, the variation of average torque with the amplitude of the third order harmonic is much milder than the one of IPM machine reported in [139]. The average torque having the optimal third order harmonic, in which  $a_3 = 1/6$ , is only 1.8% higher than the one having the conventional inverse cosine airgap length shaping, which will be shown later. However, in terms of the torque ripple, it shows that the torque ripple is lower when the third order harmonic is less.

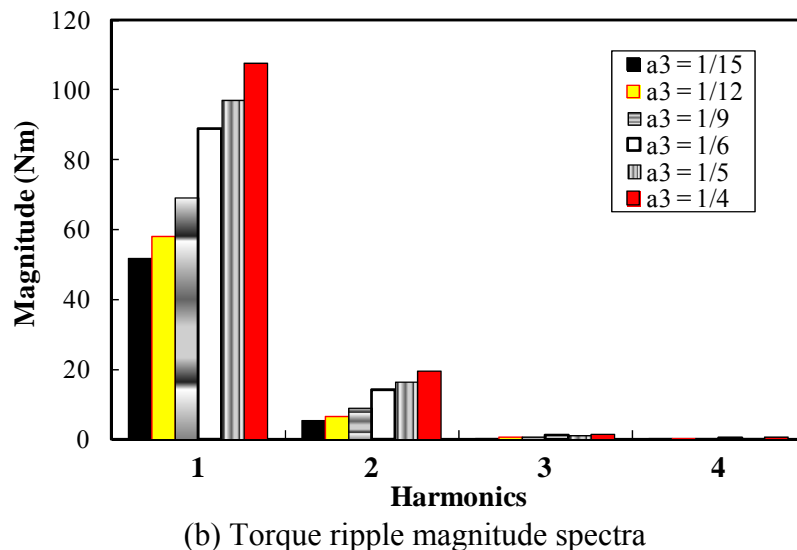
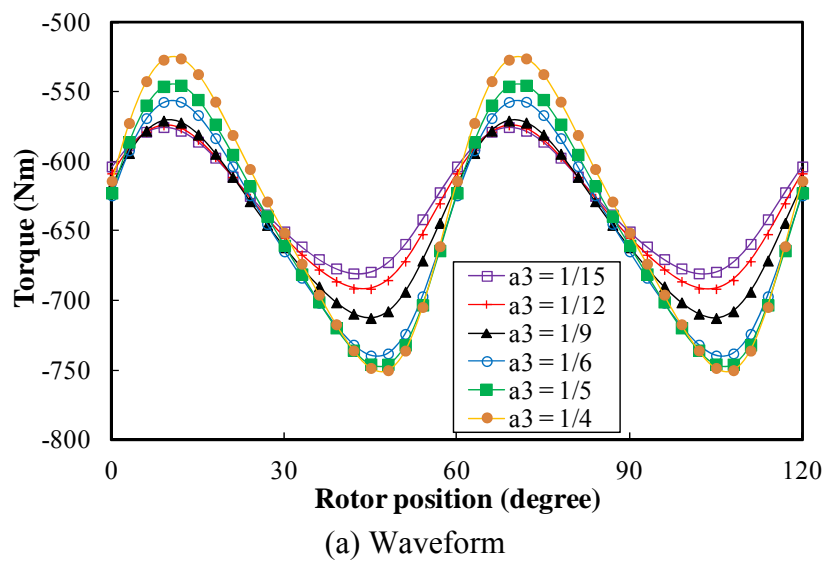


Fig. 7.4. Torque variation with third order harmonic amplitude based on inverse cosine airgap length shaping utilizing third order harmonic when  $I_a = 19A$ ,  $I_f = 12A$ , and  $\beta = -6^\circ$ .

For the modified inverse cosine airgap length shaping utilizing the third order harmonic, it is investigated when  $a_3 = 1/9$ . As shown Fig. 7.5, both the average torque and torque ripple reduce modestly when  $\delta_{ad}$  increases.

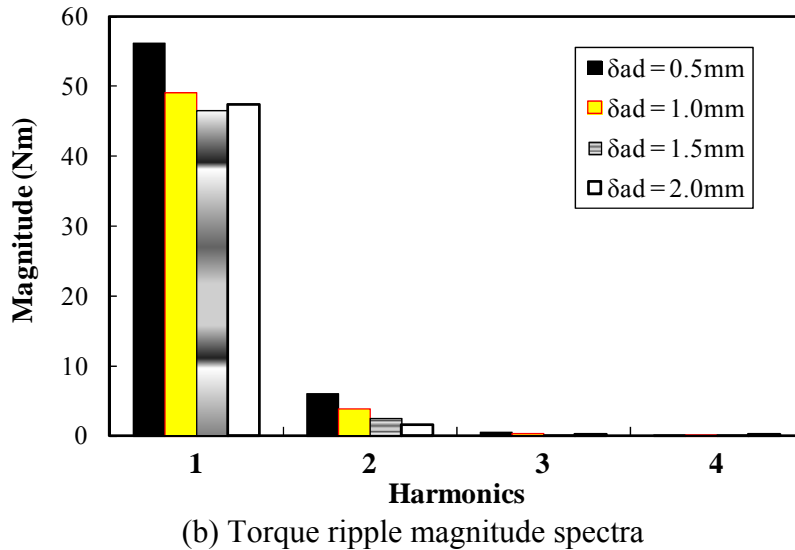
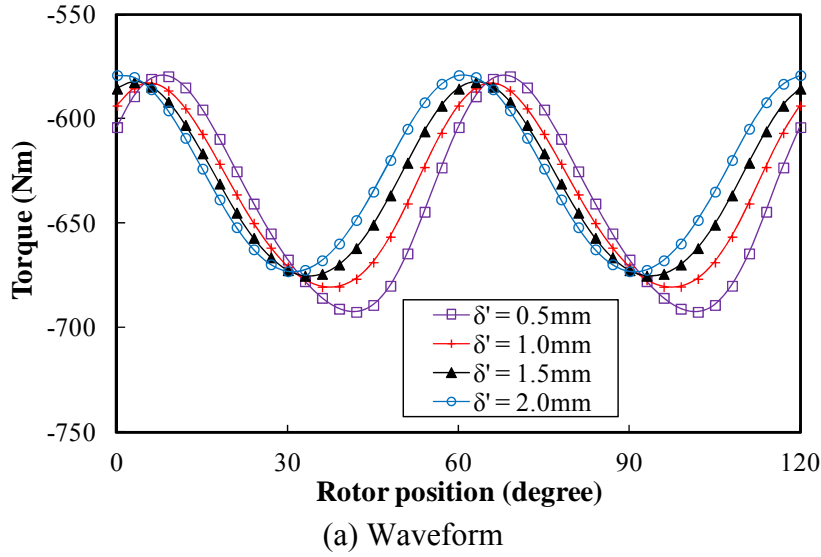


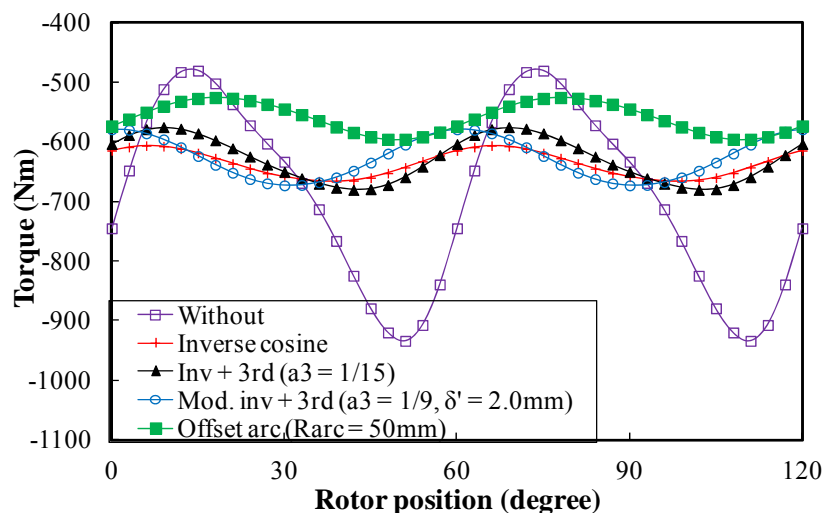
Fig. 7.5. Torque ripple variation with equivalent airgap length representing lamination reluctance based on modified inverse cosine airgap length shaping utilizing third order harmonic when  $a_3 = 1/9$ ,  $I_a = 19A$ ,  $I_f = 12A$ , and  $\beta = -6^\circ$ .

Based on the foregoing results, the optimal designs of each rotor shaping method are compared in Fig. 7.6. It can be seen that, compared with the one without rotor shaping, the torque ripple of EE machines can be reduced by all the rotor shaping methods investigated. Amongst the different rotor shaping methods the conventional inverse cosine airgap length shaping method is the best one for this application, which has the highest average torque and lowest torque ripple.

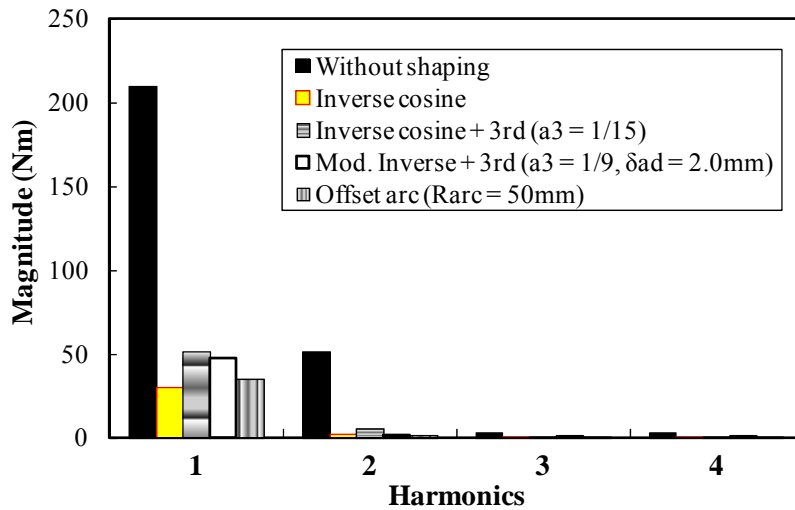
Being different from IPM machines, the average torques with or without utilizing the third order harmonic are only slightly different. As mentioned foregoing, the average torque with the optimal third order harmonic, in which  $a_3 = 1/6$ , is only 1.8% higher than the one having the inverse cosine airgap length shape. When  $a_3 = 1/15$ , where the torque ripple is lower, the

average torque is even 1.3% lower than the one having inverse cosine airgap length shape.

In order to explain the different outcomes between EE and PM machines, the full load field distributions of EE machines having optimal rotor shapes are shown in Fig. 7.7 and investigated. It can be seen that, for the offset centre arc shape with  $R_{arc} = 50\text{mm}$ , its airgap is largest within these four designs. Therefore, it has the lowest average torque. When utilizing the third order harmonic, the airgap length near the rotor pole shoulder is smaller than the one having the inverse cosine airgap length rotor shape. Therefore, for the EE machines having the rotor shaping utilizing the third order harmonic, the average airgap length is slightly smaller, which results in slightly higher average torque. However, except the heavier magnetic saturation due to the smaller average airgap length, the smaller airgap length near the rotor pole shoulder results in higher  $q$ -axis magnetic field, which causes the magnetic saturation in the stator and the rotor pole shoulder even heavier, as shown in Fig. 7.7. Furthermore, since the influence of magnetic saturation in the laminations is much higher in EE machines, which has been explained and illustrated in chapter 6, the heavier magnetic saturation, especially along  $q$ -axis, in return reduces the slightly higher average torque due to the smaller average airgap length. Therefore, in EE machines, compared with the one having inverse cosine airgap length shape, in total, the average torque can only be increased by 1.8% even for the rotor shaping having the optimal third order harmonic.

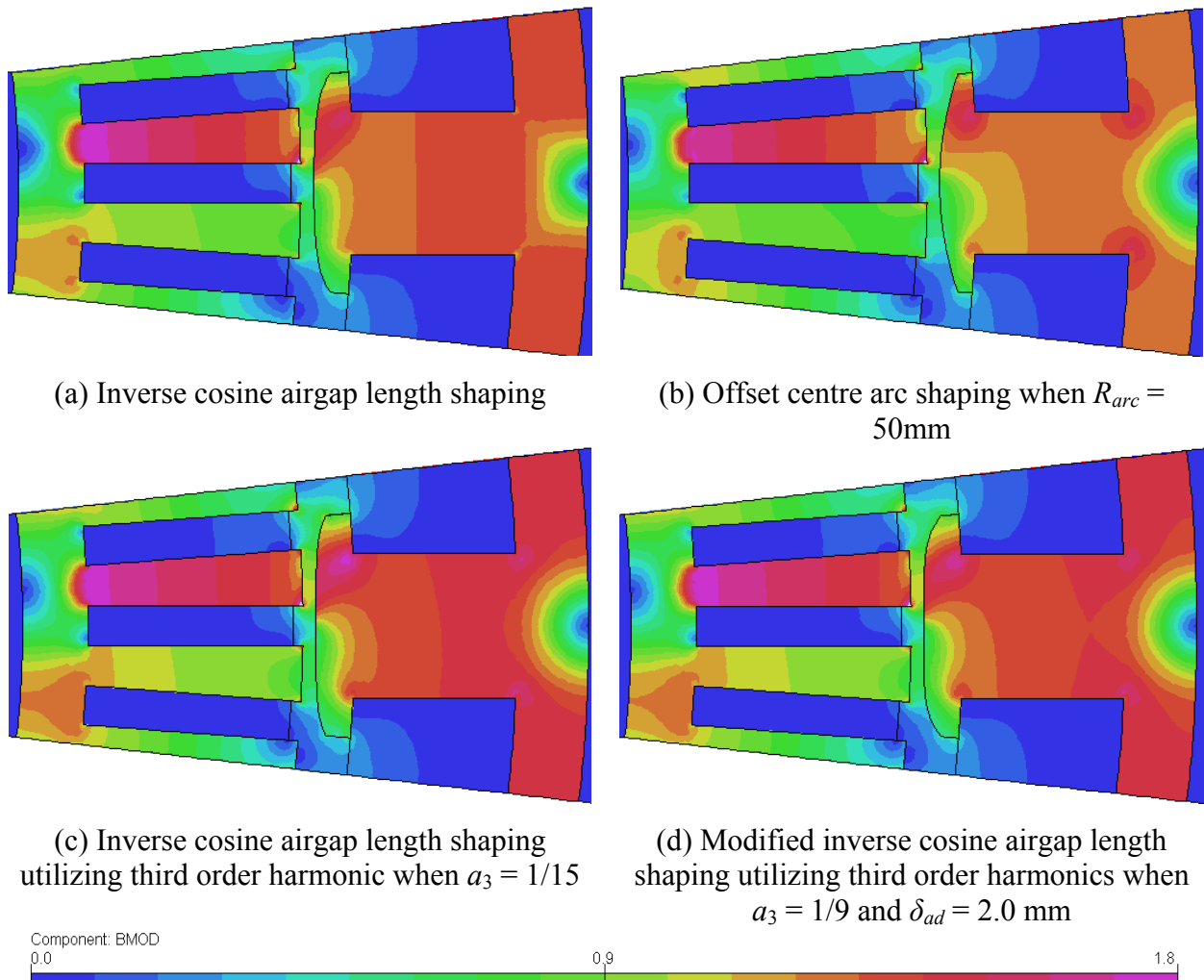


(a) Waveform



(b) Torque ripple magnitude spectra

Fig. 7.6. Comparison of different rotor shaping methods in EE machines when  $I_a = 19A$ ,  $I_f = 12A$  and  $\beta = -6^\circ$ .



(a) Inverse cosine airgap length shaping

(b) Offset centre arc shaping when  $R_{arc} = 50mm$

(c) Inverse cosine airgap length shaping utilizing third order harmonic when  $a_3 = 1/15$

(d) Modified inverse cosine airgap length shaping utilizing third order harmonics when  $a_3 = 1/9$  and  $\delta_{ad} = 2.0 mm$

Fig. 7.7. Magnetic field distributions when  $I_a = 19A$ ,  $I_f = 12A$ ,  $\beta = -6^\circ$ , and  $\theta = 0^\circ$ .

### 7.3.2 Comparison between EE and PM Machines

The influence of rotor shaping on EE and PM machines is compared based on their full load torques in Fig. 7.8 and Table 7-2. Without rotor shaping, the EE and PM machines have the same average output torque. The PM machine is shaped using the cosine magnet shape utilizing the third order harmonic, which has been shown better than the cosine magnet shape in [60]. The EE machine is based on the inverse cosine airgap length shape, which is shown foregoing the best design for this application.

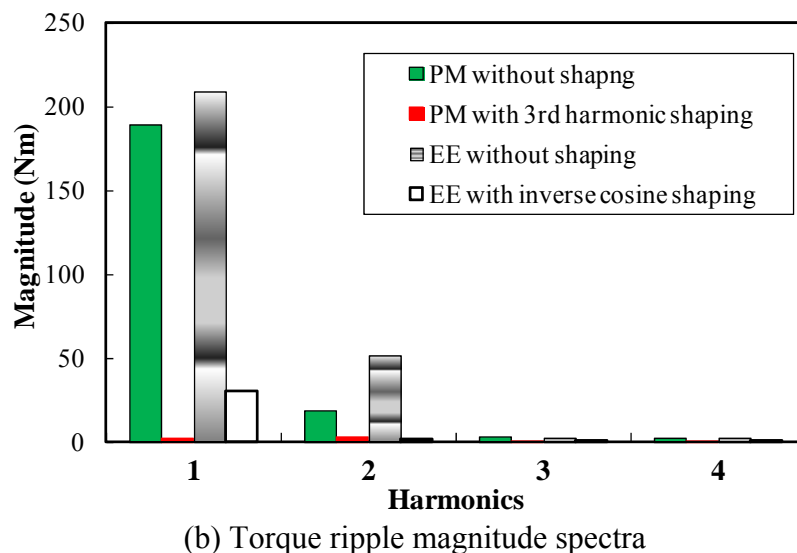
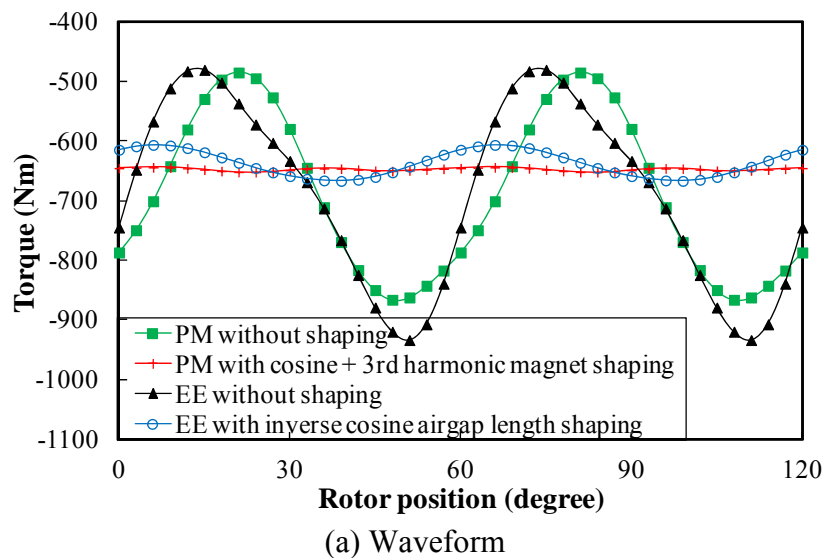


Fig. 7.8. Comparison on influence of rotor shaping between EE and PM machines when they are on full load.

Table 7-II Comparison on influence of rotor shaping

Nm		Without shaping	Shaped
PM	Average torque	-687.4	-647.7
	P-p torque ripple	381.1	8.0
EE	Average torque	-687.4	-638.6
	P-p torque ripple	453.2	60.3

Without utilizing the third order harmonic, the average torque of the EE machine having the inverse cosine airgap length shape is only 1.4% lower than the one of PM machine having the cosine magnet shape utilizing the third order harmonic. Again, it is due to the influence of magnetic saturation. As can be seen from Fig. 7.9, with the inverse cosine airgap length shape, the magnetic saturation of EE machine is greatly reduced than the one without shaping. The influence of larger airgap length is partially compromised by the influence of magnetic saturation and, hence, the average torque reduces less. Therefore, it can be concluded that, different from PM machines, it can barely improve the average torque in EE machines further by utilizing the third order harmonic.

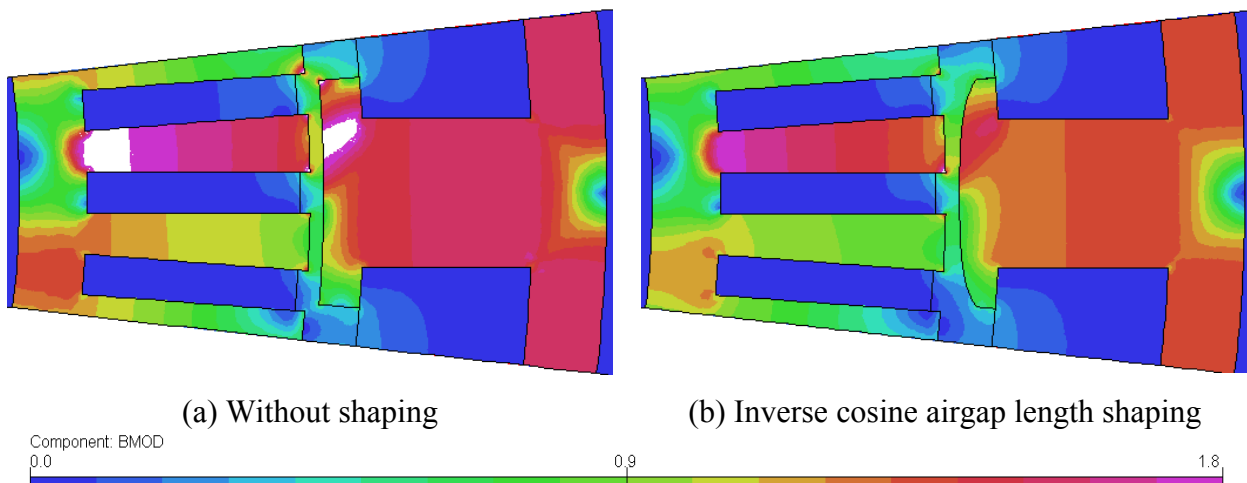


Fig. 7.9. Magnetic field distributions of EE machines when  $I_a = 19A$ ,  $I_f = 12A$ ,  $\beta = -6^\circ$ , and  $\theta = 30^\circ$  (White represents that flux density is higher than 1.8T).

It can also be seen from Fig. 7.8 and Table 7-2 that the torque ripple is reduced by rotor shaping for both PM and EE machines. However, the torque ripple can be more effectively reduced in PM machines than EE machines using rotor shaping. In order to explain the difference, the full load permeability distributions of PM and EE machines are shown in Fig. 7.10 and investigated. It can be seen that, for SPM machines, the magnetic reluctance is

almost constant. The principle of rotor shaping in SPM machines is reduce the permanent magnet MMF harmonics. Due to the significantly large equivalent airgap length, which almost equals to the sum of mechanical airgap and magnet, the influence of magnetic saturation on torque ripple is negligible unless when the magnetic saturation is significantly heavy and the torque ripple is low. Therefore, the torque ripple of SPM machines is low when the magnets are well shaped. However, for EE machines, instead of airgap length, the MMF of field winding is constant. The principle of rotor shaping is to achieve inverse cosine magnetic reluctance distribution. Furthermore, for EE machines, since the equivalent airgap is simply the mechanical airgap and much smaller than the one of SPM machines, the influence of magnetic saturation in the lamination is much higher. When EE machines are on load, due to the influence of  $q$ -axis magnetic field, the magnetic saturation, particularly the one at the rotor pole shoulder, is asymmetric with  $d$ -axis, as shown in Fig. 7.10. Therefore, although the mechanical airgap length is shaped to the inverse cosine shape, the asymmetric magnetic saturation, especially one at the rotor pole shoulder, makes the on load magnetic reluctance distribution less symmetric than SPM machines. Therefore, even with the rotor shaped, the torque ripple of the EE machine is still higher than the one of SPM machines. In other words, the rotor shaping is less effective on torque ripple reduction in EE machines than SPM machines due to the influence of the asymmetric magnetic saturation.

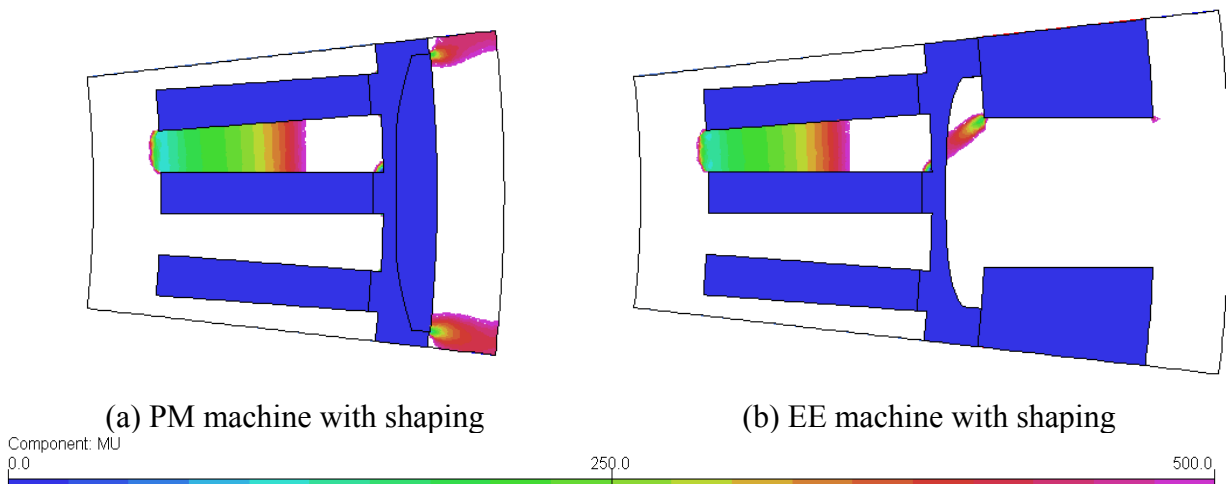


Fig. 7.10. Relative permeability distributions of PM and EE machines under full load (White represents that relative permeability is higher than 500).

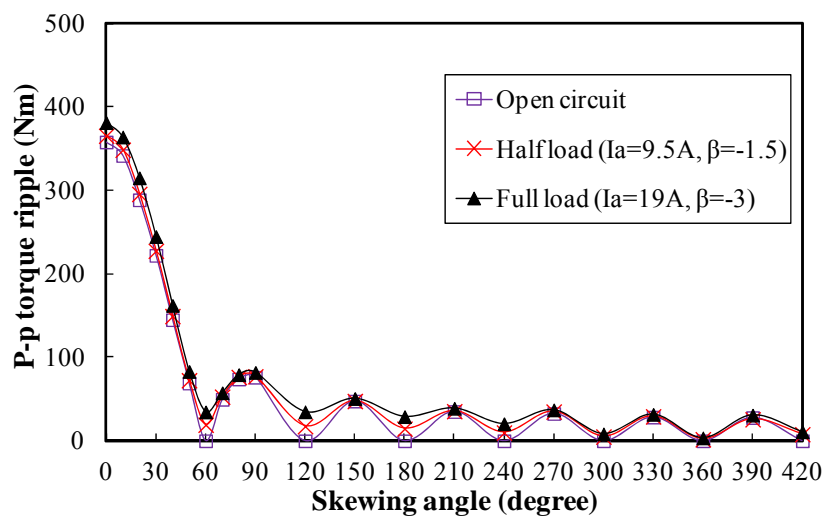
#### 7.4 Influence of Skewing

Except the rotor shaping, skewing is another widely used method to reduce the torque ripple. Skewing is also often employed together with other methods to further reduce the

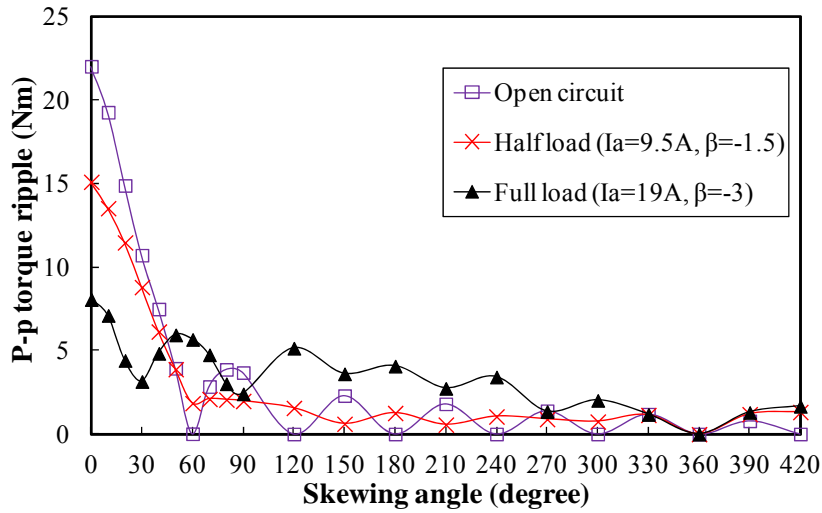
torque ripple. However, it has been shown in chapter 3 that, for PM machines, the torque ripple is not always reduced by skewing, especially when the torque ripple is reduced to very low level by the rotor shaping already. Therefore, in this section, the effectiveness of skewing on the torque ripple reduction in EE machines with or without rotor shaping is investigated and compared with PM machines as well.

In order to analyse the variation of torque ripple with skewing in EE machines, it is necessary to define the on-load torque components. As shown in (4.4) and (4.5), for all the electric machines, the on-load torque can be divided into two parts. One is due to the input electrical power and well-known as the EM torque. The other one is due to the variation of system magnetic energy, which is defined as the cogging torque of EE machines in this chapter.

The investigation is carried out based on rotor skewing calculated by 2D multi-slice FE method having 20 slices. The variation of torque ripple with different skewing angles of EE and PM machines with and without rotor shaping is given in Figs. 7.11 and 7.12. For PM machines, the torque ripples vary in the ways predicted in chapter 3. The open circuit cogging torque is eliminated by skewing when the skewing angle is  $k \times 60^\circ$ . For the on-load torque ripples, they cannot be eliminated by skewing, except when the skewing angle is  $360^\circ$  electrical, which is impractical. When the torque ripple is dominated by the EM components, such as full load torque ripple with rotor shaping in Fig. 7.11, the skewing is less effective on torque ripple reduction. Although, the torque ripple can still reduce slightly by skewing for this application, it has been shown in chapter 3 that the torque ripple may also be increased after skewing.

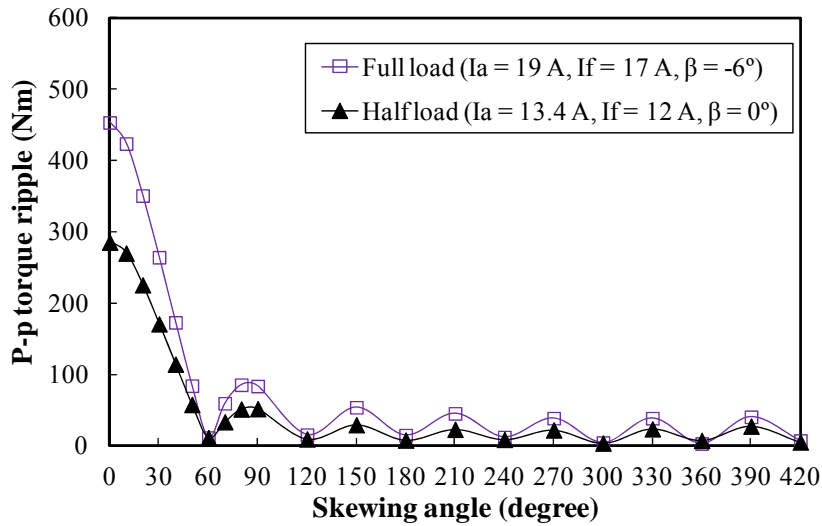


(a) Without rotor shaping

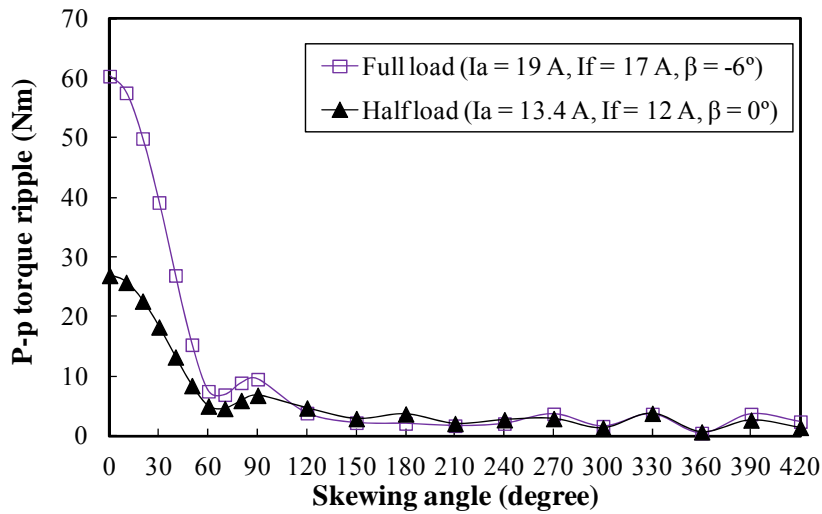


(b) With cosine magnet shape utilizing third order harmonic

Fig. 7.11. Torque ripple variation with different skewing angles of PM machines.



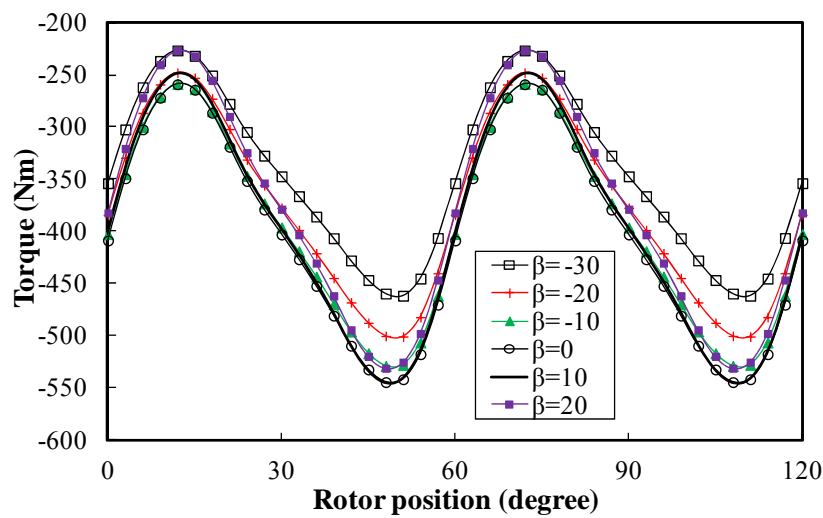
(a) Without rotor shaping



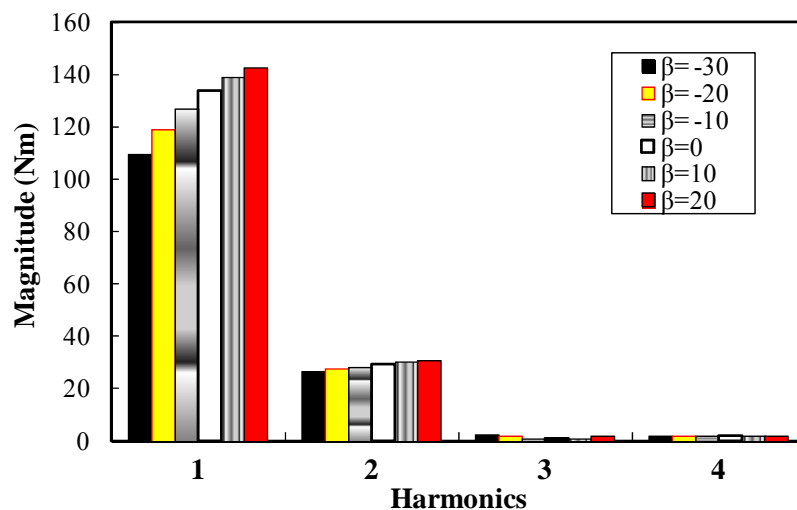
(b) With inverse cosine airgap length shape

Fig. 7.12. Torque ripple variation with different skewing angles of EE machines.

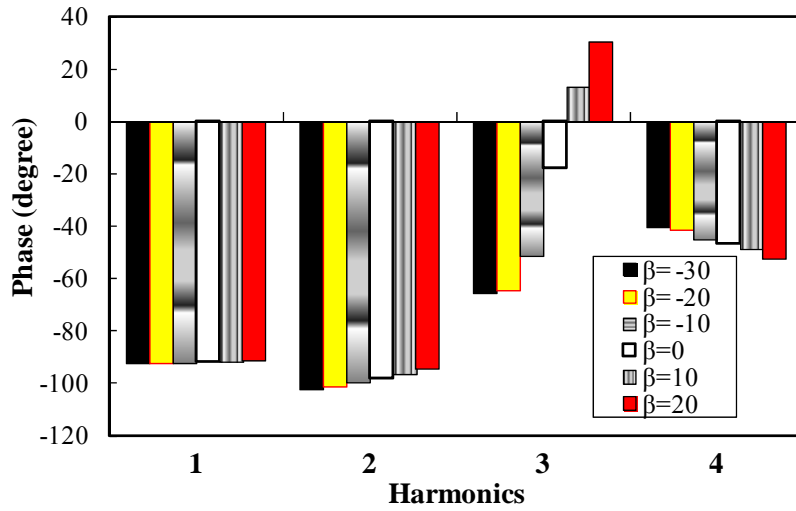
For the EE machine without rotor shaping, the variation of torque ripples with skewing angle is similar to the one of PM machine without skewing, as shown in Figs. 7.11(a) and 7.12(a). It suggests that the torque ripples, both half- and full-load, are dominated by the cogging torque. This is also confirmed by the torque ripple variation with the current phase advance angle without rotor skewing, as shown in Figs. 7.13 and 7.14. When the current phase advance angle changes, although the magnitude of fundamental torque ripple changes steadily, which is due to the EM torque ripple, the phase of torque ripple remains almost the same. Therefore, as shown in Fig. 7.12(a), the torque ripples, both half and full loads, are the lowest when the skewing angle is  $k \times 60^\circ$ .



(a) Torque waveforms

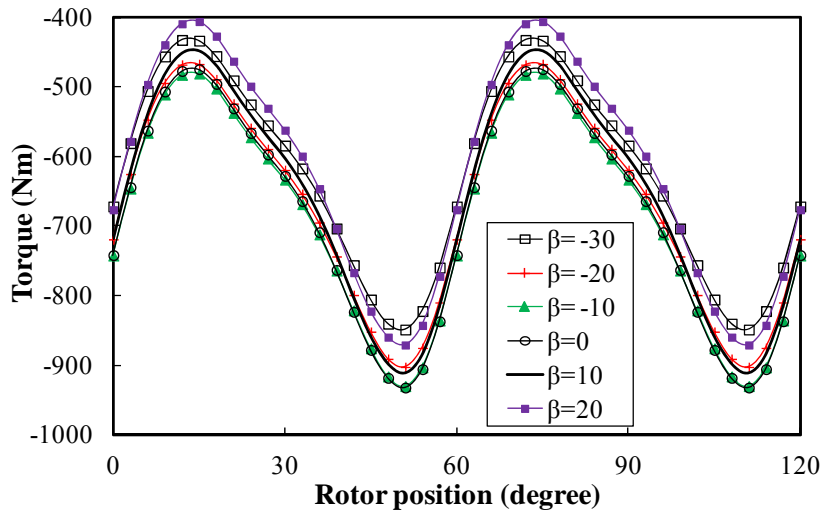


(b) Torque ripple magnitude spectra

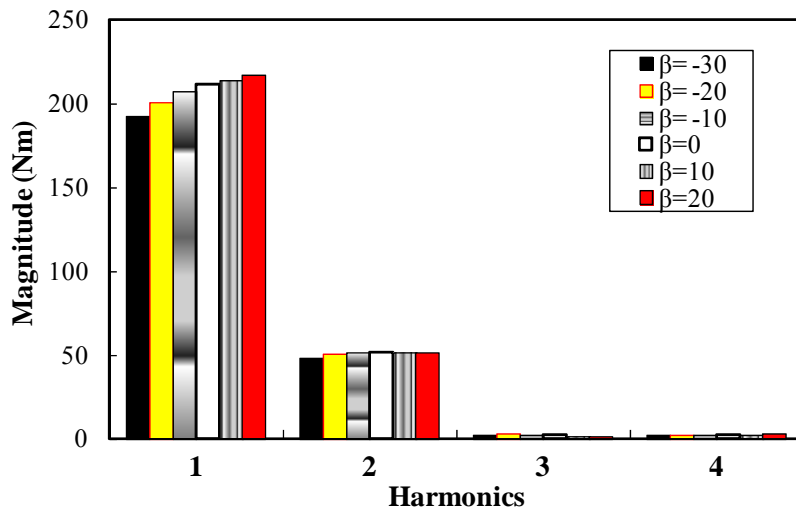


(c) Torque ripple phase spectra

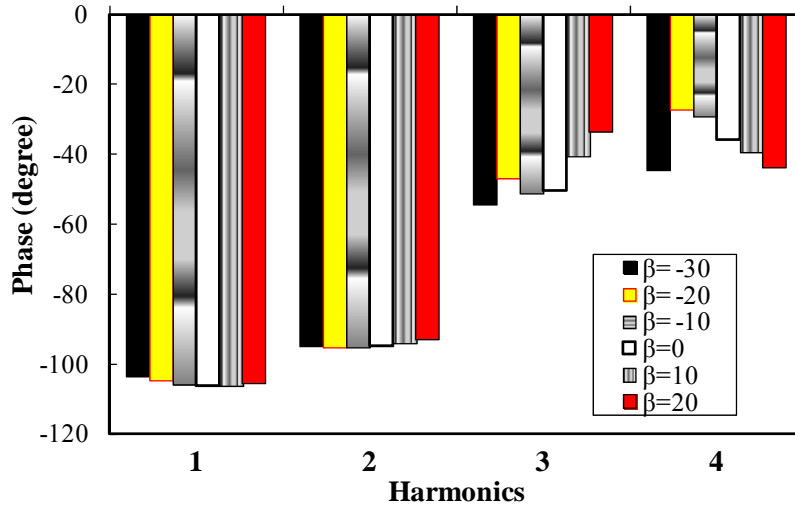
Fig. 7.13. Torque ripple variation with current phase advance angle of EE machine without rotor shaping and skewing when  $I_a = 13.4$  A and  $I_f = 12$  A.



(a) Torque waveforms



(b) Torque ripple magnitude spectra

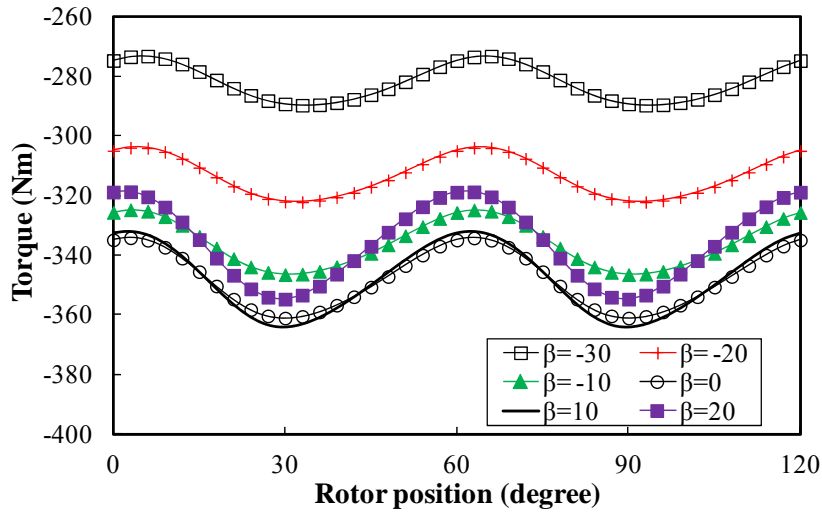


(c) Torque ripple phase spectra without skewing

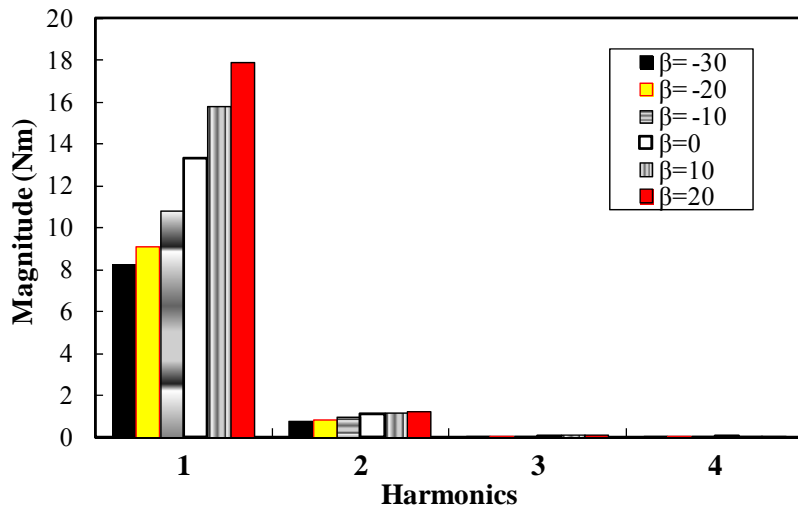
Fig. 7.14. Torque ripple variation with current phase advance angle of EE machine without rotor shaping and skewing when  $I_a = 19$  A and  $I_f = 17$  A.

For the EE machine with the inverse cosine airgap length shape, the torque ripples without skewing are much lower than the EE machine without shaping. However, compared with the PM machine having rotor shaped, the torque ripple of rotor shaped EE machine is much higher due to the influence of asymmetric permeability distribution. With the skewing, the torque ripple of the rotor shaped EE machine can still be reduced significantly. It also can be seen from Fig. 7.12 that the torque ripples is lower when  $\theta_{sk} = 70^\circ$  than the one when  $\theta_{sk} = 60^\circ$ , which suggests that the cogging torque is much lower and EM torque ripple is dominated by 5<sup>th</sup> harmonic.

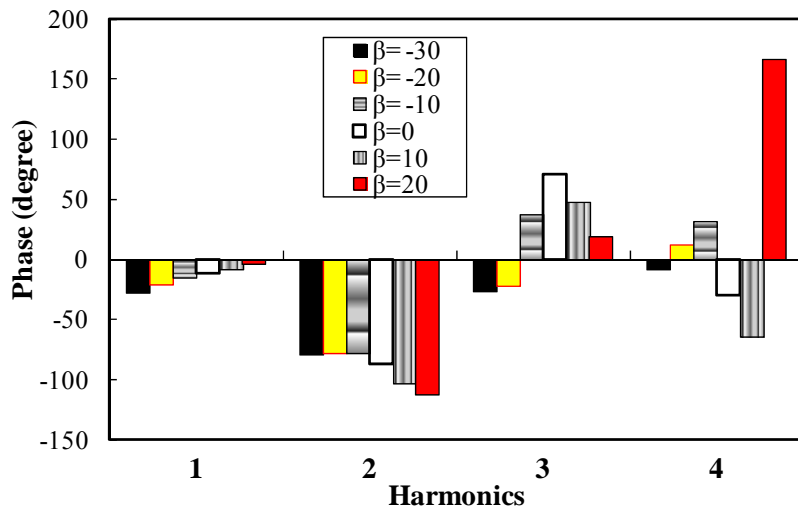
In order to explain the torque ripple variation with the skewing angle, the torque ripple variation with the current phase advance angle of EE machine with rotor shaping and without rotor skewing is investigated. As can be seen from Figs. 7.15 and 7.16, for both the half and full loads, the phase of torque ripple varies with the current advance angle mildly. Therefore, with skewing, both half load and full load torque ripples can be reduced further. Since the variation of torque ripple phase on full load is less than the one on half load when the current phase advance angle changes, the full load torque ripple is reduced more than the half load torque ripple, as shown in Fig. 7.12.



(a) Torque waveforms

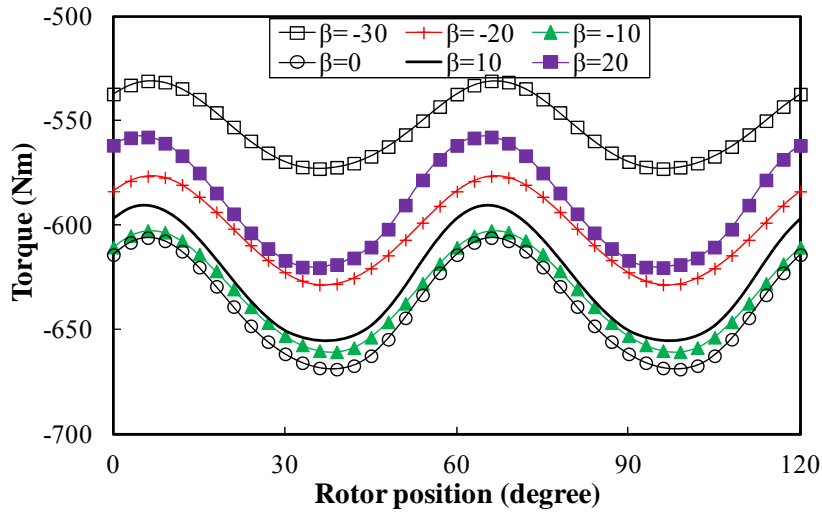


(b) Torque ripple magnitude spectra

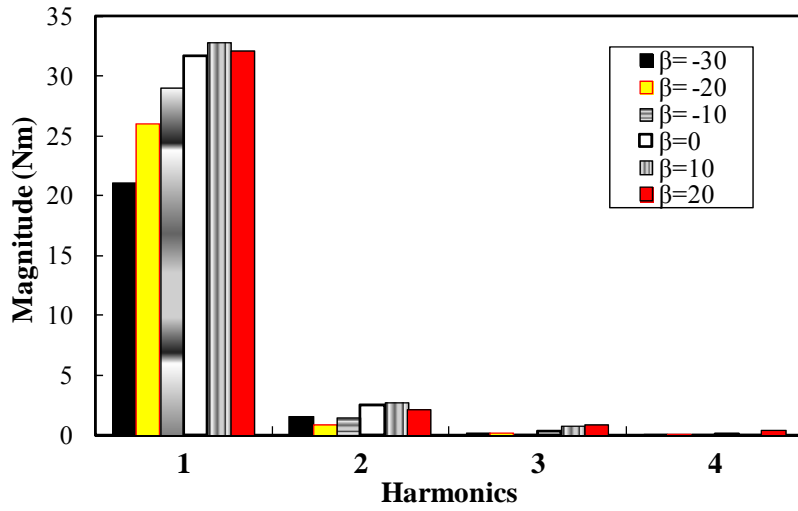


(c) Torque ripple phase spectra

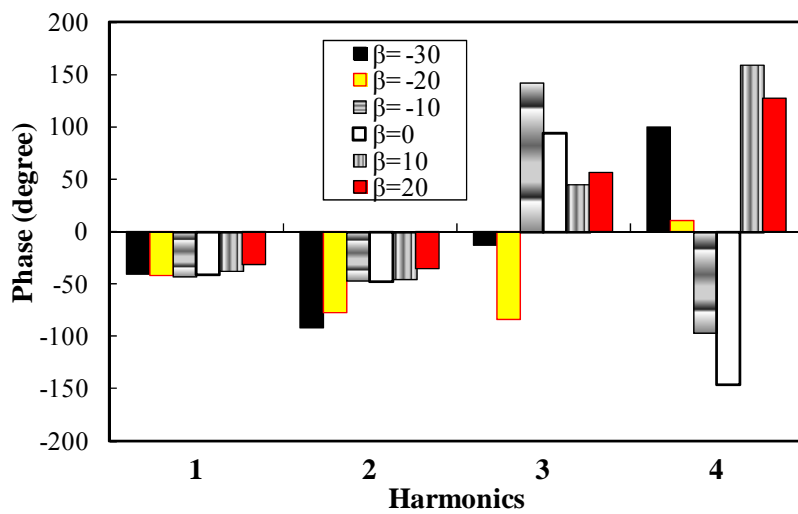
Fig. 7.15. Torque variation with current phase advance angle of EE machine with inverse cosine airgap length shape and without skewing when  $I_a = 13.4$  A and  $I_f = 12$  A.



(a) Torque waveforms



(b) Torque ripple magnitude spectra



(c) Torque ripple phase spectra

Fig. 7.16. Torque variation with current phase advance angle of EE machine with inverse cosine airgap length shape and without skewing when  $I_a = 19$  A and  $I_f = 17$  A.

In order to further reveal the mechanism behind, the variation of permeability distribution of EE machines with rotor shaping when  $I_a = 19$  A and  $I_f = 17$  A is investigated. As can be seen from Fig. 7.17, the asymmetric permeability distribution due to the  $q$ -axis magnetic field remains unless when the  $q$ -axis current is low. Therefore, the variation of the torque ripple with the current phase advance angle and hence the influence of skewing in EE and PM machines are different, as foregoing illustrated.

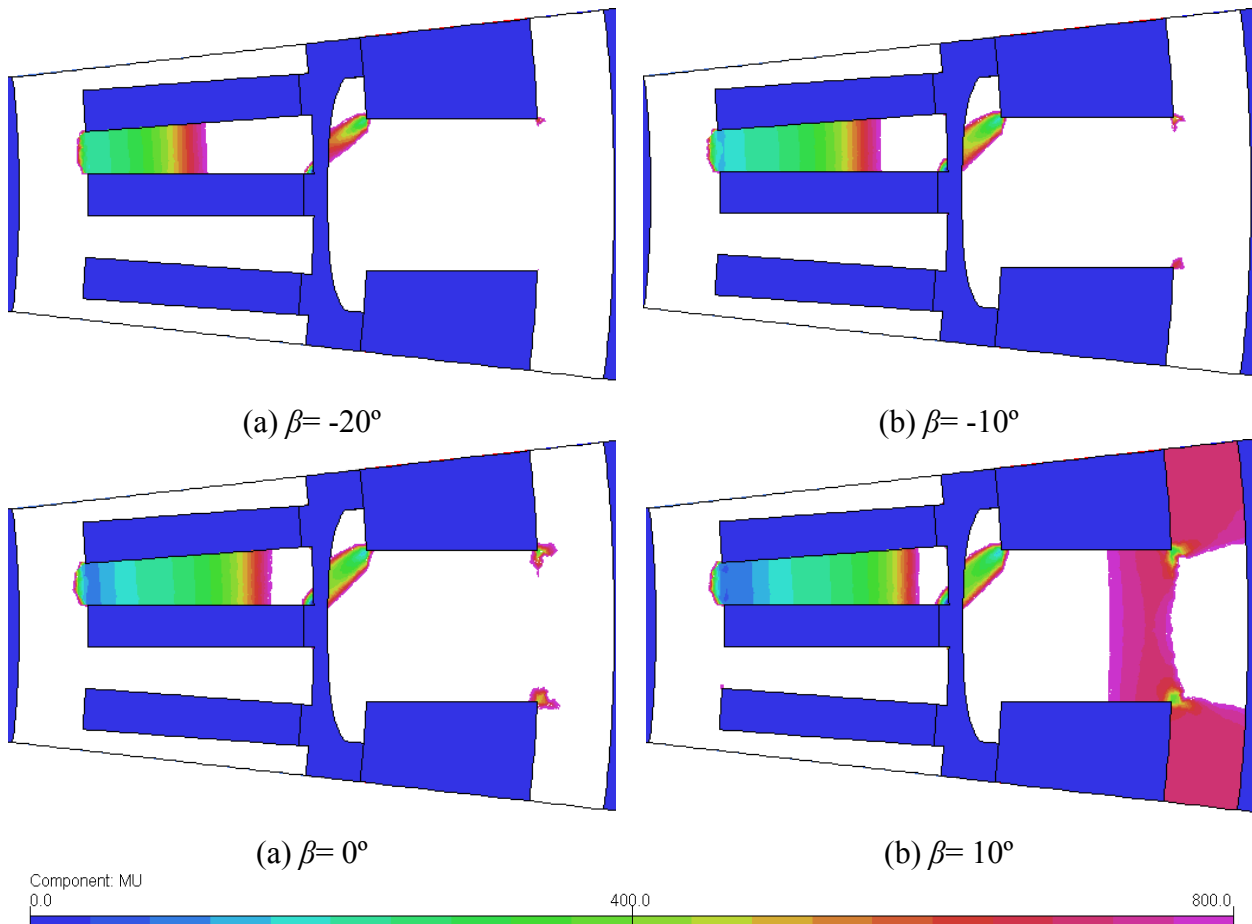
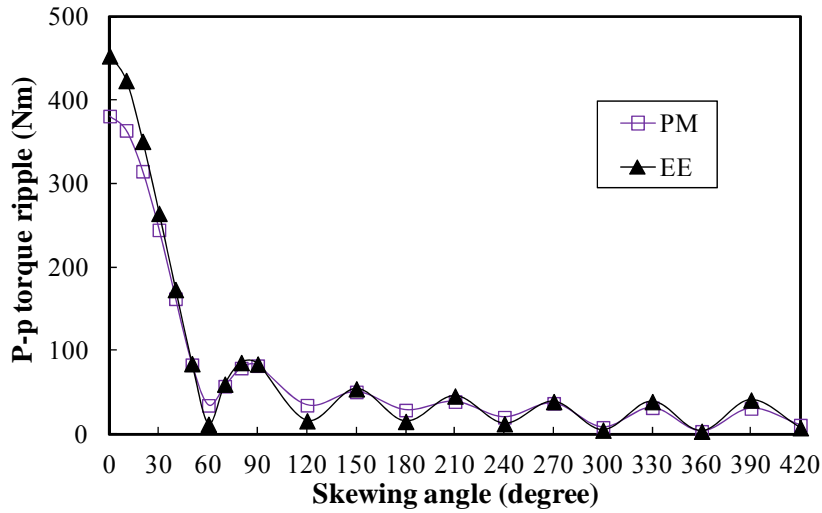


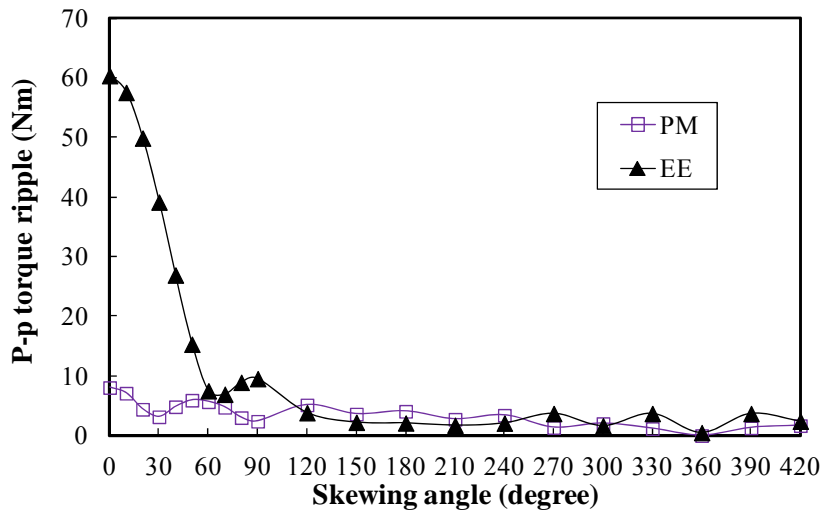
Fig. 7.17. Relative permeability distributions of EE machine with inverse cosine airgap length shaping when  $I_a = 19$  A and  $I_f = 17$  A (White represents that relative permeability is higher than 800).

Based on Figs. 7.11 and 7.12, the influence of skewing on torque ripple reduction in EE and PM machines can be directly compared based on the full load torque ripples in Fig. 7.18. It can be seen that EE machines, with or without rotor skewing, can achieve the same low level of torque ripple with PM machines when the skewing is employed.

The influence of skewing on the average torque in EE and PM machines is compared in Fig. 7.19. It can be seen that the influence of skewing on average torque is the same in EE and PM machines and, hence, can be represented by the average torque skewing factor given in chapter 3.



(a) Without shaping



(b) With rotor shaping

Fig. 7.18. Full load torque ripple variation with skewing angle of EE and PM machines.

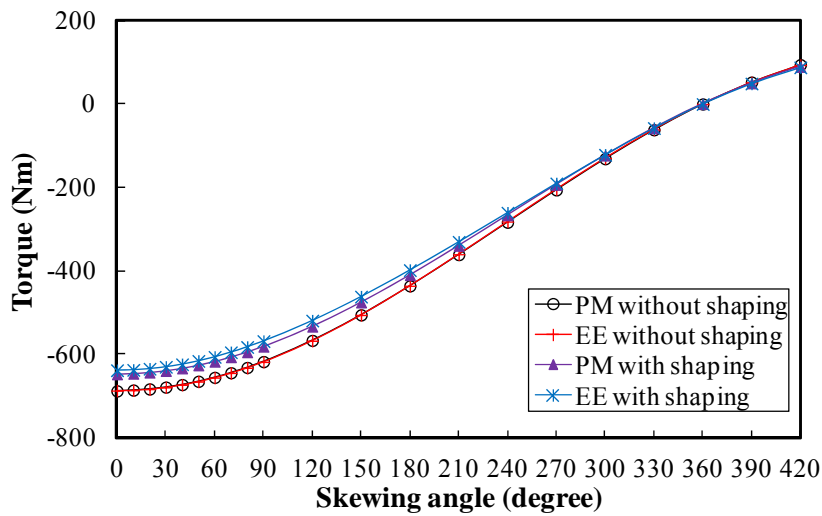


Fig. 7.19. Average torque variation with skewing angle of EE and PM machines when on full load.

## 7.5 Summary

The influence of rotor shaping and skewing on EE machines is investigated and compared with PM machines.

Based the investigation, it is concluded that the average torque of the EE machine having the inverse cosine airgap length shape is slightly lower than the one of PM machine having the cosine magnet shape utilizing the third order harmonic. It can barely improve the average torque of EE machines further by utilizing the third order harmonic. Due to the asymmetric magnetic saturation, the rotor shaping is less effective on torque ripple reduction in EE machines than SPM machines. However, with the rotor skewing, EE machine still can achieve the same low level of torque ripple with PM machines.

# CHAPTER 8 GENERAL CONCLUSION AND FUTURE WORK

## 8.1 Conclusions

EE and PM machines are two most widely employed electric machines, especially for direct drive applications. Although PM machines have the advantages of high torque density and efficiency, with recent significant increase in the price of rare-earth magnets, EE machines, which are non-rare-earth magnet machines, are increasingly attractive as the potential replacement candidate. In this thesis, the torque characteristics, both average torque and torque ripple, of EE and PM machines are comparatively investigated. The investigation is summarized as follows.

### 8.1.1 Average Torque Optimisation and Comparison

The optimisation of electric machines is always one of the most important topics. The optimisation of PM machines having internal rotor has been discussed intensively in literature. In chapter 2, an analytical model of external rotor PM machines is developed for the optimisation of the maximum torque per volume and validated by both FE and experimental results. It is shown that, instead of the optimal split ratio, which is close to 1, the derivation of optimal flux density ratio and stator split ratio is more useful to guide the designs of external rotor PM machines. The torque density of external rotor PM machines is maximum when the average airgap flux density is slightly lower than half of the maximum flux density in the stator.

In chapter 6, the simplified analytical optimisation and comparison of two torque densities, i.e., torque per volume and torque per weight, between PM and EE machines are presented based on internal rotor machines. It is shown that, for EE machines, the torque is maximum when the excitation and armature copper losses are the same. There is an optimal pole number to maximize the torque densities and it is preferable for large volume applications. The comparison between PM and EE machines shows that PM machines can exhibit more than  $\sqrt{2}$  times torque densities of EE machines when they have the same copper loss. The comparison between optimal  $T/V$  and  $T/G$  designs shows that the optimal  $T/G$  designs have significantly higher split ratio and more cost-effective than the optimal  $T/V$  designs.

### **8.1.2 Torque Ripple Minimization**

Apart from the average torque optimisation, the torque ripple minimization is another important issue, since the machine is directly connected to the load in the DD systems and, hence, the requirement on the torque ripple is much higher than the one in the geared systems.

In chapter 3, the influence of skewing on torque ripples in PM machines is investigated. It is found that the effectiveness of skewing largely depends on the axial variation of torque ripple phase but less on its magnitude under skewing. It is further found that, in both linear and nonlinear cases, the EM and on-load torque ripples cannot be fully eliminated by skewing one on-load torque ripple period or any other angles, except  $360^\circ$  electrical, which is impractical. This is due to the fact that the EM torque ripple, especially its phase, of each slice is different due to the axial variation of equivalent current phase advance angle introduced by the skewing. In nonlinear cases, the EM torque ripple variation is further aggravated by the axial variation of magnetic saturation. The EM torque ripple as well as the on-load torque ripples may be even increased by skewing, especially when the cogging torque is low and electric loading is high. Furthermore, it is also found that, by optimising the skewing angle and current phase advance angle together, the improved skewing is able to reduce the torque ripple further to meet the stringent torque ripple requirement over the whole load range when the conventional skewing fails.

The influence of rotor shaping and skewing on EE machines is investigated and compared with PM machines in chapter 7. It shows that the average torque of the EE machine having the inverse cosine airgap length shape is only slightly lower than the one of PM machines with the rotor shaping utilizing the third order harmonic. However, it can barely improve the average torque of EE machines further by utilizing the third order harmonic. Due to the asymmetric magnetic saturation, the rotor shaping is less effective on torque ripple reduction in EE machines than SPM machines. However, using the rotor skewing, EE machines can still achieve the same low level of torque ripple as PM machines.

### **8.1.3 On-load Torque Separation**

Meanwhile, in order to further understand the characteristics of on-load torque and, hence, improve it, the separation of the on-load torque of PM machines into its individual torque components is investigated as well.

In chapter 4, the investigation is focused on the average torque separation. It is found that, although the Maxwell stress tensor and virtual work principle should result in identical

torques in normal FE analyses when appropriate FE meshes are used, the average torques calculated by these two methods are found to be different when the FP method is employed. This is due to the influence of equivalent rotational magnetic saliency in the stator, which causes a part of PM torque being improperly attributed to the reluctance torque when the Maxwell stress tensor method is employed. However, by using the virtual work principle, this is eliminated, and, hence, the average torque components can still be appropriately separated and analysed.

In chapter 5, the calculation of on-load cogging torque of PM machines, which is most difficult challenge for the on-load torque separation, is investigated. It is found that vast majority of existing methods for calculating the cogging torque, no matter whether analytical or numerical methods, neglect the influence of load, or are inappropriate in considering the influence of load. Without using the frozen permeability method, the torque calculated by the virtual work principle includes the magnetic energy due to the armature field. When using the frozen permeability method, the resultant torque based on the Maxwell stress tensor with the on-load permanent magnet field only has nonzero average torque and, hence, is not the on-load cogging torque. However, all the shortcomings of existing methods can be avoided and, hence, the on-load cogging torque can be calculated appropriately using the proposed method based on the combination of the virtual work principle and frozen permeability method. For the implementation of the proposed method, an improved frozen permeability method, which makes the magnetic energy with on-load permanent magnet field only can be calculated according to the B-H curve, has been developed as well.

## **8.2 Future Work**

Following the investigation in this thesis, the future research can be listed as follows.

### **8.2.1 Ways of Reducing $Q$ -axis Magnetic Field in EE Machines**

As shown in chapter 7, the asymmetric magnetic saturation, which is due to the  $q$ -axis magnetic field, causes the rotor shaping less effective on torque ripple reduction in EE machines. It is also shown in chapter 6 that, the magnetic saturation, along both  $d$ - and  $q$ -axes, results in lower magnetic permeability and, hence, average torque. Therefore, it is desirable to reduce the  $q$ -axis magnetic field in EE machines. Definitely, the rotor pole shoe height, especially the rotor pole shoulder height, is one of key parameters to be investigated.

### **8.2.2 Torque Ripple Reduction in EE Machines Using Combined Rotor Shapes**

Due to the asymmetric magnetic saturation, which is due to q-axis magnetic field, the rotor shapings are less effective on torque ripple reduction in EE machines. In order to achieve the similar torque ripple as PM machines, skewing needs to be employed in EE machines. However, the skewing results in lower average torque, more complicated machine structure and higher cost. Therefore, other torque ripple reduction methods, such as combining different rotor shapes within one EE machine, may be preferred instead of skewing.

## References

- [1] Global Wind Energy Council, "Global wind report: annual market update 2011," available: [http://gwec.net/wp-content/uploads/2012/06/Annual\\_report\\_2011\\_lowres.pdf](http://gwec.net/wp-content/uploads/2012/06/Annual_report_2011_lowres.pdf).
- [2] Global Wind Energy Council (GWEC), "Global wind 2009 report," available: <http://www.gwec.net/index.php?id=167>.
- [3] European Wind Energy Association, "Wind energy – the facts – executive summary," available: [http://www.ewea.org/fileadmin/ewea\\_documents/documents/publications/WETF/Facts\\_Summary.pdf](http://www.ewea.org/fileadmin/ewea_documents/documents/publications/WETF/Facts_Summary.pdf).
- [4] Global Wind Energy Council (GWEC), "Wind force 12: a blueprint to achieve 12% of the world's electricity from wind power by 2020," available: [http://www.ewea.org/fileadmin/ewea\\_documents/documents/publications/WF12/wf\\_12-2005.pdf](http://www.ewea.org/fileadmin/ewea_documents/documents/publications/WF12/wf_12-2005.pdf).
- [5] U.S. Department of Energy, "2010 solar technologies market report," available: <http://www.nrel.gov/docs/fy12osti/51847.pdf>.
- [6] Renewable UK, "Marine energy in the UK: state of the industry report 2012," available: <http://www.hi-energy.org.uk/Downloads/General%20Documents/Wave%20and%20Tidal%20SOI%202012.pdf>.
- [7] Emerging energy research, "Global ocean energy markets and strategies: 2010–2030," available: [http://www.emerging-energy.com/uploadDocs/Excerpt\\_GlobalOceanEnergyMarketsandStrategies2010.pdf](http://www.emerging-energy.com/uploadDocs/Excerpt_GlobalOceanEnergyMarketsandStrategies2010.pdf).
- [8] World energy council, "2010 survey of energy resource," available: [http://www.worldenergy.org/documents/ser\\_2010\\_report\\_1.pdf](http://www.worldenergy.org/documents/ser_2010_report_1.pdf).
- [9] M. Ehsani, G. Yimin, and J. M. Miller, "Hybrid electric vehicles: architecture and motor drives," *Proc. IEEE*, vol. 95, no. 4, pp. 719-728, Apr. 2007.
- [10] C. C. Chan, "The state of the art of electric, hybrid, and fuel cell vehicles," *Proc. IEEE*, vol. 95, no. 4, pp. 704-718, Apr. 2007.
- [11] Z. Q. Zhu and D. Howe, "Electrical machines and drives for electric, hybrid, and fuel cell vehicles," *Proc. IEEE*, vol. 95, no. 4, pp. 746-765, Apr. 2007.
- [12] Z. Q. Zhu and C. C. Chan, "Electrical machine topologies and technologies for electric, hybrid, and fuel cell vehicles," in *IEEE Veh. Power Propulsion Conf.*, Harbin, China, 2008, pp. 1-6.
- [13] Z. Q. Zhu, "Fractional slot permanent magnet brushless machines and drives for electric and hybrid propulsion systems," in *Elect. Veh. Renew. Energies*, Monaco, 2009.
- [14] J. D. Santiago, H. Bernhoff, B. Ekergrd, S. Eriksson, S. Ferhatovic, R. Waters, and M. Leijon, "Electrical motor drivelines in commercial all-electric vehicles: a review," *IEEE Trans. Veh. Technol.*, vol. 61, no. 2, pp. 475-484, Feb. 2012.
- [15] A. M. El-Refaeie, "Motors/generators for traction /propulsion applications: a review," in *IEEE Int. Elect. Mach. Drives Conf.*, Niagara Falls, Canada, 2011, pp. 490-497.
- [16] W. P. Cao, B. C. Mecrow, G. J. Atkinson, J. W. Bennett, and D. J. Atkinson, "Overview of electric motor technologies used for more electric aircraft (MEA)," *IEEE Trans. Ind. Electron.*, vol. 59, no. 9, pp. 3523-3531, Sep. 2012.
- [17] J. Ribrant, and L. M. Bertling, "Survey of failures in wind power systems with focus on Swedish wind power plants during 1997–2005," *IEEE Trans. Energy Convers.*, vol. 22, no. 1, pp. 167-173, March 2007.
- [18] P. J. Tavner, J. Xiang, and F. Spinato, "Reliability analysis for wind turbines," *Wind Energy*, vol. 10, no. 1, pp. 1-18, 2007.

- [19] F. Spinato, P. J. Tavner, G. J. W. van Bussel, and E. Koutoulakos, "Reliability of wind turbine subassemblies," *IET Renew. Power Generat.*, vol. 3, no. 4, pp. 387-401, 2009.
- [20] R. S. Semken, M. Polikarpova, Ro, x, ytta, P., J. Alexandrova, J. Pyrhonen, J. Nerg, A. Mikkola, and J. Backman, "Direct-drive permanent magnet generators for high-power wind turbines: benefits and limiting factors," *IET Renew. Power Generat.*, vol. 6, no. 1, pp. 1-8, 2012.
- [21] H. Polinder, F. F. A. van der Pijl, G. J. de Vilder, and P. J. Tavner, "Comparison of direct-drive and geared generator concepts for wind turbines," *IEEE Trans. Energy Convers.*, vol. 21, no. 3, pp. 725-733, Sep. 2006.
- [22] H. Li and Z. Chen, "Overview of different wind generator systems and their comparisons," *IET Renew. Power Generat.*, vol. 2, no. 2, pp. 123-138, 2008.
- [23] L. H. Hansen, L. Helle, F. Blaabjerg, E. Ritchie, and S. Munk-Nielsen, "Conceptual survey of Generators and Power Electronics for Wind Turbines," Risø Nat. Lab., Roskilde, Denmark, Tech. Rep., 2001.
- [24] Q. Gao, C. Liu, B. Xie, and X. Cai, "Evaluation of the mainstream wind turbine concepts considering their reliabilities," *IET Renew. Power Generat.*, vol. 6, no. 5, pp. 348-357, 2012.
- [25] M. Aydin, Z. Q. Zhu, T. A. Lipo, and D. Howe, "Minimization of cogging torque in axial-flux permanent-magnet machines: design concepts," *IEEE Trans. Magn.*, vol. 43, no. 9, pp. 3614-3622, Sep. 2007.
- [26] M. Aydin, H. Surong, and T. A. Lipo, "Torque quality and comparison of internal and external rotor axial flux surface-magnet disc machines," *IEEE Trans. Ind. Electron.*, vol. 53, no. 3, pp. 822-830, Jun. 2006.
- [27] K. M. Rahman, N. R. Patel, T. G. Ward, J. M. Nagashima, F. Caricchi, and F. Crescimbin, "Application of direct-drive wheel motor for fuel cell electric and hybrid electric vehicle propulsion system," *IEEE Trans. Ind. Appl.*, vol. 42, no. 5, pp. 1185-1192, Sep./Oct. 2006.
- [28] G. De Donato, F. G. Capponi, G. A. Rivellini, and F. Caricchi, "Integral-slot versus fractional-slot concentrated-winding axial-flux permanent-magnet machines: comparative design, FEA, and experimental tests," *IEEE Trans. Ind. Appl.*, vol. 48, no. 5, pp. 1487-1495, Sep./Oct. 2012.
- [29] H. Weh and H. May, "Achievable force densities for permanent magnet excited machines in new configurations," in *Proc. Int. Conf. Elect. Mach.*, Munchen, 1986, pp. 1107-1111.
- [30] Y. Zhao and J. Chai, "Power factor analysis of transverse flux permanent machines," in *Int. Conf. Elect. Mach. Syst.*, Nanjing, China, 2005, pp. 450-459.
- [31] M. Cheng, W. Hua, J. Zhang, and W. Zhao, "Overview of stator-permanent magnet brushless machines," *IEEE Trans. Ind. Electron.*, vol. 58, no. 11, pp. 5087-5101, Nov. 2011.
- [32] Z. Q. Zhu, "Switched flux permanent magnet machines - innovation continues," in *Int. Conf. Elect. Mach. Syst.*, Beijing, China, 2011, pp. 1-10.
- [33] K. T. Chau, C. C. Chan, and L. Chunhua, "Overview of permanent-magnet brushless drives for electric and hybrid electric vehicles," *IEEE Trans. Ind. Electron.*, vol. 55, no. 6, pp. 2246-2257, Jun. 2008.
- [34] Y. Liao, F. Liang, and T. A. Lipo, "A novel permanent magnet motor with doubly salient structure," *IEEE Trans. Ind. Appl.*, vol. 31, no. 5, pp. 1069-1078, Sep./Oct. 1995.

- [35] W. Hua, Z. Q. Zhu, M. Cheng, Y. Pang, and D. Howe, "Comparison of flux-switching and doubly-salient permanent magnet brushless machines," in *Int. Conf. Elect. Mach. Syst.*, Nanjing, China, 2005, pp. 165-170
- [36] R. P. Deodhar, S. Andersson, I. Boldea, and T. J. E. Miller, "The flux-reversal machine: a new brushless doubly-salient permanent-magnet machine," *IEEE Trans. Ind. Appl.*, vol. 33, no. 4, pp. 925-934, Jul./Aug. 1997.
- [37] C. Wang, S. A. Nasar, and I. Boldea, "Three-phase flux reversal machine (FRM)," *IEE Proc. Elect. Power Appl.*, vol. 146, no. 2, pp. 139-146, Mar. 1999.
- [38] E. Hoang, A. H. ben-Ahmed, and J. Lucidarme, "Switching flux permanent magnet polyphase machines," in *Proc. Eur. Conf. Power. Electron. Appl.*, Trondheim, Norway, 1997, pp. 903-908.
- [39] J. T. Chen and Z. Q. Zhu, "Winding configurations and optimal stator and rotor pole combination of flux-switching PM brushless AC machines," *IEEE Trans. Energy Convers.*, vol. 25, no. 2, pp. 293-302, Jun. 2010.
- [40] J. T. Chen and Z. Q. Zhu, "Comparison of all- and alternate-poles-wound flux-switching PM machines having different stator and rotor pole numbers," *IEEE Trans. Ind. Appl.*, vol. 46, no. 4, pp. 1406-1415, Jul./Aug. 2010.
- [41] J. T. Chen, Z. Q. Zhu, and D. Howe, "Stator and rotor pole combinations for multi-tooth flux-switching permanent-magnet brushless AC machines," *IEEE Trans. Magn.*, vol. 44, no. 12, pp. 4659-4667, Dec. 2008.
- [42] J. T. Chen, Z. Q. Zhu, S. Iwasaki, and R. P. Deodhar, "A novel E-core switched-flux pm brushless AC machine," *IEEE Trans. Ind. Appl.*, vol. 47, no. 3, pp. 1273-1282, May/June. 2011.
- [43] J. T. Chen, Z. Q. Zhu, S. Iwasaki, and R. P. Deodhar, "A novel hybrid-excited switched-flux brushless AC machine for EV/HEV applications," *IEEE Trans. Veh. Technol.*, vol. 60, no. 4, pp. 1365-1373, May 2011.
- [44] A. S. Thomas, Z. Q. Zhu, R. L. Owen, G. W. Jewell, and D. Howe, "Multiphase flux-switching permanent-magnet brushless machine for aerospace application," *IEEE Trans. Ind. Appl.*, vol. 45, no. 6, pp. 1971-1981, Nov./Dec. 2009.
- [45] A. Thomas, Z. Zhu, and L. Wu, "Novel modular rotor switched-flux permanent magnet machines," *IEEE Trans. Ind. Appl.*, vol. 48, no. 6, pp. 2249-2258, Nov./Dec. 2012.
- [46] J. Cros and P. Viarouge, "Synthesis of high performance PM motors with concentrated windings," *IEEE Trans. Energy Convers.*, vol. 17, no. 2, pp. 248-253, Jun. 2002.
- [47] A. M. El-Refaie, "Fractional-slot concentrated-windings synchronous permanent magnet machines: opportunities and challenges," *IEEE Trans. Ind. Electron.*, vol. 57, no. 1, pp. 107-121, Jan. 2010.
- [48] F. Magnussen and H. Lendenmann, "Parasitic effects in PM machines with concentrated windings," *IEEE Trans. Ind. Appl.*, vol. 43, no. 5, pp. 1223-1232, Sep./Oct. 2007.
- [49] N. Bianchi, S. Bolognani, M. D. Pre, and G. Grezzani, "Design considerations for fractional-slot winding configurations of synchronous machines," *IEEE Trans. Ind. Appl.*, vol. 42, no. 4, pp. 997-1006, Jul./Aug. 2006.
- [50] L. Alberti and N. Bianchi, "Theory and design of fractional-slot multilayer windings," in *IEEE Energy Conv. Congr. Expo.*, Phoenix, USA, 2011, pp. 141-145.
- [51] P. B. Reddy, A. M. El-Refaie, H. Kum-Kang, J. K. Tangudu, and T. M. Jahns, "Comparison of interior and surface PM machines equipped with fractional-slot concentrated windings for hybrid traction applications," *IEEE Trans. Energy Convers.*, vol. 27, no. 3, pp. 593-602, Sep. 2012.

- [52] R. Pena, J. C. Clare, and G. M. Asher, "Doubly fed induction generator using back-to-back PWM converters and its application to variable-speed wind-energy generation," *Proc. Inst. Elect. Eng. - Elect. Power Appl.*, vol. 143, no. 3, pp. 231-241, May 1996.
- [53] R. Cardenas, R. Pena, S. Alepuz, and G. Asher, "Overview of control system for the operation of DFIGs in wind energy application," *IEEE Trans. Ind. Electron.*, vol. 59, no. 5, pp. 2041-2048, May 2012.
- [54] T. H. Liu, J. R. Fu, and T. A. Lipo, "A strategy for improving reliability of field-oriented controlled induction motor drives," *IEEE Trans. Ind. Appl.*, vol. 29, no. 5, pp. 910-918, Sep./Oct. 1993.
- [55] Y. Zhao and T. A. Lipo, "Space vector PWM control of dual three-phase induction machine using vector space decomposition," *IEEE Trans. Ind. Appl.*, vol. 31, no. 5, pp. 1100-1109, Sep./Oct. 1995.
- [56] R. O. C. Lyra and T. A. Lipo, "Torque density improvement in a six-phase induction motor with third harmonic current injection," *IEEE Trans. Ind. Appl.*, vol. 38, no. 5, pp. 1351-1360, Sep./Oct. 2002.
- [57] L. Alberti and N. Bianchi, "Experimental tests of dual three-phase induction motor under faulty operating condition," *IEEE Trans. Ind. Electron.*, vol. 59, no. 5, pp. 2041-2048, May 2012.
- [58] J. F. Eastham, T. Cox, and J. Proverbs, "Application of planar modular windings to linear induction motors by harmonic cancellation," *IET Elect. Power Appl.*, vol. 4, no. 3, pp. 140-148, 2010.
- [59] E. Levi, R. Bojoi, F. Profumo, H. A. Toliyat, and S. Williamson, "Multiphase induction motor drives - a technology status review," *IET Elect. Power Appl.*, vol. 1, no. 4, pp. 489-516, 2007.
- [60] I. Boldea, *The Electrical Generators Handbook: Synchronous Generators*. Boca Raton: Taylor & Francis, 2006.
- [61] R. Qu, Y. Liu, and J. Wang, "Review of superconducting generator topologies for direct-drive wind turbines," *IEEE Trans. on Appl. Supercond.*, vol. 23, no. 3, pp. 5201108-5201108, Jun. 2013.
- [62] C. Rossi, D. Casadei, A. Pilati, and M. Marano, "Wound rotor salient pole synchronous machine drive for electric traction," in *Conf. Rec. IEEE Industry Appl.*, Tampa, Florida, 2006, pp. 1235-1241.
- [63] G. Friedrich, "Experimental comparison between wound rotor and permanent magnet synchronous machine for integrated starter generator applications," in *IEEE Energy Conv. Congr. Expo*, Atlanta, USA, 2010, pp. 1731-1736.
- [64] A. Griffo, D. Drury, T. Sawata, and P. H. Mellor, "Sensorless starting of a wound-field synchronous starter/generator for aerospace applications," *IEEE Trans. Ind. Electron.*, vol. 59, no. 9, pp. 3579-3587, Sep. 2012.
- [65] C. A. Luongo, P. J. Masson, T. Nam, D. Mavris, H. D. Kim, G. V. Brown, M. Waters, and D. Hall, "Next generation more-electric aircraft: a potential application for HTS superconductors," *IEEE Trans. on Appl. Supercond.*, vol. 19, no. 3, pp. 1055-1068, Jun. 2009.
- [66] H. Liu, L. Xu, M. Shangguan, and W. N. Fu, "Finite element analysis of 1 mw high speed wound-rotor synchronous machine," *IEEE Trans. Magn.*, vol. 48, no. 11, pp. 4650-4653, Nov. 2012.
- [67] R. Schiferl, A. Flory, W. C. Livoti, and S. D. Umans, "High-temperature superconducting synchronous motors: economic issues for industrial applications," *IEEE Trans. Ind. Appl.*, vol. 44, no. 5, pp. 1376-1384, Sep./Oct. 2008.

- [68] M. L. Bash and S. D. Pekarek, "Modeling of salient-pole wound-rotor synchronous machines for population-based design," *IEEE Trans. Energy Convers.*, vol. 26, no. 2, pp. 381-392, Jun. 2011.
- [69] M. L. Bash and S. Pekarek, "Analysis and validation of a population-based design of a wound-rotor synchronous machine," *IEEE Trans. Energy Convers.*, vol. 27, no. 3, pp. 603-614, Sep. 2012.
- [70] C. C. Mi, L. Yongbin, and H. Karmaker, "Modeling of the starting performance of large solid-pole synchronous motors using equivalent circuit approach," *IEEE Trans. Magn.*, vol. 45, no. 12, pp. 5399-5404, Dec. 2009.
- [71] D. G. Dorrell and M. Popescu, "Effect of winding asymmetries and winding connection on small synchronous machines," *IEEE Trans. Ind. Appl.*, vol. 47, no. 6, pp. 2453-2459, Nov./Dec. 2011.
- [72] G. Traxler-Samek, T. Lugand, and M. Uemori, "Vibrational forces in salient pole synchronous machines considering tooth ripple effects," *IEEE Trans. Ind. Electron.*, vol. 59, no. 5, pp. 2258-2266, May 2012.
- [73] K. Yamazaki, S. Tamiya, K. Shima, and T. Fukami, "Reduction of magnetic saturation by using additional permanent magnets in synchronous machines," in *IEEE Energy Conv. Congr. Expo.*, Phoenix, USA, 2011, pp. 141-145.
- [74] A. G. Jack, B. C. Mecrow, and J. A. Haylock, "A comparative study of permanent magnet and switched reluctance motors for high-performance fault-tolerant applications," *IEEE Trans. Ind. Appl.*, vol. 32, no. 4, pp. 889-895, Jul./Aug. 1996.
- [75] K. M. Rahman, B. Fahimi, G. Suresh, A. V. Rajarathnam, and M. Ehsani, "Advantages of switched reluctance motor applications to EV and HEV: design and control issues," *IEEE Trans. Ind. Appl.*, vol. 36, no. 1, pp. 111-121, Jan./Feb. 2000.
- [76] B. C. Mecrow, E. A. El-Kharashi, J. W. Finch, and A. G. Jack, "Preliminary performance evaluation of switched reluctance motors with segmental rotors," *IEEE Trans. Energy Convers.*, vol. 19, no. 4, pp. 679-686, Dec. 2004.
- [77] K. Vijayakumar, R. Karthikeyan, S. Paramasivam, R. Arumugam, and K. N. Srinivas, "Switched reluctance motor modeling, design, simulation, and analysis: a comprehensive review," *IEEE Trans. Magn.*, vol. 44, no. 12, pp. 4605-4617, Dec. 2008.
- [78] H.-C. Chang and C.-M. Liaw, "Development of a compact switched-reluctance motor drive for EV propulsion with voltage-boosting and PFC charging capabilities," *IEEE Trans. Veh. Technol.*, vol. 58, no. 7, pp. 3198-3215, Sep. 2009.
- [79] X. D. Xue, K. W. E. Cheng, T. W. Ng, and N. C. Cheung, "Multi-objective optimization design of in-wheel switched reluctance motors in electric vehicles," *IEEE Trans. Ind. Electron.*, vol. 57, no. 9, pp. 2980-2987, Sep. 2010.
- [80] J.-M. Park, K. Sung-Il, H. Jung-Pyo, and L. Jung-Ho, "Rotor design on torque ripple reduction for a synchronous reluctance motor with concentrated winding using response surface methodology," *IEEE Trans. Magn.*, vol. 42, no. 10, pp. 3479-3481, 2006.
- [81] N. Bianchi, S. Bolognani, D. Bon, and M. Dai Pre, "Torque harmonic compensation in a synchronous reluctance motor," *IEEE Trans. Energy Convers.*, vol. 23, no. 2, pp. 466-473, Jun. 2008.
- [82] N. Bianchi, S. Bolognani, D. Bon, and M. Dai Pre, "Rotor flux-barrier design for torque ripple reduction in synchronous reluctance and PM-assisted synchronous reluctance motors," *IEEE Trans. Ind. Appl.*, vol. 45, no. 3, pp. 921-928, May/Jun. 2009.

- [83] Y. Amara, L. Vido, M. Gabsi, E. Hoang, A. Hamid Ben Ahmed, and M. Lecrivain, "Hybrid excitation synchronous machines: energy-efficient solution for vehicles propulsion," *IEEE Trans. Veh. Technol.*, vol. 58, no. 5, pp. 2137-2149, Jun. 2009.
- [84] L. Yang, "Twenty five years development of global NdFeB magnet industry," *J. Magn. Mater. Devices*, vol. 39, no.6, pp. 9-18, Dec. 2008.
- [85] M. Sagawa, S. Fujimura, N. Togawa, H. Yamamoto, and Y. Matsuura, "New material for permanent magnets on base of Nd and Fe," *J. Appl. Phys.*, vol. 55, Part IIA, pp. 2083-2087, 1985.
- [86] N. Bianchi and A. Lorenzoni, "Permanent magnet generators for wind power industry: an overall comparison with traditional generators," in *Int. Conf. Opportunities Advances Int. Elect. Power Generat.*, 1996, pp. 49-54.
- [87] G. Komurgoz and T. Gundogdu, "Comparison of salient pole and permanent magnet synchronous machines designed for wind turbines," in *IEEE Power Electron. Mach. Wind Appl.*, Denver, USA, 2012, pp. 1-5.
- [88] M. Bash, S. Pekarek, S. Sudhoff, J. Whitmore, and M. Frantzen, "A comparison of permanent magnet and wound rotor synchronous machines for portable power generation," in *Power Energy Conf. Illinois*, Urbana, USA, 2010, pp. 1-6.
- [89] J. H. Walker, "Output coefficient of synchronous machines: a new concept," *Proc. Inst. Elect. Eng.*, vol. 115, no. 12, pp. 1-5, Dec. 1968.
- [90] V. B. Honsinger, "Sizing equations for electrical machinery," *IEEE Trans. Energy Convers.*, vol. EC-2, no. 1, pp. 116-121, Mar. 1987.
- [91] S. Huang, J. Luo, F. Leonardi, and T. A. Lipo, "A general approach to sizing and power density equations for comparison of electrical machines," *IEEE Trans. Ind. Appl.*, vol. 34, no. 1, pp. 92-97, Jan./Feb. 1998.
- [92] S. Huang, J. Luo, F. Leonardi, and T. A. Lipo, "A comparison of power density for axial flux machines based on general purpose sizing equations," *IEEE Trans. Energy Convers.*, vol. 14, no. 2, pp. 185-192, Jun. 1999.
- [93] D. E. Hesmondhalgh, D. Tipping, and M. Amrani, "Design and construction of a high-speed high-performance direct-drive handpiece," *IEE Proc. Elect. Power Appl.*, vol. 134, No. 6, pp. 286-296, Nov. 1987.
- [94] F. B. Chaaban, "Determination of the optimum rotor/stator diameter ratio of permanent magnet machines," *Electr. Mach. Power Syst.*, vol. 22, pp. 521-531, 1994.
- [95] F. B. Chaaban and El-Hajj, "A cost-effective design approach for per permanent magnet machines," *Electr. Mach. Power Syst.*, vol. 28, pp. 893-900, 2000.
- [96] Z. Q. Zhu, K. Ng, and D. Howe, "Design and analysis of high-speed brushless permanent magnet motors," in *Proc. IEE Int. Conf. Elect. Mach Drives*, Cambridge, UK, 1997, pp. 381-358.
- [97] Y. Pang, Z. Q. Zhu, and D. Howe, "Analytical determination of optimal split ratio for permanent magnet brushless motors," *IEE Proc. Elect. Power Appl.*, vol. 153, no. 1, pp. 7-13, Jan. 2006.
- [98] L. J. Wu, Z. Q. Zhu, J. T. Chen, Z. P. Xia, and G. W. Jewell, "Optimal split ratio in fractional-slot interior permanent-magnet machines with non-overlapping windings," *IEEE Trans. Magn.*, vol. 46, no. 5, pp. 1235-1242, May 2009.
- [99] J. Tapia, J. Pyrhonen, J. Puranen, S. Nyman, and P. Lindh, "Optimal design of large permanent magnet synchronous generators", *IEEE Trans. Magn.*, vol. 49, no. 1, pp. 642-650, Jan. 2013.
- [100] Y. Shen, Z. Q. Zhu, and L. J. Wu, "Analytical determination of optimal split ratio for overlapping and none-overlapping winding external rotor PM brushless machines," in *IEEE Int. Elect. Mach. Drive Conf.*, Niagara Falls, Canada, May 2011, pp. 41-46.

- [101] Y. Shen, and Z. Q. Zhu, "Analytical prediction of optimal split ratio for fractional-slot external rotor PM brushless machines," *IEEE Trans. Magn.*, vol. 47, no. 10, pp. 4187-4190, Oct. 2011.
- [102] J. Wang, D. Howe, and Z. Lin, "Design optimization of short-stroke single-phase tubular permanent-magnet motor for refrigeration applications," *IEEE Trans. Ind. Electron.*, vol. 57, no. 1, pp. 327-334, Jan. 2010.
- [103] A. Di Gerlando, G. Foglia, M. F. Iacchetti, and R. Perini, "Axial flux PM machines with concentrated armature windings: design analysis and test validation of wind energy generators," *IEEE Trans. Ind. Electron.*, vol. 58, no. 9, pp. 3795-3805, Sep. 2011.
- [104] A. Boglietti, A. Cavagnino, M. Lazzari, and S. Vaschetto, "Preliminary induction motor electromagnetic sizing based on a geometrical approach," *IET Elect. Power Appl.*, vol. 6, no. 9, pp. 583-592, 2012.
- [105] H. Lee and M. D. Noh, "Optimal design of radial-flux toroidally wound brushless DC machines," *IEEE Trans. Ind. Electron.*, vol. 58, no. 2, pp. 444-449, Feb. 2011.
- [106] R. Vermaak and M. J. Kamper, "Design aspects of a novel topology air-cored permanent magnet linear generator for direct drive wave energy converters," *IEEE Trans. Ind. Electron.*, vol. 59, no. 5, pp. 2104-2115, May 2012.
- [107] V. Delli Colli, F. Marignetti, and C. Attaianesi, "Analytical and multiphysics approach to the optimal design of a 10-MW DFIG for direct-drive wind turbines," *IEEE Trans. Ind. Electron.*, vol. 59, no. 7, pp. 2791-2799, Jul. 2012.
- [108] M.-F. Hsieh and Y.-C. Hsu, "A generalized magnetic circuit modeling approach for design of surface permanent-magnet machines," *IEEE Trans. Ind. Electron.*, vol. 59, no. 2, pp. 779-792, Feb. 2012.
- [109] K. I. Laskaris and A. G. Kladas, "Internal permanent magnet motor design for electric vehicle drive," *IEEE Trans. Ind. Electron.*, vol. 57, no. 1, pp. 138-145, Jan. 2010.
- [110] J. H. J. Potgieter and M. J. Kamper, "Torque and voltage quality in design optimization of low-cost non-overlap single layer winding permanent magnet wind generator," *IEEE Trans. Ind. Electron.*, vol. 59, no. 5, pp. 2147-2156, May 2012.
- [111] G. Y. Sizov, D. M. Ionel, and N. A. O. Demerdash, "Modeling and parametric design of permanent-magnet AC machines using computationally efficient finite-element analysis," *IEEE Trans. Ind. Electron.*, vol. 59, no. 6, pp. 2403-2413, Jun. 2012.
- [112] J. Aubry, H. Ben Ahmed, and B. Multon, "Sizing optimization methodology of a surface permanent magnet machine-converter system over a torque-speed operating profile: application to a wave energy converter," *IEEE Trans. Ind. Electron.*, vol. 59, no. 5, pp. 2116-2125, May 2012.
- [113] N. Bianchi and S. Bolognani, "Design optimisation of electric motors by genetic algorithms," *IEE Proc. Elect. Power Appl.*, vol. 145, no. 5, pp. 475-483, 1998.
- [114] J. D. Ede, Z. Q. Zhu, and D. Howe, "Optimal split ratio for high-speed permanent magnet brushless DC motors," in *Proc. Int. Conf. Elect. Mach. Sys.*, Shenyang, China, 2001, vol. 2, pp. 909-912.
- [115] M. Celebi, "Weight optimization of a salient pole synchronous generator by new genetic algorithm validated by finite element analysis," *IET Elect. Power Appl.*, vol. 3, no. 4, pp.324-333, 2009.
- [116] Y. Tang, Y. Xu, J. Hu, J. Zou, and S. Li, "Optimization of split ratio to design the PM brushless DC motor," in *Proc. Int. Conf. Elect. Mach. Sys.*, Tokyo, Japan, Nov. 2009, pp. 1-5.

- [117] D. Evans, Z. Azar, L. J. Wu, and Z. Q. Zhu, "Comparison of optimal design and performance of PM machines having non-overlapping windings and different rotor topologies," in *Proc. IET Int. Conf. Power Electron., Mach., Drives*, Brighton, UK, Apr. 2010, pp. 1-7.
- [118] M. Barcaro, N. Bianchi, and F. Magnussen, "Permanent-magnet optimization in permanent-magnet-assisted synchronous reluctance motor for a wide constant-power speed range," *IEEE Trans. Ind. Electron.*, vol. 59, no. 6, pp. 2495-2502, Jun. 2012.
- [119] A. J. Rix and M. J. Kamper, "Radial-flux permanent-magnet hub drives: a comparison based on stator and rotor topologies," *IEEE Trans. Ind. Electron.*, vol. 59, no. 6, pp. 2475-2483, Jun. 2012.
- [120] T. M. Jahns and W. L. Soong, "Pulsating torque minimization techniques for permanent magnet AC motor drives - a review," *IEEE Trans. Ind. Appl.*, vol. 43, no. 2, pp. 321-330, Apr. 1996.
- [121] Z. Q. Zhu and D. Howe, "Influence of design parameters on cogging torque in permanent magnet machines," *IEEE Trans. Energy Convers.*, vol. 15, no. 4, pp. 407-412, Dec. 2000.
- [122] N. Bianchi and S. Bolognani, "Design techniques for reducing the cogging torque in surface-mounted PM motors," *IEEE Trans. Ind. Appl.*, vol. 38, no. 5, pp. 1259-1265, Sep./Oct. 2002.
- [123] L. Zhu, S. Z. Jiang, Z. Q. Zhu, and C. C. Chan, "Analytical methods for minimizing cogging torque in permanent-magnet machines," *IEEE Trans. Magn.*, vol. 45, no. 4, pp. 2023-2031, Apr. 2009.
- [124] Z. Q. Zhu, S. Ruangsinchaiwanich, Y. Chen, and D. Howe, "Evaluation of superposition technique for calculating cogging torque in permanent-magnet brushless machines," *IEEE Trans. Magn.*, vol. 42, no. 5, pp. 1597-1603, May 2006.
- [125] D. Zarko, D. Ban, and T. A. Lipo, "Analytical solution for cogging torque in surface permanent-magnet motors using conformal mapping," *IEEE Trans. Magn.*, vol. 44, no. 1, pp. 52-65, Jan. 2008.
- [126] L. J. Wu, Z. Q. Zhu, D. Staton, M. Popescu, and D. Hawkins, "An improved subdomain model for predicting magnetic field of surface-mounted permanent magnet machines accounting for tooth-tips," *IEEE Trans. Magn.*, vol. 47, no. 6, pp. 1693-1704, Jun. 2011.
- [127] T. Li and G. Slemon, "Reduction of cogging torque in permanent magnet motors," *IEEE Trans. Magn.*, vol. 24, no. 6, pp. 2901-2903, Nov. 1988.
- [128] J. De La Ree and N. Boules, "Magnet shaping to reduce induced voltage harmonics in PM machines with surface mounted magnets," *IEEE Trans. Energy Convers.*, vol. 6, no. 1, pp. 155-161, Mar. 1991.
- [129] J. De La Ree and N. Boules, "Induced voltage harmonic reduction of PM cylindrical machines," *IEEE Trans. Ind. Appl.*, vol. 28, no. 3, pp. 619-624, May/June. 1992.
- [130] Z. Q. Zhu, S. Ruangsinchaiwanich, N. Schofield, and D. Howe, "Reduction of cogging torque in interior-magnet brushless machines," *IEEE Trans. Magn.*, vol. 39, no. 5, pp. 3238-3240, Sep. 2003.
- [131] W. Fei and P. Luk, "Torque ripple reduction of a direct-drive permanent magnet synchronous machine by material-efficient axial pole pairing," *IEEE Trans. Ind. Appl.*, vol. 59, no. 6, pp. 2601-2611, Jun. 2012.
- [132] Y. Li, J. Zou, and Y. Lu, "Optimum design of magnet shape in permanent-magnet synchronous motors," *IEEE Trans. Magn.*, vol. 39, no. 6, pp. 3523-3526, Nov. 2003.
- [133] M. F. Hsieh and Y. S. Hsu, "An investigation on influence of magnet arc shaping upon back electromotive force waveforms for design of permanent-magnet brushless motors," *IEEE Trans. Magn.*, vol. 41, no. 10, pp. 3949-3951, Oct. 2005.

- [134] Y. Pang, Z. Q. Zhu, and D. Howe, "Self-shielding magnetized vs shaped parallel magnetized PM brushless as motors," in *Int. Trans. Elect. Mach. Energy Convers. Syst.*, vol. 5-B, no. 1, pp. 13-19, 2005.
- [135] P. Zheng, J. Zhao, J. Han, J. Wang, Z. Yao, and R. Liu, "Optimization of the magnetic pole shape of a permanent-magnet synchronous motor," *IEEE Trans. Magn.*, vol. 43, no. 6, pp. 2531-2533, Jun. 2007.
- [136] Y. Li, J. Xing, T. Wang, and Y. Lu, "Programmable design of magnet shape for permanent-magnet synchronous motors with sinusoidal back EMF waveforms," *IEEE Trans. Magn.*, vol. 44, no. 9, pp. 2163-2167, Sep. 2008.
- [137] S. A. Evans, "Salient pole shoe shapes of interior permanent magnet synchronous machines," in *Int. Conf. Elect. Mach.*, Rome, 2010, pp. 1-6.
- [138] Z. Q. Zhu, K. Wang, and G. Ombach, "Optimal magnet shaping with third order harmonic for maximum torque in brushless AC machines," in *Proc. IEE Int. Conf. Elect. Mach Drives*, Bristol, UK, 2012, pp. 1-6.
- [139] K. Wang, Z. Q. Zhu, G. Ombach, and W. Chlebosz, "Optimal rotor shape with third harmonic for maximizing torque and minimizing torque ripple in IPM motors," in *Int. Conf. Elect. Mach.*, Marseille France, 2012, pp. 397-403.
- [140] P. S. Shin, S. H. Woo, and C. S. Koh, "An optimal design of large scale permanent magnet pole shape using adaptive response surface method with Latin Hypercube sampling strategy," *IEEE Trans. Magn.*, vol. 45, no. 3, pp. 1214-1217, Mar. 2009.
- [141] Y. Pang, Z. Q. Zhu, and Z. J. Feng, "Cogging torque in cost-effective surface-mounted permanent-magnet machines," *IEEE Trans. Magn.*, vol. 47, no. 9, pp. 2269-2276, Sep. 2011.
- [142] S. Lee, Y.-J. Kim, and S.-Y. Jung, "Numerical investigation on torque harmonics reduction of interior PM synchronous motor with concentrated winding," *IEEE Trans. Magn.*, vol. 48, no. 2, pp. 927-930, Feb. 2012.
- [143] R. W. Wieseman, "Graphical determination of magnetic fields practical applications to salient-pole synchronous machine design," *Trans. Amer. Inst. Elect. Eng.*, vol. XLVI, pp. 141-154, Feb. 1927.
- [144] D. Ginsberg, A. L. Jokl, and L. M. Blum, "Calculation of no-load wave shape of salient-pole AC generators," *Trans. Amer. Inst. Elect. Eng.*, vol. 72, no. 2, pp. 974-980, Oct. 1953.
- [145] L. Ovacik and S. J. Salon, "Shape optimization of nonlinear magnetostatic problems using the finite element method embedded in optimizer," *IEEE Trans. Magn.*, vol. 32, no. 5, pp. 4323-4325, Sep. 1996.
- [146] A. Frias, P. Pellerrey, A. K. Lebouc, C. Chillet, V. Lanfranchi, G. Friedrich, L. Albert, and L. Humbert, "Rotor and stator shape optimization of a synchronous machine to reduce iron losses and acoustic noise," in *IEEE Veh. Power Propulsion Conf.*, Seoul, Korea, 2012, pp. 98-103.
- [147] J. F. Eastham, D. M. Ionel, M. J. Balchin, T. Betzer, and E. Demeter, "Finite element analysis of an interior-magnet brushless DC machine, with a step-skewed rotor," *IEEE Trans. Magn.*, vol. 33, no. 2, pp. 2117-2119, Mar. 1997.
- [148] G. H. Jang, J. W. Yoon, K. C. Ro, N. Y. Park, and S. M. Jang, "Performance of a brushless DC motor due to the axial geometry of the permanent magnet," *IEEE Trans. Magn.*, vol. 33, no. 5, pp. 4101-4103, Sep. 1997.
- [149] M. A. Alhamadi and N. A. Demerdash, "Modeling of effects of skewing of rotor mounted permanent magnets on the performance of brushless DC motors," *IEEE Trans. Energy Convers.*, vol. 6, no. 4, pp. 721-729, Dec. 1991.

- [150] M. Lukaniszyn, M. JagieLa, and R. Wrobel, "Optimization of permanent magnet shape for minimum cogging torque using a genetic algorithm," *IEEE Trans. Magn.*, vol. 40, no. 2, pp. 1228-1231, Mar. 2004.
- [151] K. H. Kim, D. J. Sim, and J. S. Won, "Analysis of skew effects on cogging torque and BEMF for BLDCM," in *Conf. Rec. IEEE Ind. Appl. Soc. Ann. Meeting*, Dearborn, MI, Oct. 1991, pp. 191-197.
- [152] D. C. Hanselman, "Effect of skew, pole count and slot count on brushless motor radial force, cogging torque and back EMF," *IEE Proc. Electr. Power Appl.*, vol. 144, no. 5, pp. 325-330, 1997.
- [153] J. Pyrhonen, T. Jokinen, and V. Hrabovcova, *Design of Rotating Electrical Machines*, Chichester, UK: Wiley, 2008.
- [154] M. A. Alhamadi and N. A. Demerdash, "Modeling and experimental verification of the performance of a skew mounted permanent magnet brushless DC motor drive with parameters computed from 3D-FE magnetic field solutions," *IEEE Trans. Energy Convers.*, vol. 9, no. 1, pp. 26-35, Mar. 1994.
- [155] M. A. Alhamadi and N. A. Demerdash, "Three dimensional magnetic field computation by a coupled vector-scalar potential method in brushless DC motors with skewed permanent magnet mounts-the formulation and FE grids," *IEEE Trans. Energy Convers.*, vol. 9, no. 1, pp. 1-14, Mar. 1994.
- [156] F. Piriou and A. Razek, "A model for coupled magnetic-electric circuits in electric machines with skewed slots," *IEEE Trans. Magn.*, vol. 26, no. 2, pp. 1096-1100, Mar. 1990.
- [157] S. Williamson, T. J. Flack, and A. F. Volschenk, "Representation of skew in time-stepped two-dimensional finite-element models of electrical machines," *IEEE Trans. Ind. Appl.*, vol. 31, no. 5, pp. 1009-1015, Sep./Oct. 1995.
- [158] S. L. Ho and W. N. Fu, "A comprehensive approach to the solution of direct-coupled multislice model of skewed rotor induction motors using time-stepping eddy-current finite element method," *IEEE Trans. Magn.*, vol. 33, no. 3, pp. 2265-2273, May 1997.
- [159] S. L. Ho, W. N. Fu, and H. C. Wong, "Direct modeling of the starting process of skewed rotor induction motors using a multi-slice technique," *IEEE Trans. Energy Convers.*, vol. 14, no. 4, pp. 1253-1258, Dec. 1999.
- [160] J. J. C. Gyselinck, L. Vandeveld, and J. A. A. Melkebeek, "Multi-slice FE modeling of electrical machines with skewed slots-the skew discretization error," *IEEE Trans. Magn.*, vol. 37, no. 5, pp. 3233-3237, Sep. 2001.
- [161] J. C. Urresty, J. R. Riba, L. Romeral, and A. Garcia, "A simple 2-D finite-element geometry for analyzing surface-mounted synchronous machines with skewed rotor magnets," *IEEE Trans. Magn.*, vol. 46, no. 11, pp. 3948-3954, Nov. 2010.
- [162] B. Weilharter, O. Biro, S. Rainer, and A. Sterneck, "Computation of rotating force waves in skewed induction machines using multi-slice models," *IEEE Trans. Magn.*, vol. 47, no. 5, pp. 1046-1049, May 2011.
- [163] P. Dziwniel, B. Boualem, F. Piriou, J. P. Ducreux, and P. Thomas, "Comparison between two approaches to model induction machines with skewed slots," *IEEE Trans. Magn.*, vol. 36, no. 4, pp. 1453-1457, Jul. 2000.
- [164] S. Williamson and C. I. McClay, "The effect of axial variations in saturation due to skew on induction motor equivalent-circuit parameters," *IEEE Trans. Ind. Appl.*, vol. 35, no. 3, pp. 1323-1331, Nov./Dec. 1999.
- [165] H. Karmaker and A. M. Knight, "Investigation and simulation of fields in large salient-pole synchronous machines with skewed stator slots," *IEEE Trans. Energy Convers.*, vol. 20, no. 3, pp. 604-610, Sep. 2005.

- [166] H. S. Chen, D. G. Dorrell, and M. C. Tsai, "Design and operation of interior permanent-magnet motors with two axial segments and high rotor saliency," *IEEE Trans. Magn.*, vol. 46, no. 9, pp. 3664-3675, Sep. 2010.
- [167] Z. Azar, Z. Q. Zhu, and G. Ombach, "Influence of electric loading and magnetic saturation on cogging torque, back-EMF and torque ripple of PM machines", *IEEE Trans. Magn.*, vol. 48, no. 10, pp. 2650-2658, Oct. 2012.
- [168] R. Islam, I. Husain, A. Fardoun, and K. McLaughlin, "Permanent-magnet synchronous motor magnet designs with skewing for torque ripple and cogging torque reduction," *IEEE Trans. Ind. Appl.*, vol. 45, no. 1, pp. 152-160, Jan./Feb. 2009.
- [169] J. H. Walker and N. Kerruish, "Open-circuit noise in synchronous machines," *Proc. IEE Power Eng.*, vol. 107, no. 36, pp. 505-512, 1960.
- [170] K. J. Binns and M. Dye, "Effects of slot skew and iron saturation on cogging torques in induction machines," *Proc. Inst. Elect. Eng.*, vol. 117, no. 7, pp. 1249-1252, Jul. 1970.
- [171] X. B. Bomela and M. J. Kamper, "Effect of stator chording and rotor skewing on performance of reluctance synchronous machine," *IEEE Trans. Ind. Appl.*, vol. 38, no. 1, pp. 91-100, Jan./Feb.2002.
- [172] Y. Li and M. Chunting Chris, "Doubly salient permanent-magnet machine with skewed rotor and six-state commutating mode," *IEEE Trans. Magn.*, vol. 43, no. 9, pp. 3623-3629, Sep. 2007.
- [173] J. A. Guemes, A. M. Iraolagoitia, J. I. Del Hoyo, and P. Fernandez, "Torque analysis in permanent-magnet synchronous motors: a comparative study," *IEEE Trans. Energy Convers.*, vol. 26, no. 1, pp. 55-63, Mar. 2011.
- [174] S.-H. Han, T. M. Jahns, W. L. Soong, M. K. Guven, and M. S. Illindala, "torque ripple reduction in interior permanent magnet synchronous machines using stators with odd number of slots per pole pair," *IEEE Trans. Energy Convers.*, vol. 25, no. 1, pp. 118-127, Mar. 2010.
- [175] D. G. Dorrell and M. Popescu, "Odd stator slot numbers in brushless DC machines - an aid to cogging torque reduction," *IEEE Trans. Magn.*, vol. 47, no. 10, pp. 3012-3015, Oct. 2011.
- [176] N. Bianchi, S. Bolognani, and A. D. F. Cappello, "Reduction of cogging force in PM linear motors by pole-shifting," *IEE Proc. Elect. Power Appl.*, vol. 152, no. 3, pp. 703-709, 2005.
- [177] L. Dosiek and P. Pillay, "Cogging torque reduction in permanent magnet machines," *IEEE Trans. Ind. Appl.*, vol. 43, no. 6, pp. 1565-1571, Nov.-Dec. 2007.
- [178] Y. Yang, X. Wang, C. Zhu, and C. Huang, "Study of magnet asymmetry for reduction of cogging torque in permanent magnet motors," in *IEEE Conf. Ind. Electron. Appl.*, Xi'an, China2009, pp. 2325-2328.
- [179] C. S. Koh, H. s. Yoon, K. W. Nam, and H. S. Choi, "Magnetic pole shape optimization of permanent magnet motor for reduction of cogging torque," *IEEE Trans. Magn.*, vol. 33, no. 2, pp. 1822-1827, Mar. 1997.
- [180] C. S. Koh and J. S. Seol, "New cogging-torque reduction method for brushless permanent-magnet motors," *IEEE Trans. Magn.*, vol. 39, no. 6, pp. 3503-3506, Nov. 2003.
- [181] K. Halbach, "Design of permanent magnet multipole magnets with oriented rare earth cobalt material," *Nucl. Instrum. Methods*, vol. 169, pp. 1-10, 1980.
- [182] Z. Q. Zhu, Z. P. Xia, Y. F. Shi, D. Howe, A. Pride, and X. J. Chen, "Performance of Halbach magnetized brushless ac motors," *IEEE Trans. Magn.*, vol. 39, no. 5, pp. 2992-2994, Sep. 2003.

- [183] J. Holtz and L. Springob, "Identification and compensation of torque ripple in high-precision permanent magnet motor drives," *IEEE Trans. Ind. Appl.*, vol. 43, no. 2, pp. 309-320, Apr. 1996.
- [184] N. Matsui, T. Makino, and H. Satoh, "Autocompensation of torque ripple of direct drive motor by torque observer," *IEEE Trans. Ind. Appl.*, vol. 29, no. 1, pp. 187-194, Jan./Feb. 1993.
- [185] J. X. Xu, S. K. Panda, Y. J. Pan, T. H. Lee, and B. H. Lam, "A modular control scheme for PMSM speed control with pulsating torque minimization," *IEEE Trans. Ind. Appl.*, vol. 51, no. 3, pp. 526-536, Jun. 2004.
- [186] Z. Q. Zhu, Y. Liu, and D. Howe, "Minimizing the influence of cogging torque on vibration of PM brushless machines by direct torque control," *IEEE Trans. Magn.*, vol. 42, no. 10, pp. 3512-3514, Oct. 2006.
- [187] H. Zhu, X. Xiao, and Y. D. Li, "Torque ripple reduction of the torque predictive control scheme for permanent-magnet synchronous motors," *IEEE Trans. Ind. Electron.*, vol. 59, no. 2, pp. 871-877, Feb. 2012.
- [188] M. Dai, A. Keyhani, and T. Sebastian, "Torque ripple analysis of a PM brushless DC motor using finite element method," *IEEE Trans. Energy Convers.*, vol. 19, no. 1, pp. 40-45, Mar. 2004.
- [189] M. S. Islam, S. Mir, T. Sebastian, and S. Underwood, "Design considerations of sinusoidally excited permanent-magnet machines for low-torque-ripple applications," *IEEE Trans. Ind. Appl.*, vol. 41, no. 4, pp. 955-962, Jul./Aug. 2005.
- [190] M. S. Islam, R. Islam, and T. Sebastian, "Experimental verification of design techniques of permanent-magnet synchronous motors for low-torque-ripple applications," *IEEE Trans. Ind. Appl.*, vol. 47, no. 1, pp. 88-95, Jan./Feb. 2011.
- [191] G. Qi, J. T. Chen, Z. Q. Zhu, D. Howe, L. B. Zhou, and C. L. Gu, "Influence of skew and cross-coupling on flux-weakening performance of permanent-magnet brushless AC machines," *IEEE Trans. Magn.*, vol. 45, no. 5, pp. 2110-2117, May 2009.
- [192] N. Bianchi and S. Bolognani, "Magnetic models of saturated interior permanent magnet motors based on finite element analysis," in *Proc. IEEE Ind. Appl. Conf.*, 1998, vol. 1, pp. 27-34.
- [193] J. Hu, J. Zou, and W. Liang, "Finite element calculation of the saturation dq-axes inductance for a direct drive PM synchronous motor considering cross-magnetization," in *Proc. 5th Int. Conf. Power Electron. Drive Syst.*, 2003, vol. 1, pp. 677-681.
- [194] J. K. Tangudu, T. M. Jahns, A. M. El-Refaie, and Z. Q. Zhu, "Segregation of torque components in fractional-slot concentrated-winding interior PM machines using frozen permeability," in *Proc. IEEE Energy Convers. Congr. Expo.*, California, USA, 2009, pp. 3814-3821.
- [195] S. Williamson and A. M. Knight, "Performance of skewed single-phase line-start permanent magnet motors," *IEEE Trans. Ind. Appl.*, vol. 35, no. 3, pp. 577-582, May/June 1999.
- [196] G. H. Kang, J. P. Hong, G. T. Kim, and J. W. Park, "Improved parameter modeling of interior permanent magnet synchronous motor based on finite element analysis," *IEEE Trans. Magn.*, vol. 36, no. 4, pp. 1867-1870, Jul. 2000.
- [197] J. A. Walker, D. G. Dorrell, and C. Cossar, "Flux-linkage calculation in permanent-magnet motors using the frozen permeabilities method," *IEEE Trans. Magn.*, vol. 41, no. 10, pp. 3946-3948, Oct. 2005.

- [198] S. Y. Kwak, J. K. Kim, and H. K. Jung, "Characteristic analysis of multilayer-buried magnet synchronous motor using fixed permeability method," *IEEE Trans. Energy Convers.*, vol. 20, no. 3, pp. 549-555, Sep. 2005.
- [199] J. A. Walker, D. G. Dorrell, and C. Cossar, "Effect of mutual coupling on torque production in switched reluctance motors," *J. Appl. Physics*, vol. 99, no. 10, pp. 08R304-08R304-3, 2006.
- [200] K. Shirai, Y. Tokikuni, K. Shima, T. Fukami, R. Hanaoka, and S. Takata, "Causes of increase in the terminal voltage of a permanent-magnet-assisted salient-pole synchronous machine," in *Proc. Int. Conf. Electr. Mach. Syst.*, Tokyo, Japan, 2009, pp. 1-6.
- [201] G. Dajaku and D. Gerling, "Magnetic radial force density of the PM machine with 12-teeth/10-poles winding topology," in *Proc. IEEE Int. Elect. Mach. Drives Conf.*, Miami, USA, 2009, pp. 1715-1720.
- [202] Z. P. Xia, Z. Q. Zhu, L. J. Wu, and G. W. Jewell, "Comparison of radial vibration forces in 10-pole/12-slot fractional slot surface-mounted and interior PM brushless AC machines," in *Proc. Int. Conf. Elect. Mach.* Rome, Italy, 2010, pp. 1-6.
- [203] S. Salon, S. Bhatia, and D. Burow, "Some aspects of torque calculations in electrical machines," *IEEE Trans. Magn.*, vol. 33, no. 2, pp. 2018-2021, Mar. 1997.
- [204] J. Coulomb, "A methodology for the determination of global electromechanical quantities from a finite element analysis and its application to the evaluation of magnetic forces, torques and stiffness," *IEEE Trans. Magn.*, vol. 19, no. 6, pp. 2514-2519, Nov. 1983.
- [205] W. Muller, "Comparison of different methods of force calculation," *IEEE Trans. Magn.*, vol. 26, no. 2, pp. 1058-1061, Mar. 1990.
- [206] M. Marinescu and N. Marinescu, "Numerical computation of torques in permanent magnet motors by Maxwell stresses and energy method," *IEEE Trans. Magn.*, vol. 24, no. 1, pp. 463-466, Jan. 1988.
- [207] D. Howe and Z. Q. Zhu, "The influence of finite element discretisation on the prediction of cogging torque in permanent magnet excited motors," *IEEE Trans. Magn.*, vol. 28, no. 2, pp. 1080-1083, Mar. 1992.
- [208] D. M. Ionel, M. Popescu, M. I. McGilp, T. J. E. Miller, and S. J. Dellinger, "Assessment of torque components in brushless permanent-magnet machines through numerical analysis of the electromagnetic field," *IEEE Trans. Ind. Appl.*, vol. 41, no. 5, pp. 1149-1158, Sep./Oct. 2005.
- [209] M. Popescu, D. M. Ionel, T. J. E. Miller, S. J. Dellinger, and M. I. McGilp, "Improved finite element computations of torque in brushless permanent magnet motors," *Inst. Electr. Eng. Proc. Electr. Power Appl.*, vol. 152, no. 2, pp. 271-276, 2005.
- [210] N. Bianchi and L. Alberti, "MMF harmonics effect on the embedded FE analytical computation of PM motors," *IEEE Trans. Ind. Appl.*, vol. 46, no. 2, pp. 812-820, Mar./Apr. 2010.
- [211] N. A. Demerdash, R. Wang and R. Secunde, "Three dimensional magnetic fields in extra high speed modified Lundell alternators computed by a combined vector-scalar magnetic potential finite element method," *IEEE Trans. Energy Convers.*, vol. 7, no. 2, pp. 353-366, Jun. 1992.
- [212] Z. Q. Zhu, "Fractional slot permanent magnet brushless machines and drives for electrical and hybrid propulsion systems," *Int. J. Comput. Math. Electr. Electron. Eng.*, vol. 30, no. 1, pp. 9-31, 2011.

- [213] D. G. Dorrell, M. Hsieh, and A. M. Knight, "Alternative rotor designs for high performance brushless permanent magnet machines for hybrid electric vehicles," *IEEE Trans. Magn.*, vol. 48, no. 2, pp. 835-838, Feb. 2012
- [214] A. Wang, Y. Jia, and W. L. Soong, "Comparison of five topologies for an interior permanent-magnet machine for a hybrid electric vehicle," *IEEE Trans. Magn.*, vol. 47, no. 10, pp. 3606-3609, Oct. 2011.
- [215] E. M. Tsampouris, M. E. Beniakar, and A. G. Kladas, "Geometry optimization of PMSMs comparing full and fractional pitch winding configurations for aerospace actuation applications," *IEEE Trans. Magn.*, vol. 48, no.2, pp. 943-946, Feb. 2012.
- [216] M. Villani, M. Tursini, G. Fabri, and L. Castellini, "High reliability permanent magnet brushless motor drive for aircraft application," *IEEE Trans. Ind. Electron.*, vol. 59, no. 5, pp. 2073-2081, May 2012.
- [217] W. Fei, P. Luk, J. Ma, J. X. Shen, and G. Yang, "A high-performance line-start permanent magnet synchronous motor amended from a small industrial three-phase induction motor," *IEEE Trans. Magn.*, vol. 45, no. 10, pp. 4724-4727, Oct. 2009.
- [218] T. J. E. Miller, M. Popescu, C. Cossar, and M. I. McGilp, "Computation of the voltage-driven flux-MMF diagram for saturated PM brushless motors," in *Rec. Ind. Appl. Conf.*, 2005, vol. 2, pp. 1023-1028.
- [219] Y. Liu, Z. Q. Zhu, and D. Howe, "Direct torque control of brushless DC drives with reduced torque ripple," *IEEE Trans. Ind. Appl.*, vol. 41, no. 2, pp. 599-608, Mar.-Apr. 2005.
- [220] R. H. Park, "Two-reaction theory of synchronous machines generalized method of analysis-part I," *Trans. Amer. Inst. Elect. Eng.*, vol. 48, no. 3, pp. 716-727, 1929.
- [221] R. H. Park, "Two-reaction theory of synchronous machines-II," *Trans. Amer. Inst. Elect. Eng.*, vol. 52, no. 2, pp. 352-354, 1933.
- [222] M. Barcaro, N. Bianchi, and F. Magnussen, "Remarks on torque estimation accuracy in fractional-slot permanent magnet motors," *IEEE Trans. Ind. Electron.*, vol. 59, no. 6, pp. 2565-2572, Jun. 2012.
- [223] F. Meier and J. Soulard, "Dq theory applied to a permanent magnet synchronous machine with concentrated windings," in *Proc. IET Conf Power Electron., Mach., Drives*, 2008, pp. 194-198.
- [224] A. Zulu, B. Mecrow, and M. Armstrong, "Investigation of the dq-equivalent model for performance prediction of flux-switching synchronous motors with segmented-rotors," *IEEE Trans. Ind. Electron.*, vol. 59, no. 6, pp. 2393-2402, Jun. 2011.
- [225] P. Campbell, "Comments on energy stored in permanent magnets," *IEEE Trans. Magn.*, vol. 36, no. 1, pp. 401-403, Jan. 2000.
- [226] Y. Kano, T. Kosaka, and N. Matsui, "A simple nonlinear magnetic analysis for axial-flux permanent-magnet machines," *IEEE Trans. Ind. Electron.*, vol. 57, no. 6, pp. 2124-2133, Jun. 2010.
- [227] H. Lee and M. D. Noh, "Optimal design of radial-flux toroidally wound brushless DC machines," *IEEE Trans. Ind. Electron.*, vol. 58, no. 2, pp. 444-449, Feb. 2011.
- [228] Z. Q. Zhu, "A simple method for measuring cogging torque in permanent magnet machines," in *IEEE Power Energy Society General Meeting*, 2009, pp. 1-4.

# **APPENDIX A ANALYTICAL MODELING AND INVESTIGATION OF TRANSIENT RESPONSE OF PM MACHINES WITH THREE-PHASE SHORT-CIRCUIT FAULT**

This section aims to find effective methods to avoid irreversible demagnetisation in PM machines by suppressing the short-circuit current. An analytical model is developed to predict the transient currents, overcoming the problems of previous steady state models which may significantly underestimate the short-circuit current. Although the developed analytical model is simple, it can accurately reveal the relationship between the short-circuit response and design parameters, as its high accuracy is validated by transient finite element analyses and experiments. The characteristics of short-circuit behavior are investigated and several guidelines for improving the short-circuit performance are obtained to aid the machine design

## **A.1 Introduction**

Permanent magnet (PM) machines become increasingly popular in many applications, such as wind power generations and electrical vehicles. However, the irreversible demagnetisation of the magnets in PM machines is a major concern, especially under short-circuit faults which may occur. Many well-known ways of protecting the magnet from demagnetisation are based on the improvement of demagnetisation withstand capability, e.g. the magnet positioning in the rotor [A1], magnet shaping [A2], enlarging air-gap length, and increasing magnet thickness etc. However, these methods have their own limitations, such as reducing electromagnetic performance, requiring more magnets, or needing freedom to change rotor design. This paper aims to find effective design methods to avoid irreversible demagnetisation by suppressing short-circuit current rather than the foregoing techniques. For this purpose, it is helpful to analytically reveal the relationship between the short-circuit response and machine parameters.

Research on the short-circuit failure has a long history [A3]-[A16]. Many works were based on numerically solving the differential equations or finite element (FE) method [A5]-[A11]. However, these methods provide less insight and are time-consuming, and, hence, not as convenient as analytical techniques for machine design and optimisation. The classic 3-phase short-circuit analytical model [A12] mainly focused on generators having damping windings and/or solid poles and was too complicated. Further, the attention was focused on the influence of transient and sub-transient reactances due to conductive components in the rotor

[A14]-[A16]. Thus, it is not appropriate to use for guiding the design of PM machines where synchronous reactance parameters dominate. The influence of synchronous reactance parameters was investigated in [A11] by using a simple analytical model and the design issues were discussed as well. The study considered the magnet flux linkage and saliency ratio, specifically to interior PM machines. However, the model was only developed for the steady state short-circuit current response, which may be inadequate for assessing the risk of demagnetisation. As being well-known and shown later, the transient short-circuit current can be significantly larger than the steady state current. Therefore, it is desirable for the machine design to have a simple analytical model for the transient short-circuit response, which can accurately reveal the influence of synchronous reactance parameters on short-circuit performance.

In this paper, an analytical model of transient response is developed for PM machines without damping windings and solid poles. The expressions of peak transient currents, which may be significantly higher than the steady state one, are obtained. Compared with the classic model, it is simpler and only relies on the synchronous reactance parameters. Hence, it can accurately reveal the relationship between the short-circuit response and design parameters, as its high accuracy is validated by transient FE analyses and experiments. The characteristics of short-circuit behavior are summarized and several guidelines for improving the short-circuit performance are obtained to aid the machine design.

## A.2 Analytical Model

Assuming the machine with initial q-axis current remains at synchronous speed and there is no irreversible demagnetization and negligible eddy currents, the analytical 3-phase symmetric short-circuit model for salient-pole PM machines without damping winding and solid poles is given by

$$\begin{bmatrix} 0 \\ 0 \end{bmatrix} = \begin{bmatrix} R & -\omega L_q \\ \omega L_d & R \end{bmatrix} \begin{bmatrix} I_d(t) \\ I_q(t) \end{bmatrix} + \begin{bmatrix} L_d & 0 \\ 0 & L_q \end{bmatrix} \frac{d}{dt} \begin{bmatrix} I_d(t) \\ I_q(t) \end{bmatrix} + \begin{bmatrix} 0 \\ E \end{bmatrix} \quad (\text{A.1})$$

The response can be divided into two parts:

- 1) Initial current response ( $I_q(0) \neq 0$  and  $E = 0$ )

$$I_d(t)_I = I_q(0) \frac{L_q}{L_d} \frac{1}{\cos \theta_0} e^{-t/\tau} \sin(\omega_d t) \quad (\text{A.2})$$

$$I_q(t)_I = I_q(0) \frac{1}{\cos \theta_0} e^{-t/\tau} \cos(\omega_d t + \theta_1) \quad (\text{A.3})$$

2) EMF response ( $I_q(0) = 0$ , and  $E = \omega \psi_{pm}$ )

$$I_d(t)_E = -\frac{\omega L_q \omega \psi_{pm}}{\omega^2 L_d L_q + R^2} \left[ 1 - \frac{1}{\sin \varphi} e^{-t/\tau} \sin(\omega_d t + \varphi) \right] \quad (\text{A.4})$$

$$I_q(t)_E = -\frac{R \omega \psi_{pm}}{\omega^2 L_d L_q + R^2} \left[ 1 - \frac{L_d \omega}{R} \frac{1}{\sin \varphi} e^{-t/\tau} \cos(\omega_d t + \varphi - \theta_1) \right] \quad (\text{A.5})$$

$$\tau = 2L_d L_q / [R(L_d + L_q)] \quad (\text{A.6})$$

$$\omega_d = \sqrt{\omega^2 - \left[ \frac{R(L_d - L_q)}{2L_d L_q} \right]^2} \quad (\text{A.7})$$

$$\varphi = \text{acos} \left[ \frac{R(L_d + L_q)}{2L_d L_q} \sqrt{\frac{L_d L_q}{\omega^2 L_d L_q + R^2}} \right] \quad (\text{A.8})$$

$$\theta_1 = \text{asin} \left[ \frac{R(L_q - L_d)}{2\omega L_d L_q} \right] \quad (\text{A.9})$$

where  $L_d$ ,  $L_q$ , and  $R$  are the  $d$ - and  $q$ -axis inductances and phase resistance, respectively,  $\omega$  is the synchronous electrical angular speed,  $\psi_{pm}$  is the magnitude of the fundamental of PM flux linkage, and  $\tau$  is the electrical time constant.

By applying  $L_d = L_q = L$ , the analytical model for non-salient-pole PM machines can be presented as

$$\begin{bmatrix} 0 \\ 0 \end{bmatrix} = \begin{bmatrix} R & -\omega L \\ \omega L & R \end{bmatrix} \begin{bmatrix} I_d(t) \\ I_q(t) \end{bmatrix} + \begin{bmatrix} L & 0 \\ 0 & L \end{bmatrix} \frac{d}{dt} \begin{bmatrix} I_d(t) \\ I_q(t) \end{bmatrix} + \begin{bmatrix} 0 \\ E \end{bmatrix} \quad (\text{A.10})$$

1) Initial current response ( $I_q(0) \neq 0$  and  $E = 0$ )

$$I_d(t)_I = I_q(0) e^{-t/\tau} \sin(\omega t) \quad (\text{A.11})$$

$$I_q(t)_I = I_q(0) e^{-t/\tau} \cos(\omega t) \quad (\text{A.12})$$

$$I_m(t)_I = \sqrt{I_d(t)_I^2 + I_q(t)_I^2} = |I_q(0)| e^{-t/\tau} \quad (\text{A.13})$$

2) EMF response ( $I_q(0) = 0$  and  $E = \omega \psi_{pm}$ )

$$I_d(t)_E = -\frac{\omega^2 L \psi_{pm}}{\omega^2 L^2 + R^2} \left[ 1 - \frac{1}{\sin\varphi} e^{-t/\tau} \sin(\omega t + \varphi) \right] \quad (\text{A.14})$$

$$I_q(t)_E = -\frac{R\omega\psi_{pm}}{\omega^2 L^2 + R^2} \left[ 1 - \frac{1}{\cos\varphi} e^{-t/\tau} \cos(\omega t + \varphi) \right] \quad (\text{A.15})$$

$$I_m(t)_E = \sqrt{I_d(t)_E^2 + I_q(t)_E^2} = \frac{\omega\psi_{pm}}{\sqrt{\omega^2 L^2 + R^2}} \sqrt{1 - 2\cos(\omega t) e^{-t/\tau} + e^{-2t/\tau}} \quad (\text{A.16})$$

$$\tau = L/R \quad (\text{A.17})$$

$$\varphi = \text{atan}(\omega L/R) = \text{atan}(\omega\tau) \quad (\text{A.18})$$

It is worth noting three significant advantages of the developed model: (a) Compared with the classic model in [A12], [A14]-[A16], which were developed for machines having damping windings or solid poles, the models and responses are much simpler for most PM machines since there are no transient and sub-transient parameters. Hence, it is beneficial to the understanding, analysis, and design of the machines. (b) The models are capable of predicting not only steady state currents but also transient current responses, which may be significantly larger than the former. Therefore, the developed models are capable of assessing the risk of demagnetisation and can be used for guiding the machine design. (c) The model is also applicable when the initial current is not zero

### A.3 Influence of Machine Parameters

In order to guide the machine design, the influence of synchronous parameters on short circuit behavior is investigated analytically. The initial current is set to zero due to two reasons: (a) The initial current response, as shown in (A.13), is simply the damped current. (b) Its peak value is the same as  $I_q(0)$ . For most cases,  $I_q(0)$  is much lower than the current component due to the EMF.

The investigation is firstly based on the non-salient-pole machines model, which is simpler and helps to easily understand the behavior. The influence of saliency will be investigated later. For the demagnetisation consideration, the focus is especially on the transient current peaks, which may be significantly larger than the steady state values.

To ease the analysis, the currents are rewritten as the functions of rotor position,  $\theta = \omega t$ ,

$$I_d(\theta) = -\frac{\omega^2 L \psi_{pm}}{\omega^2 L^2 + R^2} \left[ 1 - \frac{\sin(\theta + \varphi)}{\sin\varphi} e^{-\theta/(\omega\tau)} \right] \quad (\text{A.19})$$

$$I_q(\theta) = -\frac{R\omega\psi_{pm}}{\omega^2L^2 + R^2} \left[1 - \frac{\cos(\theta + \varphi)}{\cos\varphi} e^{-\theta/(\omega\tau)}\right] \quad (\text{A.20})$$

$$I_m(\theta) = \sqrt{I_d(\theta)^2 + I_q(\theta)^2} = \frac{\omega\psi_{pm}}{\sqrt{\omega^2L^2 + R^2}} \sqrt{1 - 2\cos\theta e^{-\theta/\omega\tau} + e^{-2\theta/\omega\tau}} \quad (\text{A.21})$$

$$I_{ms} = \frac{\omega\psi_{pm}}{\sqrt{\omega^2L^2 + R^2}} \quad (\text{A.22})$$

$$I_{ds} = \frac{\omega^2L\psi_{pm}}{\omega^2L^2 + R^2} = I_{ms}\sin\varphi \quad (\text{A.23})$$

$$I_{qs} = \frac{R\omega\psi_{pm}}{\omega^2L^2 + R^2} = I_{ms}\cos\varphi \quad (\text{A.24})$$

where  $I_{ds}$ ,  $I_{qs}$ , and  $I_{ms}$  are the  $d$ -axis,  $q$ -axis, and total steady-state short circuit currents, respectively.

### A.3.1 Variation of Current Waveforms

Since  $\varphi = \text{atan}(\omega L/R) = \text{atan}(\omega\tau)$ , the current waveforms only rely on  $\omega L/R$ . Assuming steady state currents are one p.u., the short circuit current waveforms with different  $\omega L/R$  are shown in Figs. A.1-A.3. Together with (A.19)-(A.21), several useful conclusions can be drawn as follows.

- 1) The  $d$ -axis current reaches peak when  $\theta = \pi$  while the  $q$ -axis current peaks when  $\theta = \pi/2$ . However, the total current peak lies between  $\theta = \pi/2$  and  $\theta = \pi$ . The higher  $\omega L/R$ , the closer its peak position to  $\theta = \pi$ . Hence, at higher speed, the current change rate is higher, which results in higher eddy current.
- 2) With the increased  $\omega L/R$ , the oscillation is more significant and the damping is slower, since the responses are close to the one of pure inductive load. In this case, the peak currents are much higher than the steady state ones.

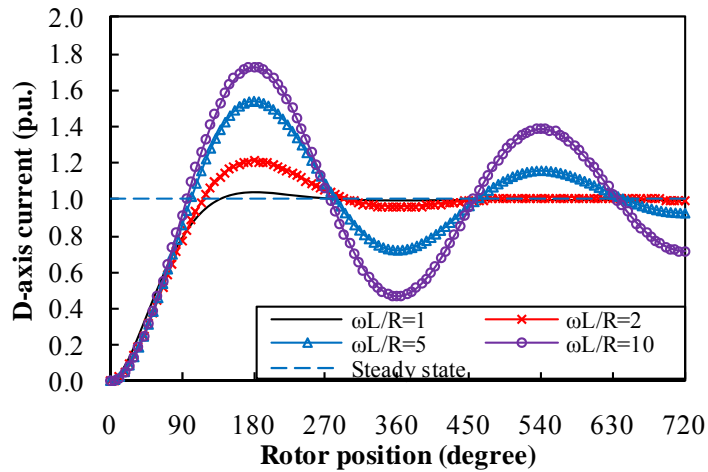


Fig. A.1. *D*-axis current waveform variation with  $\omega L/R$  when its steady state current is 1 p.u..

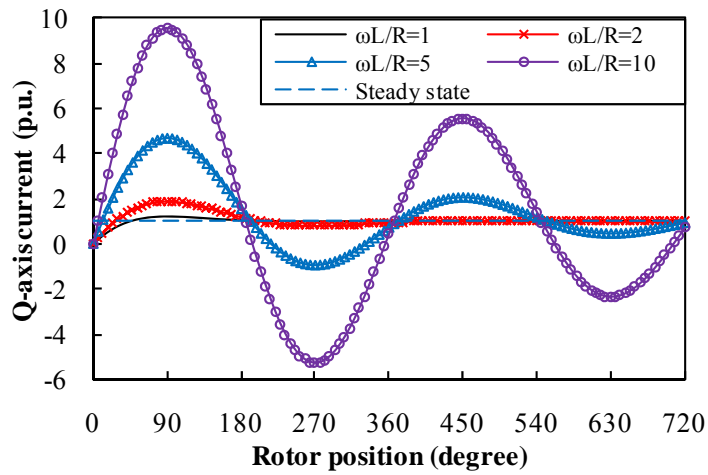


Fig. A.2. *Q*-axis current waveform variation with  $\omega L/R$  when its steady state current is 1 p.u..

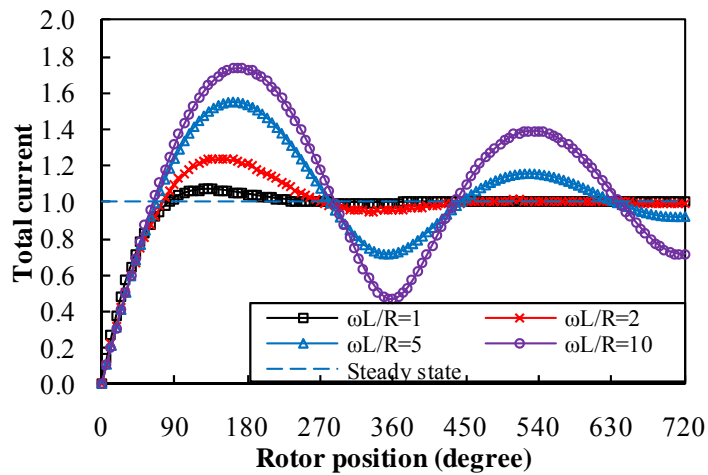


Fig. A.3. Total current waveform variation with  $\omega L/R$  when its steady state current is 1 p.u..

### A.3.2 Variation of Peak Currents

Combining the current waveforms with their steady state currents, the peak transient currents,  $I_{dpeak}$  and  $I_{qpeak}$ , can be obtained as

$$I_{dpeak} = |I_d(\theta = \pi)| = \frac{\psi_{pm}}{L} \frac{\omega^2 L^2}{\omega^2 L^2 + R^2} (1 + e^{-\frac{R\pi}{\omega L}}) \quad (A.25)$$

$$I_{qpeak} = |I_q(\theta = \frac{\pi}{2})| = \frac{\psi_{pm}}{L} \frac{\omega LR}{\omega^2 L^2 + R^2} (1 + \frac{\omega L}{R} e^{-\frac{R\pi}{2\omega L}}) \quad (A.26)$$

According to (A.25), (A.26) and Fig. A.4, which can be used to predict the peak currents when  $\psi_{pm}$ ,  $\omega$ , and  $R$  vary, it can be seen that

- 1)  $I_{dpeak}$ ,  $I_{qpeak}$ , and  $I_{mpeak}$  are proportional to  $\psi_{pm}/L$ .
- 2) With fixed  $\psi_{pm}/L$ , all the peak currents increase when  $\omega L/R$  is higher.
- 3) For  $I_{dpeak}$  and  $I_{mpeak}$ , their limiting values are  $2\psi_{pm}/L$  (twice of their steady state values) when  $\omega L/R$  approaches infinity.
- 4) For  $I_{qpeak}$ , its limiting value is  $\psi_{pm}/L$  ( $\omega L/R$  times of its steady state value) when  $\omega L/R$  approaches infinity

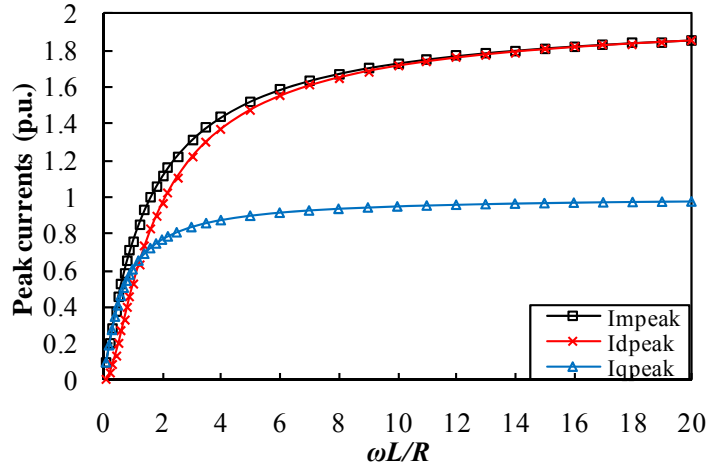


Fig. A.4. Variation of peak currents versus  $\omega L/R$  when  $\psi_{pm}/L = 1$ .

However, to design a PM machine for most applications, which do not require flux weakening operation,  $\omega$ ,  $\psi_{pm}$  and  $R$  are almost fixed due to the voltage and efficiency requirements. It is desirable to obtain the peak current characteristics with variable  $L$  and fixed  $\omega$ ,  $\psi_{pm}$ , and  $R$ . For  $\omega = 1$  p. u. and  $\psi'_{pm} = 1$  p. u., the per unit peak current value can be derived as

$$I'_{dpeak} = \frac{L'}{L'^2 + R'^2} (1 + e^{-R'\pi/L'}) \quad (A.27)$$

$$I'_{qpeak} = \frac{R'}{L'^2 + R'^2} (1 + \frac{L'}{R'} e^{-\frac{R'\pi}{2L'}}) \quad (A.28)$$

As can be seen from Figs. A.5-A.7:

- 1) With the same  $L'$ , the peak short circuit currents are lower when  $R'$  is higher.
- 2)  $I'_{dpeak}$  peaks when  $L'$  is close to  $R'$ . When  $L'$  approaches 1, its limiting value is 2 while  $R'$  decreases.
- 3)  $I'_{qpeak}$  decreases when  $L'$  increases. When  $L'$  is close to 0,  $I'_{qpeak}$  is close to  $1/R'$ . When  $L'$  approaches 1, it is close to 1.
- 4)  $I'_{mpeak}$  decreases and is close to 2 when  $R'$  is very low and  $L'=1$ .

Hence, it is desirable to have either higher  $R'$  or higher  $L'$ , which results in lower  $I'_{qpeak}$  and  $I'_{mpeak}$ , and consequently, lower peak torque and lower demagnetization MMF. However, a higher  $R'$  results in lower efficiency. Therefore, a higher  $L'$  is desirable.

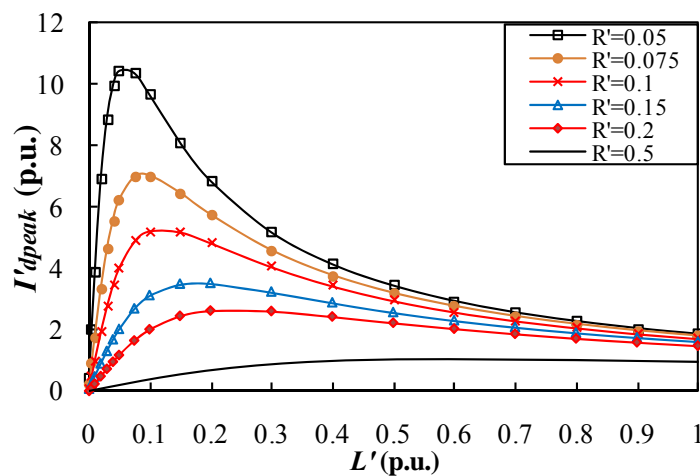


Fig. A.5. Variation of  $I'_{dpeak}$  versus  $L'$  and  $R'$ .

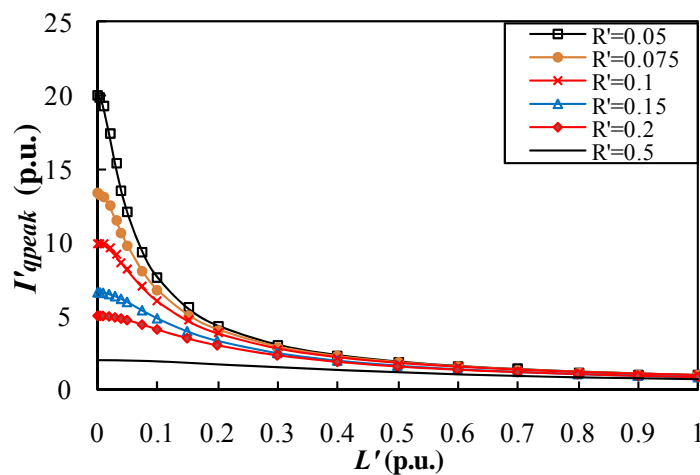


Fig. A.6. Variation of  $I'_{qpeak}$  versus  $L'$  and  $R'$ .

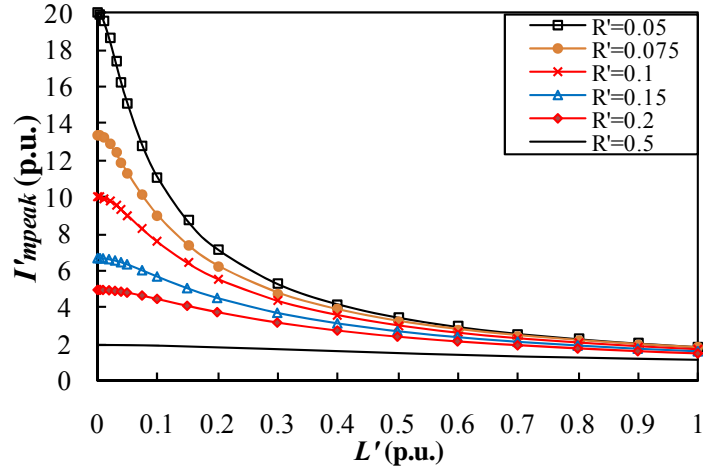


Fig. A.7. Variation of  $I'_{mpeak}$  versus  $L'$  and  $R'$ .

### A.3.3 Influence of Saliency

Based on salient-pole machine model and using the saliency ratio  $\varepsilon = L_q/L_d$ , the short circuit behavior can be investigated. For  $\omega' = 1$  p.u.,  $\psi'_{pm} = 1$  p.u., and  $R' = 0.05$  p.u., increasing the saliency ratio  $\varepsilon$  does help to reduce  $I_{qpeak}$ , as shown in Fig. A.9. When  $\omega L_d/R$  is larger,  $I_{qpeak}$  is almost inversely proportional to the saliency ratio  $\varepsilon$ . However, as shown in Figs. A.8 and A.10,  $I_{dpeak}$  and  $I_{mpeak}$  are larger when the saliency ratio  $\varepsilon$  is larger although the influence is significant only when  $\omega L_d/R$  is lower.

Using the salient-pole machine model, the following conclusions can be obtained: (a) when  $\omega L_d/R$  approaches infinity, the limiting values of  $I_{dpeak}$  and  $I_{mpeak}$  are both equal to  $2\psi_{pm}/L_d$ , which is twice of their steady state values. (b) For  $I_{qpeak}$ , its limiting value is  $\psi_{pm}/L_q$ , which is  $\omega L_d/R$  times of its steady state value.

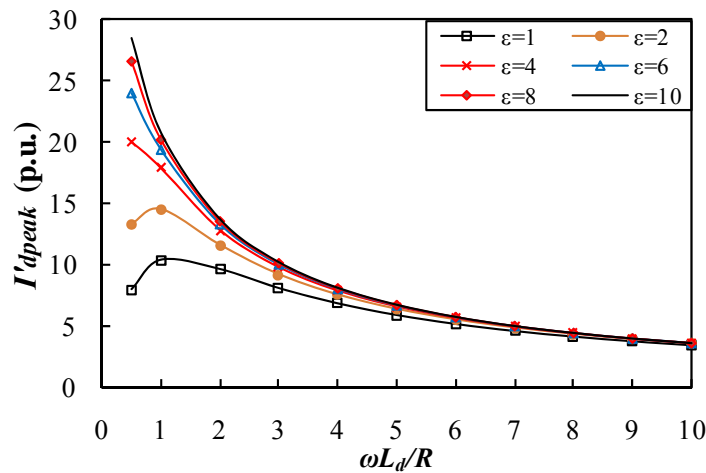


Fig. A.8. Variation of  $I'_{dpeak}$  versus  $\omega L_d/R$  and  $\varepsilon$  when  $R' = 0.05$  p.u..

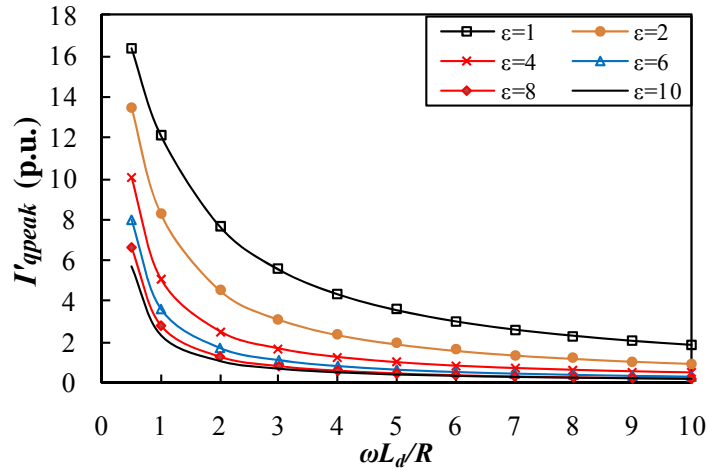


Fig. A.9. Variation of  $I'_{qpeak}$  versus  $\omega L_d/R$  and  $\varepsilon$  when  $R'=0.05$  p.u..

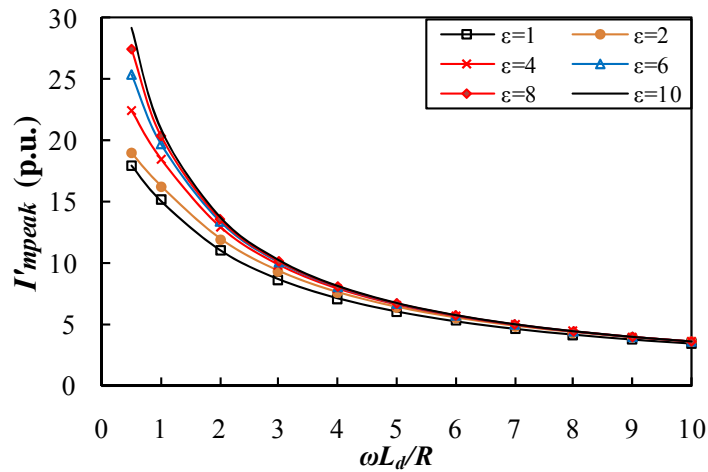


Fig. A.10. Variation of  $I'_{mpeak}$  versus  $\omega L_d/R$  and  $\varepsilon$  when  $R'=0.05$  p.u..

#### A.4 Finite Element and Experimental Validation

To verify the analytical model, both FE simulation and experiments are conducted based on a SPM machine, its cross-section and phase back-EMF waveform are shown in Figs. A.11 and A.12 and the parameters are given in Table A-I.

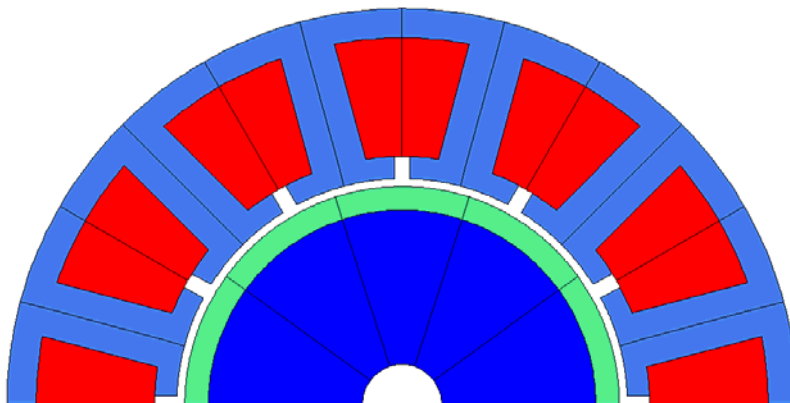


Fig. A.11. Cross-section of experimental SPM machine.

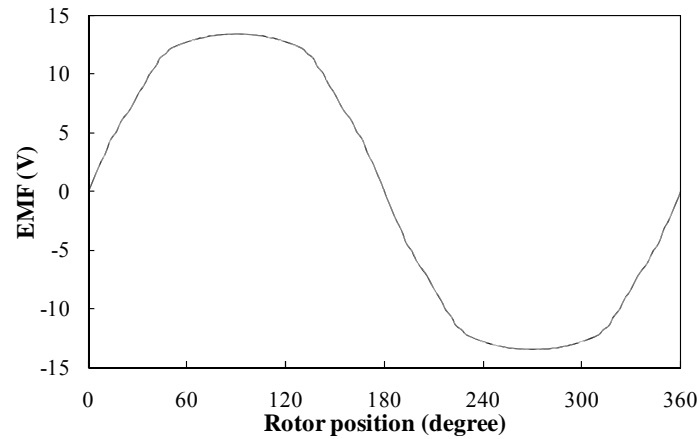


Fig. A.12. Phase EMF of experimental SPM machine at 400rpm.

Table A-I Parameters of experimental machine

Machine Parameters			
Rated speed	400rpm	Effective axial length	50mm
Slot number	12	Magnet thickness	3mm
Pole number	10	Magnet remanence	1.2T
Stator outer radius	50mm	Number of turns per phase	132
Stator inner radius	28.5mm	Slot opening	2mm
Yoke height	3.7mm	PM flux linkage $\psi_{pm}$	69.8mWb
Tooth body width	7.1mm	Phase resistance 20°C ( $R_a$ )	0.300Ω
Airgap	1mm	$D$ - and $q$ -axis inductance	3.37mH
Rotor outer radius	27.5mm		

The experimental setup is shown in Figs. A.13 and A.14. A DC motor is used to drive the experimental machine at the specified speed when the 3-phase short-circuit fault occurs. Three single-phase inductors are employed to control the short-circuit current while the external resistances are used to control the initial current and avoid the voltage spikes when the switches are turned off. They are detailed in Fig. A.14 and Table A-II.

The transient FE simulation is carried out using Opera FE software. To keep the same operation conditions as the experiment, the related external circuit is set as shown in Fig. A.15. The initial current is controlled by 3-phase balanced current sources while the 3-phase short circuit fault is invoked by the switches. Eddy currents are neglected in the FE model to

keep the same condition as the analytical model.

The analytical results are predicted based on the parameters, which are listed in Table A-I and Table A-II.

The measured, FE and analytically predicted short circuit current waveforms are shown in Fig. A.16 while the peak currents and steady state currents with different  $\omega L/R$  by changing the speed are shown in Figs. A.17 and A.18. As can be seen from the results:

- 1) The analytically predicted transient short-circuit currents based on the developed model agree well with the experimental and FE results.
- 2) The transient peak currents are significantly larger than the steady state ones. Hence, the developed model is useful to assess the risk of demagnetization.

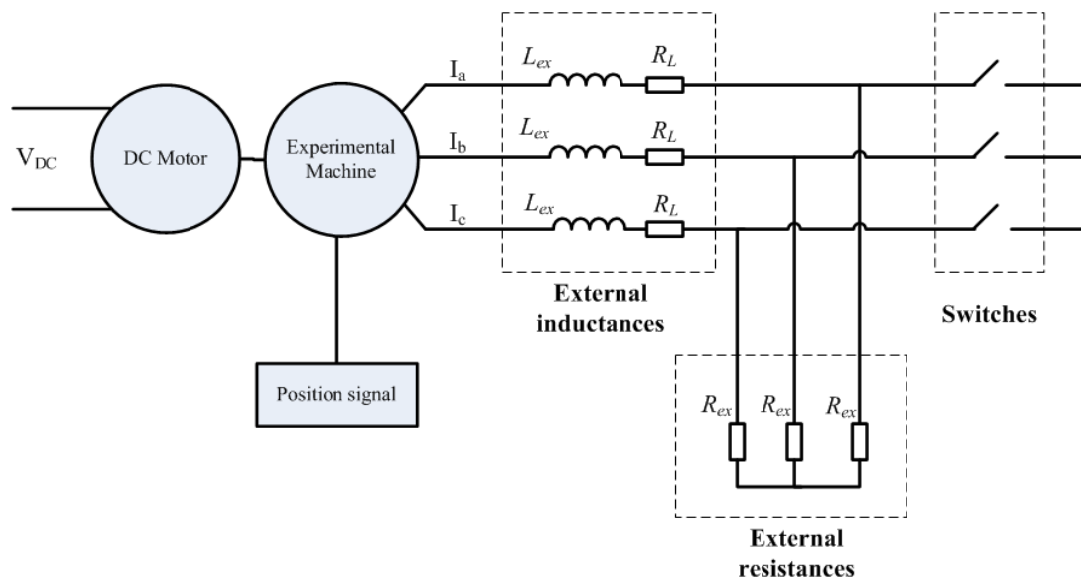


Fig. A.13. System connection for 3-phase short-circuit experiment.

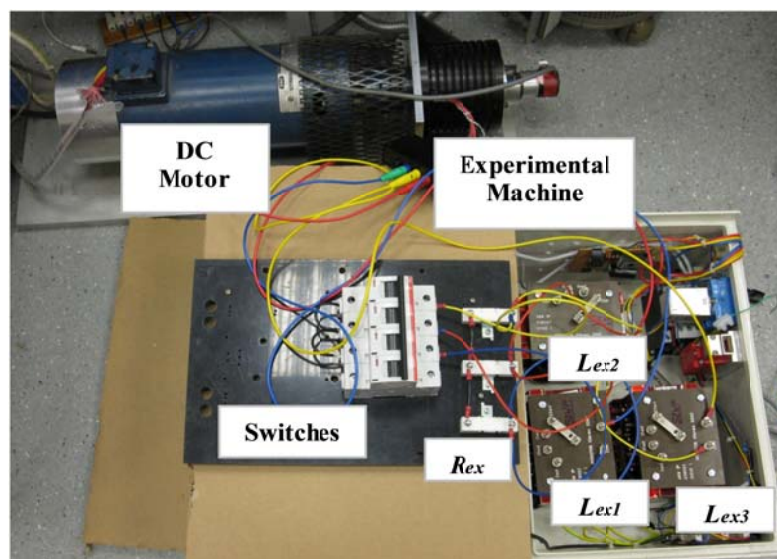


Fig. A.14. Test rig of 3-phase short-circuit experiment.

Table A-II External inductors and resistances

Inductance of external inductor $L_{ex}$	37.9mH
Resistance of external inductor $R_L$	0.188 $\Omega$
External resistance $R_{ex}$	33 $\Omega$

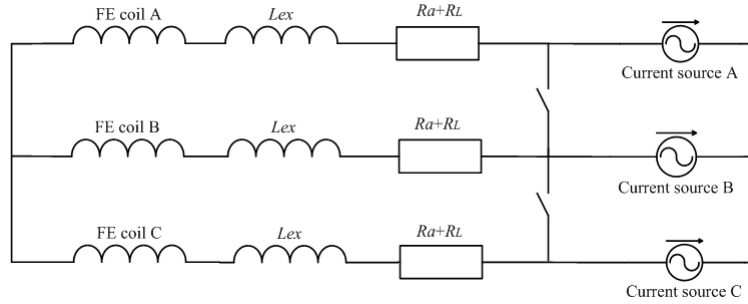


Fig. A.15. External circuit for FE simulation.

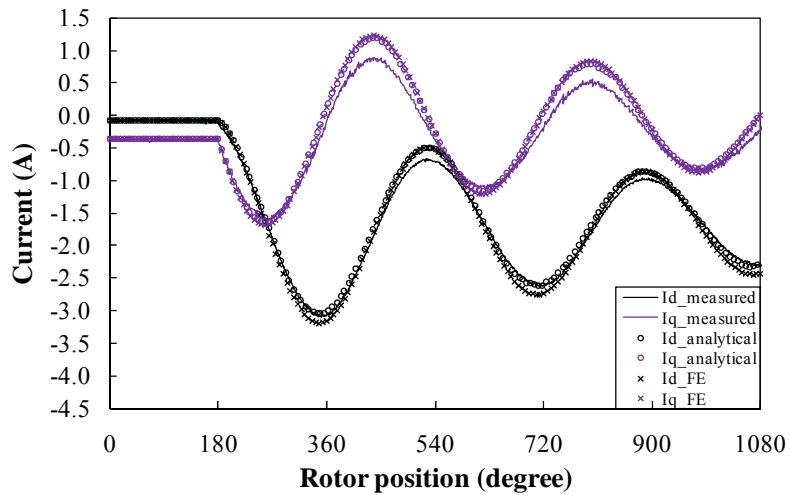


Fig. A.16. Measured, FE, and analytically predicted short-circuit waveforms when  $\omega L/R = 15.9$ .

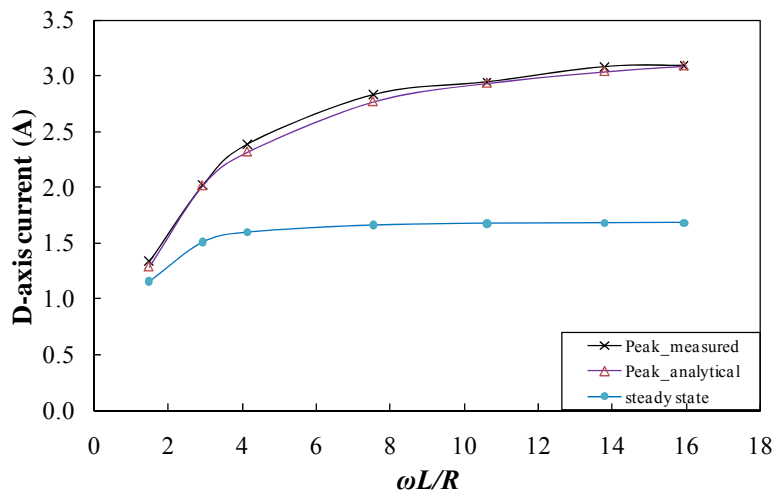


Fig. A.17. Measured and predicted peak and steady state d-axis currents versus  $\omega L/R$ .

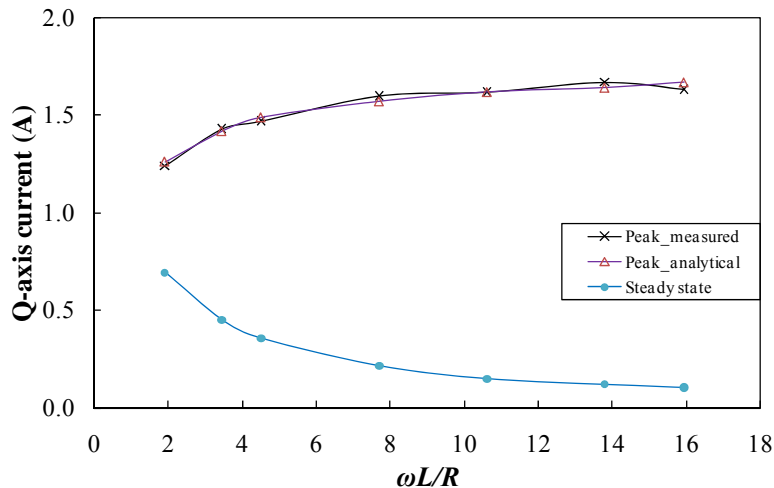


Fig. A.18. Measured and predicted peak and steady state  $q$ -axis currents versus  $\omega L/R$ .

## A.5 Conclusions

In this paper, a simple analytical model has been developed for predicting 3-phase short-circuit currents for both salient-pole and non-salient-pole PM machines without damping windings and solid poles. It is simple yet accurate, as validated by transient FE analyses and experimental results. It has been used to investigate the influence of machine parameters on the peak short-circuit currents. Hence, it is useful for the machine design to avoid the irreversible demagnetisation under short-circuit faults.

## References

- [A1] K. C. Kim, K. Kim, and J. Lee, "Demagnetization analysis of permanent magnets according to rotor types of interior permanent magnet synchronous motor," *IEEE Trans. Magn.*, vol. 45, no. 6, pp. 2799-2802, 2009.
- [A2] K. C. Kim, S. B. Lim, D. H. Koo, and J. Lee, "The shape design of permanent magnet for permanent magnet synchronous motor considering partial demagnetization," *IEEE Trans. Magn.*, vol. 42, no. 10, pp. 3485-3487, 2006.
- [A3] B. C. Mecrow, A. G. Jack, J. A. Haylock, and J. Coles, "Fault-tolerant permanent magnet machine drives," *IEE Pro. Elect. Power Appl.*, vol. 143, no. 6, pp. 437-442, 1996.
- [A4] A. G. Jack, B. C. Mecrow, and J. A. Haylock, "A comparative study of permanent magnet and switched reluctance motors for high-performance fault-tolerant applications," *IEEE Trans. Ind. Appl.*, vol. 32, no. 4, pp. 889-895, 1996.
- [A5] X. H. Wang, Y. G. Sun, B. Ouyang, W. J. Wang, Z. Q. Zhu, and D. Howe, "Transient behavior of salient-pole synchronous machines with internal stator winding faults," *IEE Pro. Elect. Power Appl.*, vol. 149, no. 2, pp. 143-151, 2002.
- [A6] D. Bi, X. Wang, Z. Q. Zhu, and D. Howe, "Improved transient simulation of salient-pole synchronous generator with internal and ground faults in the stator winding," *IEEE Trans. Energy Convers.*, vol. 20, no. 1, pp. 128-134, 2002.
- [A7] S. Chevailler, L. Feng, and A. Binder, "Short-circuit faults in distributed and concentrated windings of PM synchronous motors," *Eur. Conf. Power Electron. Appl.*, pp. 1-10, 2007.

- [A8] M. Dai, A. Keyhani, and T. Sebastian, "Fault analysis of a PM brushless DC motor using finite element method," *IEEE Trans. Energy Convers.*, vol. 20, no. 1, pp. 1-6, 2005.
- [A9] C. Gerada, K. Bradley, and M. Summer, "Winding turn-to-turn faults in permanent magnet synchronous machine drives," in *IEEE Ind. Appl. Conf.*, 2005, vol. 2, pp. 1029-1036.
- [A10] G. X. Zhao, L. J. Tian, Q. P. Shen, and R. Y. Tang, "Demagnetization analysis of permanent magnet synchronous machines under short circuit fault," in *Asia-Pacific Power Energy Eng. Conf.*, 2010, pp. 1-4.
- [A11] B. A. Welchko, T. M. Jahns, W. L. Soong, and J. M. Nagashima, "IPM synchronous machine drive response to symmetrical and asymmetrical short circuit faults," *IEEE Trans. Energy Convers.* vol. 18, no. 2, pp. 291-298, 2003.
- [A12] C. Concordia, *Synchronous Machines, Theory and Performance*. John Wiley and Sons, New York, 1951.
- [A13] Z. Sun, J. Wang, D. Howe, and G. Jewell, "Analytical prediction of the short-circuit current in fault-tolerant permanent-magnet machines," *IEEE Trans. Ind. Electron.*, vol. 55, no. 12, pp. 4210-4217, 2008.
- [A14] M. Qiao, X. Zhang, and X. Ren, "Research of the mathematical model and sudden symmetrical short circuit of the multi-phase permanent-magnet motor," in *Int. Conf. Power Syst. Tech.*, 2002, pp. 769-773.
- [A15] S. K. Cheng, and W. L. Liu, "Analysis of sudden short circuit current for PMSG," in *IEEE Veh. Power Propulsion Conf.*, 2008, pp. 1-4.
- [A16] K. W. Klontz, T. J. E. Miller, H. Karmaker, and P. Zhong, "Short-circuit analysis of permanent-magnet generators," in *IEEE Int. Elect. Mach. Drives Conf.* 2009, pp. 1080-1087.

## APPENDIX B DESIGNS OF 3kW PM PROTOTYPE MACHINES

In this section, the designs of 3kW PM prototype machines are reported. First, the preliminary design, which is done by Siemens Wind Power, Denmark, is examined. Second, the rotor shaping methods are investigated to reduce the significant cogging torque and torque ripple. The slot dimensions are further investigated to improve the torque density. Finally, the demagnetization under short circuit conditions is discussed as well.

### B.1 Preliminary design

The detailed parameters and cross-section of the preliminary design are summarized in Table B-I and Fig. B.1.

Table B-I Parameters of preliminary design

Parameters	value	Parameters	value
Rotor outer diameter	420 mm	Effective axial length	110 mm
Slot number	84	Pole number	28
Airgap length	1 mm	Magnet thickness	3.8 mm
Remanence @ 60°C	1.17 T	Coercive force @ 60°C	880 kA/m
Rated speed	170 rpm	Number of turns per phase	392
Rated current (RMS)	5.83 A	Stator outer diameter	390.4 mm
Stator inner diameter	340.4 mm	Slot height	15.5 mm
Stator yoke thickness	10 mm	Slot width	7.3 mm
Rotor yoke thickness	10 mm	Slot wedge height	1 mm
Coil temperature (rated)	95°C	Magnet temperature (rated)	60°C
Rotor steel	S355	Resistance 20°C	1.528 Ω
Stator lamination	M470-65A		

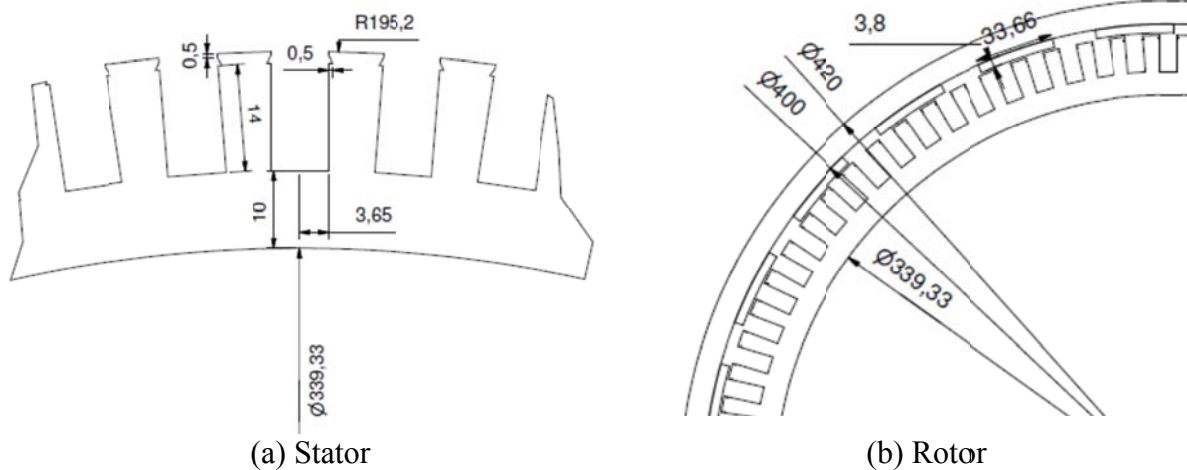


Fig. B.1. Cross-sections of preliminary design of 3.2kW DD PM machine.

The performance, such as magnetic field distribution, back EMFs, cogging torque, and on-load torque, of the preliminary design is shown in Figs. B.2-B.6. It can be seen that, due to the non-shaped magnets, the back EMF is rich of harmonics. The cogging torque and hence the full load torque ripple are significant. The current phase advance angle is referred to the positive  $q$ -axis. The optimal current phase advance angle for generator operation is 180, e.g. the armature current only has negative  $q$ -axis component.

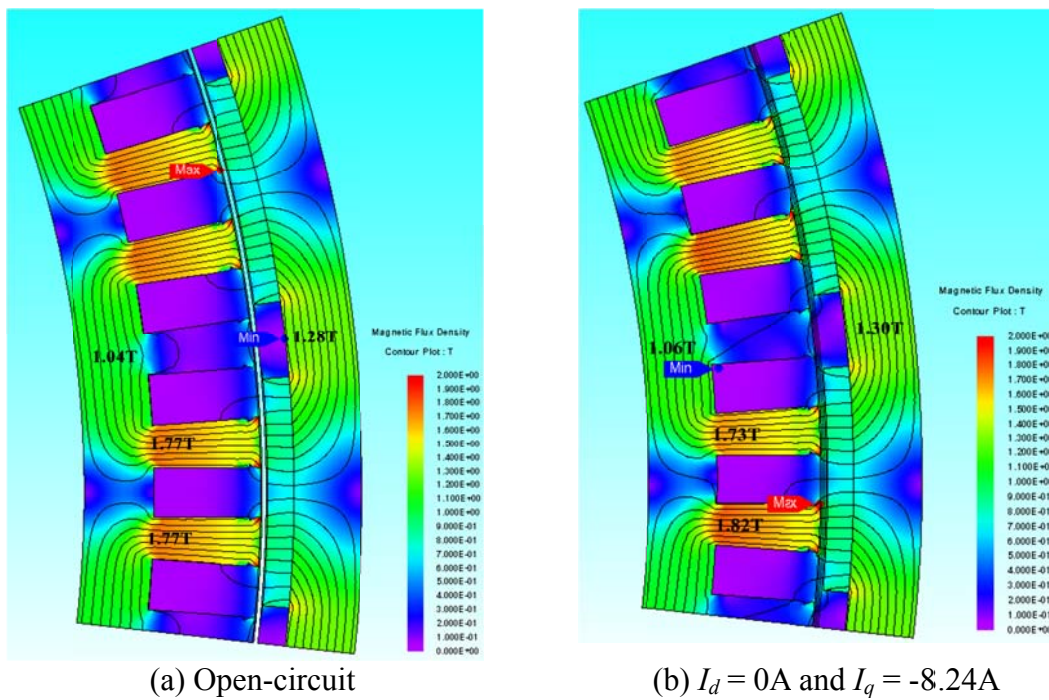
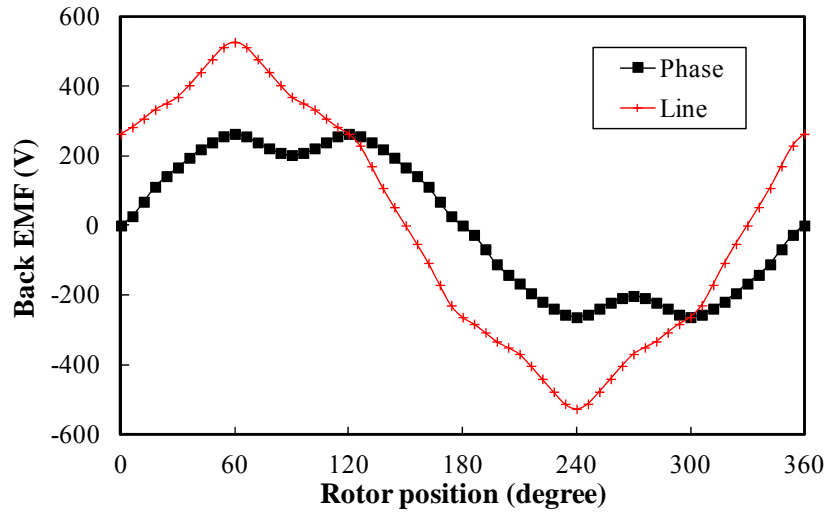
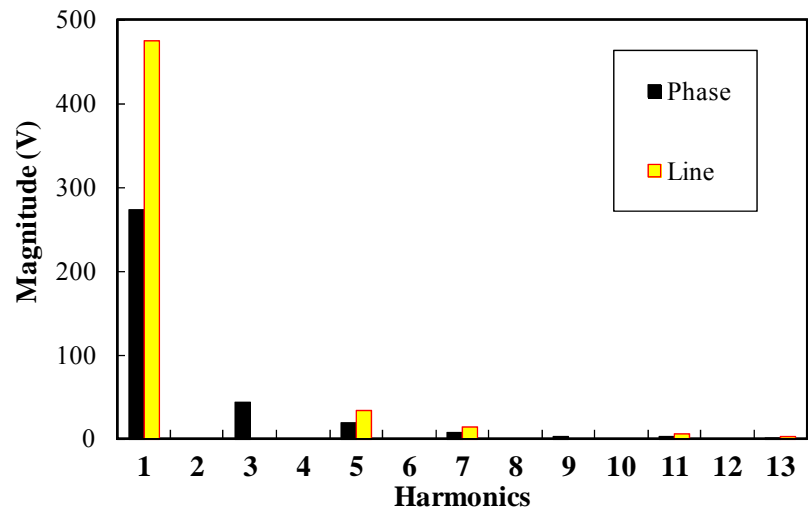


Fig. B.2. Magnetic field distributions of preliminary design.



(a) Back EMF waveforms



(b) Phase back EMF waveforms

Fig. B.3. Back EMF waveforms and spectra of preliminary design when  $n = 170\text{rpm}$ .

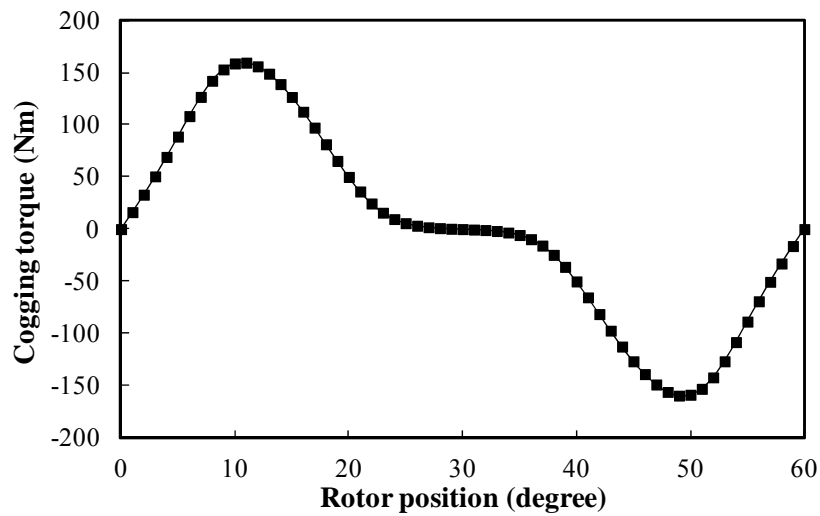


Fig. B.4. Cogging torque of preliminary design.

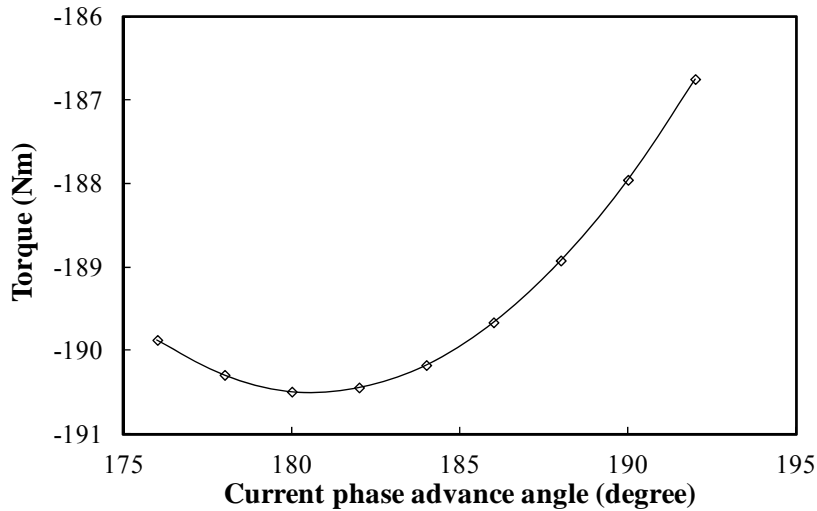


Fig. B.5. Variation of average torque with current phase advance angle when  $I_d = 5.83A$ .

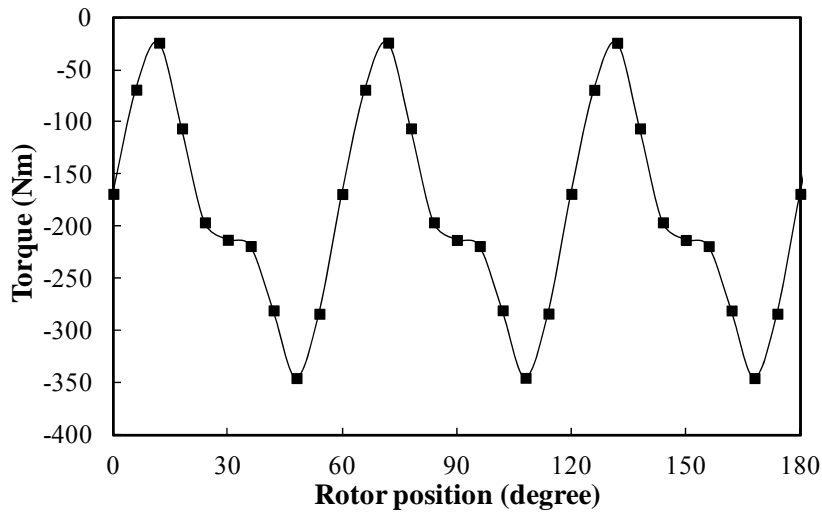


Fig. B.6. Torque waveform when  $I_d = 0A$  and  $I_q = -8.24A$ .

In order to evaluate the demagnetization withstand capability, radial flux densities of magnet are extracted out from the FE results. The inner surface of magnet, which is most close to the stator, is most likely to be demagnetized. However, in order to avoid the numerical error on the boundary between two types of materials, the probes are set symmetrically 0.1mm below the magnet surface, as shown in Fig. B.7.

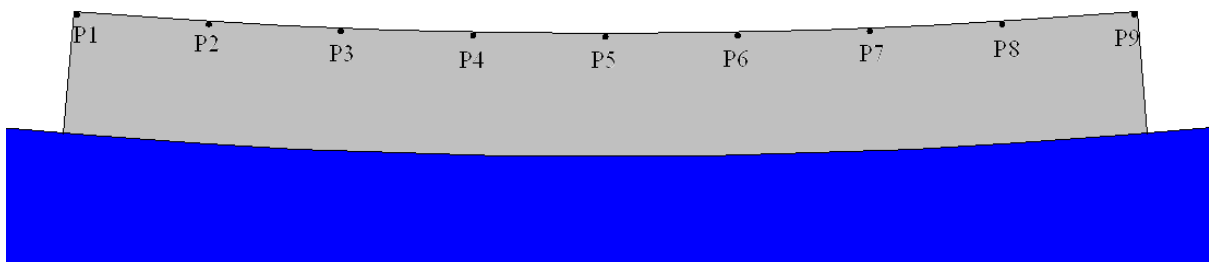


Fig. B.7. Illustration of probe locations.

In order to implement the short circuits, the external circuit, as shown in Fig. B.8, is used.

The parameters are set as follow.

- Before the short circuit, the machine is on rated load and  $R_{sc}$  is  $10^8\Omega$ .
- During 3-phase short circuit,  $R_{sc}$  is changed to  $10^{-8}\Omega$  and the input currents are set to 0A. The short circuit occurs when the terminal voltage of one phase crosses zero, which is the worst case.
- During 2-phase short circuit,  $R_{sc}$  between phase A and phase B is set to  $10^{-8}\Omega$ . The other two  $R_{sc}$  remain  $10^8\Omega$ . The input currents are set to 0A. The short circuit occurs when the line-line voltage between phase A and phase B crosses zero, which is the worst case for 2-phase short circuit.
- The influence of eddy current is neglected and the end winding inductances are set to zero.
- Since the mechanical time constant is much bigger than electrical time constant, the rotor speed is assumed to be constant during simulation.

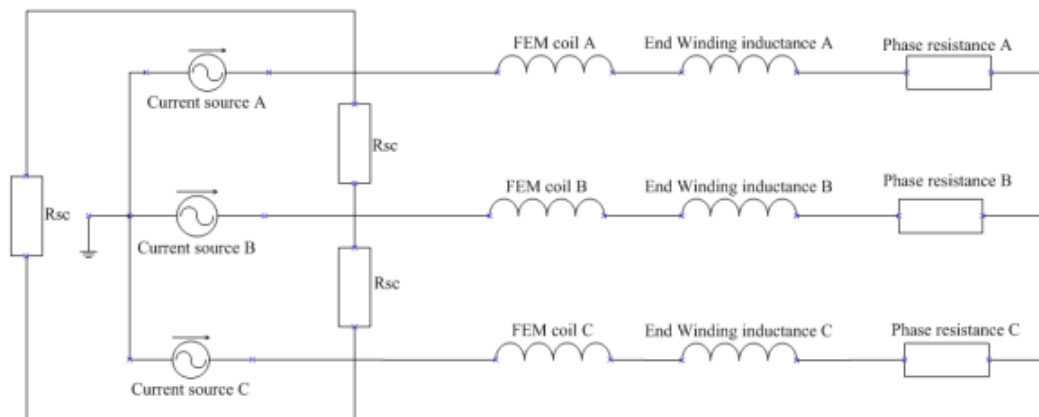


Fig. B.8. External circuit for short circuit simulations.

The short circuit performance, such as flux densities in magnet, short circuit current, and short circuit torque, is shown in Figs. B.9-B.11 and Table B-II. It can be seen that:

- When it is on full load, the magnets are safe.
- The 3-phase short circuit is more critical than 2-phase short circuit in terms of the short circuit current and the magnet demagnetization.
- The magnets are just thick enough to withstand the 3-phase short circuit from rated load, which is the worst case.
- The short circuit current and torque are significant for the preliminary design.

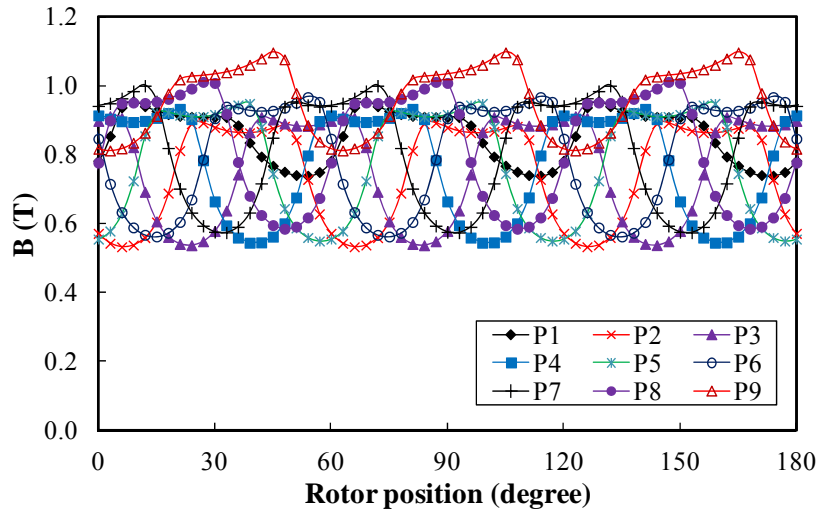
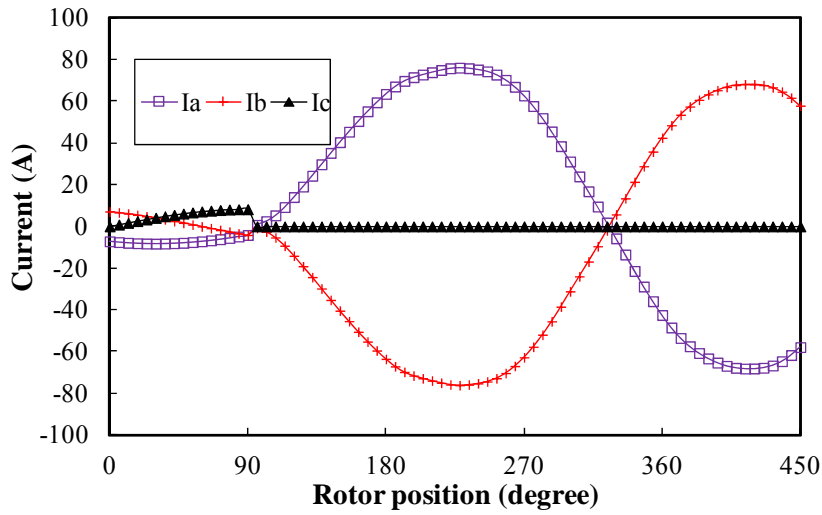
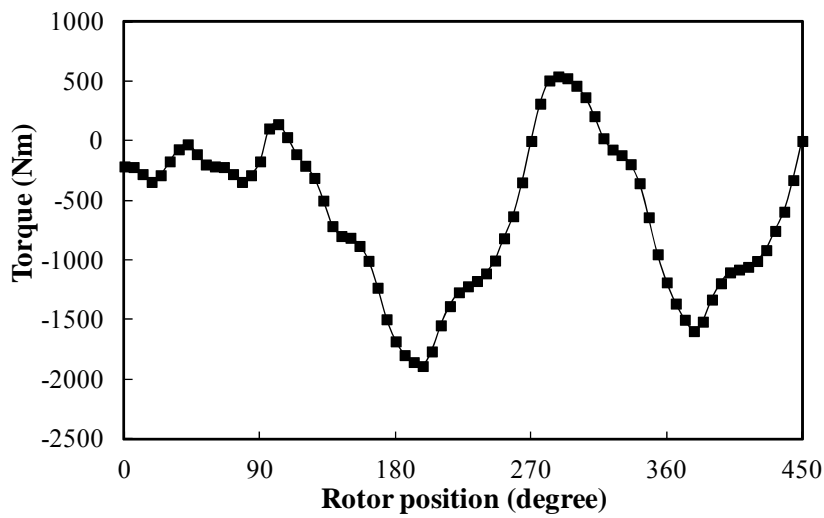


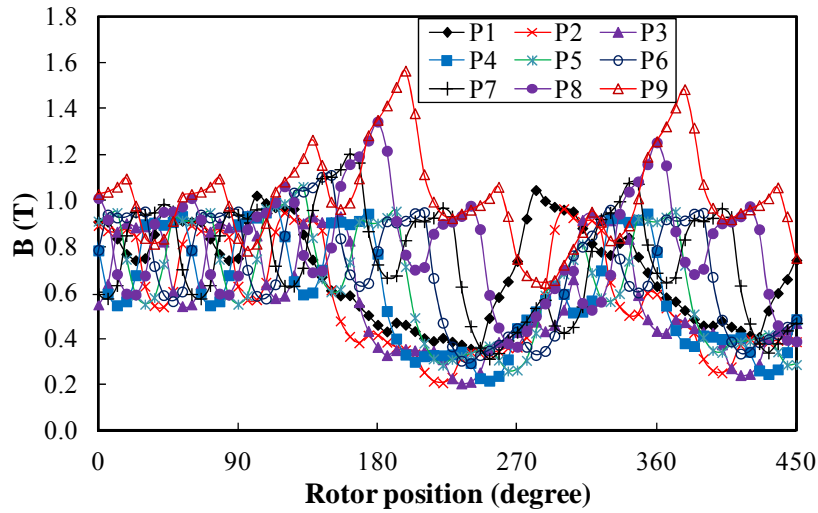
Fig. B.9. Radial flux densities variation of probes at rated load.



(a) Phase current waveforms

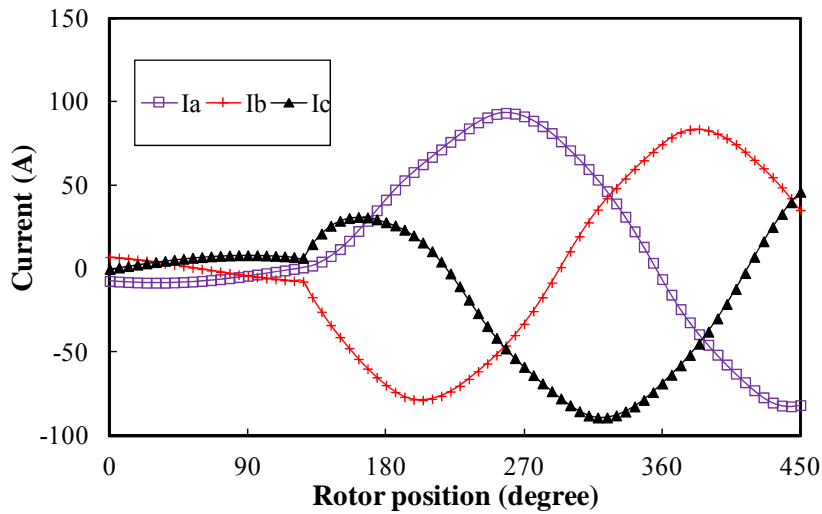


(b) Torque waveform

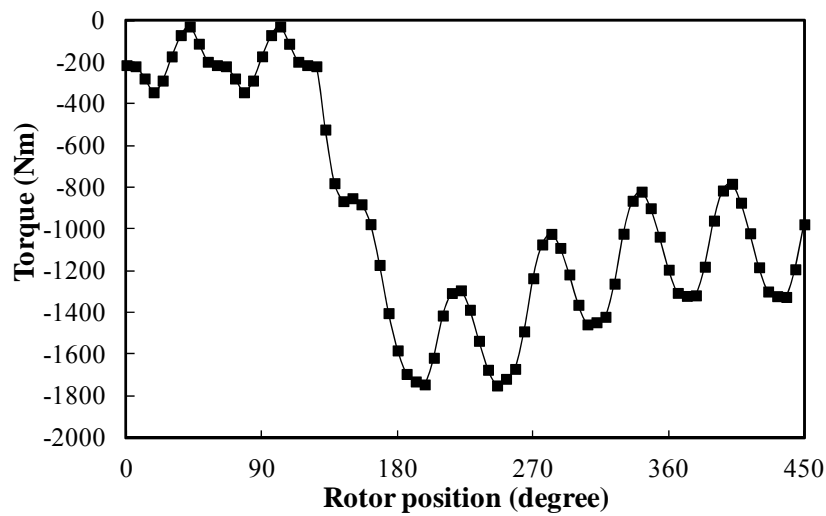


(c) Radial flux densities variation of probes

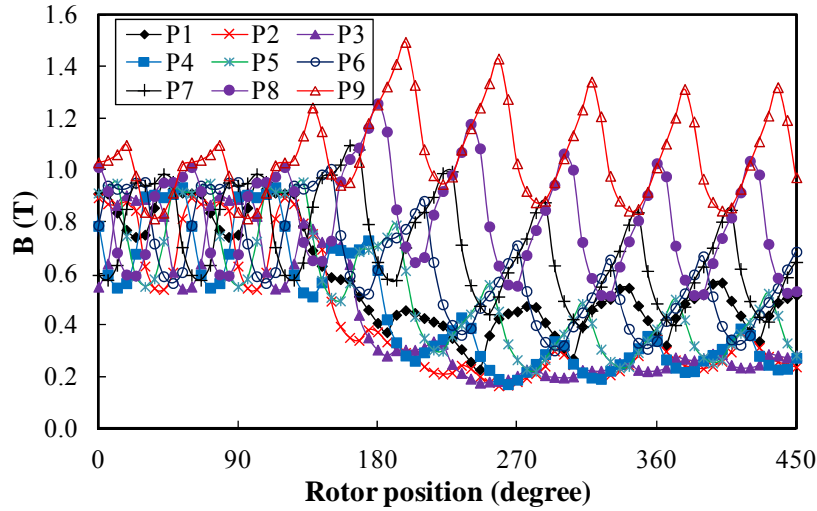
Fig. B.10. Performance of 2-phase short circuit from rated load.



(a) Phase current waveforms



(b) Torque waveform



(c) Radial flux densities variation of probes

Fig. B.11. Performance of 3-phase short circuit from rated load.

Table B-II Demagnetization withstand capability

	Rated load	2-phase short circuit	3-phase short circuit
Peak current (A)	8.24	76.06	93.5
Peak torque (Nm)	345	1888	1749
Min. radial flux density in the magnet (T)	0.533	0.205	0.165

## B.2 Investigation of Rotor Shaping

Since the machine is developed for direct drive wind power applications, it has stringent requirement on the torque pulsations, defined as half of the peak-peak (p-p) value. The cogging torque and on-load torque ripple in whole operation range should be less than 0.5% and 1% of the rated torque, respectively. Since the required rated torque is 194.84Nm, the maximum allowed peak-peak values of cogging torque and torque ripple are 1.948Nm and 3.896Nm, respectively. In order to reduce the significant cogging torque and torque ripple, it is necessary to employ rotor shaping.

### B.2.1 Investigation of Pole Arc to Pole Pitch Ratio

The simplest way of rotor is changing the pole arc to pole pitch ratio  $\alpha_p$ . The variation of cogging torque with different pole arc to pole pitch ratio is shown in Fig. B.12. It can be seen that the cogging torque can be reduced significantly by optimising  $\alpha_p$ . The cogging torque is lowest when  $\alpha_p = 0.705$ . However, even with the optimal  $\alpha_p$ , the cogging torque, whose peak

to peak value is 42Nm, is still much larger than the requirement (1.948Nm).

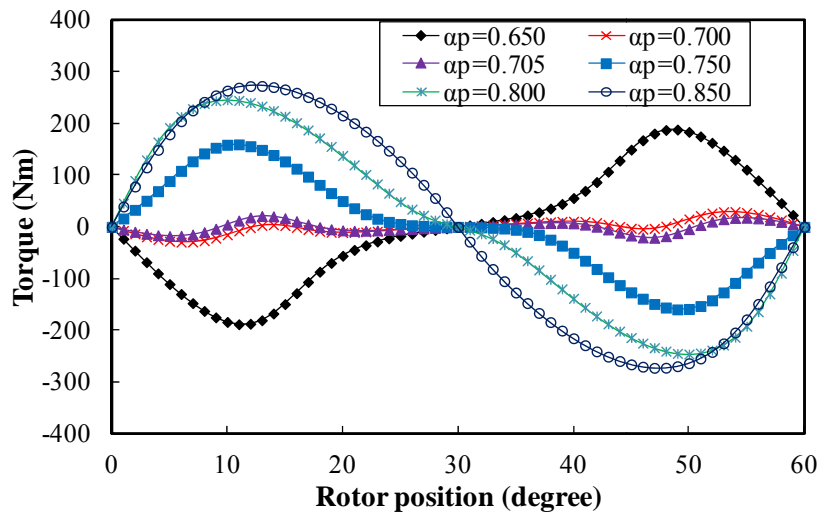


Fig. B.12. Variation of cogging torque with pole arc to pole pitch ratio.

### B.2.2 Investigation of Sinusoidal Magnet Shaping

It has been concluded that it is impossible to achieve the torque ripple requirement by only optimising  $\alpha_p$ . Therefore, it is necessary to introduce better magnet shaping method. Ideally, the sinusoidal open circuit airgap flux density distribution is desired. When neglecting the flux leakage and approximating the relative permeability of magnet by 1, the magnet shape can be derived as  $h(\theta) = h_m \cos(p\theta)$  shown in Fig. 1.14 [136]. However, in actual machines, the flux leakage exists. In order to compensate the influence of flux leakages, in [134], a new way of sinusoidal magnet shaping, as shown in Fig. 1.15, is developed.

In this section, the magnet shaping is based on the method developed in [134] and shown in Fig. B.13. Since the minimum airgap length and maximum magnet height are fixed, the variation of cogging torque with  $h_e$  and  $\alpha_p$  is investigated and shown in Figs. B.14 and B.15. It can be seen that, for each  $\alpha_p$ , there is an optimal  $h_e$  to minimum the cogging torque. For larger  $\alpha_p$ , the lower minimum cogging torque can be achieved. When  $\alpha_p$  is larger than 0.95, the peak-peak value of minimum cogging torque can be less than 0.6Nm.

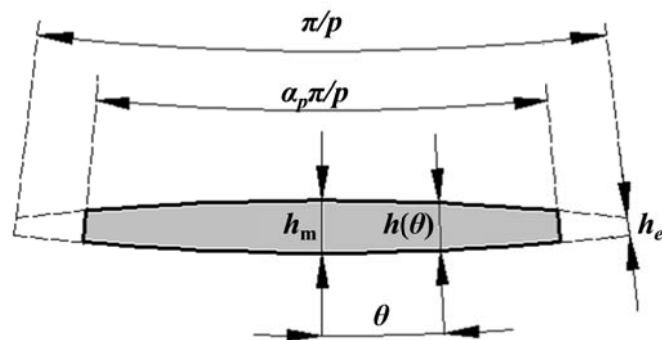
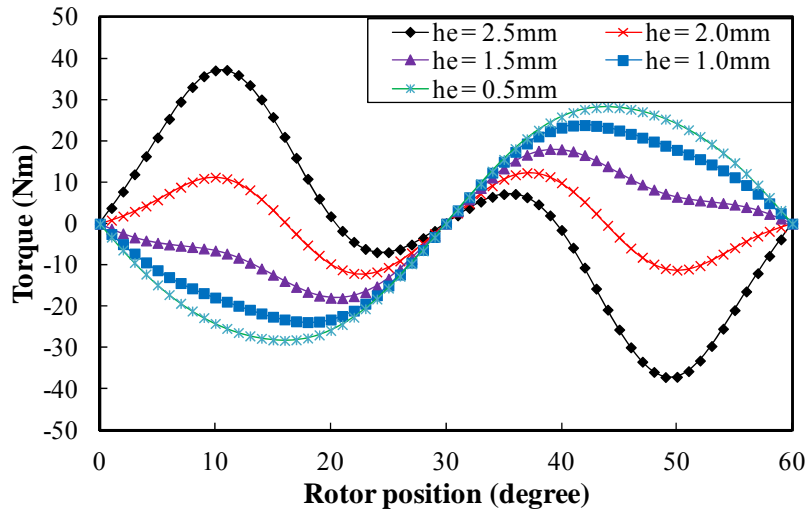
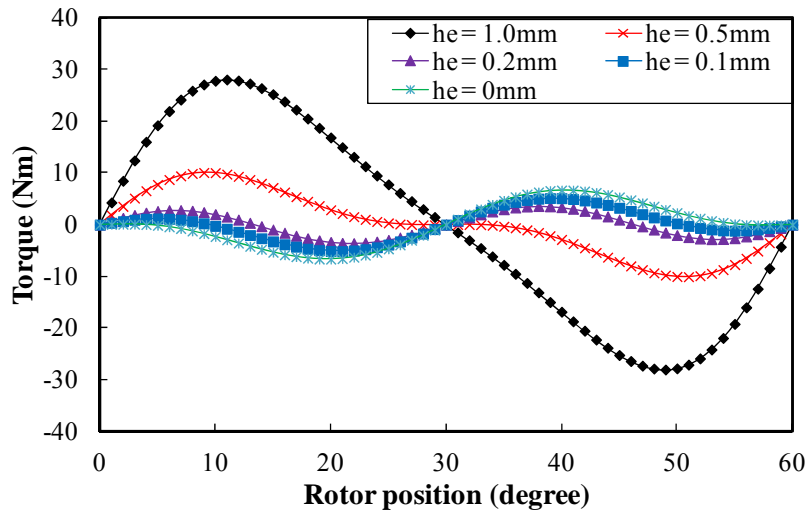


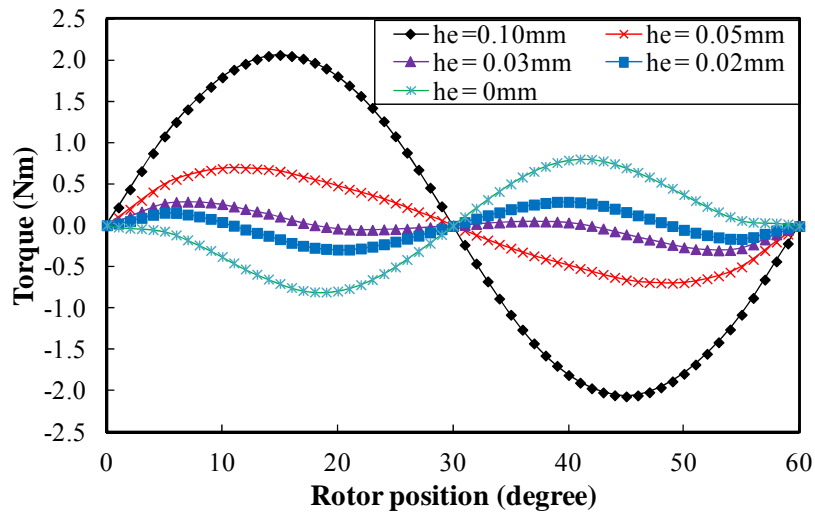
Fig. B.13. Illustration of sinusoidal magnet shaping.



(a) Cogging torque waveforms when  $\alpha_p = 0.75$



(b) Cogging torque waveforms when  $\alpha_p = 0.85$



(c) Cogging torque waveforms when  $\alpha_p = 0.95$

Fig. B.14. Variation of cogging torque with  $\alpha_p$  and  $h_e$ .

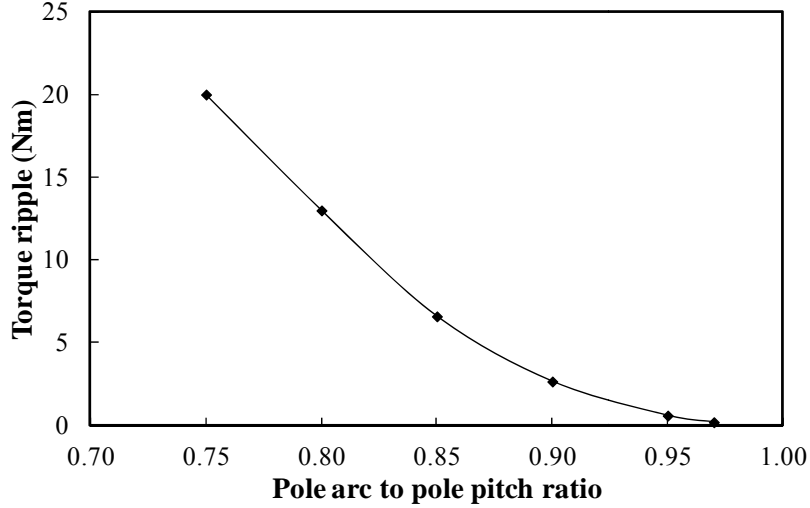


Fig. B.15. Variation of peak-peak value of minimum cogging torque with  $\alpha_p$ .

According to the torque ripple requirements, the candidate design can be obtained with sinusoidal shaping when  $\alpha_p=0.95$  and  $h_e=0.02\text{mm}$ . The cogging torque and full load torque will be shown later. The peak-peak value of its cogging torque is  $0.56\text{Nm}$  and the peak-peak value of the full load torque is  $1.9\text{Nm}$ . However, due to the magnet shaping, the average of full load torque is reduced to  $-163.7\text{Nm}$  when  $I_q = -8.24\text{A}$  and  $I_d = 0\text{A}$ .

### B.2.3 Investigation of Modified Sinusoidal Magnet Shaping

In order to achieve the stringing low torque ripple with less average torque reduction, another sinusoidal magnet shaping is developed and given by Fig. B.16, (B.1), and (B.2).

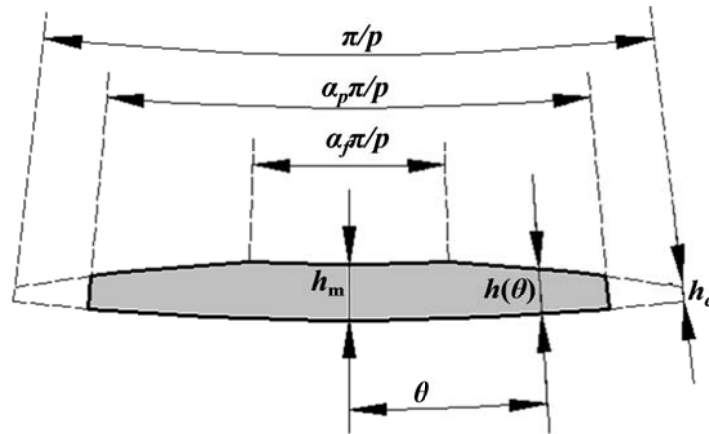


Fig. B.16. Illustration of modified sinusoidal magnet shaping.

$$h(\theta) = h_m \text{ when } \theta \leq \alpha_f \pi / (2p) \quad (\text{B.1})$$

$$h(\theta) = h_e + (h_m - h_e) \cos\left[\frac{\theta - \alpha_f \pi / (2p)}{\pi / (2p) - \alpha_f \pi / (2p)} \frac{\pi}{2}\right] \text{ when } \theta > \alpha_f \pi / (2p) \quad (\text{B.2})$$

where  $\alpha_f$  is the ratio magnet part with maximum height to the pole pitch. When  $\alpha_f = 0$  and  $h_e = 0$ mm, the magnet height varies sinusoidally.

By scanning  $\alpha_f$ ,  $\alpha_p$ , and  $h_e$ , another candidate design can be obtained using the modified sinusoidal shaping when  $\alpha_p = 0.95$ ,  $\alpha_f = 0.27$ , and  $h_e = 0.926$ mm. As will be shown later, its peak-peak cogging torque is 1.841Nm, average full load torque is -187.8Nm, and the peak-peak full load torque ripple is 2.89Nm.

### B.2.4 Comparison between Different Shaping Methods

In this section, the influence of sinusoidal and modified sinusoidal shaping methods is illustrated based on the comparison with the preliminary design. For the one having sinusoidal shaping,  $\alpha_p = 0.95$  and  $h_e = 0.02$ mm. For the modified sinusoidal shaping,  $\alpha_p = 0.95$ ,  $\alpha_f = 0.27$ , and  $h_e = 0.926$ mm. The other parameters remain the same as the ones listed in Table B-I. The performance of three designs, such as cogging torque, back EMF, on-load torque, is shown in Figs. B.18-B.21 and compared in Table B-III. It can be seen that:

- The torque ripples can be reduced effectively to meet the stringent requirements by both the sinusoidal and modified sinusoidal shaping methods.
- Using the sinusoidal shaping method, although it is able to achieve the stringent torque ripple requirements, its torque is reduced significantly. Compared with the preliminary design, the full load torque of sinusoidal shaped one is 14.3% lower.
- By using the modified sinusoidal shaping, the torque is compromised less. The full load torque is 14.7% higher than the sinusoidally shaped one and only 1.7% lower than the one of preliminary design.
- The third order EMF harmonic of the modified sinusoidally shaped design is significant.

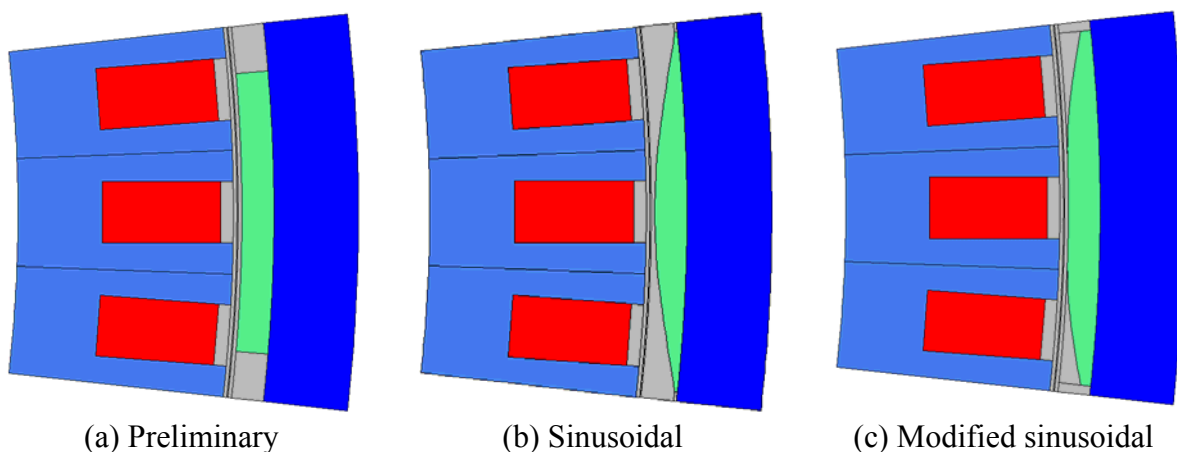


Fig. B.17. Cross-sections of three designs.

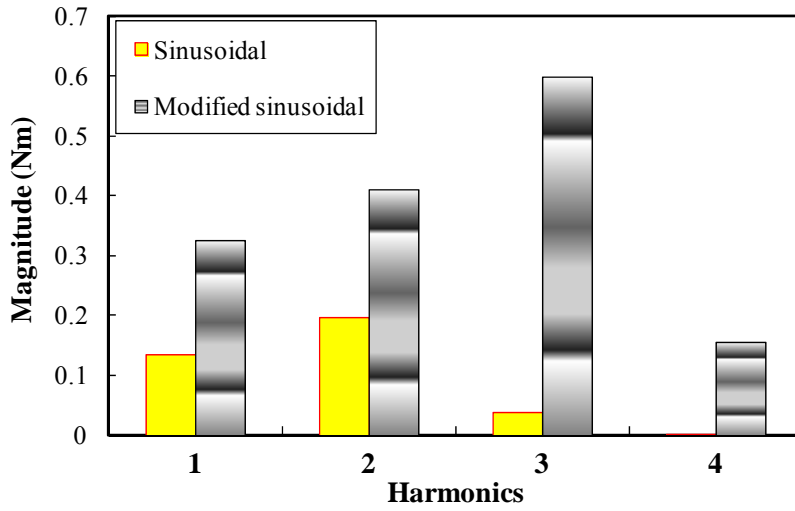
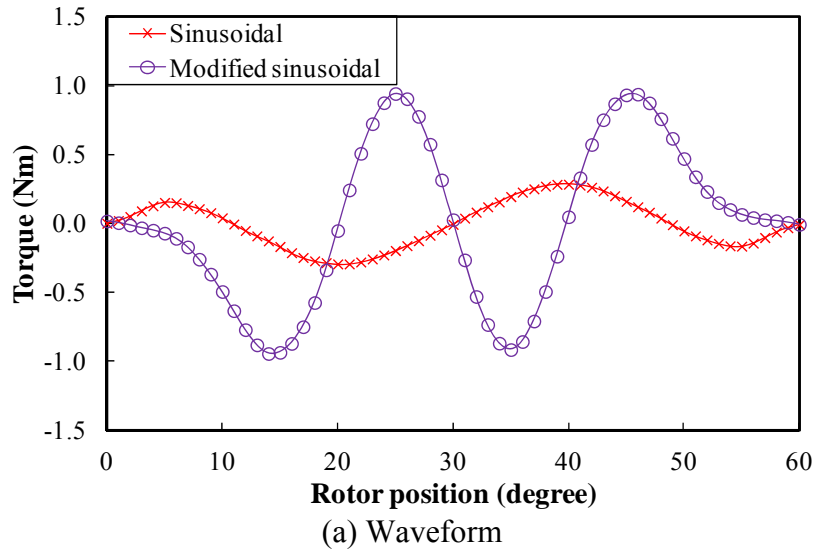
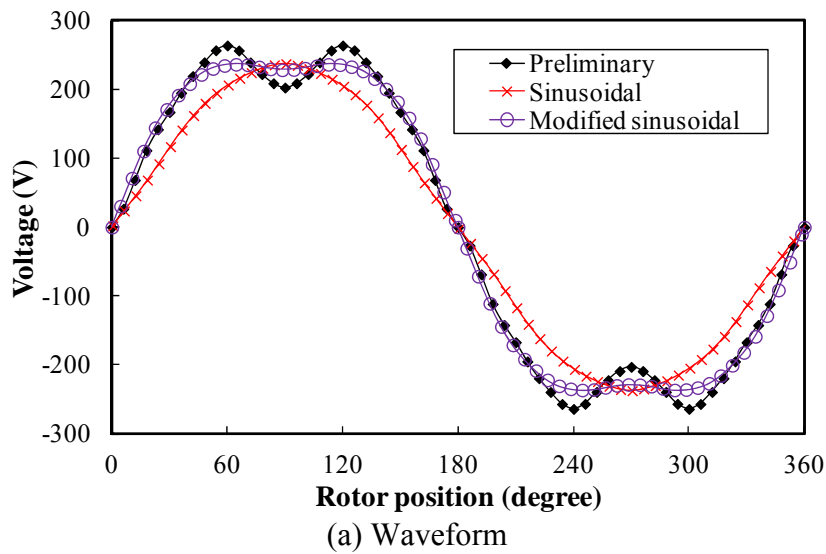
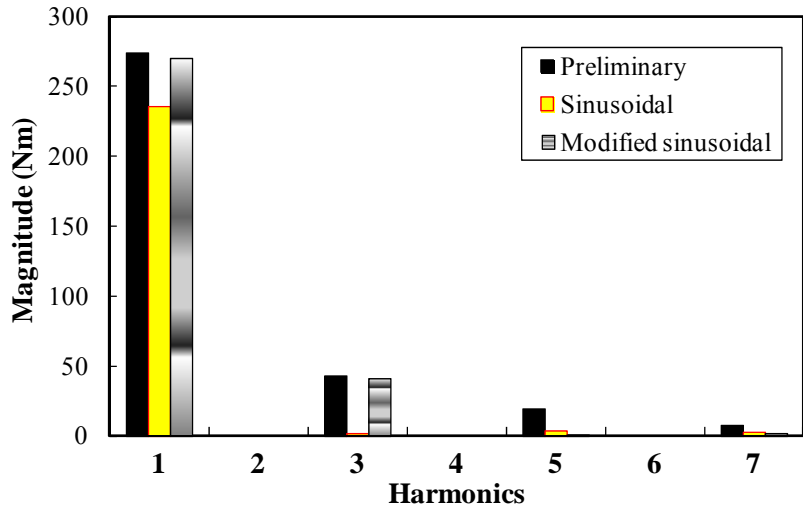


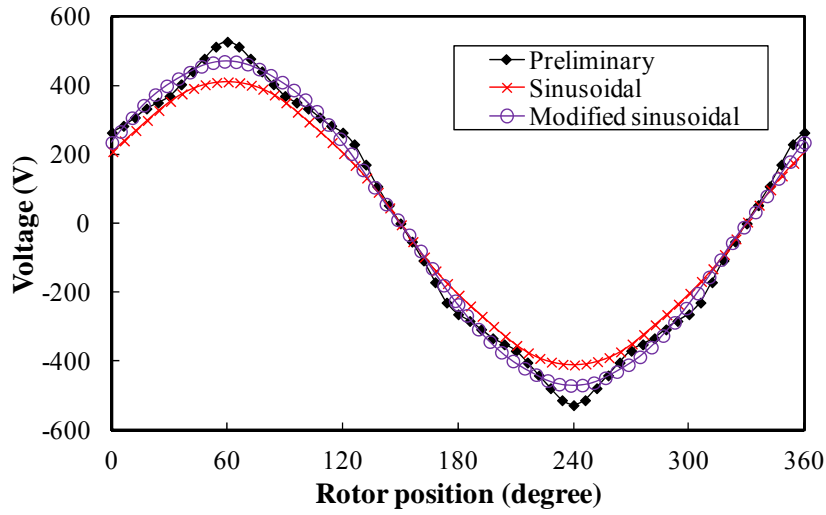
Fig. B.18. Cogging torque waveforms (preliminary one is shown in Fig. B.4 and not included due to its significant magnitude).



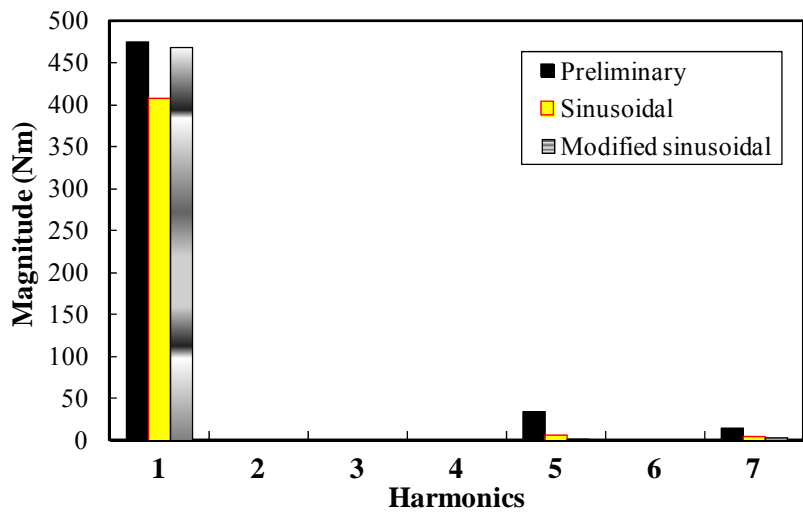


(b) Spectra

Fig. B.19. Phase back EMFs at 170rpm.



(a) Waveform



(b) Spectra

Fig. B.20. Line-line back EMFs at 170rpm.

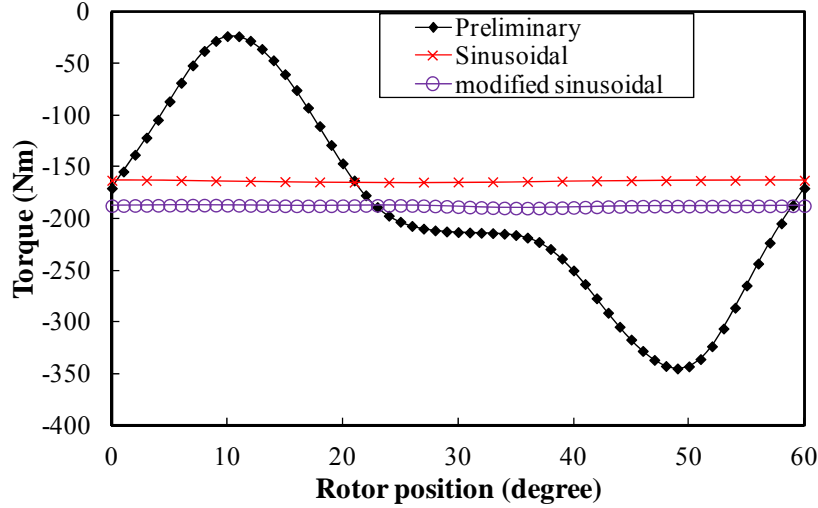


Fig. B.21. Full load torque waveforms when  $I_d = 0A$  and  $I_q = -8.24A$ .

Table B-III Comparison between three rotor shaping methods

	Preliminary	Sinusoidal	Modified sine.
Open circuit			
P-p cogging torque (Nm)	319.10 (83.4%)	0.57 (0.17%)	1.88 (0.5%)
Phase back EMFs @ 170rpm (V)			
Fundamental	273.90	235.72	270.62
3	43.17	1.86	41.14
5	19.48	3.39	0.60
7	7.81	2.16	1.70
Output torque @ $I_q=-8.24, I_d=0A$			
Average torque (Nm)	-191.13	-163.69	-187.85
P-p torque ripple (Nm)	321.29 (84.0%)	1.90 (0.58%)	2.89 (0.77%)

Based on the design using the modified shaping method, the number of turn per phase is increased to 406 to achieve the required average torque (194.84Nm). For the design having  $\alpha_p = 0.95$ ,  $\alpha_f = 0.27$ ,  $h_e = 0.926\text{mm}$ , and  $N_a = 406$ , the cogging torque remains the same as the cross marked one shown in Fig. B.18. The full load torque is shown in Fig. B.22. The average rated torque is 194.5Nm and its peak-peak torque ripple is 3.0Nm (0.7%).

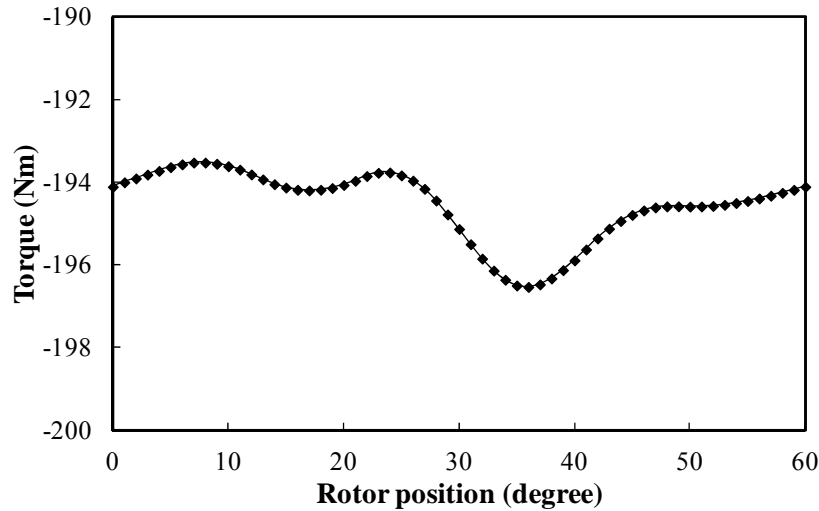


Fig. B.22. Full load torque waveform when  $\alpha_p = 0.95$ ,  $\alpha_f = 0.27$ ,  $h_e = 0.926\text{mm}$ ,  $N_a = 406$ ,  $I_d = 0\text{A}$ , and  $I_q = -8.24\text{A}$ .

### B.3 Slot Dimensions Optimisation

As can be seen from Fig. B.1(a), the slot is relative shallow and with large slot opening. Therefore, in this section, the torque variation with the slot dimensions is investigated. In order to consider the influence of magnetic saturation, the investigation is carried out by nonlinear FEA based on Opera. The other constraints and assumptions are listed as follows:

- The rotor remains the optimal magnet design using modified sinusoidal shaping, whose  $R_o = 420\text{mm}$ ,  $R_{ri} = 400\text{mm}$ ,  $h_m = 3.8\text{mm}$ ,  $\alpha_p = 0.95$ ,  $\alpha_f = 0.27$ , and  $h_e = 0.926\text{mm}$ . The airgap length remains 1mm.
- The stator outer diameter is 390.4mm. The stator inner diameter changes with slot depth to maintain the stator yoke thickness as 10mm. The slot wedge depth is 1mm.
- The number of turns per phase is 406.
- The full load copper loss remains the same. Therefore, the rated current changes proportionally to the square root of the effective slot area, i.e., the slot area below the slot wedge, as shown in Figs. B.23 and B.24

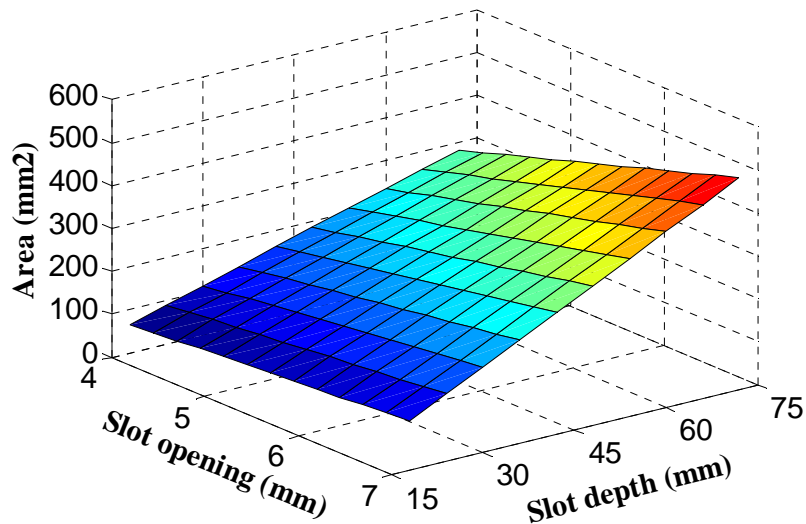


Fig. B.23. Variation of effective slot area with slot dimensions.

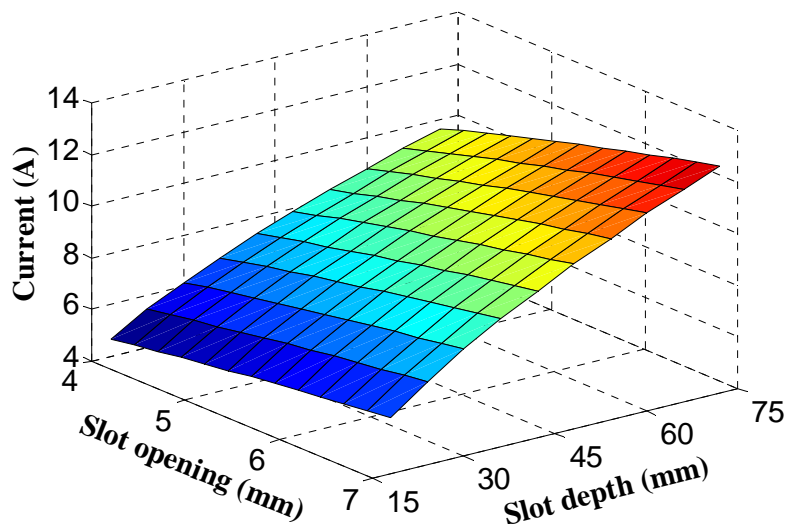


Fig. B.24. Variation of full load current with slot dimensions.

The variation of full load torque with slot dimensions is shown in Figs. B.25 and B.26. It can be seen that

- When the slot depth increases, the output torque first increases due to higher current and then decreases due to magnetic saturation.
- For each slot depth, there will be an optimal slot opening to maximize the torque and the optimal slot opening decreases with the slot depth.
- The average torque is maximum when the slot depth is 66mm and the slot opening is 5mm. However, the average torque saturates when the slot depth is larger than 51mm, as shown in Fig. B.26.

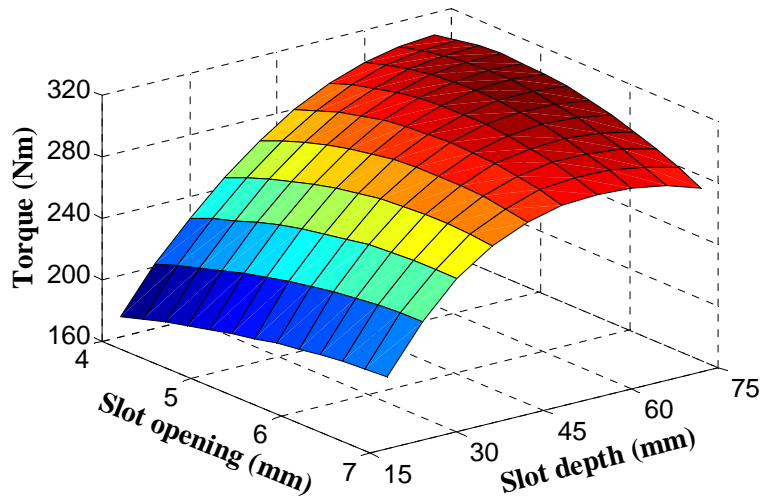


Fig. B.25. Variation of full load average torque with slot dimensions.

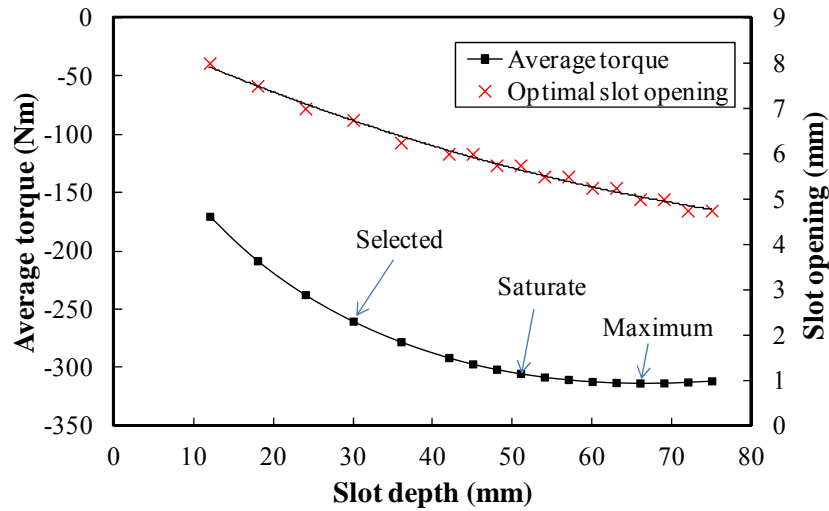
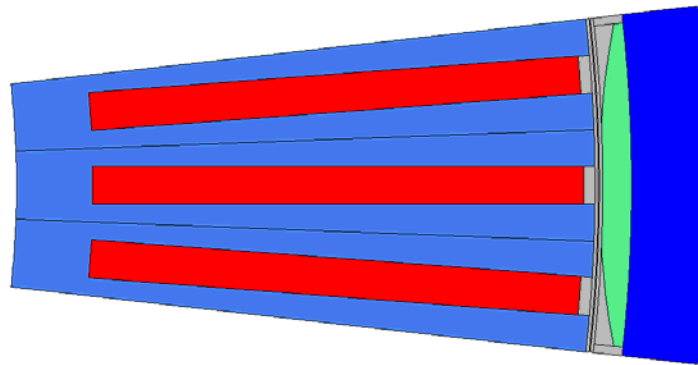


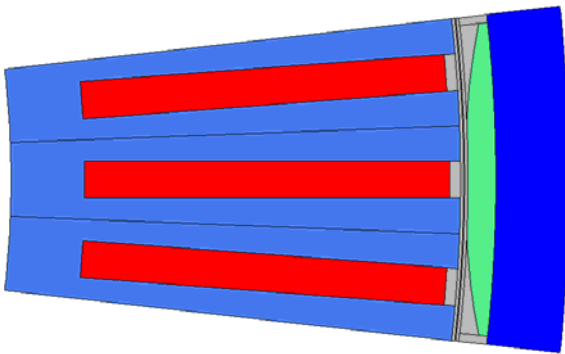
Fig. B.26. Variation of maximum average torque and optimal slot opening with slot depth.

On the other hand, as shown in Fig. B.27, even for the saturated design, the slot is very depth (51mm), which results in narrow minimum teeth width, heavy magnetic saturation, and high slot leakage. Based on the comparison in Fig. B.27 and Table B-IV, another design, whose slot depth is 30mm and the slot opening is 6mm, is selected for the actual prototype machine based on following considerations:

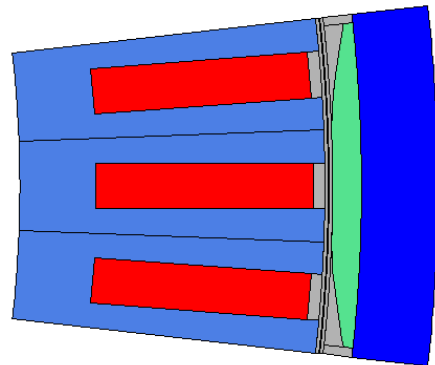
- Compared with the maximum torque design, the average torque is reduced from 313Nm to 257Nm. However, the slot area is almost halved from 322mm<sup>2</sup> and 171mm<sup>2</sup>. In other words, the copper mass is almost halved.
- The smaller slot depth to slot opening ratio eases the manufacturing, such as the end windings.
- Wider minimum tooth width also reduces the magnetic saturation and increases the stator mechanical stress.



(a) Maximum torque (slot depth = 66mm)



(b) Saturated (slot depth = 51mm)



(c) Selected (slot depth = 30mm)

Fig. B.27. Cross-sections of three designs.

Table B-IV Comparison of three designs with different slot dimensions

	Maximum design	Saturated design	Selected design
Slot depth (mm)	66	51	30
Slot opening (mm)	5	5	6
Effective slot area (mm <sup>2</sup> )	322	247	171
Minimum teeth width (mm)	4.6	5.7	6.1
Stator inner diameter (mm)	238.4	268.4	310.4
Phase current (RMS) (A)	10.35	9.07	7.54
Average torque (Nm)	-313	-302	-257
B at slot bottom (T)	1.83	1.74	1.69

### B.3 Investigation on Demagnetization Withstand Capability

As concluded previously, the magnet shaping can greatly reduce the torque ripples. However, the demagnetization withstand capability is consequently reduced due to the thinner magnet, especially for the pole edges. Therefore, in this section, the demagnetization withstand capability of the machine with shaped magnet is investigated.

Meanwhile, it is also concluded in section B.1 that the 3-phase short circuit is more critical than 2-phase short circuit in terms of the magnet demagnetization. Therefore, the investigation is based on the 3-phase short circuit. The external circuit and switch condition are the same as mentioned foregoing.

In order to consider the influence of rotor shaping, the investigation is based on the design, whose slot depth is 30mm, slot opening is 6mm,  $N_a = 406$ ,  $\alpha_p = 0.925$ ,  $\alpha_f = 0.22$ , and  $h_e = 1.011$ mm. The other conditions are listed in Table B-V and the probe locations are illustrated in Fig. B.28.

Table B-V Parameters for short circuit simulations

Rotor speed (rpm)	170
Phase resistance @ 95°C ( $\Omega$ )	1.269
$I_d$ (A)	0
$I_q$ (A)	8.245

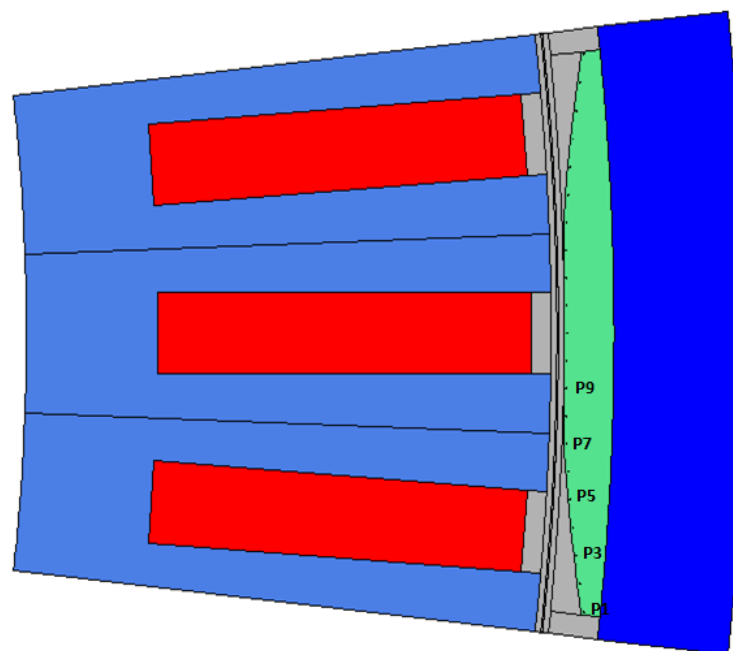


Fig. B.28. Locations of flux density probes.

The 3-phase short circuit performance of the investigated design is shown in Fig. B.29. It can be seen that the most part of magnet is demagnetized. Compared with the preliminary design in Fig. B.11, it can be concluded that this is mainly due to the influence of magnet shaping, since the short circuit currents are almost the same as the preliminary design.

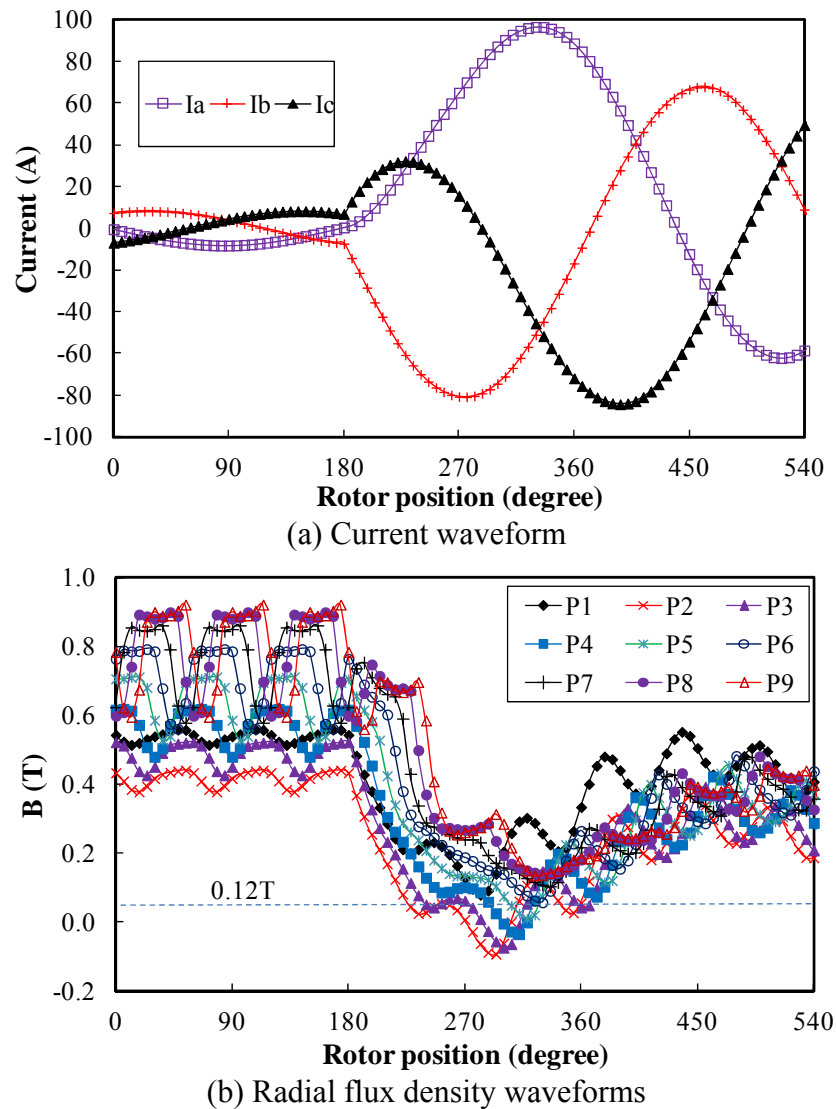


Fig. B.29. 3-phase short circuit performance from full load of machine having  $\alpha_p = 0.925$ ,  $\alpha_f = 0.22$ , and  $h_e = 1.011\text{mm}$ .

However, on the other hand, the rotor shaping is essential to achieve the stringent torque ripple requirement. Therefore, the ways of increasing the demagnetization withstand capability when the rotor shaping is employed are strongly desirable and can be developed as follows.

First, it can be developed based on reducing the demagnetizing field. It can be further divided into two categories. One is based on reducing the short circuit current, which has been discussed intensively in appendix A. The other one is based on increasing the

demagnetizing resistance, which equals to the sum of mechanical airgap length and magnet thickness for SPM machines.

Second, it also can be developed by increasing operation points of the magnet, which means thicker magnet or smaller airgap length. Since the minimum airgap length is limited by mechanical requirement, thicker magnets are preferred. However, in addition to the higher cost, it also should be noticed that the induced EMF and short circuit current will be higher as well due to the higher permanent magnet flux linkage.

Therefore, the variation of demagnetization during 3-phase short circuit is investigated based on two sets of  $h_m/\delta$ . One is  $h_m/\delta = 3.8$ , which is the same as preliminary design. It is also well known that the airgap flux density saturates with  $h_m/\delta$ , as illustrated in Fig. B.30. Therefore, the utilization of magnet is lower when  $h_m/\delta$  is higher. Therefore, another one is based on  $h_m/\delta = 3.0$ , which is lower than the preliminary design. However, due to lower  $h_m/\delta$ , the number of turn per phase has to be increased accordingly to produce the same average torque. The other constraints are listed in Table B.VI.

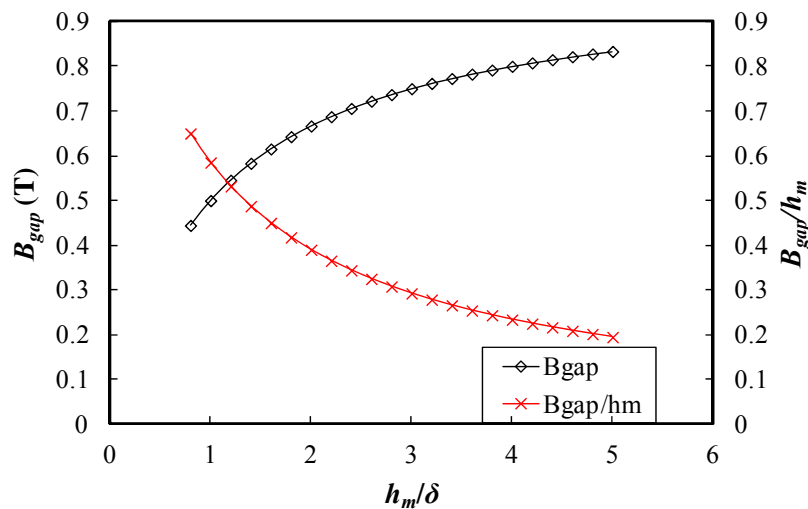


Fig. B.30. Variation of average airgap flux density with  $h_m/\delta$ .

Table B-VI Constraints for investigation on different airgap length

Parameters	Value	Parameters	Value
Shared			
Out diameter	420mm	Rotor yoke	10mm
Slot depth	30mm	Rotor yoke	10mm
Slot opening	6mm	Magnet shape	Proportional to Fig. B.28
$I_a$	5.83A		

$h_m/\delta = 3.8$			
$N_a$	406	$R_a @ 95^\circ\text{C}$	1.269 $\Omega$
$h_m/\delta = 3.0$			
$N_a$	420	$R_a @ 95^\circ\text{C}$	1.358 $\Omega$

The variation of lowest radial flux density during 3-phase short circuit from rated load is shown in Figs. B.31 and B.32 and compared in Table B-VII. It can be seen that, for both designs, the minimum equivalent airgap length to prevent irreversible demagnetization is 7.6mm. However, when  $h_m/\delta = 3.0$ , less magnet is used and hence it is cheaper. The larger airgap also eases the manufacturing. The only drawback is that the efficiency is slightly lower due to increased number of turns. Therefore, the prototype is developed based on  $h_m/\delta = 3.0$ .

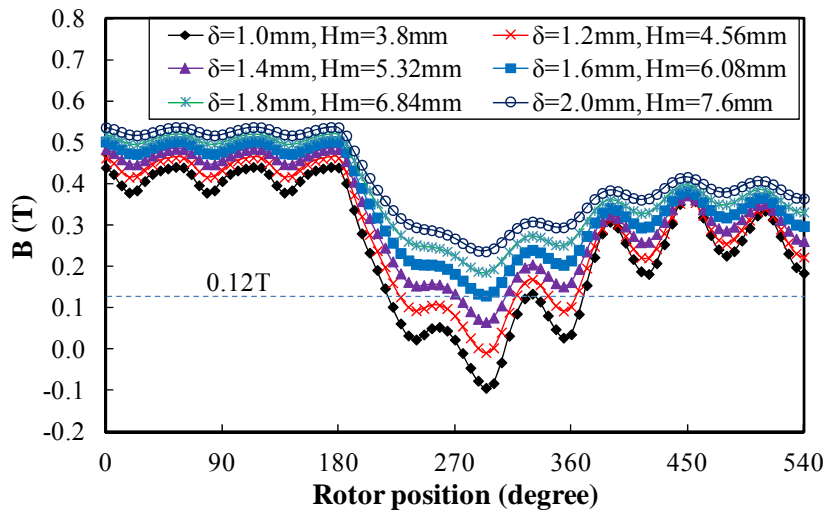


Fig. B.31. Radial component of lowest flux density in the magnet when  $h_m/\delta = 3.8$ .

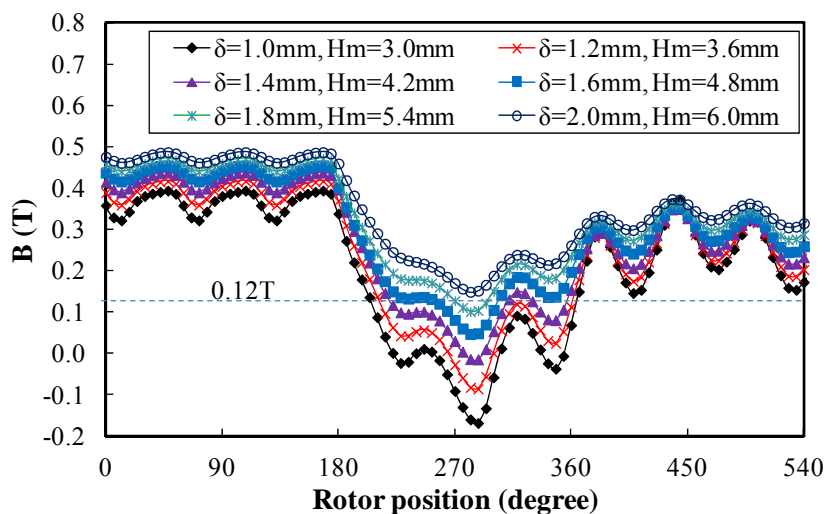


Fig. B.32. Radial component of lowest flux density in the magnet when  $h_m/\delta = 3.0$ .

Table B-VII Comparison between minimum airgap length with different  $h_m/\delta$

	$h_m/\delta = 3.8$	$h_m/\delta = 3.0$
Min. $B$ (T)	0.133	0.132
Min. $h_m + \delta$ (mm)	7.68	7.6
Airgap length $\delta$ (mm)	1.6	1.9
Magnet height $h_m$ (mm)	6.08	5.7

#### B.4 Development of Prototype Machine

Based on the foregoing investigation, it shows that the performance, such as efficiency, short circuit current, demagnetization withstand capability, is better than the preliminary design when the slot depth is increased to 30mm and slot opening is reduced to 6mm. However, since the mechanical drawings have been produced based on the preliminary design, the actual prototype machine still based on the same stator of the preliminary design with the rotor and airgap length updated.

Furthermore, since extra rotor teeth, as shown in Fig. B. 33, are needed to ease the manufacturing, the magnet shape is updated with the influence of extra rotor teeth considered.



Fig. B.33. Illustration of rotor teeth for manufacturing.

As a comparison, both the design of actual machine and the design having deeper slots are given in Table B-VIII and Figs. B.34-B.38.

Table B-VIII Summary of two qualified designs

		Deep slot	Actual
<b>ROTOR GEOMETRY</b>			
Rotor outer diameter	mm	426.4	
Rotor yoke thickness	mm	10	
Magnet		38HT	
Magnet height	mm	6	
Pole arc to pole pitch ratio		0.95	0.97
Flat arc to pole pitch ratio		0.2	0.2
Magnet edge height @ pole pitch	mm	2.3	2.15
Airgap length	mm	2	
Pole number	-	28	
<b>STATOR GEOMETRY</b>			
Stator inner diameter	mm	304	339.4
Stator outer diameter	mm	384	390.4
Stator yoke thickness	mm	10	
Slot number	-	84	
Slot depth	mm	30	15.5
Slot width	mm	6	7.3
Wedge height	mm	1	1.5
Stator core length	mm	110	
<b>WINDING DATA</b>			
Number of turns per phase	-	420	
Resistance DC 20°C	Ω	1.048	1.755
<b>OPEN CIRCUIT @ 20°C</b>			
<b>Phase EMF (peak) @ 170rpm</b>			
Fundamental	V	296.97	296.59
3	V	45.30	41.10
5	V	1.75	3.54
7	V	3.43	1.96
<b>Line-line EMF (peak)</b>			
Fundamental	V	514.37	513.71
5	V	3.03	6.18
7	V	5.95	3.41
Cogging torque (peak-peak)	Nm	1.64	1.64
Cogging torque/ rated torque	--	0.42%	0.41%
<b>FULL LOAD @ <math>I_a=5.83A</math></b>			
Current advance angle	Deg	180	
Average rated torque	Nm	-196.25	-195.83
Torque ripple (peak-peak)	Nm	2.52	3.03
Torque ripple/rated torque	--	0.44%	0.77%
Input power	W	3493.71	3486.23
Copper loss	W	138.64	231.97
Iron loss	W	59.94	59.96
Rated efficiency	--	94.33%	91.63%

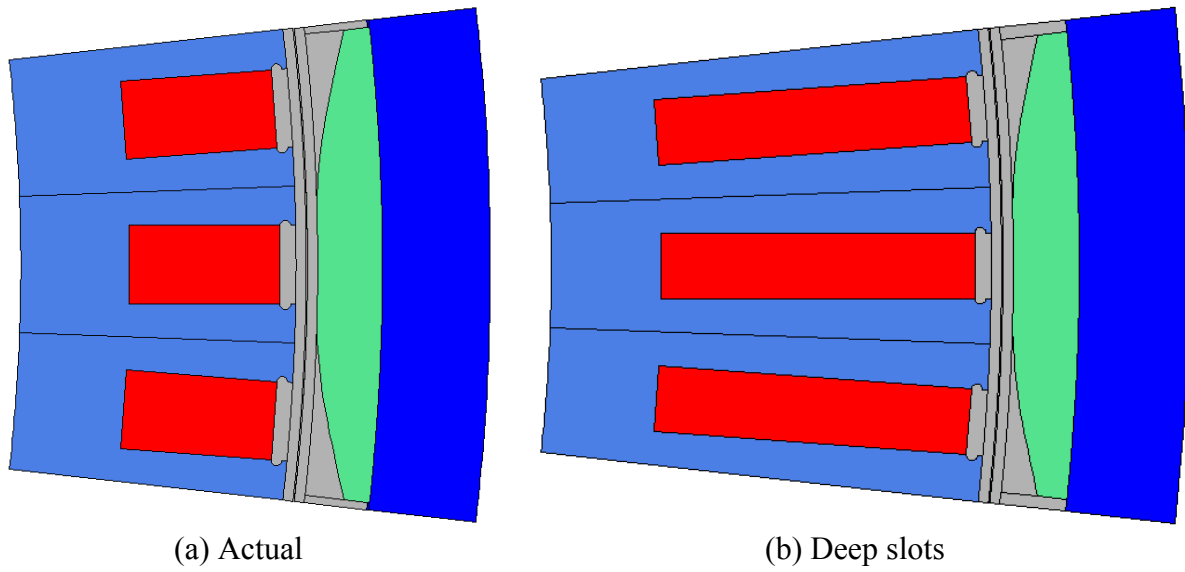


Fig. B.34. Cross-sections of two designs.

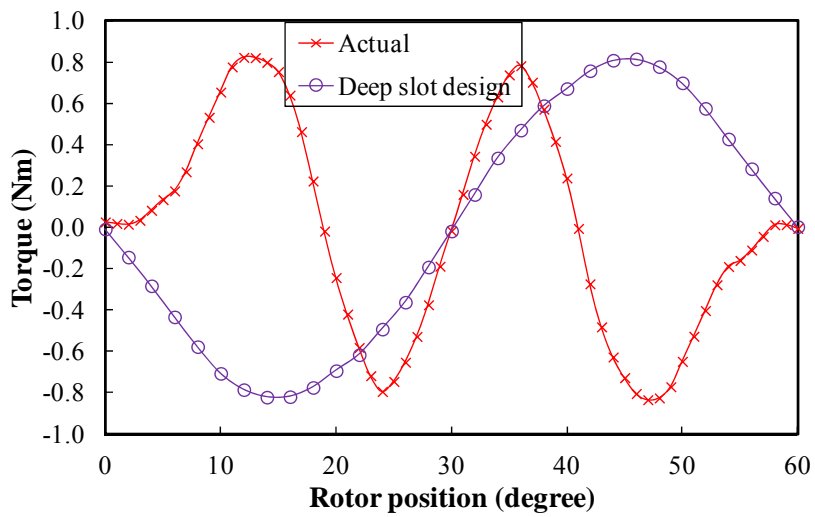
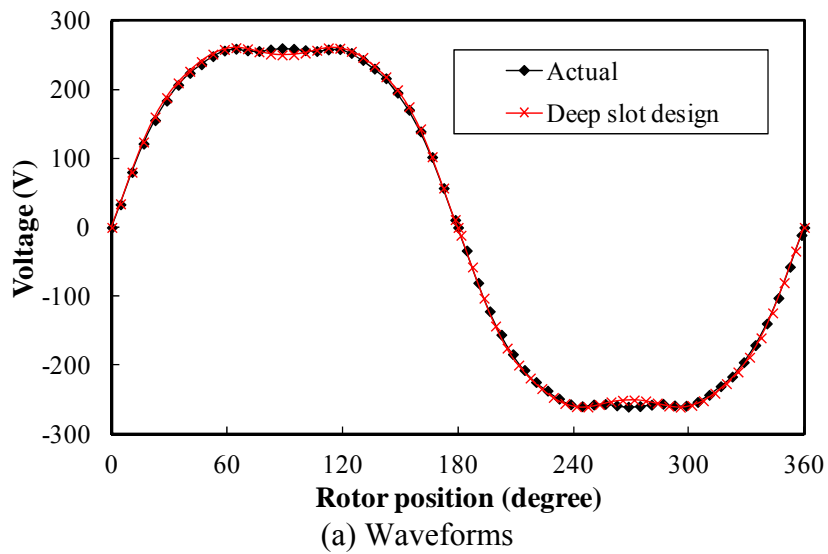
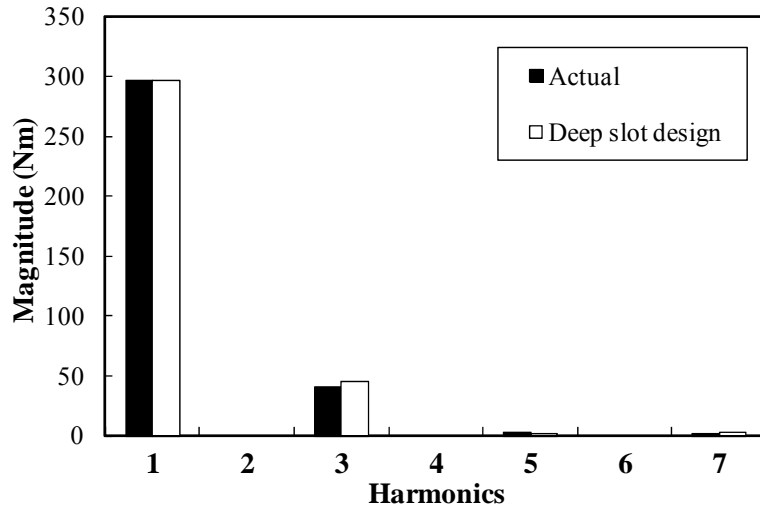


Fig. B.35. Cogging torque waveforms.

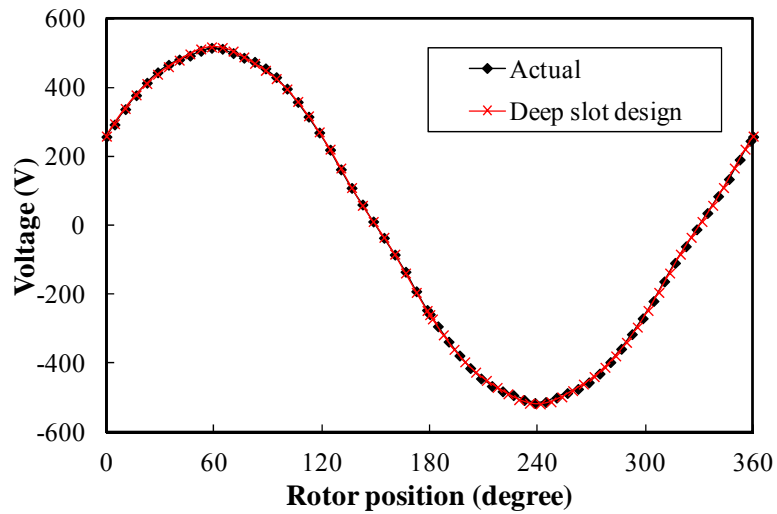


(a) Waveforms

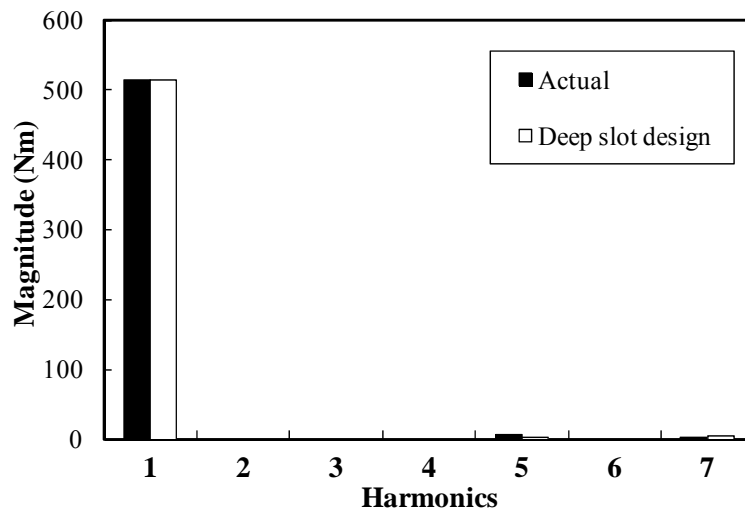


(b) Spectra

Fig. B.36. Phase back EMF waveforms and spectra when  $n = 170$ rpm.



(a) Waveforms



(b) Spectra

Fig. B.37. Line-line back EMF waveforms and spectra when  $n = 170$ rpm.

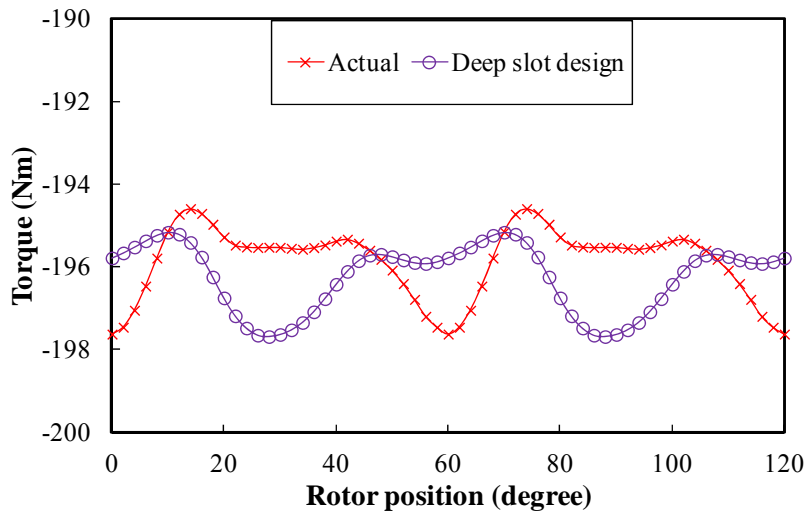


Fig. B.38. Torque waveforms when  $I_d = 0A$ , and  $I_q = -8.24A$ .

## APPENDIX C DESIGN OF EE AND PM PROTOTYPE MACHINES FOR COMPARISON ON ROTOR SHAPING AND SKEWING

In this section, the detailed design procedure of EE and PM prototype machines for the investigation of chapter 7 is reported.

### C.1 Design of EE Machine

#### C.1.1 Analytical Optimisation

The EE machine is developed from the PM prototype machine given in chapter 3 using the same stator.

As shown in chapter 6, for EE machines, the average output torque can be calculated as:

$$T = \frac{\pi \alpha_p k_\phi D_o \lambda_\delta}{16\sqrt{2} \rho p \delta'} \sqrt{\frac{L_{ef}^2 p_{cua} p_{cuf} A_a A_f k_a k_f}{(L_{ef} + L_a)(L_{ef} + L_f)}} \quad (C.1)$$

When the total copper loss is given, which is due to the efficiency and cooling constraints, the output torque peaks when

$$p_{cua} = p_{cuf} = p_{cu}/2 \quad (C.2)$$

If the total armature and field winding slot area of the whole machine ( $A_t = A_a + A_f$ ) is constant, the slot areas of armature and field windings can be optimised for minimum copper loss as

$$\partial T / \partial A_a = 0 \quad (C.3)$$

$$\text{i.e. } A_a = A_f = A_t/2 \quad (C.4)$$

Therefore, the maximum torque can be obtained when the slot area of armature winding equals to that of field winding.

On the other hand, the relationships between current densities, slot areas, and copper losses can be given as:

$$p_{cua} = 3I_a^2 R_a = \rho_{cu} (L_{ef} + L_{aend}) A_a k_{pa} J_a^2 \quad (C.5)$$

$$p_{cuf} = I_f^2 R_f = \rho_{cu} (L_{ef} + L_{fend}) A_f k_{pf} J_f^2 \quad (C.6)$$

Therefore, for the optimal design, in which  $p_{cua} = p_{cuf} = p_{cu}/2$  and  $A_a = A_f = A_t/2$ , the

relationship between the current densities can be given as

$$\frac{J_f}{J_a} = \sqrt{\frac{k_{pf}(L_{ef} + L_{aend})}{k_{pa}(L_{ef} + L_{fend})}} \quad (C.7)$$

In this section, the end windings of the distributed armature windings are approximated by half circles, which are 104.26mm per end. The end windings of concentrated field windings are approximated by rectangle, which are 44.25mm per end, assuming the rotor pole body width is half of pole pitch. Hence, for this EE machine, the optimal current density ratio is

$$\frac{J_f}{J_a} = \sqrt{\frac{0.6 * 1.947}{0.42 * 1.40}} = 1.4 \quad (C.8)$$

With the maximum current density fixed as 10A/mm<sup>2</sup>, the full-load field and armature current densities can be obtained as  $J_f = 10 \text{ A/mm}^2$  and  $J_a = 7.14 \text{ A/mm}^2$ . When the number of turn per pole is set to 100,  $I_f = 17\text{A rms}$ . When the number of turns per phase is set to 420,  $I_a = 19 \text{ A}$ .

### C.1.2 Current Phase Advance Angle Optimisation

The reluctance torque is neglected during the foregoing analytical optimization. The current phase advance angle is optimized further to take reluctance torque into the consideration.

Since it is a generator, the current phase advance angle is referred to the negative  $q$ -axis. As shown in Figs. C.1 and C2, the optimal current phase advance angles for half-load and full-load are 0° and -6° electrical, respectively.

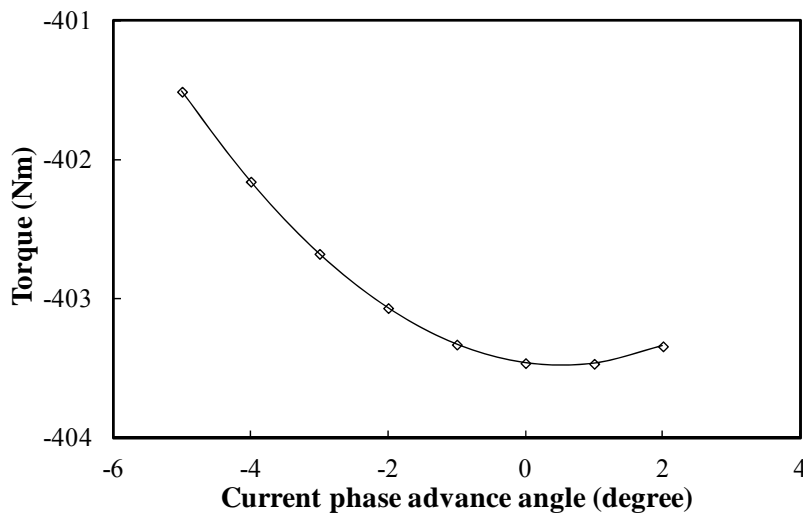


Fig. C.1. Variation of average torque with current phase advance angle when  $I_a = 13.4 \text{ A}$  and  $I_f = 12 \text{ A}$ .

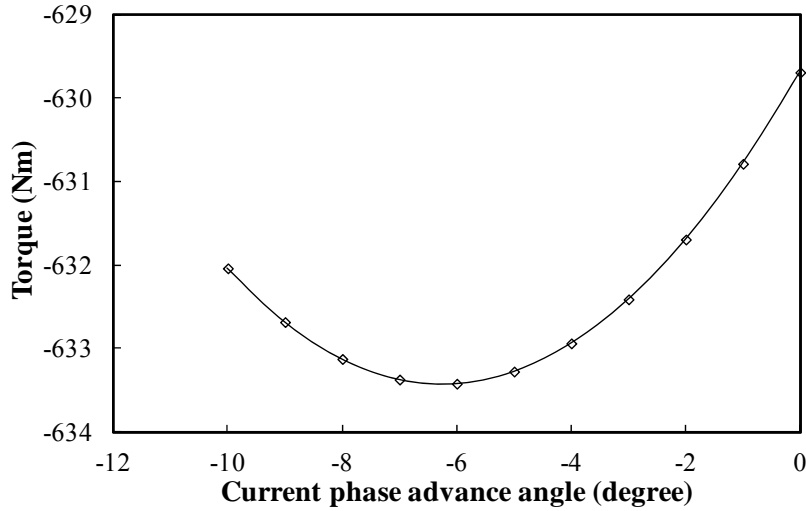


Fig. C.2. Variation of average torque with current phase advance angle when  $I_a = 19$  A and  $I_f = 17$  A.

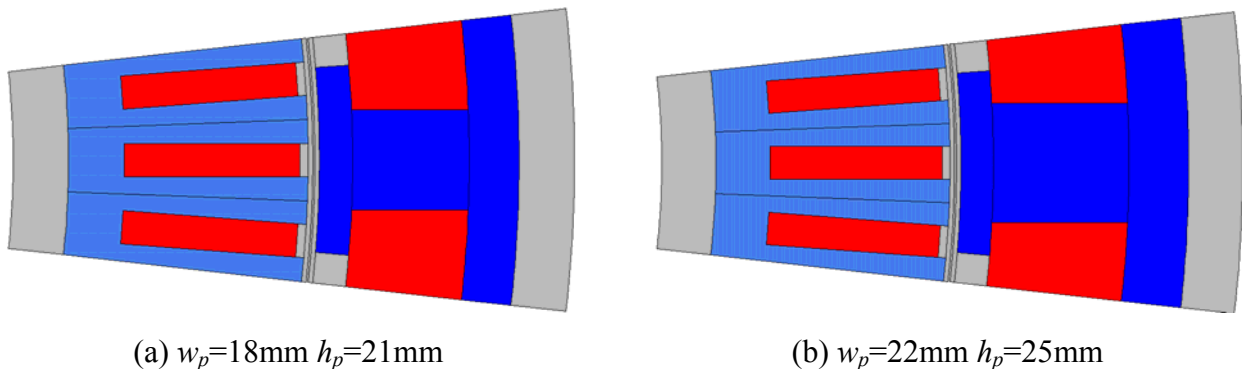
### C.1.3 Optimisation of Rotor Dimensions

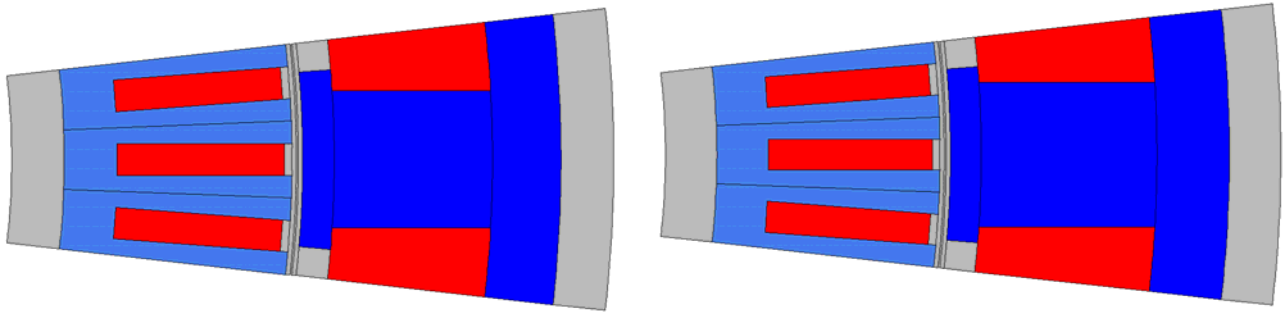
With the current phase advance angle fixed as optimal one, the rotor pole dimensions are optimised further.

As concluded in previous section, the output torque peaks when the rotor slot area is the same as the stator slot area. Based on the rectangular cross section of field wind slot area, the relationship of pole body width and pole body length can be obtained as:

$$h_p = \frac{A_f}{2p(\tau - w_p)} \quad (C.9)$$

The machine cross sections with different rotor poles are shown in Fig. C.3. According to the torque results in Fig. C.4, the torque increases slowly when the rotor pole body is wider. This is due to the lower magnetic saturation. However, the machine rotor is bigger, heavier, and more expensive. As a compromise between the torque and rotor weight, the rotor pole body width is selected as 22mm, which is half of the rotor pole pitch. Without rotor shaping, the cross-section of EE machine is shown in Fig. C.3.





(a)  $w_p=26\text{mm}$   $h_p=30\text{mm}$

(b)  $w_p=28\text{mm}$   $h_p=34\text{mm}$

Fig. C.3. Machine cross-sections with different rotor poles.

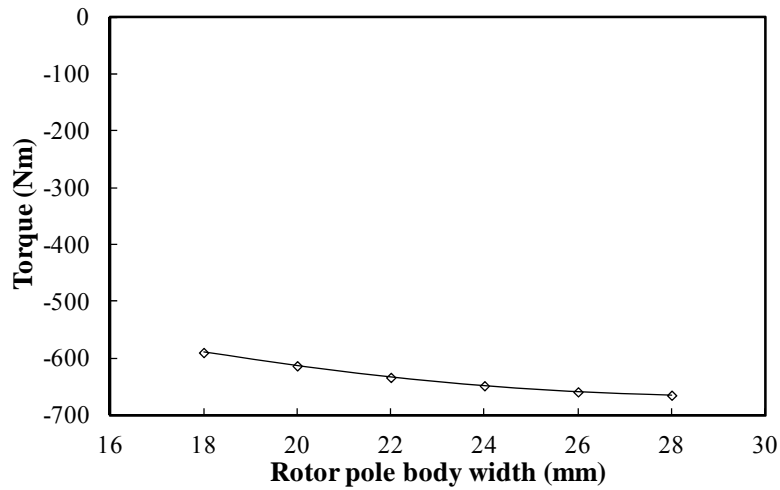
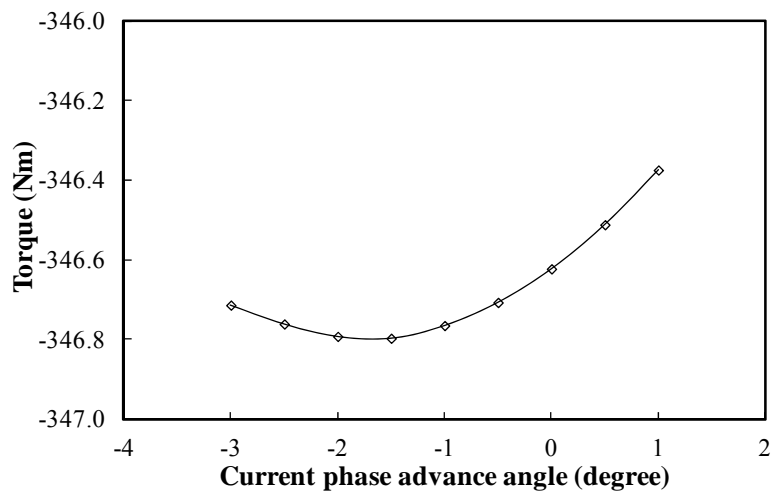


Fig. C.4. Definition of current phase advance angle.

## C.2 Design of PM Machine

In order to make fair comparison, it is better to optimise the PM machine under the same maximum armature current.

The optimal current phase advance angles for the PM machine are optimised first for the half and full loads, respectively, as shown in Fig. C.5.



(a)  $I_a = 9.5\text{A}$

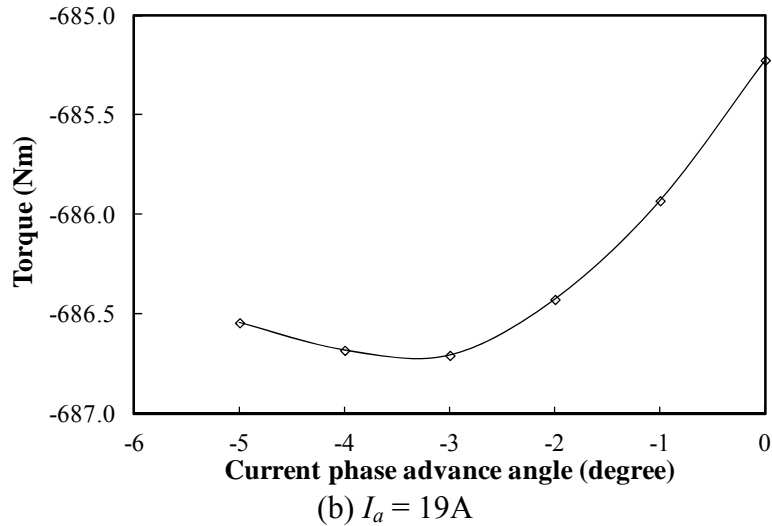


Fig. C.5. Average torque variation of PM machine with current phase advance angle.

Based on full load current and the optimal current phase advance angle, the magnet shape is also optimised to minimize the full load torque ripple, as shown in Fig. C.6. The full load torque ripple is the lowest when  $h_e=1.8mm$ . Therefore, the optimal PM machine is developed and shown in Fig. C.7.

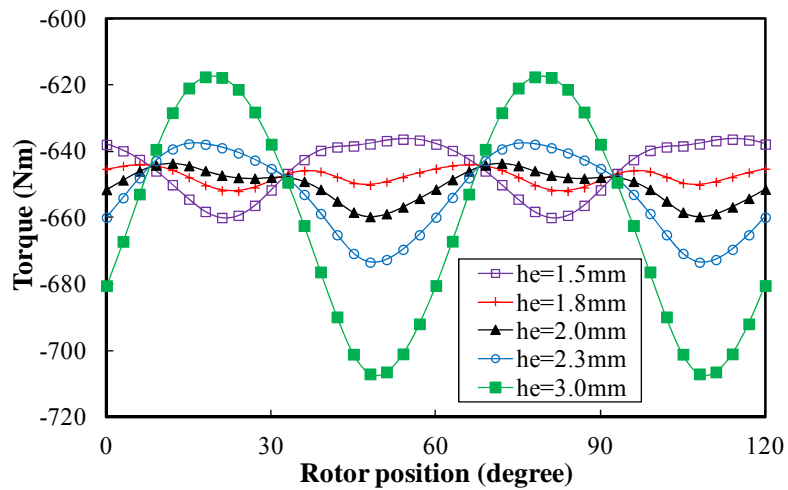


Fig. C.6. Torque variation with magnet shapes without skewing when  $I_a = 19A$ .

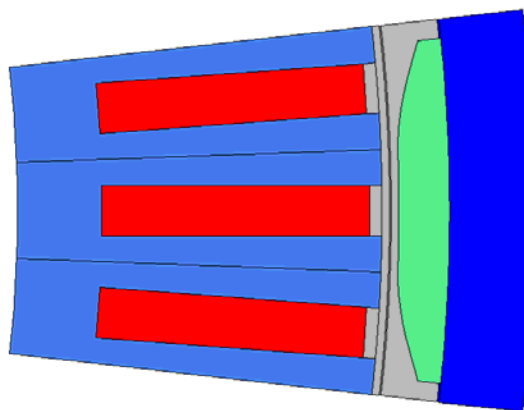


Fig. C.7. Cross-section of PM machine.

## APPENDIX D PUBLICATIONS

### Journal papers published or in press:

- [J1] W. Q. Chu and Z. Q. Zhu, "Investigation of torque ripples in permanent magnet synchronous machines with skewing," *IEEE Trans. Magn.*, vol. 49, no. 3, pp. 1211-1220, Mar. 2013.
- [J2] W. Q. Chu and Z. Q. Zhu, "Average torque separation in permanent magnet synchronous machines using frozen permeability," *IEEE Trans. Magn.*, vol. 49, no. 3, pp. 1202-1210, Mar. 2013.
- [J3] W. Q. Chu and Z. Q. Zhu, "On-load cogging torque calculation in permanent magnet machines," *IEEE Trans. Magn.*, in press.
- [J4] W. Q. Chu and Z. Q. Zhu, "Reduction of on-load torque ripple in permanent magnet synchronous machines by improved skewing," *IEEE Trans. Magn.*, in press.
- [J5] W. Q. Chu, Z. Q. Zhu, and Y. Shen, "Analytical optimisation of external rotor permanent magnet machines," *IET Electr. Syst. Transp.*, in press.

### Journal papers submitted:

- [J6] W. Q. Chu, Z. Q. Zhu, and J. T. Chen, "Simplified analytical optimisation and comparison of torque densities between electrically excited and permanent magnet machines," submitted to *IEEE Trans. Ind. Electron.*.

### Conference papers:

- [C1] W. Q. Chu and Z. Q. Zhu, "Analytical modeling and investigation of transient response of PM machines with 3-phase short-circuit fault," in *Proc. IEEE Int. Electr. Mach. Drives Conf.*, Niagara Falls, Canada, May 2011, pp. 125-130.
- [C2] W. Q. Chu and Z. Q. Zhu, "Optimal split ratio and torque comparison of surface-mounted permanent magnet machines having inner or outer rotor," in *Proc. IET Int. Conf. Power Electron., Mach. Drives*, Bristol, UK, Mar. 2012, pp. 1-6.
- [C3] W. Q. Chu, Z. Q. Zhu, and J. T. Chen, "Analytical optimization and comparison of torque densities between permanent magnet and electrically excited machines," in *Proc. XXth Int. Conf. Electr. Mach.*, Marseille, France, Sep. 2012, pp. 1192-1198.